IMRPOVING THE TRIBOLOGICAL AND CORROSION PROPERTIES OF ZR702 AND ZIRCALOY-4 ALLOYS BY CERAMIC CONVERSION TREATMENT

by

Shiling ZHANG



UNIVERSITY OF BIRMINGHAM

A Thesis submitted to

University of Birmingham

for the degree of

DOCTOR OF PHILOSOPHY

School of Metallurgy and Materials

University of Birmingham

December 2016

UNIVERSITY OF
BIRMINGHAM

University of Birmingham Research Archive

e-theses repository

This unpublished thesis/dissertation is copyright of the author and/or third parties. The intellectual property rights of the author or third parties in respect of this work are as defined by The Copyright Designs and Patents Act 1988 or as modified by any successor legislation.

Any use made of information contained in this thesis/dissertation must be in accordance with that legislation and must be properly acknowledged. Further distribution or reproduction in any format is prohibited without the permission of the copyright holder.

SYNOPSIS

Zirconium and its alloys are widely used as cladding materials in nuclear industry, as valves in chemical industry, and even as medical implants in the medical industry, because of their advantageous properties such as low thermal neutron cross section, good corrosion resistance, good biocompatibility and high mechanical properties. However, wear of zirconium components is a major issue for demanding applications due to the characterised poor tribological properties (low hardness and high friction coefficient). Corrosion has also long been reported to cause great economic losses. This project was therefore aimed to improve the tribological and corrosion properties of Zr702 (chemical grade) and Zircaloy-4 (nuclear grade) materials through ceramic conversion (CC) treatment.

To this end, a series of CC treatments at different temperatures for varying periods of time were therefore carried out on both Zr702 and Zircaloy-4 alloys. In addition, the first trial of duplex surface treatment was conducted on Zr702 alloy to study the response of the CC formed ceramic layer to oxygen boost diffusion (OBD) and to increase the oxygen diffusion zone (ODZ). Microstructural characterisations using optical microscopy, XRD, GDOES, SEM/EDX and TEM etc., were performed for all surface treated samples, and the mechanical, corrosion, and tribological properties of selected samples were evaluated.

The results have shown that the CC treatment can successfully produce a ceramic layer on both alloys via thermal oxidation. The ceramic layer is mainly made up of m-ZrO_2 with traces of t-ZrO_2. A substoichiometric oxide $ZrO_{0.27}$ is formed at the metal/oxide

interface with a preferred orientation with the substrate α-Zr. The oxide layer has a columnar structure and lateral cracks parallel to the metal/oxide interface is noticed. More lateral cracks have been found to form with the increase of the treatment temperature and/or time. The oxide layer formed on Zircaloy-4 alloy is thicker but with more pore/crack defects when compared with that formed on Zr702 under the same treatment condition.

Electrochemical polarisation tests have shown improved anti-corrosion property after most CC and duplex surface treatments due to the separation of substrate zirconium from the corrosion solution. Medium-temperature CC treated samples exhibit the best corrosion resistance: Zr702-5350, Zr702-5310 and Zr702-5610 for Zr702 alloy; Zry4-5310, Zry4-5610 for Zircaloy-4 alloy.

CC treatments investigated can also improve the wear properties of both Zr702 and Zircaloy-4. The optimal treatment conditions for Zr702 and Zircaloy-4 are found to be 530 °C/10 hours and 500 °C/10 hours with an improvement in wear resistance of 3.7×10^3 and 8.9×10^2 times respectively. The main wear mechanism has changed from adhesive wear for the as-received materials to mild abrasive wear of the CC treated samples. The optimal CC treated Zircaloy-4 (Zry5-5310) can effectively reduce the fretting wear of Zircaloy-4 in both DI water and 3.5 wt% NaCl by 19.2 and 18.7 times respectively due to the elimination of wear/galling craters.

Oxygen boost diffusion (OBD) in both two-step (CC+OBD) and three-step (CC+OBD+TO) duplex surface treatments can further increase the wear performance of Zr702 due to reduced porosity and cracks in the oxide layer and thickened oxygen diffusion zone.

ACKNOLEDGEMNTS

Firstly, I would like to express my sincere gratitude towards my supervisors Prof. Hanshan Dong and Dr. Xiaoying Li for their invaluable guidance and support on my PhD study. I could not imagine my PhD without their kind advices and patient mentor.

Also I would like to thank all of the help and encouragement that I received from my colleagues at Surface Engineering group, including Dr. Xiao Luo, Dr. Dennis Formosa, Dr. Kaijie Lin, Dr. Zhenxue Zhang, Dr. Yangchun Dong, Dr. Santiago Corujeira Gallo, Mr Shaojun Qi, Mr Behnam Mashtbozarg, etc.

My sincere thanks go to all of the technicians at School of Metallurgy and Materials such as Mr. Jaswinder Singh, Mr. Christopher Cooper, Mr Paul Stanley, Mrs Theresa Morris etc. for allowing me the access to the lab equipment and facilities. Special thanks should also be given to Dr. Daniel Reed for his selfless support on the *in situ* XRD test. Also all of the kind help from Prof. Zhenbing Cai (Southwest Jiaotong University, China) on the fretting test is fully acknowledged.

I would also like to show my full appreciation for the financial support from School of Metallurgy and Materials for kindly waiving my tuition fee and China Scholarship Council (CSC) for the maintenance stipend.

Last but not the least, I would like to express my gratitude to my family and friends, especially my parents and brother, for their constant love and support during both good and bad times.

CONTENTS

1 INTRODUCTION 1

1.1 Background 1

1.2 Aim and objectives 2

2 LITERATURE REVIEW 3

2.1 Zirconium alloys 3

2.1.1 Historic notes 3

2.1.2 Classification 5

2.1.3 Physical metallurgy 8

2.1.3.1 Phase transformation 8

2.1.3.2 Heat treatment 10

2.1.4 Properties and application of zirconium alloys 12

2.2 Degradation of zirconium alloys 15

2.2.1 Friction and wear of zirconium 18

2.2.1.1 Introduction 18

2.2.1.2 Friction of zirconium alloys 19

2.2.1.3 Wear of zirconium alloys 22

2.2.1.3.1 Adhesive wear of zirconium alloys 23

2.2.1.3.2 Abrasive wear 27

2.2.1.4 Fretting wear 30

2.2.1.5 Factors affecting wear of zirconium alloys 32

2.2.2 Corrosion of zirconium alloys 34
2.2.2.1 Introduction 34
2.2.2.2 Electrochemical corrosion of zirconium alloys 35
2.2.2.3 Factors affecting corrosion of zirconium alloys 38
2.3 Oxidation of zirconium alloys 39
2.3.1 Zr-O phase diagram 39
2.3.2 Oxidation kinetics 41
2.3.2.1 Pre-transition oxidation 41
2.3.2.2 Transition oxidation 43
2.3.2.3 Post-transition oxidation 44
2.3.3 Oxide microstructure 44
2.4 Surface engineering of zirconium alloys 47
2.4.1 Introduction of surface engineering 47
2.4.2 Surface coating of zirconium alloys 48
2.4.3 Surface modification of zirconium alloys 49
2.4.3.1 Ion implantation 50
2.4.3.2 Laser assisted surface treatment 50
2.4.3.3 Thermochemical and electrochemical methods 51
2.4.4 Ceramic conversion treatment and hybrid treatment 53
2.5 Summary 55
3 EXPRIMENTAL 57

3.1 Materials and sample preparation 57

3.2 Surface treatment 58

3.2.1 Ceramic conversion (CC) treatment 58

3.2.2 Duplex surface treatment 59

3.3 Characterisation and property evaluation 61

3.3.1 Microstructure characterisation 61

3.3.1.1 Preparation of metallographic samples 61

3.3.1.2 Optical microscopy 62

3.3.1.3 Scanning electron microscopy (SEM) 62

3.3.1.4 Glow discharge optical emission spectroscopy (GDOES) 63

3.3.1.5 X-ray diffraction (XRD) 64

3.3.1.5.1 *In situ* XRD 65

3.3.1.6 Transmission electron microscopy (TEM) 66

3.3.2 Mechanical property measurement 68

3.3.2.1 Microhardness and load bearing capacity 68

3.3.2.2 Nanoindentation 69

3.3.3 Corrosion test 71

3.3.4 Surface roughness and tribological test 72

3.3.4.1 Surface roughness 72

3.3.4.2 Reciprocating wear test 72

3.3.4.3 Coefficient of friction 74

3.3.4.4 Fretting wear test 75

4 EXPERIMENTAL RESULTS 76

4.1 Microstructure of as-received materials 76

4.2 Microstructure of CC treated samples 81

4.2.1 Surface morphology 81

4.2.2 Surface roughness 88

4.2.3 GDOES chemical composition depth distribution in sample layers 91

4.2.4 XRD analysis of the sample layer 93

4.2.4.1 Zr702 94

4.2.4.2 Zircaloy-4 99

4.2.4.3 Metal/oxide interface 103

4.2.4.4 *In situ* XRD 105

4.2.5 Layer structures 108

4.2.5.1 SEM observation 108

4.2.5.2 TEM characterisation 118

4.3 Microstructure of duplex treated (CC+OBD) samples 125

4.3.1 Surface morphology 125

4.3.2 Surface roughness 125

4.3.3 GDOES depth chemical composition of the sample layer 127

4.3.4 XRD analysis of the sample surface 130

4.3.5 Layer quality observation (SEM) 133

4.3.5.1 SEM observation 133

4.3.5.2 TEM characterisation 136

4.4 Mechanical properties 138

4.4.1 Hardness of CC treated samples 138

4.4.2 Hardness of duplex treated samples 145

4.4.3 Load bearing capacity 149

4.4.3.1 CC Treated samples 149

4.4.3.2 Duplex treated samples 153

4.5 Electrochemical corrosion 155

4.5.1 CC treated samples 155

4.5.1.1 Zr702 155

4.5.1.2 Zircaloy-4 162

4.5.2 Duplex treated samples 166

4.6 Tribological properties 168

4.6.1 Reciprocating wear test 168

4.6.1.1 CC treated samples 169

4.6.1.2 Duplex treated samples 179

4.6.2 Fretting test 184

4.6.2.1 Friction coefficients and fretting wear volume losses of tested samples 185

4.6.2.2 Post fretting observation 188

5 DISCUSSION 192
5.1 Microstructure of ceramic layer 192
5.1.1 Surface morphology 192
5.1.2 Phases evolution 194
5.1.3 Structure 196
5.1.4 Cracks 198
5.2 Oxidation kinetics 202
5.2.1 Reaction order and breakaway oxidation 202
5.2.2 Reaction process and activation energy 204
5.2.3 Role of alloying element (Sn) 210
5.3 Corrosion property 211
5.3.1 Pitting corrosion 212
5.3.2 Uniform corrosion 213
5.3.3 Defects accelerated localised corrosion 214
5.4 Tribological property 216
5.4.1 As-received Zr alloys 216
5.4.2 CC treated zirconium alloys 218
5.4.3 Duplex treated samples 222
6 CONCLUSIONS 225
7 FUTURE WORK 231
8 APPENDIX 232

8.1 List of figures 232

8.2 List of tables 244

8.3 List of abbreviations 245

9 REFERENCES 247

1 INTRODUCTION

1.1 Background

Zirconium and its alloys are materials of choice for water-cooled nuclear reactors due to their low thermal neutron absorption cross section, high corrosion resistance and adequate mechanical properties[1]; in addition, zirconium alloys are widely used for chemical processing equipment (such as pumps, valves, heat exchangers etc.) because of their excellent corrosion resistance in most corrosive solutions. Recently, zirconium alloys are also used to make such body implants as hip and knee joint prostheses due to their relatively good mechanical properties and good biocompatibility[2].

However, zirconium and its alloys are generally very soft (<250HV)[3] and characterised by poor tribological properties. Their coefficient of friction is high (~0.65) and their wear resistance is much lower than other materials for nuclear and chemical applications, such as nickel alloys and stainless steel[4]. For example, fretting wear has been reported to occur to Zr pressure tubes in nuclear power reactors, which raises a major safety concern[5]. In addition, corrosion induced failure has also long reported to occur zirconium components[6, 7] which can cause great economic losses on. Therefore, how to improve the wear and corrosion resistance of zirconium alloys and thus extend the life-span of demanding zirconium components is a timely task from both a scientific and technological point of view, which forms the primary theme of the present project.

Ceramic conversion treatment has been widely adopted on titanium alloys, and thus it is likely that a dense adherent ceramic layer can be formed on the surface of zirconium alloys. Therefore, it is necessary to study the responses of zirconium alloys to ceramic

conversion treatment and identify the optimised treatments for zirconium alloys to improve their tribological and corrosion properties.

1.2 Aim and objectives

The aim of this project was to enhance the tribological and corrosion properties of both nuclear grade Zircaloy-4 and commercial grade Zr702 zirconium alloys through ceramic conversion (CC) treatment. The specific scientific and technological objectives of this investigation were:

- To study the response of zirconium alloys to CC treatment based on thermal oxidation in air and the effect of oxygen boost diffusion (OBD) treatment on the pre-formed ceramic layer by CC treatment;
- To characterise the composition, phase constituents, microstructures and surface morphologies of the CC treatment and OBD treated zirconium alloy surfaces.;
- To assess the mechanical properties (hardness, Young's modulus and load bearing capacity) of the surface treated Zircaloy-4 and Zr702 alloys;
- To evaluate the tribological (friction and wear) and corrosion properties of the modified surfaces of Zr702 and Zircaloy-4 alloys;
- To study the mechanisms involved of Zr702 and Zircaloy-4 alloys to advance scientific understanding.

2 LITERATURE REVIEW

2.1 Zirconium alloys

2.1.1 Historic notes

The element zirconium, ranked the 19th in abundance of the earth's crust[8], was discovered by Klaproth in 1789. But it was not isolated as a metal until 1824, when Berzelius prepared a very impure metal powder by reduction of potassium fluorozirconate with potassium metal[9]. The reaction is governed by Equation 2.1-1.

$$K_2ZrF_6+4K \rightarrow Zr+6KF \qquad \text{Equation 2.1-1}$$

A hundred years later, a purified metal was produced by VanArkel and DeBoer using the iodide decomposition process, as shown in Equation 2.1-2. This process has been used till today as a method to purify zirconium and hafnium[10].

$$ZrI_4(solid) \xrightarrow{600℃} Zr(solid)+2I_2(gas) \qquad \text{Equation 2.1-2}$$

In 1947, W.J. Kroll at the U.S. Bureau of Mines in Albany developed the magnesium reduction method (Kroll process)[11] to extract the metal from zirconium tetrachloride, which is governed by the reaction (Equation 2.1-3).

$$2Mg(liquid)+ZrCl_4(gas) \rightarrow 2MgCl_2(liquid)+Zr(solid) \qquad \text{Equation 2.1-3}$$

During this period, Kaufman and Utermeyer corrected the measurements of the thermal neutron cross section of zirconium and found that zirconium has a low thermal neutron absorption cross section[10]. The favourable low thermal neutron absorption cross section of zirconium, together with its high resistance to severe corrosion environments,

especially in high temperature steam, gave rise to the idea of making use of zirconium as cladding materials in nuclear reactors, which provided the initial stimulus for the development of the zirconium industry. In the early 1950s, the highly purified zirconium was found to have inconsistent corrosion and oxidation properties[12], thus bringing forward the development of high performance zirconium alloys.

The most beneficial alloying element was found to be tin as it can reduce the harmful effect of nitrogen impurities within the alloy[13], and hence the first zirconium alloy, named Zircaloy-1 containing 2.5%Sn (% stands for weight percentage thereafter), was developed. This development was further improved upon allowing for the creation of Zircaloy-2 (1.5%Sn, 0.15%Fe, 0.1%Cr and 0.05%Ni) and Zircaloy-4(1.5%Sn, 0.2%Fe and0.1%Cr) alloys[14].

At a later time, niobium was added to zirconium alloys for improved in-reactor corrosion performance[15]. Zr-1%Nb was produced for pressurized water reactors and Zr-2.5Nb% was also reported to be very corrosion resistant. Both Zr-1%Nb and Zr-2.5Nb% are widely used in the nuclear industry[16].

Modern Zr-Nb-Sn alloys have been developed with a decrease of tin content while increasing the niobium content of the alloy. This is because the reduction of tin content was observed to be related to a decreased corrosion rate and also found to be able to delay the breakaway oxidation period in terms of corrosion kinetics[17, 18].

However, the use of zirconium and its alloys was initially limited to the governmental nuclear programmes; as soon as being available commercially, zirconium and its alloys quickly found their use in the chemical process industry[19]. In addition, zirconium is

non-toxic and has a relatively good biocompatibility, leading to its application in medical implants[2].

2.1.2 Classification

Specifications for zirconium and its alloys are issued by the American Society for Testing and Materials (ASTM) , which uses the Unified Numbering System (UNS) code -where R6XXXX designates zirconium[20].

Due to the low solubility of alloying elements in zirconium, the commercially available zirconium alloys can be generally classified into three series based on their alloying elements, i.e. Zr-Sn, Zr-Nb, and Zr-Sn-Nb alloys, with the binary phase diagrams of Zr-Sn and Zr-Nb shown in Figure 2.1-1 and Figure 2.1-2 respectively[21].

With regards to specific applications, zirconium alloys can also be divided into commercial grade and nuclear grade[14, 22], where the classification is largely based on the amount of hafnium (Hf) contained: nuclear grade zirconium has significantly lower level of Hf less than 0.010 %.

The compositions of most commonly used zirconium alloys with their UNS codes are listed in Table 2.1-1[12, 23, 24].

Table 2.1-1 Compositions of most commonly used zirconium alloys[12, 23, 24]

Alloy design (NUS No.)	**Composition (%)**									
	Zr+Hf (min)	Hf (max)	Sn	Nb	Fe	Cr	Ni	Fe+Cr	Fe+Cr+Ni	O (max)
Nuclear grades										
Zircaloy-2 (R60802)	--	0.010	1.20-1.70	--	0.07-0.20	0.05-0.15	0.03-0.08	--	0.18-0.38	--
Zircaloy-4 (R60804)	--	0.010	1.20-1.70	--	0.18-0.24	0.07-0.13	--	0.28-0.37	--	--
Zr-2.5Nb (R60901)	--	0.010	--	2.40-2.80	--	--	--	--	--	--
Zr-1.0%Nb-0.01%Sn	--	0.010	0.01	0.91	0.08	0.01max	0.01max	--	--	--
Commercial grades										
Zr702 (R60702)	99.2	4.5	--	--	--	--	--	0.2max	--	0.16
Zr704 (R60704)	97.5	4.5	1.0-2.0	--	--	--	--	0.2-0.4	--	0.18
Zr705 (R60705)	95.5	4.5	--	2.0-3.0	--	--	--	0.2max	--	0.18

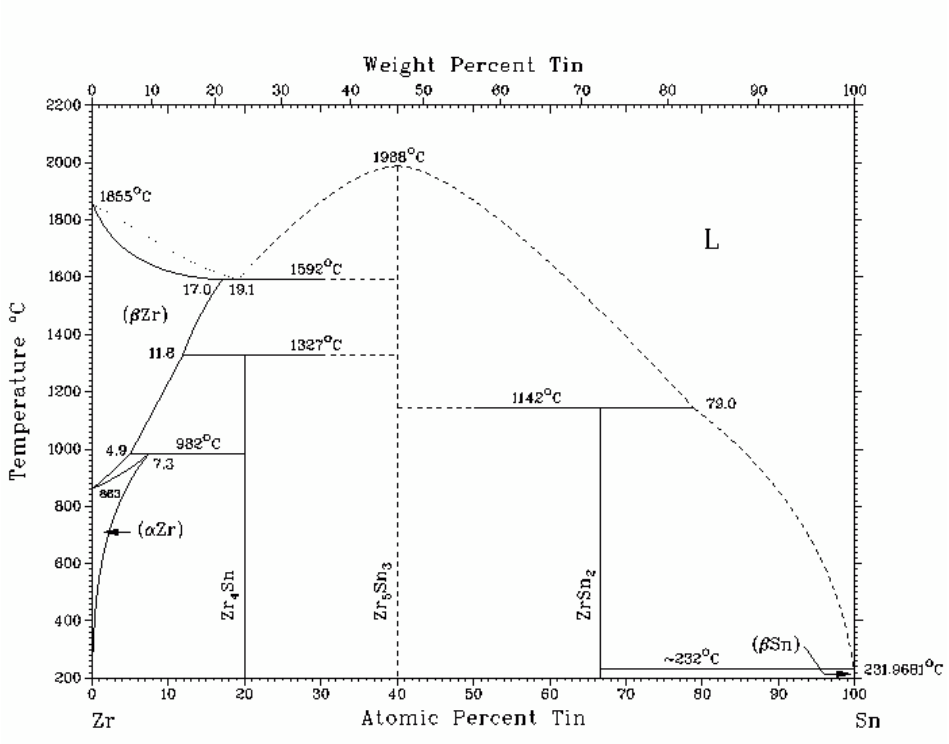


Figure 2.1-1 Zr-Sn binary phase diagram[21]

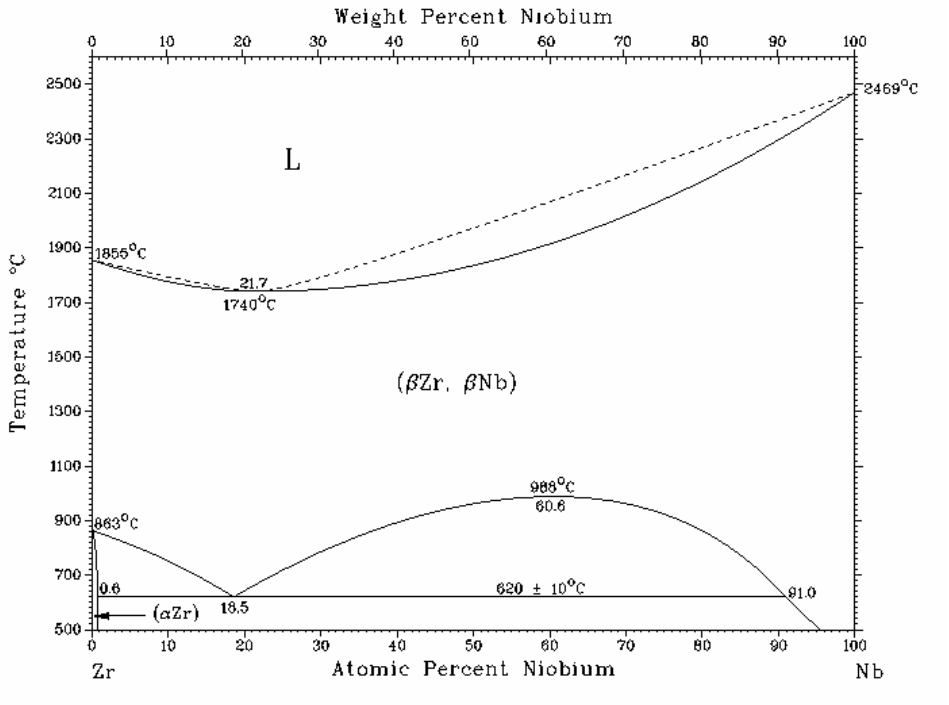


Figure 2.1-2 Zr-Nb binary phase diagram[21]

2.1.3 Physical metallurgy

2.1.3.1 Phase transformation

Zirconium has four different forms of crystal structure[25]: hexagonal ω phase, hexagonal close packed (HCP) α phase, and two body centred cubic (BCC) phases β and ω' phase respectively. Figure 2.1-3[25] depicts the temperature-pressure phase diagram for the phases mentioned above. It should be noted here that ω' phase is not included in the temperature pressure graph as it can only be obtained at a very high pressure up to 30GPa[25].

As shown in Figure 2.1-3[25], when the pressure increases at room temperature, the HCP structured α phase changes to the hexagonal structured ω phase at 2GPa[26]. Another allotropic transformation occurs at ambient pressure. When heated from room temperature to about 1136 K at the atmospheric pressure, zirconium transforms from α phase to β phase[10]. This temperature is noted as the transformation temperature.

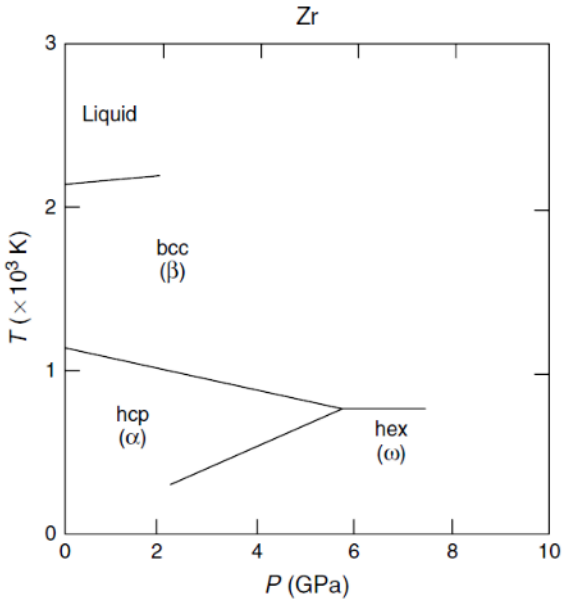


Figure 2.1-3 Temperature-pressure phase diagram of zirconium[25]

According to previous research, this transformation temperature is highly dependent on the alloying elements, which are therefore divided into two groups: α stabiliser and β stabilizer based on their effects on the transformation temperature[27].

α stabilizers, e.g. Sn, O, Hf, Al, etc., will stabilize the α phase, and increase the allotropic transformation temperature; an example of an α stabilised (Zr-Sn alloy) phase diagram is given in Figure 2.1-1[21].

β stabilizers, e.g. Nb, Fe, Cr, Ni, etc., decreases the transformation temperature. The phase diagram of a typical Zr with β stabilizer, i.e. Nb, is as shown in Figure 2.1-2[21].

It should also be noted that the overall effect of the alloying element on the transformation temperature is a combination of all stabilising effects. The real transformation temperatures of different zirconium alloys are therefore experimentally determined.

During the fabrication process, a HCP crystal structure will initiate and grow simultaneously as zirconium is cooling from β phase provided that the temperature is higher than the allotropic transformation temperature[25]. As the atomic packing factors of HCP and BCC cells are 0.74 and 0.68 respectively, there is a volumetric change and hence a generated distortion when allotropic transformation occurs. The alloying elements added in zirconium alloys as well as heat treatment insensitive and low solubility intermetallic compound formers, to some degree can address this distortion [28].

2.1.3.2 Heat treatment

In order to create zirconium alloys with a good combination of microstructure, chemical and mechanical properties, different heat treatment methods are required. One of the main principal basis of these treatments is the allotropic phase transformation, as the resultant product properties vary with the cooling rate and alloying elements, etc. The size and distribution of intermetallic compounds greatly depend on the cooling rates from β phase to α phase. The higher the cooling rate, the smaller the size and more randomly distributed the intermetallic compounds[10].

The commonly used heat treatment procedures for zirconium alloys are listed below.

1) Solution treatment: during this process, zirconium alloys will be heated to the β zone (> 865 ℃, alloys dependent), although generally the temperature chosen for this process will usually be between 1000 ℃ to 1065 ℃[29]). This temperature will be maintained for a period of time to allow for material homogenisation i.e. the complete dissolving of all second phase particles into either in grains or along grain boundaries. Significant grain growth could occur if zirconium alloys are held in the temperature for too long. Generally, no solution treatment is carried out on unalloyed zirconium[10].

2) Quenching: the material will be quenched after homogenization. It is during this step that allotropic transformation occurs, where β grains transform into α crystals. If cooled slowly, this will reveal a Widmanstätten structure, shown in Figure 2.1-4 (b); or if cooled rapidly, a martensitic transformation will occur resulting in the formation of a martensitic structure, shown in Figure 2.1-4 (c)[29]. Alternatively to the Widmanstätten and martensitic structures, and depending on the composition of the material, the β phase can be retained during quenching in some binary alloy configuration (Zr-Cr, Zr-

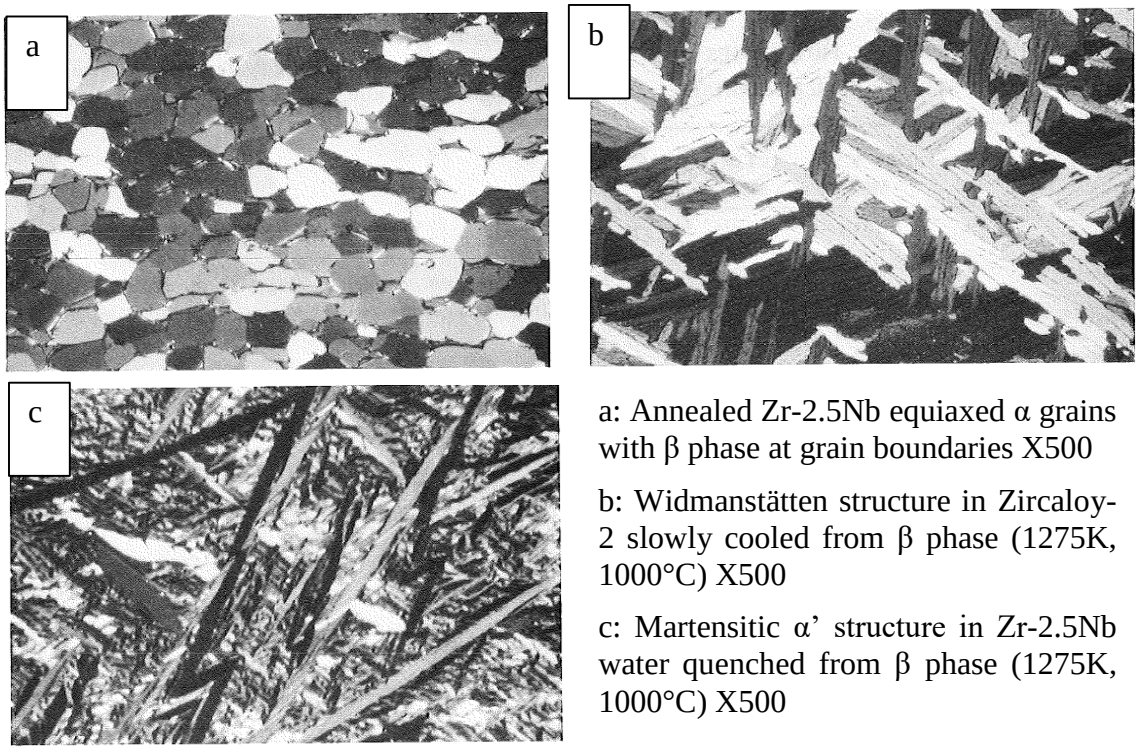
Nb, Zr-U etc.), provided that the material has higher than the critical concentrations, which is 7.2 wt%, 15 wt%, and 20 wt%[25, 30] for Cr, Nb and U respectively.

3) Cold work and recrystallization: for the fabrication of materials into different forms (shape and dimension) such as sheet, bar, plate etc. cold work like rolling, extrusion, forging etc. will be conducted. One important parameter is cold work percentage (%CW) which is measured by dimension reduction, given in Equation 2.1-4, to represent the degree of plastic deformation undergone by the worked material[31].

$$\%CW = \frac{A_0 - A_d}{A_0} \times 100 \qquad \text{Equation 2.1-4}$$

where A_0 and A_d are the cross sections before and after deformation respectively.

The main mechanism of hardening comes from the slip of crystal lattices initiated by twinning, a mechanism which occurs at the beginning of cold working process[10].



a: Annealed Zr-2.5Nb equiaxed α grains with β phase at grain boundaries X500

b: Widmanstätten structure in Zircaloy-2 slowly cooled from β phase (1275K, 1000°C) X500

c: Martensitic α' structure in Zr-2.5Nb water quenched from β phase (1275K, 1000°C) X500

Figure 2.1-4 Typical microstructures of zirconium alloys[29]

4) Annealing: after quenching and between different cold work processes, a series of heat treatments under the allotropic transformation temperature will be carried out in order to ensure a fine and uniform dispersion of second phases or compounds. Annealing treatment will restore ductility and allow further fabrication. For zirconium alloys, it is usually performed between 530 ℃ and 600 ℃, which depends on the previous cold working process and the specific material composition, to obtain the fully recrystallized materials[10, 29, 30]. On heavily cold worked materials heat treatments are normally conducted at temperatures of around 620 ~ 787 °C for times of 15 minutes or longer to accomplish the recrystallization process[10]. The resultant microstructure, shown in Figure 2.1-4 (a)[29], is an equiaxed geometry of zirconium grains with β-Nb precipitates located at the α grain boundaries. For better mechanical properties, the last annealing is often conducted at a reduced temperature to avoid complete recrystallization. This is in a stress relieved state, characterized by elongated grains and a high density of dislocations[13].

2.1.4 Properties and application of zirconium alloys

Zirconium is a greyish-white lustrous metal which has a relative density of 6.52 mg/cm^3 and a melting point of 1860 °C. Table 2.1-2 lists the main physical properties of zirconium [3, 32]. As mentioned earlier (section 2.1.3.1), zirconium has a hexagonal close-packed (HCP) crystal structure, shown in Figure 2.1-5, at ambient conditions. The HCP structure leads to strong directional property variations as given in Table 2.1-2. The strong anisotropy has a profound influence on the engineering properties of zirconium, especially in plastic deformation of the material. The low coefficient of thermal expansion (CTE), together with the high melting point, makes zirconium and its

alloys ideal for high temperature applications such as high temperature fuel cells, ceramic tubes etc.[8].

Zirconium and its alloys also exhibit a high affinity with oxygen[33]. When zirconium is exposed to air, a thin oxide layer of about 10 ~100 nm thickness is formed on the top surface[34]. Meanwhile, owing to zirconium's high reactivity with oxygen, the metal is frequently used as a gas getter in vacuum atmosphere. In such applications caution must be taken as zirconium, especially in powder form, ignites easily in air.

Table 2.1-2 Typical physical properties of zirconium [3, 32]

Atomic number	**40**
Atomic weight	91.2
Density at 300K	6.5mg/m^3
Hardness	<250HV
Melting temperature	2125K(1850°C)
Transition temperature	1135K(862°C)
Coefficient of thermal expansion at 570K	[11$\bar{2}$0] direction 6.3×10^{-6}/K [0001] direction 10.4×10^{-6}/K
Specific heat at 300K	276J/(Kg·K)
Thermal neutron capture cross section	microscope 0.18 barn macroscope 0.008cm^2/cm^3
Electric resistivity	0.44μΩ·m
Young's modulus at 300K	[11$\bar{2}$0] direction 99GPa [0001] direction 125GPa
Poisson's ratio at 300K	0.35
Lattice parameters at 300K	Hexagonal α a_0=0.323nm c_0=0.515nm Body centred cubic β a_0=0.359nm

At the same time, zirconium and its alloys are widely used in aggressive corrosive environments including high temperature steam water, i.e. chemical industry applications as valves and agitators pumps etc.[19, 28, 33, 34]. The excellent corrosion resistance, as reported[34], is attributed to the formation of the thin oxide film on the surface.

Due to their low thermal neutron absorption cross section (0.18 barn), as well as their high corrosion resistance and adequate mechanical properties, Zr alloys are also the materials of choice for the water-cooled nuclear reactor industry mainly [1]. The alloys used in nuclear industry are mainly Zr-Nb and Zr-Sn alloys[35]. And calendria tube, pressure tube, garter springs, fuel cladding and spacer are components where these alloys are used[36], with schematic diagram of fuel assembly for Pressurised Water Reactors (PWR) and Boiling Water Reactors (BWR) shown in Figure 2.1-6 (a) and (b) respectively[37]. Typical alloys used in nuclear reactors are as given previously in Table 2.1-1.

Zirconium is non-toxic and biocompatible which also enables the material to be used in the food processing industry. Meanwhile, zirconium alloys have also been used in medical application such as hip and knee joint prostheses[2].

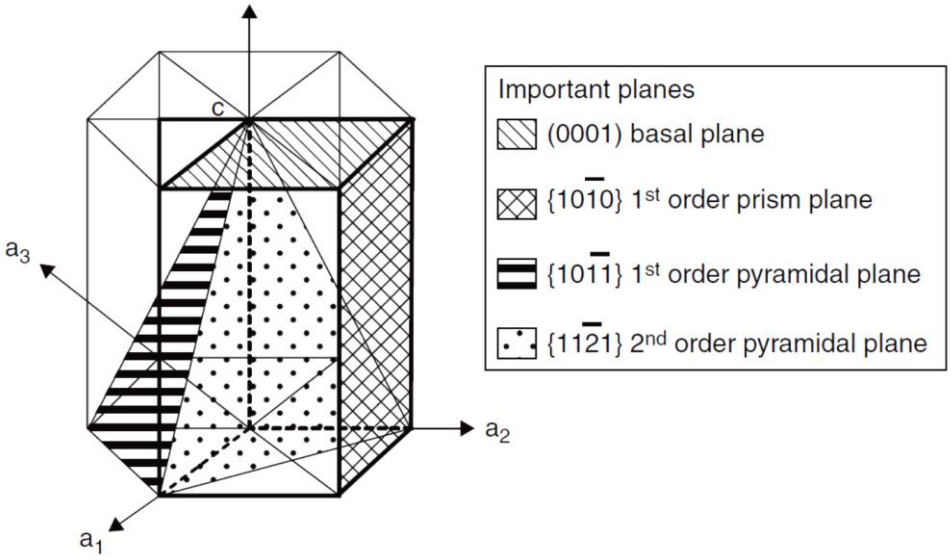


Figure 2.1-5 HCP crystallographic of Zirconium[32]

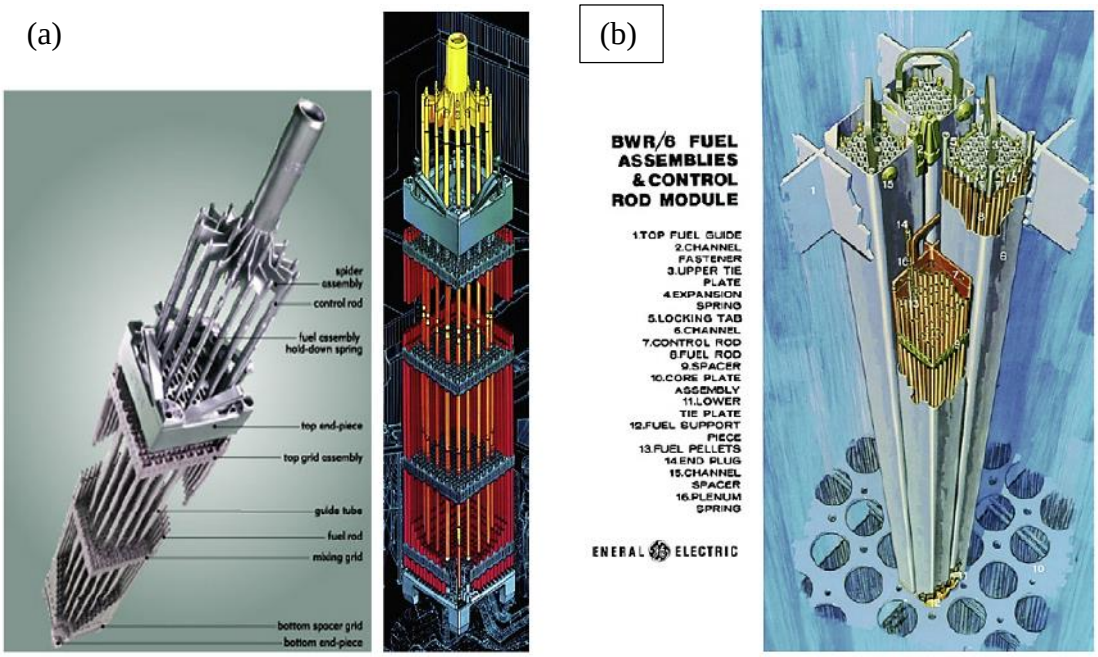


Figure 2.1-6 Fuel assembly and control rod cluster used in (a) PWR and (b) BWR[37]

2.2 Degradation of zirconium alloys

Despite of their wide application, zirconium alloys are also characterised by their poor tribological properties. They generally exhibit a low hardness (< 250HV), as given in Table 2.1-2, together with a high Coefficient of Friction (CoF) ≈ 0.65[3]. Zirconium

also has a high tendency to gall and seize when sliding in contact with other materials[38]. Research has been directed towards addressing this problem so as to improve the life-span of different zirconium components. Reasons which cause their failures include fretting wear, corrosion, and hydrogen embrittlement, which are detailed below.

Zirconium is susceptible to wear and fretting, either in zirconium claddings induced by the interaction between the cladding and spacer grids and Pellet Cladding Interactions (PCI)[39] as well as flow induced vibration[40], or in orthopaedic implants[41] such as screw–plate interfaces and modular connections of joint replacement components. And hence it can induce wear of zirconium components which would lead to the exposure of the fuel pellet, i.e. leaking.

Despite the fact that zirconium alloys exhibit an excellent resistance to a wide range of corrosive media including common acid and alkalis[10], superheated water, high temperature steam[1] etc., different forms of corrosion such as pitting[42, 43], nodular corrosion[44], stress corrosion cracking[45, 46], galvanic and crevice corrosions[42] have been reported. Therefore, corrosion of zirconium parts has also caused a great economic impact.

Hydrogen Embrittlement (HE) is a hydrogen assisted environmental degradation process happening mainly in nuclear applications, which is formally called hydrogen embrittlement, hydrogen enhanced failure, hydrogen attack, hydrogen-assisted degradation[35]. With a low solubility of only 0.07 wt%, shown in Zr-H phase diagram in Figure 2.2-1[21], zirconium hydride which is characterised by its low ductility[47] forms and precipitates. This hence leads to either short-term loss of toughness induced

failure or a stable, time-dependent crack growth called Delayed Hydrogen Cracking (DHC)[48].

Thermal and irradiative induced creep accompanies the macroscopic mechanical variations of zirconium such as hardening[49]. It can also limits internal pressure of the cladding to below primary loop operating pressure which therefore can cause 'ballooning' of the cladding materials[35].

Of those failures, wear and corrosion are of the most interest to current study and hence are further reviewed in following subsections.

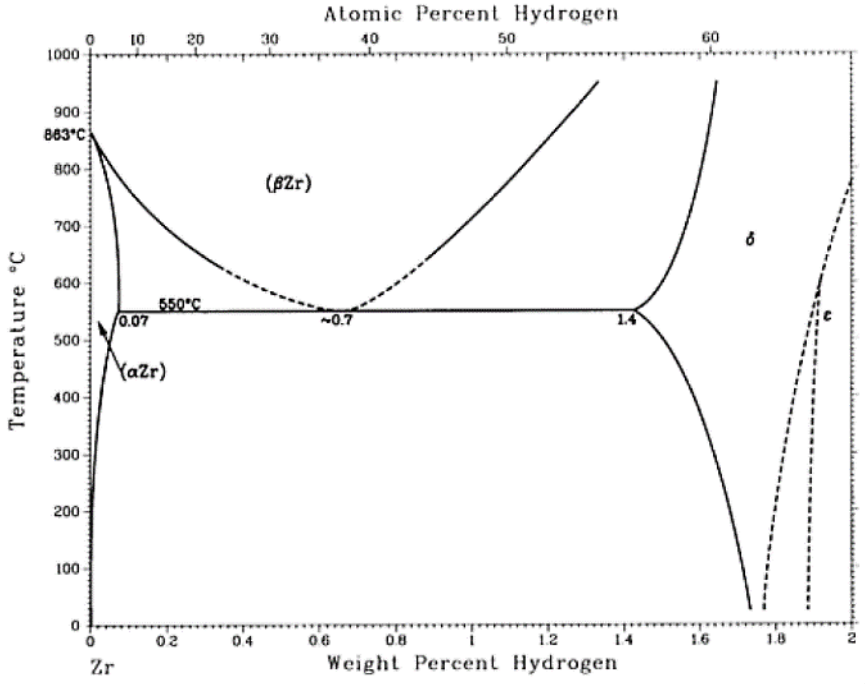


Figure 2.2-1 Zr-H binary phase diagram[21]

2.2.1 Friction and wear of zirconium

2.2.1.1 Introduction

Wear is the loss of material from contacting surfaces which have a relative motion to one another. Along with fatigue and corrosion, wear has been known as one of the three major factors which cause premature failure and hence limit the life and performance of engineering components and systems[50, 51]. Different techniques such as; reciprocating sliding[52, 53], ball/pin on disc[36, 54, 55] and cylinder-to-cylinder[56] etc., are used in the characterisation of tribological performance of zirconium alloys. Depending on the amplitude of the wear, it can be generally subdivided into two further categories; wear and fretting.

In spite of the classification of wear according to its amplitude, wear can also be divided into mild wear and severe wear based on wear track severity; or grouped into lubrication wear and unlubrication wear depending on the existence or non-existence of lubrication in the wear system; or sliding, rolling and impact wear in terms of the contact movement of the surfaces[57].

Wear as a failure mode, not only can cause great physical consequences as loss of material, wear debris and material embrittlement[58], but also induces tremendous safety risks which include leaking, inflammation, overload failure. It was estimated that up to 70% of zirconium leak failures were reported to be related to fretting and wear[59]. Close to 90% of the orthopaedic implants (screws and plates) revised were caused by wear debris caused inflammation[60]. All of those come along with large economic losses.

2.2.1.2 Friction of zirconium alloys

Friction, shown in Figure 2.2-2[61], is the force generated between two contact moving bodies, either sliding or rolling, which prohibits the relative movement between each other. Friction is proportional to the normal load, which is expressed as, $F = \mu W$, where μ is the coefficient of friction (CoF), F is the friction force and W is the normal load. The empirical results have shown that the friction force is independent of both the apparent contact area and the sliding velocity[61]. Since these are empirical conclusions, these laws may not apply to all cases.

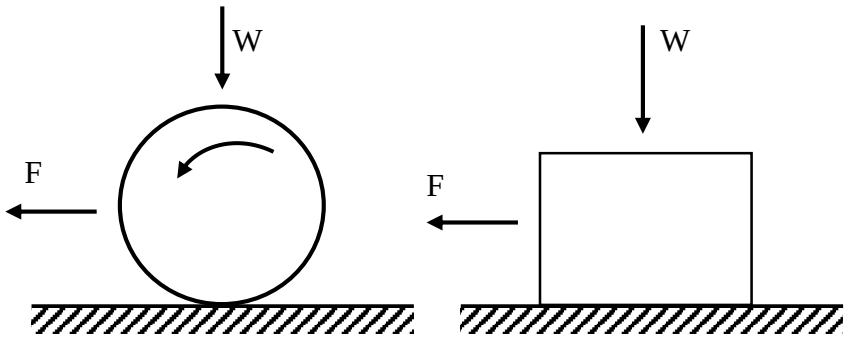


Figure 2.2-2 A schematic diagram showing a frictional force in (a) rolling and (b) sliding conditions[61]

When two clean surfaces are brought into contact, from a tribological point of view, it will be the asperities of the surfaces which touch each other and hence form cold weld joints[62], shown in Figure 2.2-3[63]. If subjected to relative motion, these cold weld joints will either deform plastically or break off which is dependent on the material's deformation characteristics. According to Bowden and Tabor[61, 64], friction is the reason which causes the adhesion and deformation (ploughing etc.) of the contacting parts with relative motion. Therefore, the friction force is the sum of the adhesion force (F_{adh}) and deformation force (F_{def}).

$$F = F_{adh} + F_{def}$$ Equation 2.2-1

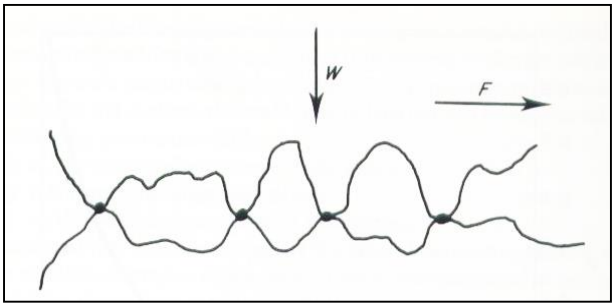


Figure 2.2-3 True contact of two solid surface

Hence, the friction characteristics of materials are related to their intrinsic crystal structures[65], chemical and mechanical properties. In principal, HCP structure has a lower number of slip directions (i.e. 6) when compared with BCC. and FCC being 8 and 12 respectively[66]. In the case of FCC structured materials, the stacking fault energy is believed to be a good indicator of the galling and wear properties [67-69]. Low stacking fault energy will reduce the effective number of slip systems and is thought to hinder the dislocation movement and lower ductility, therefore decreasing the friction. For HCP materials, anisotropy behaviour was observed and plastic deformation would either proceed in basal plane or prismatic plane, depending on the axial ratio i.e. c/a[66], whether it is higher or smaller than the ideal index for hexagonal closed packed stucture. The axial ratios for different metals at room temperatures are given in Table 2.2-1[67]. Research[70] shows that with a low axial ratio (<1.633), more cross-slip are observed and hence making the materials more susceptible to gall.

Table 2.2-1 The axel ratio of metals at room temperature[67]

metal	c/a
Be	1.568
Ti	1.587

Zr	1.593
Mg	1.623
Co	1.623
Ideal HCP	1.633
Zn	1.856
Cd	1.886

As mentioned earlier, zirconium has the hexagonal closed packed (HCP) crystallographic structure in ambient conditions, as shown in Figure 2.1-5[32]. It has an axial ratio of 1.593, which is lower than the ideal value of 1.633. Having a lower axial ratio makes the basal plane less favourable for slip than the prismatic $\{10\bar{1}0\}$ and first order pyramidal $\{10\bar{1}1\}$ planes[71], resulting in an increase in the total number of possible slip systems. The increased possible slip systems can then promote continuous junction growth, which contributes to high friction and wear loss.

Besides this, the grain size, second phase distribution, microstructure discontinuity etc. are also found to be related to the friction properties of materials. A higher chemical activity also gives rise to a higher junction strength and an increase in the friction. When materials have a relatively high ductility, a high rate of cross-slip of dislocations and low work-hardening rate, plastic deformation in the asperities will be preferred and fracture would be minimal. As a result, sliding would require more energy.

Zirconium has a high chemical activity(Figure 2.2-4 (a)) and metallurgical compatibility (Figure 2.2-4 (b))[61, 72], which leads to both strong cold welding and a high junction strength. When sliding caused shearing occurs, the high ductility of zirconium promotes rapid junction growth which will induce more wear. Low hardness also contributes to high wear rate especially in abrasive wear. It should also be noted

that the adhesive wear or galling tendency of zirconium and its alloys is a synergy of all these factors.

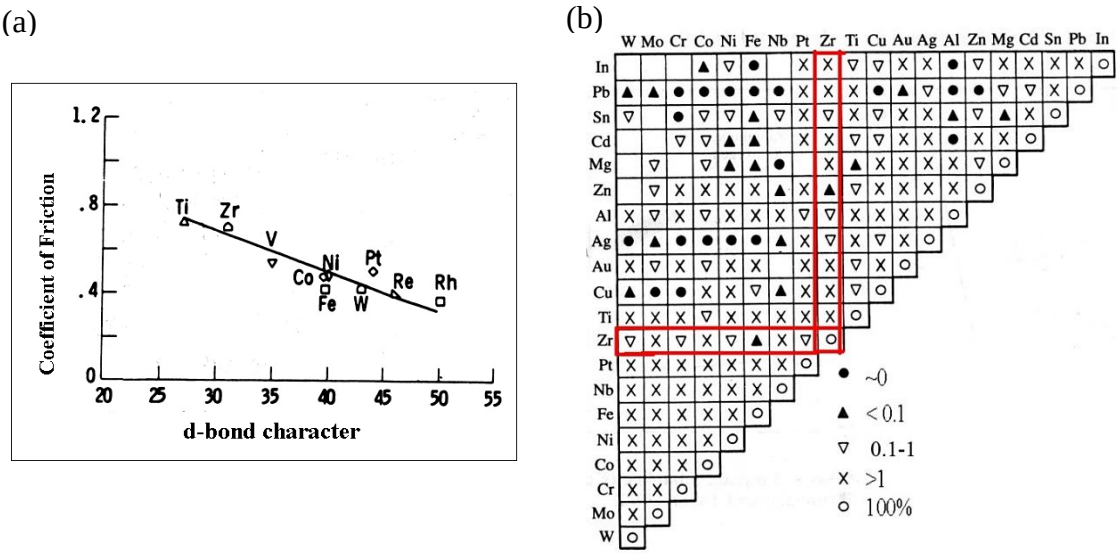


Figure 2.2-4 (a) d-bond character and (b) Metallurgical compatibility chart for metals, derived from their two phase binary diagrams, the number given means the solubility of the two different phase[61, 72]

All of these reasons contribute to the high friction coefficient (~0.56) of zirconium compared with the other metals, together with poor wear properties. In order to address this problem, an investigation of wear mechanisms of zirconium alloys is necessary.

2.2.1.3 Wear of zirconium alloys

When surfaces move relative to one other, there is an affected area, called the active layer, as shown in Figure 2.2-5. The active layer refers to the surface layer with its composition, structure thermal and mechanical properties changing during the tribological contacting state[57]. However, this is difficult to observe due to current restriction in observation technology. Thus deducing the active layer by studying of the properties of the relaxed layer, i.e. the same layer but after unloading conditions at room temperature, is of great importance to tribology. From the conclusions drawn regarding

wear mechanism, improvements in the design and material selection of a product can be made.

According to the observation of the characteristics of the relaxed layer, wear can be classified into four main categories: adhesive, abrasive, tribochemical and fatigue[62]. Of those four categories the former two are of most importance for zirconium alloys, as the latter two can be added into the former two with the influence of the tribological environment.

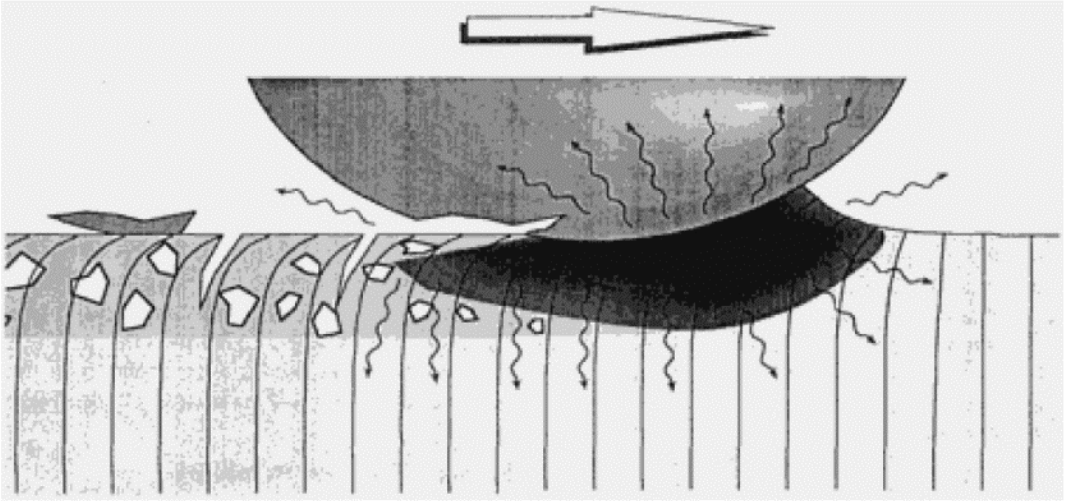


Figure 2.2-5 Schematic diagram of a tribocontact system implicating changes to the tribocontact layer[57]

2.2.1.3.1 Adhesive wear of zirconium alloys

Adhesive wear occurs on most metallic materials including zirconium. Many research studies have been devoted to the wear properties of zirconium alloys. The results of these studies have revealed a strong tendency of adhesive wear[73, 74] due to the reasons as aforementioned in section 2.2.1.2.

During sliding, if adhesive wear is to occur, there are two relevant processes to be considered, shown in Figure 2.2-6[50]:

1) Materials transfer: As previously described, cold welded junctions can be torn apart when contacting surfaces are moved relative to each other. Normally it will be in softer material where the tearing takes place. The fragmented material will be dragged away and become adhered to the harder material. This is called a material transfer process. The resultant wear track morphology characteristics are the adhesive voids and craters, shown in Figure 2.2-7 (a)[75]. The appearance of wear grooves will be explained in the following section.

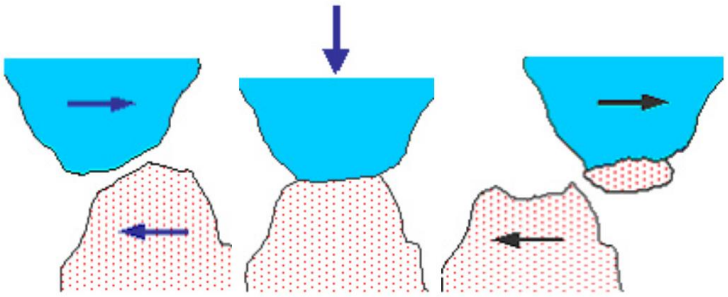


Figure 2.2-6 Material transfer during the adhesive wear process: horizontal arrowing showing the moving directions of the contacting bodies; vertical arrows depicting the applied forced[50]

2) The following step will be the removal of the transferred material, during which the transferred layer is detached and removed from the underlying materials due to the cyclic loading. At first the torn fragment follows a plate-like morphology, with a typical image shown in Figure 2.2-7 (b)[50], then under the cyclic load condition, the transferred material could go on to be milled or react (e.g. oxidation) with the surrounding environment. Eventually the bond between the transferred layer and the underlying material weakens, then finally be detached and removed from the system.

During a wear process, it should also be noted that since zirconium has a high affinity with oxygen, due to a combined effect of chemical and mechanical interactions between the contacting surfaces, the newly exposed zirconium parts or wear particles, which act

as a third body in the tribo-contact system[61], will react with oxygen/water from the surrounding environment, forming zirconium oxide. The third body oxide, which has a high hardness, will cause wear grooves shown in Figure 2.2-7 (a) and Figure 2.2-8 (a). For severe wear scenarios, plastically deformed surfaces became covered with patches of oxides, shown in Figure 2.2-8 (b)[73]. As observed in most cases, adhesive and abrasive wear mechanism are simultaneously operative, because of the zirconium oxide formation, until a steady condition is reached.

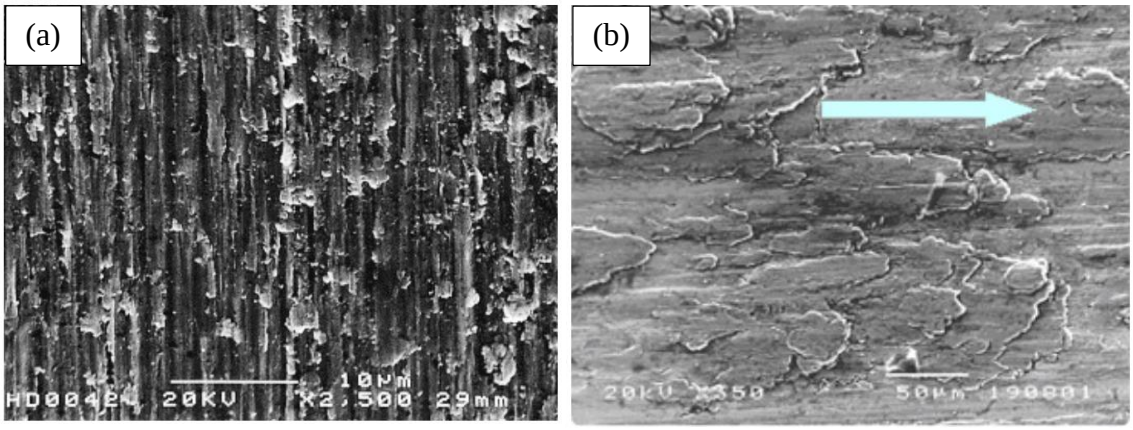


Figure 2.2-7 Morphological characteristics of adhesive wear: (a) adhesive craters on titanium (softer material) indicating material transfer; (b) transferred plate-like titanium on a steel ball (harder material), arrow showing the moving direction of tested sample[75]

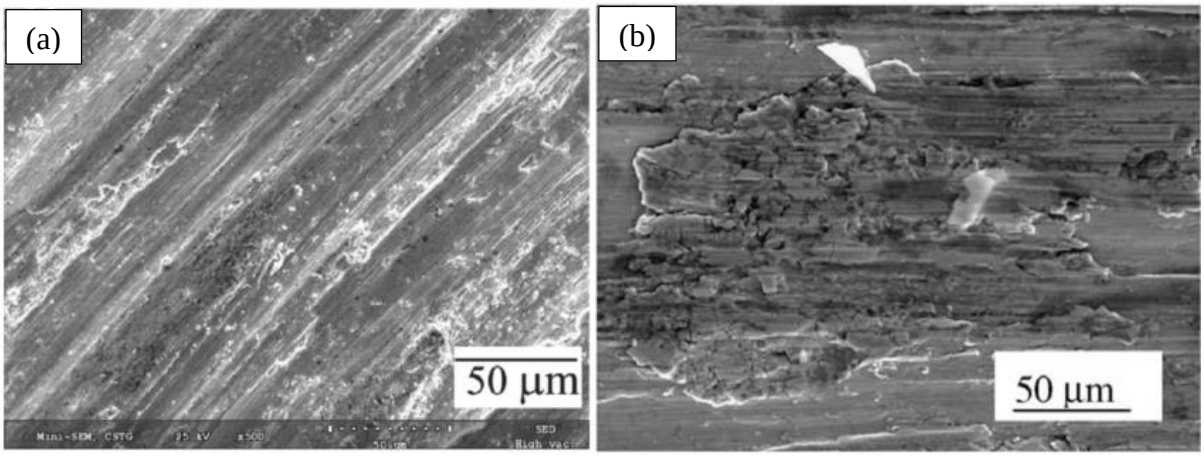


Figure 2.2-8 Wear tracks of Zircaloy-4 plate showing (a) wear grooves (b) patches of oxide on wear track[73]

In order to determine the rate of adhesive wear, Archard model [76], which is developed based on the theory of asperity contact, was used (Equation 2.2-2).

$$W = K\frac{F_N}{H} \qquad \text{Equation 2.2-2}$$

W: wear rate; F_N: normal load; H: hardness of the softer material; K: the wear coefficient.

K would be high if the two contacting surfaces have a high mutual solubility (shown in Figure 2.2-4 (b)), or if wear occurs in a vacuum or an inert atmosphere. Figure 2.2-9[74] depicts that, when sliding against itself at different atmospheric conditions, zirconium exhibits the lowest friction coefficient in a H_2 gas atmosphere, which increases in the increasing order when the test carried out in He-10%H_2, air, He and vacuum atmospheres. The reason for a lower friction coefficient in H_2 or H_2 containing He atmosphere is the tribo-chemical reaction induced zirconium hydride which acted as a lubrication because of its layered structure[74]. The negative wear rate of the disk specimen in air and vacuum (Figure 2.2-9 (b)), is due to the transfer of the zirconium on the pin specimen to the disk during the wear process, i.e. adhesive wear[74].

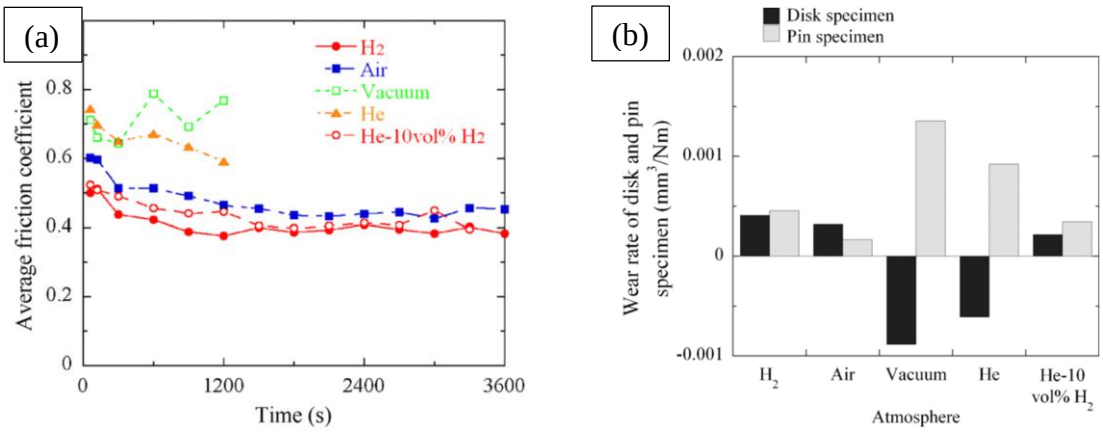
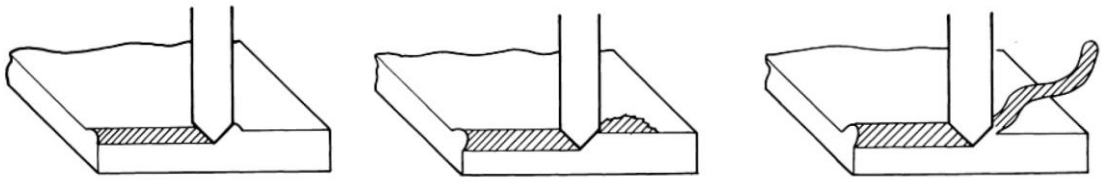


Figure 2.2-9 Results of pin on disk test of zirconium against itself at different atmospheres: (a) Friction coefficient (b) Wear rate (positive)/transfer rate (negative)[74]

2.2.1.3.2 Abrasive wear

Abrasive wear occurs when a hard surface slides against a soft surface (two-body system) or when hard particles enter the sliding interface and act as abrasives (three-body system). The soft surface will suffer material loss by the known abrasive wear[62]. The most obvious morphological characteristics of abrasive wear track is wear grooves, shown in Figure 2.2-10[57, 77, 78], therefore, abrasive wear is also termed by grooving wear by some researchers.

Depending on the ratio of the shear strength of the contact interface relative to that of the bulk materials, abrasive wear grooves are observed from three different forms of mechanisms: ploughing, wedge and cutting[57]. When the load is really light, ploughing happens with materials only displaced from the grooves to the side (Figure 2.2-10 (a)). In this case, there is no material loss and surface damages are in the form of dislocations at the near surface areas. With the load increasing when the ratio (between the shear strength of the contacting surface with the shear strength of the bulk material) reaches 0.5~1.0, wedge grooves occur where part of the materials from the grooves is worn out and maybe pile up in front of the abrasive tip (Figure 2.2-10 (b)). The most severe form of abrasive wear is cutting, during which the shear strength ratio between the contacting surface and the bulk material is so high that the abrasives act as a tool machine (Figure 2.2-10 (c)). There is no material displacement. For cutting to happen, a critical angle of the abrasive tip, depending on the abraded material, exists.



(a) Ploughing (b) Wedge (c) Cutting

Figure 2.2-10 Three different forms of ploughing grooves[57]

Microfatigue and microfracture at the worn surface may occur on ductile and brittle abraded materials respectively, shown in Figure 2.2-11[77, 78]. Repeated deformation accumulation on ductile worn surfaces leads to the fatigue, while the wear debris of brittle material comes from the crack convergence.

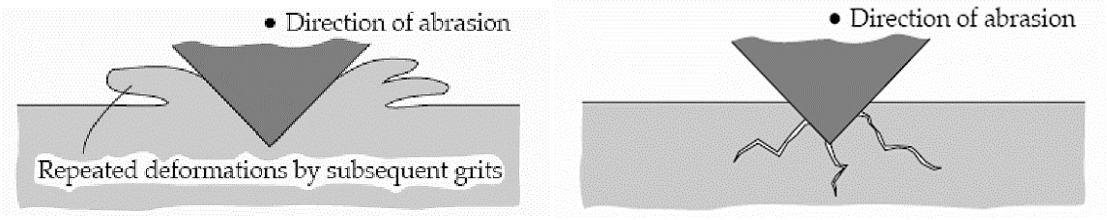


Figure 2.2-11 Microfatigue and microfracture of worn surface from ductile and brittle materials respectively[77, 78]

To determine the wear loss of materials Archard model[76], shown in Equation 2.2-3, is found to be applicable for abrasive wear.

$$V = k\frac{PL}{H} \qquad \text{Equation 2.2-3}$$

V: wear rate; k: wear coefficient; P: contact load; L: sliding distance; H: hardness of the surface being abraded. The wear rate k is dependant mainly on the shape, hardness and mechenical properties of the abrasives.

Zirconium and its alloys are soft materials, with the hardness < 250HV. In the case of abrasive wear, they often act as the abraded materials either by third body particles (work hardened or oxidized wear particles) or the high toughness counterpart, which then leads to the abrasive wear grooves as aforemntioned (Figure 2.2-8 (a)).

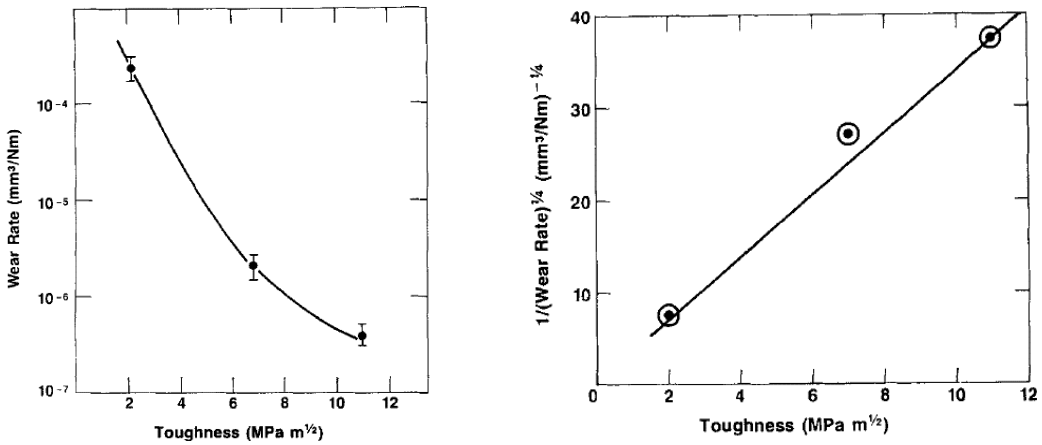


Figure 2.2-12 Zirconium oxide wear rate vs. facture toughness [79]

Lots of efforts have also been devoted to the anti-wear properties of zirconium oxide, because of its high hardness as a ceramic. Unlike metals, Archard's model could not be applied to the wear of ceramics. Toughness is of more importance than hardness for wear resistance, as the wear of ceramic mateirals occurs by fracture instead of plastic deformation[80]. Fischer[79] found that the wear resistance of zirconia (measured in air at ambient temperature with a sliding speed of 1mm/s and normal load of 9.8N) is propotional to the fourth power of fracture toughness, K_{IC}, as shown in Figure 2.2-12. Typical morphology of wear tracks are given in Figure 2.2-13, with arrows indicating the siliding direction of counterface and the mignification scale, showing that the wear of materials changes from fracture to plastic deformation with increasing toughness[79].

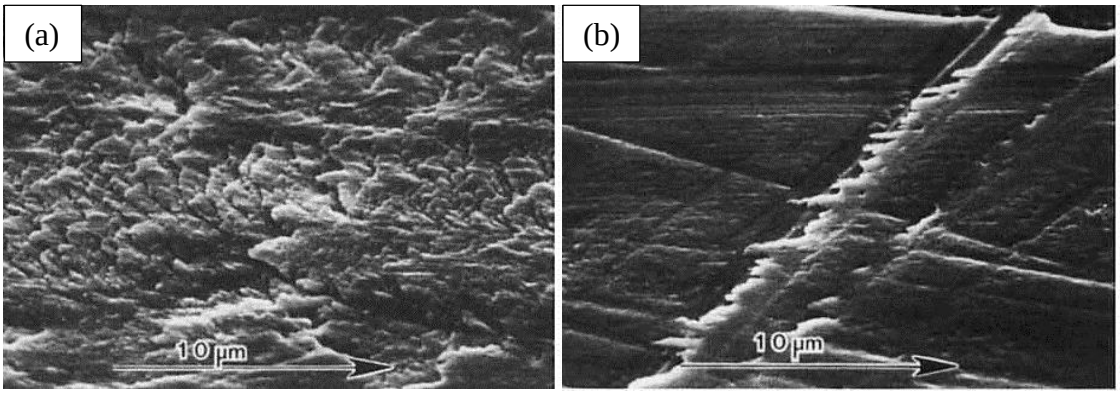


Figure 2.2-13 Typical SEM images of wear track on zirconia plates with the arrows indicating the sliding direction: (a) K_{IC} = 2.5MPa·$m^{1/2}$, cracking; (b) K_{IC} = 11.6MPa·$m^{1/2}$, grooves with plastic deformation. Arrows showing the sliding direction and magnification scale[79]

2.2.1.4 Fretting wear

Fretting wear occurs when the relative motion is of small amplitude, approximately 1-100 micrometres[4]. Vibration is one of the main causes of the fretting movement in machinery[81] such as the contacts between hubs, shrink- and press-fits, and bearing housings on loaded rotating shafts or axles, joint structures as rivets and fasteners etc..

Mindlin analysis based on Hertzian solution is used for design of experiments on fretting of a ball on a flat surface which is shown in Figure 2.2-14[82, 83]. Slip occurs when $q > \mu p$. Hence the contact consists of a non-slip region with a slip annulus. Based the shape of its friction loops (tangential force versus displacement cycle) [84-86] as depicted in Figure 2.2-15, fretting can generally be characterised by one of three different regimes: 1) elastic, which is a closed cycle on the friction loop with no observed wear and energy dissipation; 2) elastic cycle, where only part of the surface slip; 3) gross slip, which shows an parallelogram cycle[87].

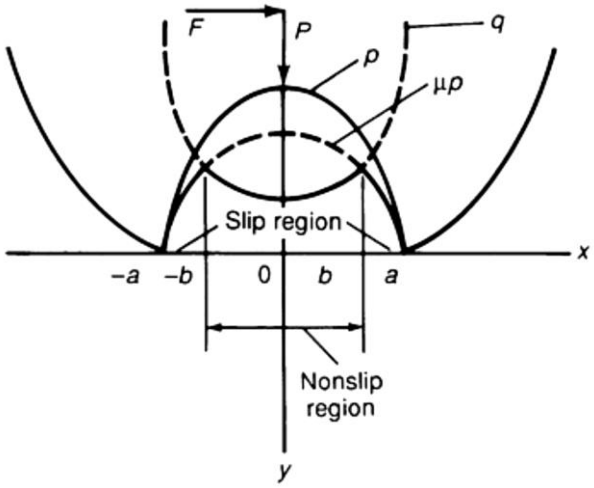
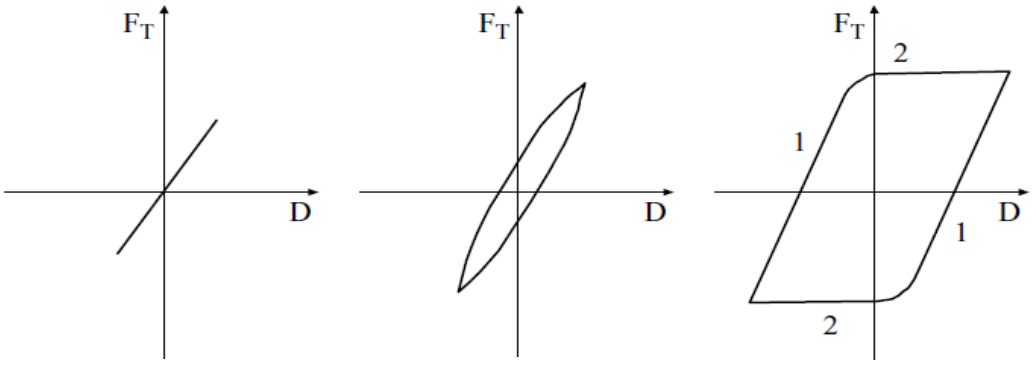


Figure 2.2-14 Contact of sphere and flat: P and F stand for the normal load and tangential force respectively; p is the pressure distribution, μp and q are the stress distribution for the friction and tangential force respectively; a is the radius of Hertzian contact, while b is the radius of the central slip area[82, 83]



(a) Elastic (b) Partial Slip (c) Gross slip

Figure 2.2-15 Different fretting regimes: (a) elastic; (b) partial slip; (c) gross slip where 1 and 2 refer to partial slip and full slip respectively[87]

Damages caused by fretting can generally divided into fretting wear and fretting corrosion, which involves adhesion, abrasion, together with fatigue and corrosion[88, 89]. In general cases, fretting happens in three stages: 1) initial metal to metal contact, where local welding, roughening of the surface occurs; fatigue cracks are initiated under cyclic stressing; 2) formation of wear debris beds; 3) a steady state, where friction is

more or less constant[90]. It should be also noted that different designs of experiments will lead to different mechanism, which adds the complexity of fretting investigations.

2.2.1.5 Factors affecting wear of zirconium alloys

It should be noted that wear is a very complicated process, and it is often the case that the real situation would be a combination of both adhesive and abrasive wear mechanisms, together with cold work, phase transformation, corrosion (from the outside environment or lubrication) etc. Therefore, any factor that may causes changes to the tribocontact system will have an effect on the tribological performance of zirconium alloys. It should also be noticed that, due to the complexity of the wear mechanisms, especially for fretting, depending on the test conditions, these factors may have a varying effect.

1. Manufacture of zirconium alloys: the performance of materials under wear conditions is highly related to the intrinsic properties of the materials themselves. Research done by King et al. [91] showed that the wear resistant of Zircaloy-4 and/or OPTIN^{TM} fuel rods in contact with springs and dimples is better than that of ZIRLO^{TM}. Manufacture of zirconium alloys sometimes causes a slightly variation in wear resistance values[5].

2. Normal load: as mentioned earlier, only the asperities will contact when two surfaces are put into contact and loaded. The real area of contact, A, is therefore directly proportional to the applied load, P[64].

$$A = \frac{P}{p_0} \qquad \text{Equation 2.2-4}$$

where p_0 is the yield pressure.

In terms of fretting it only occurs at contacting areas, it follows that the amount of wear should be directly proportional to the applied load, which is consistent with the research conclusion regarding zirconium alloys[5, 92]. This conclusion is wear mechanism related, but in most cases, the increase in normal load will induce an increase in wear volume losses[36].

3. Sliding speed/ frequency: wear of Zircaloy-4 increased with increase in sliding frequency[36]. When varying the sliding speed, the wear resistance of zirconium showed best performance at around 300 rpm of sliding speed by the micro-pitting mechanism[92].

4. Environment: wear performance of zirconium alloys was found to be environment e.g. temperature related. It was observed that zirconium alloys exhibit higher wear coefficient at 225~286°C than at a temperature above 300°C at both rubbing and impacting conditions[5]. Meanwhile, as aforementioned in section 2.2.1.3.1, when tested at different atmosphere, wear volume loss was noticed to increase in inert atmosphere than in the air[74].

5. Surface finish: some observations[93] also showed that the smoother the surface is, the more significant the damage will be. While there has also been research conducted on zirconium alloys suggesting that surface finish does not have a significant effect on fretting[5].

In terms of improving tribological properties, there are a few measures that can be taken. This includes; avoiding sliding against material that is similar to zirconium, reducing applied load, degrading the severity of environments where zirconium and its alloys are used and adding lubrications to system. However, all these methods are fully

redistricted to the design of the application, while some cannot be changed much. Therefore, the most viable option would be linked to surface engineering, i.e. changing the surface properties of zirconium alloys. More details of surface engineering of zirconium alloys are covered in section 2.4.

2.2.2 Corrosion of zirconium alloys

2.2.2.1 Introduction

Zirconium is a highly chemical reactive metal, with a redox potential of -1.53V[94] (vs. standard reference electrode (SHE)) at 25°C. It has a high oxygen affinity. Therefore, the corrosion of zirconium and its alloys are often intrinsically liked to their gradual destruction by chemical reactions with the oxygen-containing environments[95], resulting in the formation of zirconium oxide at the surface. Zirconium oxide formed at ambient conditions with a thickness of a few hundred nanometres is adherent and protective, resulting in highly corrosion resistant. However, it is really easily to break at more severe conditions.

Figure 2.2-16 shows the thermodynamics of Zr/O and other relevant systems[96, 97]. It should be noted that besides the chemically reacted oxygen, some oxygen will dissolve into the zirconium matrix. The fraction dissolving depends on the balance between the kinetics of oxidation and the kinetics of dissolution[98]. This oxygen dissolving zone is termed as the diffusion zone. It is reported that rapidly oxidized alloys generally have shallower diffusion zones when compared with zirconium alloys that are slowly oxidized[97].

It is generally believed that the oxidation of zirconium and its alloys is an oxygen inward diffusion process. During the corrosion process, the oxygen, coming from the

surrounding environment either O_2 or H_2O, reacts with zirconium. The redox reactions are shown in Equation 2.2-5 and Equation 2.2-6.

$$O_2+4e^-\rightarrow 2O^{2-} \qquad \text{Equation 2.2-5}$$

$$2O^{2-}+Zr\rightarrow ZrO_2+4e^- \qquad \text{Equation 2.2-6}$$

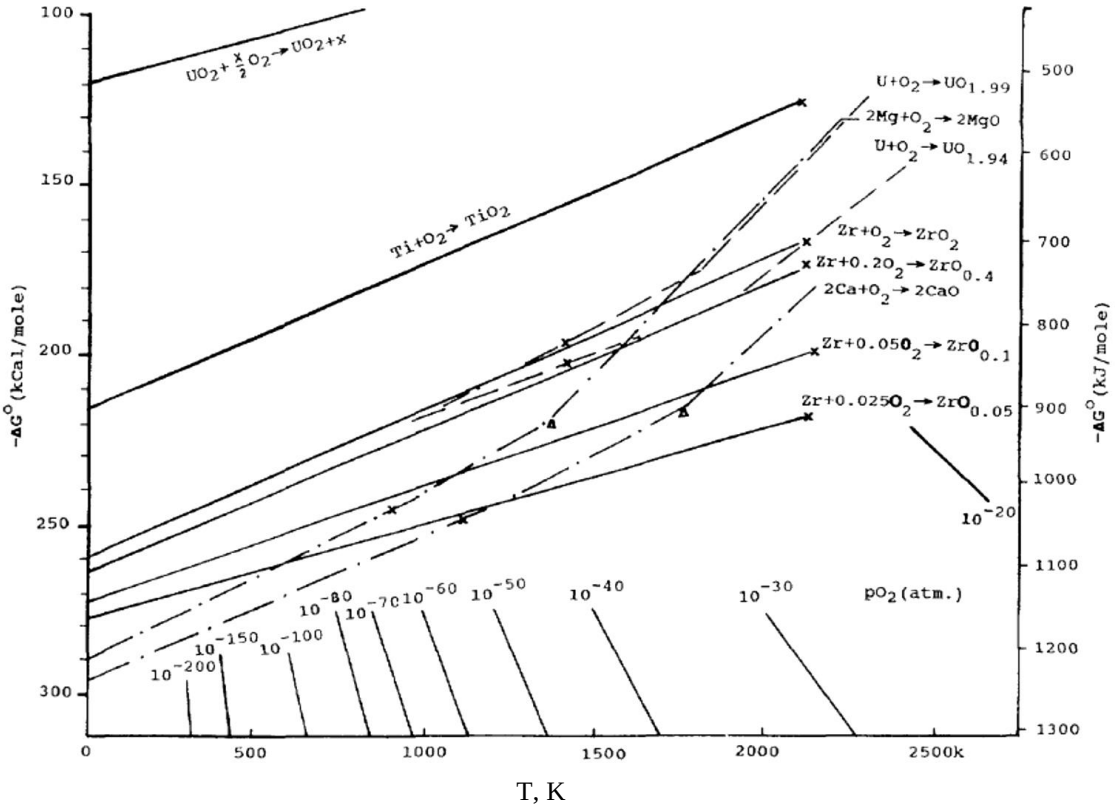


Figure 2.2-16 Darken and Gurry plot of the thermodynamics of Zr/O and other relevant systems[96, 97]

2.2.2.2 Electrochemical corrosion of zirconium alloys

Different forms of corrosion such as; pitting, stress corrosion cracking, galvanic corrosion, crevice corrosion, and fretting corrosion can occur on zirconium and its alloys[99]. Electrochemistry is the most commonly used method for the study of corrosion behaviour of metals. The polarisation curve, Figure 2.2-17[100], of the

working electrode (as anode) in an electrochemical test illustrates of the corrosion behaviour.

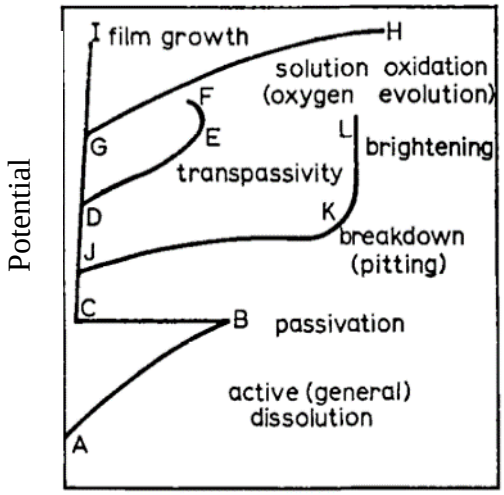


Figure 2.2-17 Schematic anodic polarisation curve for a metal[100]

With an increasing of potential, several phenomena could be observed. When the potential displaced slightly (usually less than 10mV) from the corrosion potential, E_{corr}, a linear relationship between dE and di can be found[101, 102]. The slope dE/di is termed of polarisation resistance, noted as R_p.

$$R_p = dE/di \qquad \text{Equation 2.2-7}$$

As the potential displacement increases, the polarisation curve will deviate from the linear relationship until the Tafel region[102], AB in Figure 2.2-17, where the potential exhibits linear dependence on the logarithms of current i, $logi$.

$$E - E_r = i_0 + blogi \qquad \text{Equation 2.2-8}$$

where E is the observed potential; E_r is the reversible potential; $E - E_r$ is the over-potential; i_0 is the current density; b is the Tafel slope which is related with the kinetics of corrosion.

The formation of a passivation film begins at point B, which is called the passivation potential E_{pp}, until an equilibrium thickness is reached at C, Flade potential E_F[100, 102]. After the formation of the passivation film, for some metals such as zirconium, localised breakdown of the film, especially by chloride ions, could be observed as evidenced by JK[103]. If the breakdown of the film is not observed, then some solution oxidation (GH) or transpassivity (DE) occurs, during which the oxidation of solution or passivating oxide to a soluble substrate take place[100].

As for zirconium and its alloys following the formation of a very thin oxide film, pitting corrosion in chloride solutions will be observed, due to Cl^- which will act as an absorbable anions hindering the passivation film formation on the surface of zirconium and its alloys[104]. A typical polarisation curve and surface morphology after corrosion is given in Figure 2.2-18[105].

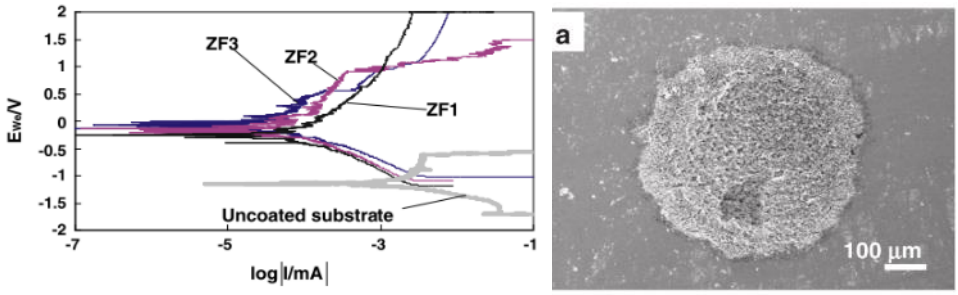


Figure 2.2-18 Typical polarisation curve and corrosion morphology on zirconium alloys[105]

It should also be noted that fretting corrosion as one form of tribocorrosion, which is a combination effect of wear and corrosion occurring on surfaces where rubbing or

impacting exists[106, 107], is often observed in tribochemical applications. Figure 2.2-19 shows the tribocorrosion contact of two metallic surfaces, which includes electrochemical activity of the wear debris with the contacting surfaces and material transfer between contacting surfaces which can radically change the composition of the surface and the wear and corrosion resistance of that surface[108].

During this process, corrosion and wear may accelerate each other. The tribocorrosion mechanisms involves the properties of contacting materials surfaces, the mechanisms of contact and the corrosion conditions[108]. Therefore, due to their complexity they are still not fully understood[106].

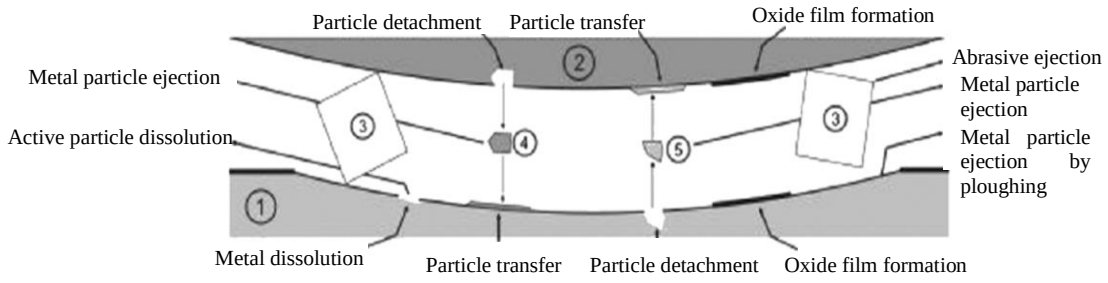


Figure 2.2-19 Schematic diagram of tribocorrosion contact of two metals[106]

2.2.2.3 Factors affecting corrosion of zirconium alloys

The environment plays an importance role in the corrosion of zirconium alloys. As investigated by Cox [98] zirconium is oxidized quicker in air than in pure oxygen due to the acceleration effect coming from the nitrogen element[109]. When in contact with stainless steel or nickel alloys, zirconium alloys tended to be more corroded, which is attributed to galvanic effects[110]. The effect is also evidenced by handle "shadows" appearing on fuel channel[109].

The presence of alloying elements and common impurities including; iron, nickel, copper, etc. are proved to promote the nodular corrosion. This may lead to quick local cladding thinning and eventually causes increase in the rate of hydrogen uptake and increase in concentration of zirconium oxide particles migrating into the coolant[44, 111, 112].

Under mechanical loadings, corrosion of zirconium alloys will be accelerated because of the combination of the effects from both wear and corrosion[113].

2.3 Oxidation of zirconium alloys

2.3.1 Zr-O phase diagram

As mentioned earlier, zirconium has a high affinity with oxygen. When dissolved in zirconium matrix, oxygen will stabilise the α phase, as shown in the zirconium-oxygen binary phase diagram in Figure 2.3-1[21]. The equilibrium solid phases in Zr-O diagram at 1 bar are bcc-Zr (β-Zr), hcp-Zr (α-Zr) and non-stoichiometric compound ZrO_{2-x} ($x \leq 0.44$). The α-Zr phase dissolves oxygen interstitially up to 35 at% at eutectic temperature 2338 K, while β-Zr has a maximum oxygen solubility of 10.5 at% at the peritectic temperature 2128 K.

It is also shown that ZrO_{2-x} exists in three crystallographic forms depending on the temperature: at low temperature ($T < 1478K$) a monoclinic phase α-ZrO_{2-x} exists; at an intermediate temperature ($1478K < T < 1798$, 2650K depending on the oxygen content) a tetragonal phase β-ZrO_{2-x} exists; and at a high temperature a cubic phase γ-ZrO_{2-x} exists. Table 2.3-1 lists the main phase transformations found in the Zr-O system. The phase transformation from β-ZrO_2 to α-ZrO_2 is a martensitic transformation, which is a diffusionless process[25].

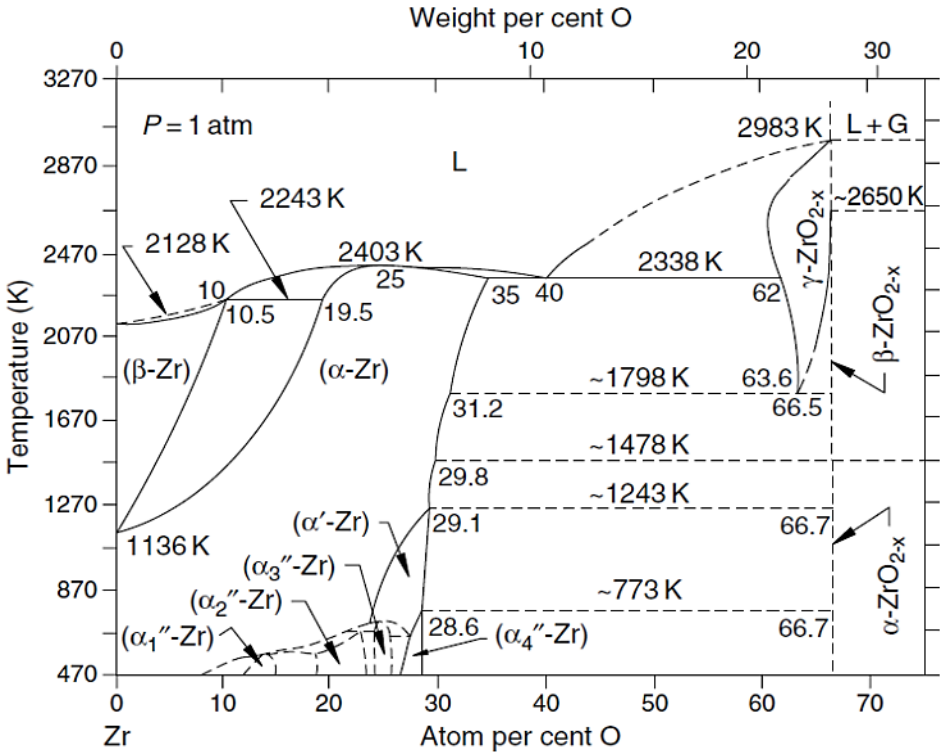


Figure 2.3-1 Phase diagram of the Zr-O system[21]

Table 2.3-1 Main phase transformations in Zr-O phase diagram

Reaction	Temperature	Reaction type
L + α-Zr ↔ β-Zr	2243K	Peritectic
L ↔ β-Zr	2128K	Melting
L ↔ α-Zr	2403K	Congruent
β-Zr ↔ α-Zr	1136K	Allotropic transformation
L ↔ α-Zr + γ-ZrO_{2-x}	2338K	Eutectic
γ-ZrO_{2-x} ↔ α-Zr + β-ZrO_{2-x}	1798K	Eutectoid
β-ZrO_{2-x} – α-Zr – α-ZrO_{2-x}	1478K	--
γ-ZrO_{2-x} ↔ β-ZrO_{2-x}	2650K	Congruent
β-ZrO_{2-x} ↔ α-ZrO_{2-x}	1478K	Congruent

2.3.2 Oxidation kinetics

Depending on the oxide film formed on zirconium and its alloys, oxidation can be divided into uniform oxidation and nodular oxidation[97]. As for uniform oxidation, the weight gain kinetics of zirconium and its alloys usually fall into two periods colloquially referred to as pre- and post-transition[98, 114]. Normally, the oxidation of zirconium and its alloys can be described by the rate law, which is shown in Equation 2.3-1.

$$\Delta m = k t^{\frac{1}{n}} \qquad \text{Equation 2.3-1}$$

Δm: the mass change during the reaction period; t: the reacted time; n: the order of reaction.

The n value is 1, 2, 3 for the linear, parabolic and cubic reactions respectively[115]. The linear oxidation is also called "breakaway" oxidation. Time to break away is considerably less in air than in oxygen and also decreases with increasing temperature[98]. Research shows that smooth surfaces have a positive effect on delaying the breakaway oxidation time[116].

According to oxidation kinetics, the oxidation mechanism is classified into pre-transition mechanism, breakaway mechanism and post transition mechanism[97, 98].

2.3.2.1 Pre-transition oxidation

It was believed initially that the pre-transition period was controlled by oxygen ion diffusion through the oxide layer[98, 115]. However, experimental results show an exponent less than 0.5 for the majority of zirconium alloys, which is not in agreement with the oxygen diffusion control where it would give a parabolic dependence with time.

It has been concluded that the rate control process is the electron transportation as a positive potential was measured across the oxide[117]. Different effect on the electrical conductivity of the oxide leads to the difference in oxidation behaviour e.g. the n exponent for Nb and Sn containing alloys in the pre-transition period is 0.45 and 0.25[118] respectively. On the other hand, β-Zr is reported to be oxidised quicker than α-Zr[119], as a result the oxidation rate of Zr-2.5Nb could be accelerated by the β-Zr phase.

Figure 2.3-2[97] is a schematic diagram showing the formation of pre-transition oxidation. As mentioned earlier, the reaction is an oxygen inward diffusion process with the reactions given in Equation 2.2-5 and equation 2.2-6. During reaction, the oxygen diffuses through the grain boundaries. The resultant phase composition is monoclinic ZrO_2 changed from tetragonal [120-122]. The metal/oxide interface is made up of zirconium oxide which is composed of amorphous and substoichiometric oxides, with the amorphous state nucleating to crystalline as the oxidation reaction progresses[123]. Microstructure observation shows that the monoclinic oxide formed on the oxide scale has a columnar crystalline structure, and the columnar width, generally of nanometres, increases with film thickness[124]. The intermetallic particles, such as Zr-Fe-Ni, remain in a metallic state [109].

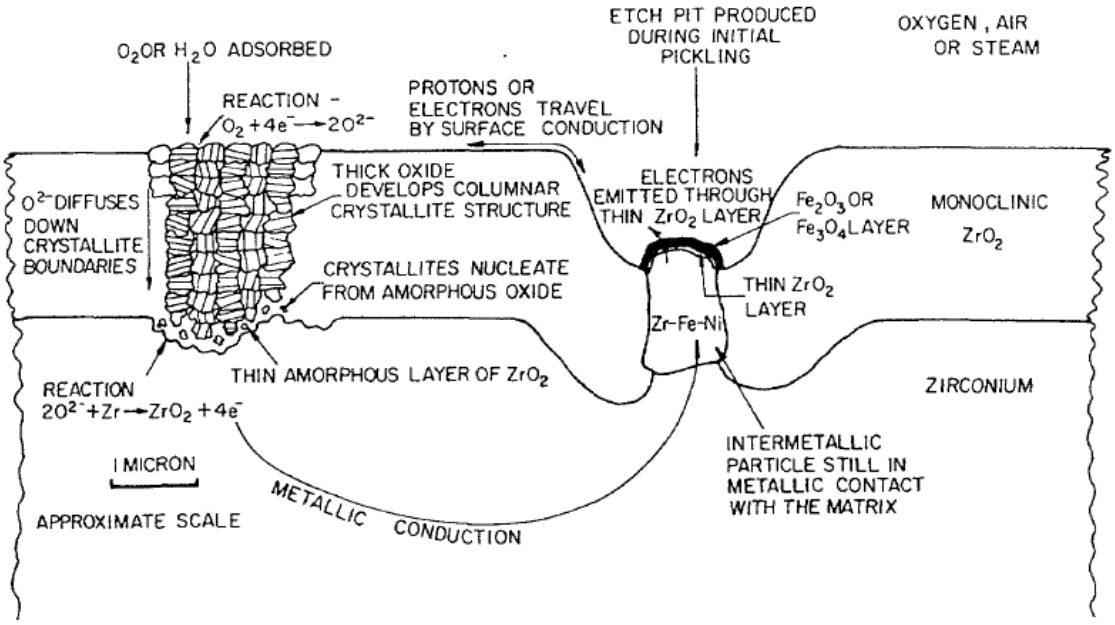


Figure 2.3-2 Schematic diagram of oxide film on Zircaloy-2 and the process occurring in it during oxidation[97, 98]

2.3.2.2 Transition oxidation

The transition process or breakaway oxidation process is indicated by the formation of porosity in the previously impervious oxide film. The oxidation rate changed to linear following the transition, and during this period, lateral cracks parallel to the oxide/metal interface begin to appear. At the same time fine pores probably at the grain boundaries starts to form a network within the oxide[98, 122]. This is accompanied by an effective reduction in the protectiveness of the oxide film. There are two main explanations for the formation of the porosity. As mentioned earlier, tetragonal ZrO_2 was first formed, and then transformed into monoclinic ZrO_2. The t-ZrO_2 → m-ZrO_2 transformation, which is martensitic (diffusionless), is accompanied by a large (3%~5%) volume expansion which is sufficient to exceed elastic and fracture limits even in relatively small grains of pure ZrO_2, thus leading to cracking[25]. The other is because of the volume increase from metal to oxide. The Pilling-Bedworth Ratio for zirconium is

1.56[125], which indicates that a compressive stress generated in an oxide scale keeps growing with the continuing oxidation reaction [126]. And hence it would cause scale cracking and spallation, directly affecting the maintenance of the protective oxide layer.

2.3.2.3 Post-transition oxidation

The post-transition period, which may also be called 'break away' oxidation, is characterised by the linear oxidation of zirconium. During this period, the oxide film would develop a pore and crack structure hence losing its protectiveness. This linear oxidation kinetics, as suggested, is an average of different oxidation rates on different surface locations[127, 128]. The whole reaction is a cyclic process[128], and the post-transition process will continue until the next cycle begins.

It should also be noted that there is a colour change linked with the thickening of the oxide layer from black / dark grey in pre-transition period to patchy grey / beige in transition stage[129, 130]. Post transition oxides are reported to be completely beige in colour[130]. .

2.3.3 Oxide microstructure

The microstructure of the oxide film formed on surfaces is of great importance to the tribological and corrosion properties of zirconium alloys. X-ray diffraction (XRD), Raman spectroscopy and Transmission Electron Microscopy (TEM) observations have shown that the oxide film consists of mainly monoclinic phase, with a minority of tetragonal phase [131-137]. A high tetragonal phase fraction is also reported when it is close to the metal/oxide interface, together with a decrease in tetragonal phase towards the surface due to the martensitic transformation from tetragonal zirconia to monoclinic zirconia.

A suboxide layer with a composition close to ZrO has been observed at the metal/oxide interface. Figure 2.3-3[137] gives a typical Electron Energy Loss Spectroscopy (EELS) line scan which depicts a Zr/O ratio of 1 at the distance of 50 ~ 100 nm. The appearance of this suboxide layer varies and has been reported to disappear during transition[137]. Besides the suboxide, there is an oxygen dissolved region, with the oxygen content varying from 0 ~ 30 at%, existing under the suboxide[97, 138].

Three different structures are reported to be observed at the oxide and metal/oxide interface via TEM and Transmission Electron Backscatter Diffraction (t-EBSD) observations. As revealed, the outmost layer is mainly made up of small equiaxed and randomly oriented oxide grains, underneath which are columnar grains distributed vertical to the oxide/metal interface[136, 139, 140]; while on the metal/oxide interface there are three different observed structures: an equiaxed monoclinic structure, an amorphous oxide, and columnar oxide with both monoclinic and tetragonal structures[139].

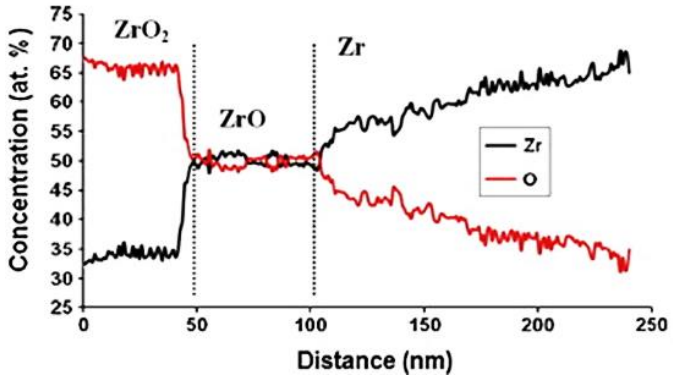


Figure 2.3-3 EELS scan of Oxide layer formed on ZIRLO™ alloy[137]

Cracks and porosity formed in the oxide are important to consider as they provide fast diffusion channels for different species[141] and accelerate the degradation of zirconium alloys as the boundary diffusion coefficient is reported to be 10^8 times greater

than that of bulk diffusion[131]. SEM observations, shown in Figure 2.3-4, have revealed periodic lateral cracking in thick oxides[140]. If they are not interconnected, these lateral cracks would not provide fast tracks for oxygen diffusion, as in the case with thin oxide films[142]. On the other hand, the porosity, usually around the grain boundaries, is also observed. The intergranular porosity grows as the oxide film becomes thicker and becomes fully connected in the direction of growing i.e. away from the interface. It has been suggested that the second phase particles which remain un-oxidised[97] and have different volume expansion rate compared with the oxidised zirconium could provide nucleation sites for the developing and propagation of these lateral cracking features[143]. However, the reason for the formation of cracks and porosity, either because of the second phase particle or the introduction of compressive stress or the martensitic phase transformation still remains unclear.

As previously described, the whole oxidation process is cyclic, and as a result, the oxide layer is a multi-layered structure, as shown in Figure 2.3-5, separated by small lateral cracks and its surrounding nanometre sized equiaxed tetragonal oxide[136].

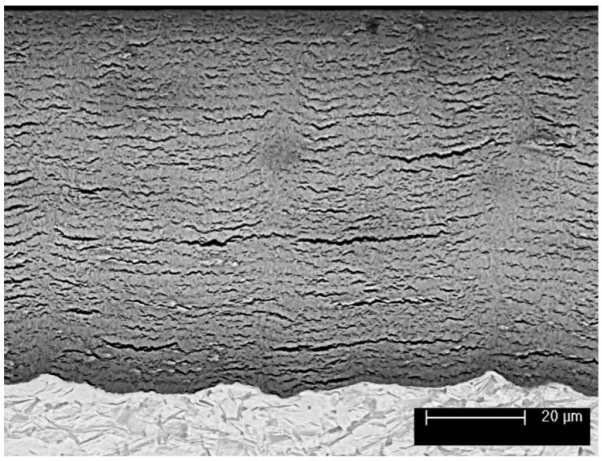


Figure 2.3-4 Cross sectional SEM images of oxide formed on zirconium alloys showing cracking parallel to the metal/oxide interface[140]

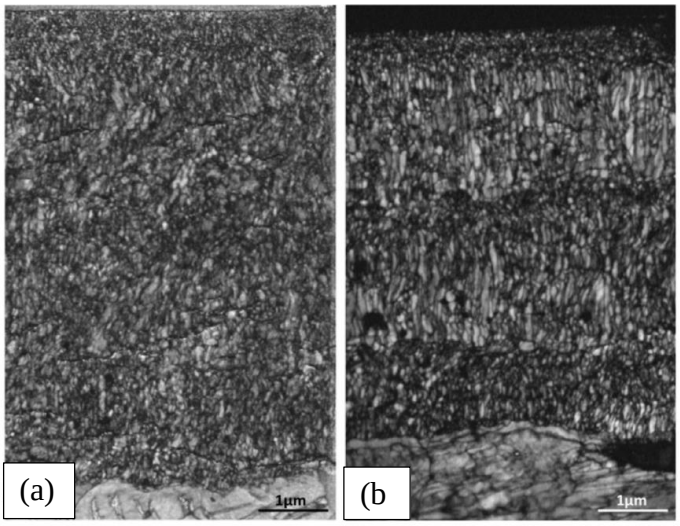


Figure 2.3-5 Band contrast maps of oxide film formed on (a) ZIRLO^{TM} (b) Zr-1.0Nb-0.1Fe, showing multi-layered oxide[136]

2.4 Surface engineering of zirconium alloys

2.4.1 Introduction of surface engineering

The methods used to improve the tribological performance of zirconium alloys, besides the changing of contacting conditions, can be generally divided into three groups, change of design, adoption of lubrication and the application of surface engineering[144]. For zirconium alloys used in nuclear and medical purpose, the use of lubrication will cause contamination or inflammation. Some efforts have been done on changing the design of spring shapes on the fretting wear behaviour of nuclear fuel rod[86], research has shown that the wear behaviour under dry conditions are considerably affected by the spring shapes. However, most of the efforts are still focused on the use of surface engineering techniques. Surface engineering has been proven to be an effective method of enhancing the properties of the surface and near surface areas of materials. It can be generally classified into two types, surface coating and surface modification.

Surface coating processes change the surface properties of a material by depositing a thin coating onto the substrate. Normally, there is an obvious boundary between the coating and the substrate because of their respective differences in chemical composition, crystal structure and mechanical properties, which leads to deboning problems. Surface modification processes can introduce new elements and change the microstructure of the surface. No deboning will occur due to nonexistence of the boundary between the layer and the substrate. Typical differences between surface coating and surface modification are shown in Figure 2.4-1. Lots of Attempts have been made to improve the tribological and biological properties of zirconium and its alloys [145-152], which will be detailed in this section.

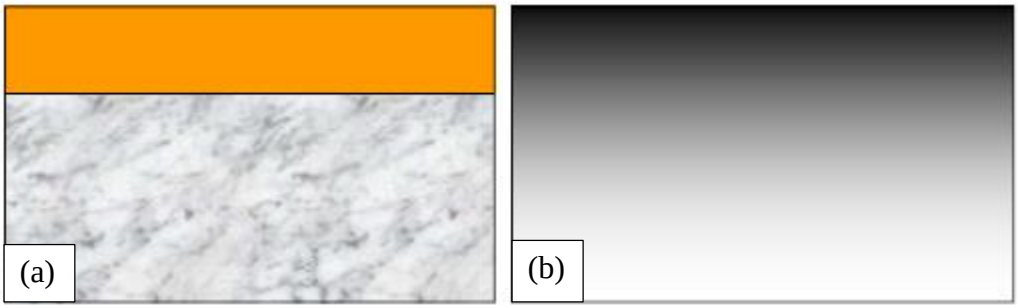


Figure 2.4-1 (a) Surface coating: a layer of different material is added to the surface; (b) Surface modification: surface composition and/or microstructure is modified.

2.4.2 Surface coating of zirconium alloys

Various surface coating techniques have been used in order to increase the surface properties of zirconium alloys, including vapour deposition, electrochemical plating, etc.

Most vapour deposition methods utilise the deposition of a zirconia or zirconium nitride film on Co-Cr[153, 154], aluminium[155], etc. materials. Regarding the deposition onto a zirconium alloy, a recent study carried out by L. Wang, X. Hu etc[156] reported that a zirconia coating in a range of 7-15μm was formed on the surface.

Characterisation of the coating found that not only did the wear resistance increase but also that the corrosion resistance remained.

A. W. Batchelor etc[157] deposited a molybdenum disulphide coating on zirconium roping wire to combat fretting and wear. Results showed that the performance of the molybdenum disulphide coating was dependant on the coating thickness. Thicker films performed better than thinner films, but overall were less durable when compared to laser surface alloying (LSA) treated ones.

Copper, nickel and iron electroplating on zirconium have been well studied. As such methods are well described for producing an adherent electroplate. Research has shown that the bonding can reach as high as 50000psi (modulus of rupture)[158]. However, most studies have been directed towards the corrosion resistance improvement. Due to the restriction of electrochemical processes, only electricity conductive materials could be plated. Hafnium, zirconium, and Zr alloys are difficult to coat with an adherent electroplate because they form a tenacious oxide film in both air and aqueous solutions[159].

The problem of surface coating technology is the poor bonding strength between substrate and coating due to the flat lamella microstructure which contains many voids and defects resulting in a high thermal insulation and crack formation[160].

2.4.3 Surface modification of zirconium alloys

Another approach to improve the surface properties of a material is to produce a strengthened surface layer within the substrate by surface modification. Due to the advantageous eliminating the bonding between substrate and modified surface, many

efforts have been made on zirconium alloys by ion implantation, laser assisted treatment, and thermochemical electrochemical methods etc.

2.4.3.1 Ion implantation

Ion implantation is a materials engineering process by which ions of a material are accelerated in an electrical field and impacted into a solid. Elements e.g. Yttrium, lanthanum, molybdenum are commonly used for the improvement of the corrosion resistance of zirconium alloys [161-163]. While nitrogen ions are implanted for tribological property enhancements.

Research shows that high dose nitrogen implantation into zirconium improves its mechanical properties, such as friction, wear, fatigue, hardness, etc.[164, 165]. In some cases, the microhardness improvement can be greater than 80%[165]. The coefficient of friction was found to be decreased and wear resistant improved. The nitride film generated by ion implantation is very sensitive to the ion dose and the substrate temperature during implantation. When the nitrogen implanted Zircaloy-4 exposed to high-temperature water, ZrN layer would be decomposed by oxygen diffused from water[166]. Moreover, from the depth profile of nitrogen implanted samples, the thickness of the modified surfaces could only reach less than one micrometre.

2.4.3.2 Laser assisted surface treatment

Laser processing of metal systems[167] is a technique where a small volume of surface of materials is melted by the high temperature generated by a laser beam. The melted zone is rapidly quenched at a rate of 10^5 to 10^8 °C/s by the substrate metal, producing fine-grain, microcrystalline, and metastable structures. After laser processing, the treated surface has three metallographic zones: the melt zone, the heat-affected zone and the unaffected base metal[168]. Laser assisted surface treatment can be generally

divided into two groups, laser surface melting (LSM) and laser surface alloying (LSA). The only major difference between them is that for laser surface alloying, the alloying elements are introduced into the surface layer during process.

Laser surface melting was reported to improve surface properties of zirconium alloys, such as corrosion in acid solutions, microhardness, and wear resistance[167-171]. Normally, the laser beam will generate a molten pool of a few hundred micrometres deep[172] depending on the beam intensity. The treated surfaces exhibit resolidified regions with several different microstructures, including ultrafine martensite[168]. Laser treatment without alloying was found to have little effect on friction[157].

LSA of zirconium alloys with elements of niobium, nickel or chromium powders produced a surface that was chemically homogeneous. LSA of zirconium alloys with niobium [172] it was found that the laser surface alloying provided a more durable friction reduction than PVD coatings, and that microhardness of zirconium alloys was increased by LSA with Nb, due to three factors; solid solution hardening with Nb, grain-size refinement by rapid cooling, and transformed β phase. However, the corrosion resistance of laser alloyed Zircaloy-4 was found to be reduced in steam at 400°C, a result of the formation of β-Zr phase and Zr hydrides.

Laser assisted treatments normally induce localized high temperature, distortion at high temperatures, and the formation of Zr-hydrides, which are the main technical limitations of laser assisted treatment.

2.4.3.3 Thermochemical and electrochemical methods

Thermochemical and electrochemical methods have also been investigated for the tribological improvement of zirconium alloys.

Electrochemical surface nitriding of zirconium alloys can form a ZrN layer on the outermost part of Zr electrode surfaces. The thickness and nitrogen concentrations at the nitrided layer increased as the applied potential was made more positive[145], which indicated that the concentration of nitrogen in the nitrided layer could be controlled by the applied potential. Nitriding of zirconium and its alloys can produce a high wear resistant surface while retaining its good corrosion resistance[145].

Anodizing is an electrochemical process used to produce a dense oxide layer on a materials surface. The voltage applied determines the thickness of the formed layer. With increasing thickness, the surface layer changes to gold, then red, green, blue and black[159]. On the other hand, this technique is can also be adopted as a method to enhance metallurgical preparation[173]. However, anodizing can only produce a very thin surface oxide film with limited protection to surface wear.

Zirconium oxidation has been extensively studies. However, it was addressed more as a problem rather than a surface modification method to improve tribological properties. Zirconium forms a visible oxide film at about 200 °C[174]. When heated in air, the reaction is primarily with oxygen rather than nitrogen. During oxidation, a surface containing a large amount of flakes forms[175]. The lower the temperature, the smaller the flake size will be. Plasma oxidation uses plasma, the forth state of matter, to bombard the substrate surface by ionized oxygen ions. Several variables will affect the plasma oxidation process: the magnitude of the voltages, temperature, gas pressure and composition, electrical potential of the substrate as well as the location of the metal within the chamber during the treatment. However, the major concern for plasma oxidation is that the treatment also causes detrimental oxidation on the equipment used.

There is often an obvious boundary between the surface oxide layer and zirconium substrate; however, with well controlled thermal oxidation conditions a diffusion-bonded “high-quality” film on Zr alloys can be formed[176]. Some preliminary work has been reported on thermal oxidation or ceramic conversion of Zr alloys[115, 177]. However, no systematic investigation has been conducted.

2.4.4 Ceramic conversion treatment and hybrid treatment

Ceramic conversion (CC) treatment is a new cost efficient and environmentally friendly surface engineering technique that was first developed by and H. Dong mainly for titanium based alloys in 1990s. After CC treatment, a ceramic oxide layer is formed on the surface, and an oxygen diffusion zone (ODZ) beneath the oxide layer. Research has shown a combined improvement in tribological, anti-corrosion and biocompatible properties. This is due to the high hardness and attractive characteristics of the titanium oxide ceramic, as well as the ODZ’s effect of hardening the material together with significant improvements in its load bearing capacity[62, 75, 178, 179]. Up to date, the CC treated titanium alloys have been industrially used in automotive and off-shore industries.

In addition to titanium based alloys, zirconium alloys can also be CC treated to improve their tribological properties[130]. For example, CC treated Zr702 and Zr705 were corrosion wear tested at 3.5 wt% NaCl solution. Results showed that the ceramic layer mainly composed of monoclinic ZrO_2 with trace amount of tetragonal ZrO_2 exhibited the best anti-corrosion wear resistance when treated at 600 °C for 10 hours and 3 hours for Zr702 and Zr705 respectively. Both samples have a thickness of about 5 μm.

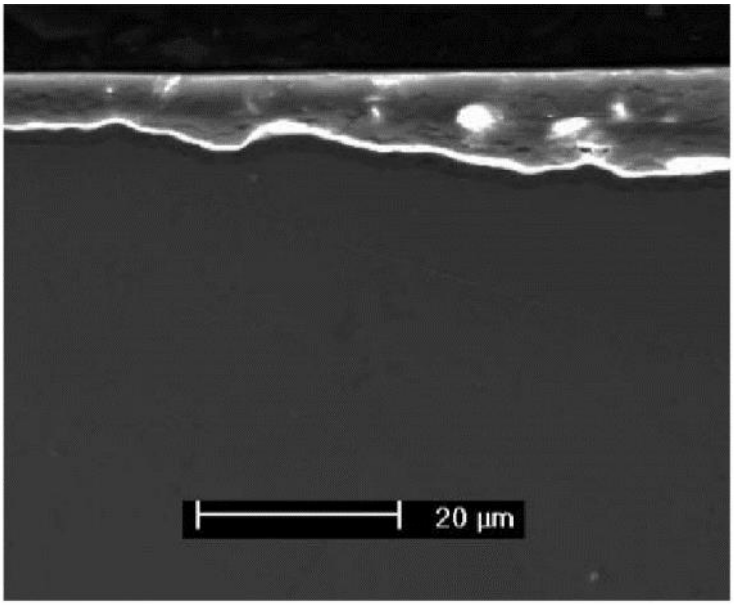


Figure 2.4-2 Cross-sectional SEM images of Zr702 after treated at 600°C for 30hours [130]

However, the hardened case for zirconium alloys is generally thin (< 1 µm) as shown in Figure 2.4-2. In order to increase the load bearing capacity, a deep-case hardening through oxygen boost diffusion (OBD), invented by Dong et al.[180] is introduced. Hence, a duplex treatment, either a two-step (CC+OBD) or three-step process (CC+OBD+CC), can be adopted. Both approaches have been studied[181] and exhibited high adhesion between the substrate and the oxide scale.

For the two-step treatment, V. Pawar et al. from Smith and Nephew Inc. [182] conducted an vacuum annealing at 685 °C for 10 hours is processed following the air oxidation with an oxide layer of about 5µm. After the treatment, the thickness of the diffusion zone was at least 10 times greater than that of the oxide layer straight after annealing. The critical load to trigger the crack was found to increase from 1.28 for undiffusion boosted sample to 2.07.

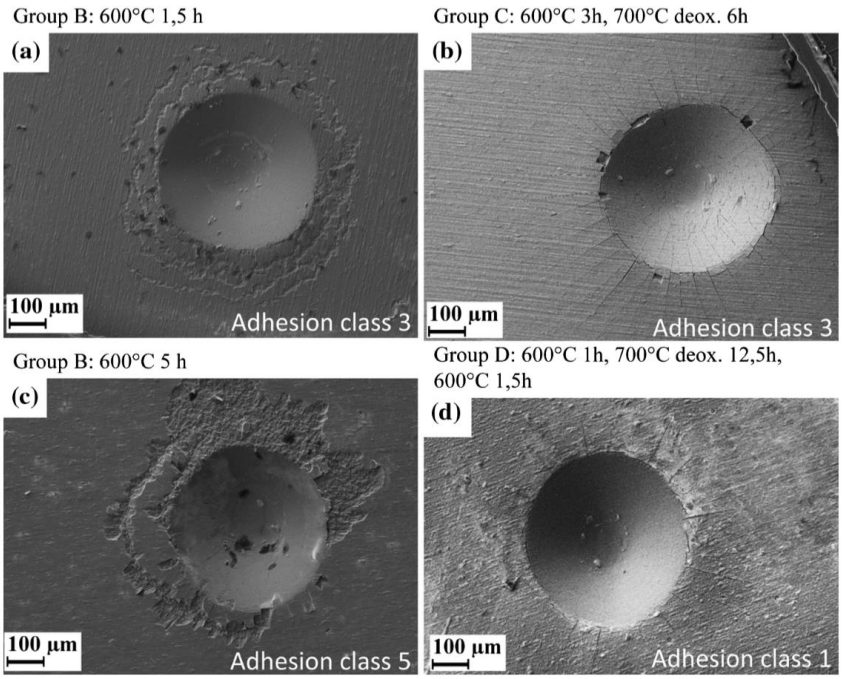


Figure 2.4-3 HRA indents for adhesion class measurements after treatments[181]

M. Reif, F. Scherm and U. Glatzel et al.[181] used a three-step process: sample was initially oxidized in air, then completely deoxidized in a vacuum furnace to achieve a fully oxygen dissolution layer, the surface of which will be oxidized in a 3rd step. The optimised condition to improve the adhesion between substrate and oxide layer is oxidation 600°C/1h, deoxidation 700°C/12.5h and 600°C/1.5h as shown in the Rockwell A-scale diamond cone indentation (HRA) test, Figure 2.4-3.

It should be pointed out that to date most oxidation studies concentrated on Zr-Nb alloys, and no systematic work has been conducted on surface engineering of Zircaloy alloy (Zr-Sn).

2.5 Summary

Zirconium and its alloys are high demanding materials due to their advantageous properties such as low thermal neutron absorption cross section, excellent corrosion

resistance to most aggressive environments, good biocompatibility and relatively good mechanical properties. However, zirconium and its alloys are also characterised by poor tribological properties, which is attributed to their hexagonal closed pack (HCP) crystal structure, high chemical activity and metallurgical compatibility, as well as the low hardness. The degradation of zirconium parts is mostly related to wear issues.

Different surface coating and surface modification methods have been investigated to improve the tribological property of zirconium alloys with limited success. Recently there are some research directed towards improving wear resistance of zirconium and its alloys via surface oxidation; however, more are focused on the oxidation mechanism and products in different mediums than on tribological behaviour of the oxidised surfaces. Thus a systematic study on the tribological response of ceramic conversion treated zirconium alloys and the wear mechanism involved is needed to identify the optimised treatment conditions and advance scientific understanding.

In addition, all the research to date on thermal oxidation treatment is focused on either commercial grades or nuclear grades. Therefore, this PhD research project was aimed to improve the tribological properties of Zr702 (commercial grade) and Zr-Sn based Zircaloy-4 (nuclear grade).

3 EXPRIMENTAL

3.1 Materials and sample preparation

Both commercial grade Zr702 and nuclear grade Zircaloy-4 were used as substrate materials for the ceramic conversion (CC) treatment conducted in this work. Zr702 was supplied in the form of plate of ~ 4 mm thickness, while Zircaloy-4 was cuboid shaped material with the cross section dimensional of ~ 25 × 30 mm^2. The chemical compositions of Zr702 and Zircaloy-4 quoted from supplier's specifications are listed in Table 3.1-1.

Table 3.1-1 Chemical composition of as-received Zr702 and Zircaloy-4

Element / Material	Zr+Hf, max	Hf, max	Fe+Cr, max	C, max	O, max
Zr702	99.2	4.5	0.20 max	0.05	0.16

Element / Material	Zr	Hf, max	Sn	Fe+Cr	Cr	Ni, max	O
Zircaloy-4	97.56-98.27	0.01	1.2-1.7	0.28-0.37	0.07-0.13	0.007	0.09-0.16

Zr702 and Zircaloy-4 were then cut to square samples with a thickness of about 4 mm and their dimensions being 20 × 20 mm^2 and 25 × 30 mm^2 respectively, using a StruersAccuton-5 cutting machine. These samples were wet grounded using silicon carbide paper from grit 120 down to grit 1200 and then polished according Struers metalog guidance until a mirror-like smooth surface (surface roughness Ra =0.02 μm) was obtained. Table 3.1-2 lists the sample preparation procedures in details.

Table 3.1-2 Sample preparation method

Step	Plane Grinding (PG)	Fine Grinding(FG)	Oxide Polishing (OP)
Surface	Silicon carbide paper	MD-Largo	MD-Chem
Abrasive Type size	Silicon carbide	Diamond 9µm	Collodial Silica 0.04µm
Suspension	Water	DiaPro Largo	OP-S with 10ml H_2O_2 (30%)
Speed, rmp	300	150	150
Forc, N	40	30	30
Time, minutes	Until Plane	5	5

3.2 Surface treatment

3.2.1 Ceramic conversion (CC) treatment

After having been polished to a surface finish of Ra = 0.02 µm, the samples were cleaned using detergent, followed with acetone by twice, in ultrasonic cleaning machine for approximately 5 minutes in each step before treatment in order to remove the contaminants on the sample surfaces which may influence the CC treatment outcomes.

Cleaned samples were then put into an air containing furnace for CC treatment. The heating rate for all of the treatment processes was set to be 8 °C/minutes. Samples were treated at different temperatures varying from 400 °C to 800 °C for 10 hours in order to study the temperature effect on the oxidation of Zr702 and Zircaloy-4. For an examination of the treatment time effect, other samples were treated at selected temperature, 400 °C, 500 °C, 530° C and 600 °C, for different time periods. The detailed samples codes and process conditions are summarised in Table 3.2-1. After the treatment samples were cooled down with the furnace until room temperature. At least three samples were treated under each condition.

Table 3.2-1 CC Treatment codes and conditions of Zr702 and Zircaloy-4

Materials		Temperature (°C)	Time (hours)
Zr702	Zircaloy-4		
Zr702-4010	Zry4-4010	400	10
Zr702-40100	Zry4-40100	400	100
Zr702-40200	Zry4-40200	400	200
Zr702-5010	Zry4-5010	500	10
Zr702-5050	Zry4-5050	500	50
Zr702-5310	Zry4-5310	530	10
Zr702-5350	Zry4-5350	530	50
Zr702-5610	Zry4-5610	560	10
Zr702-6010	Zry4-6010	600	10
Zr702-6020	Zry4-6020	600	20
Zr702-6030	Zry4-6030	600	30
Zr702-7010	Zry4-7010	700	10
Zr702-8010	Zry4-8010	800	10

3.2.2 Duplex surface treatment

In order to increase the load bearing capacity of the engineered Zr alloy surfaces, the response of zirconium alloy to oxygen boost diffusion (OBD) process to develop a thick oxygen diffusion zone (ODZ) was investigated. A series of two-step duplex surface treatments (CC + OBD) were carried out on Zr702. After samples CC treated under 700 °C/10 hours, OBD treatment was carried out in a tube vacuum furnace with varying treatment time and temperatures. The vacuum in the furnace under treatment was

controlled at 1×10^{-6} Pa at the steady state. It should also be noted that the vacuum dropped slightly but not higher than 10^{-5} Pa during the whole heating-up period. After the treatment, samples were then cooled down with the furnace. The corresponding treatment codes and conditions are listed in Table 3.2-2.

In addition, a three-step duplex treatment was also carried out for comparison. The treatment code and conditions are shown in Table 3.2-3.

Table 3.2-2 Two-step duplex surface treatment codes and conditions

Sample code	**OBD**	
	Temperature, °C	Time, hours
CC7	N/A	N/A
CC7-6010	600	10
CC7-6030	600	30
CC7-7030	700	30
CC7-8030	800	30

Table 3.2-3 Three-step duplex surface treatment codes and conditions

Sample codes	**Treatment conditions: temperature, °C/time, hours**
CC+OBD	700/10 + 800/30
CC+OBD+CC	700/10 + 800/30 + 530/10

3.3 Characterisation and property evaluation

3.3.1 Microstructure characterisation

3.3.1.1 Preparation of metallographic samples

For better revelation of the as-received materials' microstructure, samples were firstly polished using the procedure shown in Table 3.1-2. Precision Etching Coating System II (PECS II) (Gatan, UK) was adopted for a finial surface polishing. The ion polishing method is listed in Table 3.3-1.

Table 3.3-1 Ion polishing method for the as-received zirconium alloys using PECS II

Procedure	Voltage, keV	Angle, °	Time, hours
Stage 1	6	6	1
Stage 2	1	4	2

Surface morphology observation of treated samples was carried out on the surface as-treated without any further metallographic preparation in order to have an accurate examination of the treated surface.

In terms of cross sectional observation, samples were first cut and mounted at the cross section surface using conductive Bakelite. Then the samples were grounded and polished using the procedures shown in Table 3.1-2. It should also be indicated that for some of the thin surface treated layers, a nickel plating process prior to mounting and polishing for protection was carried out. The experimental set-up used is shown in Figure 3.3-1.

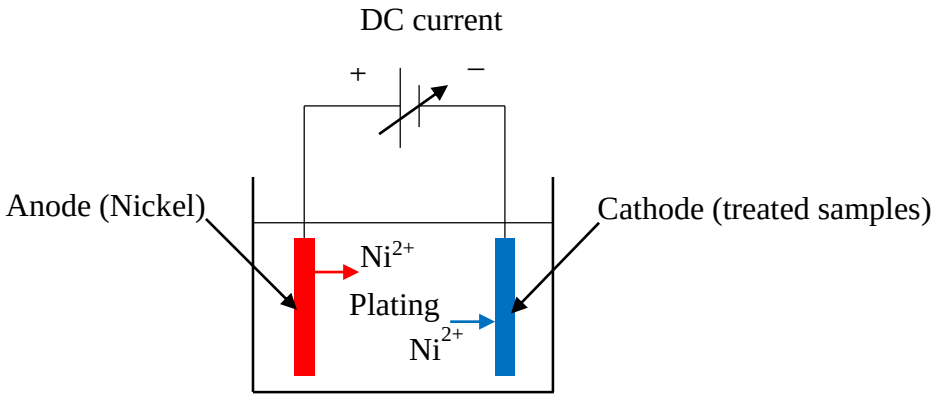


Figure 3.3-1 Schematic diagram of the nickel plating set-up

3.3.1.2 Optical microscopy

Zirconium has an obvious anisotropy thus responding well to polarising light. In addition, crystals with different orientations produce oxidised zirconium with different textures and structures, which interfere differently with polarized light. Hence polarized light was used for the microstructure observation of zirconium and its alloys in order to increase the contrast.

A Carl Zeiss polarised microscope was thus utilised for the microstructural examination of the as-received Zr702 and Zircaloy-4 materials. Meanwhile, it was also used for surface morphology and the cross sectional microstructural observation of both CC and duplex surface treated samples.

Visual morphology observation of the treated samples was also reported through the use of a Fiji digital camera.

3.3.1.3 Scanning electron microscopy (SEM)

Scanning electron microscopies, Philips XL-30, JOEL 6060 and JOEL 7000, were used for cross sectional layer quality examination of CC and duplex surface treated samples.

After load bearing capacity, corrosion and tribological tests, SEM observations were carried out as well.

All of the SEMs employed are equipped with a backscattered detector and Energy Dispersive X-ray spectroscopy (EDX). BackScattered Electron (BSE) images and EDX analysis were used for qualitative and the quantitative compositional measurements of samples.

3.3.1.4 Glow discharge optical emission spectroscopy (GDOES)

Glow Discharge Optical Emission Spectroscopy (GDOES) (Spectruma 650, German) test was carried out on all CC and duplex treated sample for the depth composition analysis. Figure 3.3-2 is the schematic diagram showing the principal for the GDOES test. Samples were placed in contact with the cathode during the test, therefore, is switched to cathode. With a high direct voltage (DC) power supply applied between the anode and cathode, electrons are generated from the sample surface and accelerated. Collision of the electrons with argon then leads to the formation of plasma, a mixture of argon cations and electrons. Acceleration of the argon cations hence induces caused the sputtering of atoms from the sample surface. The knocked out atoms' collision with the plasma therefore releases different emitted light by the returning of the atoms to the ground state from the excited state. The concentration of the elements at a certain depth is therefore obtained by analysing the characteristic emitted lights and their intensity.

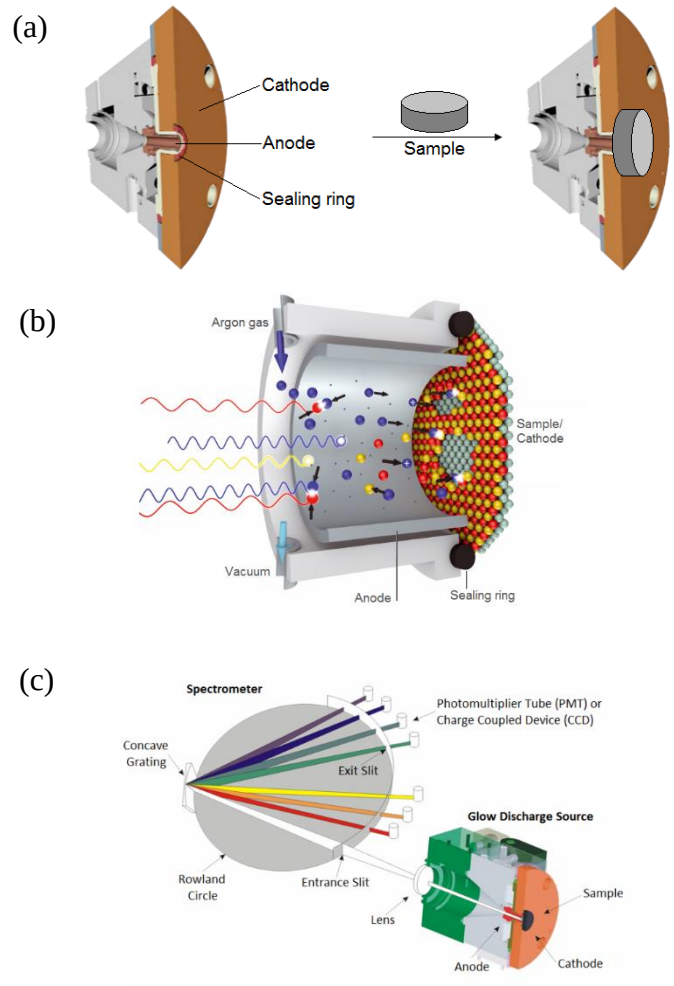


Figure 3.3-2 Schematic diagram showing working principal of GDOES machine[183]

3.3.1.5 X-ray diffraction (XRD)

When monochromatic X-ray beam is projected on surface of crystalline lattice, they interfere with the diffracted beams coming constructively when they are in phase, which gives the X-ray peaks as detected in an XRD scan. The path difference between the incident and diffracted beams, shown in Figure 3.3-3, should satisfy the Bragg's law:

$$n\lambda = 2dsin\theta \qquad \text{Equation 3.3-1}$$

where the incoming beam has a wavelength of λ and an incident angle is θ.

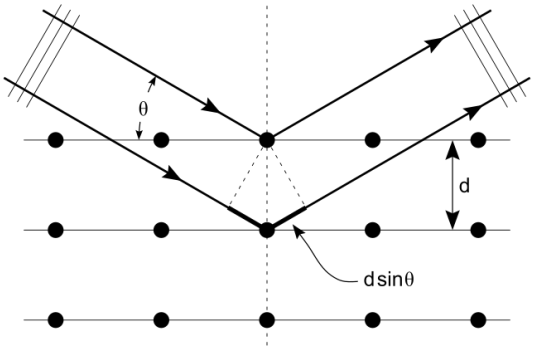


Figure 3.3-3 Schematic diagram of Bragg's law

The phase constituents of the as-received and treated surfaces were analysed using a Philips X'pert X-Ray Diffractometer with a Cu-Kα radiation (λ=1.540598Å) using 25 mA current and 35 KV accelerating voltage. A monochromatic X-ray beam was projected on the surface of the sample at incident angles from 20° to 60°. When the d-spacing, varying with different atom sizes and crystal structures, satisfies the equation, a diffraction ray will be generated. After scanning, the results obtained were analysed and indexed using X' pert High Score Plus V.2 analytical software with database PDF2004.

3.3.1.5.1 In situ XRD

In situ XRD tests at an elevated temperature of 700 °C on both Zr702 and Zircaloy-4 were conducted using a Bruker D8 diffractometers. Samples for *in situ* test were firstly cut into a dimension of 5 × 5 mm^2 with a thickness of 3 mm and then grinded and polished until a surface finish of 0.02 μm using the procedures listed in Table 3.1-2. The prepared sample was then placed into the XRD chamber connected with an air cylinder. The air flow rate was set to be 100 mL/minutes to simulate the air containing furnace as carried out for CC treatment. X-ray scanning was carried out once every 100 °C at a step size (2θ) of 0.031 ° from 20 ° to 60 ° from room temperature until the chamber temperature reached 700 °C and then continuous scans on the sample surface

was conducted for at least 10 hours. It should be noted that when the scanning was on-going, the chamber temperature was kept temporarily stationary until the scan finished. Therefore, the heating up rate of the chamber was set to be 12 °C/minutes for a good simulation of CC treatment in the air containing furnace. After the test, the results obtained were analysed using X'pert High Score software as mentioned earlier. Then the phase constituents at different temperatures and times were compared to study the phase formation during the surface treatment.

3.3.1.6 Transmission electron microscopy (TEM)

Cross sectional Transmission Electron Microscopy (TEM) was carried out on selected samples prepared in a cross sectional manner. The sample preparation method are as follows:

(1) Two slabs each with a dimension of 1.5 × 3 × 0.5 mm^3, shown in Figure 3.3-4, were cut off from treated surface and glued together using G-1 epoxy (Figure 3.3-5 (a)). The surfaces were facing each other.

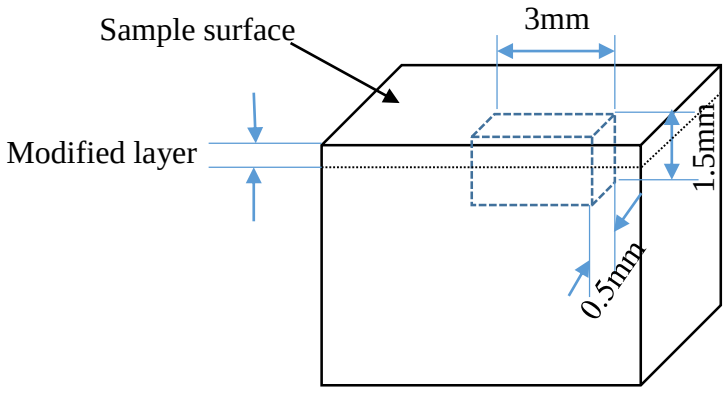


Figure 3.3-4 Schematic diagram showing slab cutting from treated surfaces

(2) The assembly was mounted to metallic coupon of Gatan Disc Grinder 200 (UK), and grinded using SiC paper of grit 1200 on both sides until a thickness of less than 50

μm. The thin assembly was then soaked in acetone for 12 hours to clean and parted into two slides. A schematic diagram is shown in Figure 3.3-5 (b).

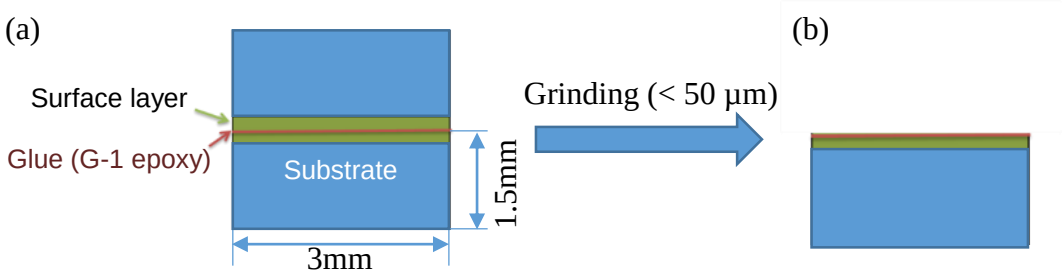


Figure 3.3-5 Schematic diagram showing (a) glued and (b) detached slabs

(3) Tungsten was then coated onto one of the two thin slide in order to protect the integrity of the surface layer before Focused Ion Beam (FIB) was used for milling the thin slide into a thickness of less than 100 nm. The SEM image of obtained sample for TEM is shown in Figure 3.3-6.

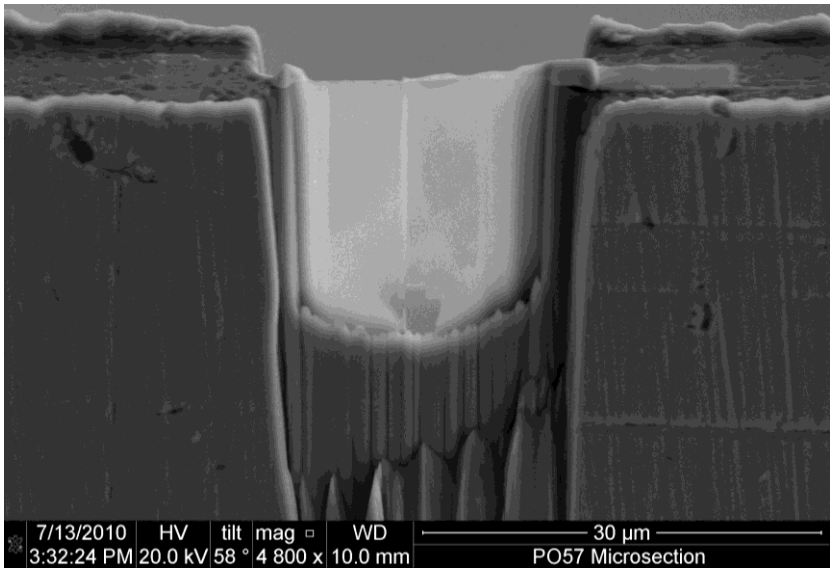


Figure 3.3-6 SEM images of FIB ion milled sampled prepared for TEM

A JOEL JEM-2100 LaB_6 transmission electron microscope (Japan), fitted with Oxford Instruments (UK) and Gatan CCD camera (UK), was used for the characterisation of phase constituent and microstructure of coatings under 200 kV.

3.3.2 Mechanical property measurement

3.3.2.1 Microhardness and load bearing capacity

Microhardness of treated sample was measured using a Vickers' microhardness indenter, and the indentation load used varies from 10 g to 500 g. Figure 3.3-7 shows a hardness indent, with its diagonals denoted as d_{v1} and d_{v2} respectively. The average value of the two diagonals d^* are later used to calculate the hardness value, as shown in Equation 3.3-2 and 3.3-3. The unit given by the teat as Vickers Pyramid Number (HV). P in Equation 3.3-3 stands for the indentation load in kgf while C_V is an indenter shape related factor, as shown in Equation 3.3-4. The included angle θ for Vickers indenter is 136 °.

$$d^* = \frac{d_{v1}+d_{v2}}{2} \qquad \text{Equation 3.3-2}$$

$$HV = C_V\left[\frac{P}{(d^*)^2}\right] \qquad \text{Equation 3.3-3}$$

$$C_V = 2\sin(\theta/2) \qquad \text{Equation 3.3-4}$$

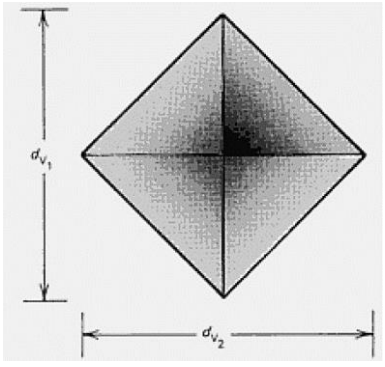


Figure 3.3-7 A microhardness indent with its diagonals d_{v1} and d_{v2}

At least three indents at the same load with interspacing were measured for each sample and then the mean value was calculated and reported, and the standard deviation used for error.

The measured microhardness vs. load graphs of different samples were then plotted and compared for load bearing capacity study. Meanwhile, indents morphology was also observed for a study of coating failure mode.

3.3.2.2 Nanoindentation

Nanoindentation test was carried out on the surface and different depths on the cross section samples to measure hardness and Young's modulus etc. A Nano Vantage Machine (Micro Material UK) with a pyramidal (Berkvich) indenter was used for the nanoindentation tests. Different from microhardness test in which the hardness is calculated from the final size of the indent, a continuous depth recording is utilised in a nanoindentation test. A typical depth vs. load curve at loading and unloading conditions is shown is Figure 3.3-8.

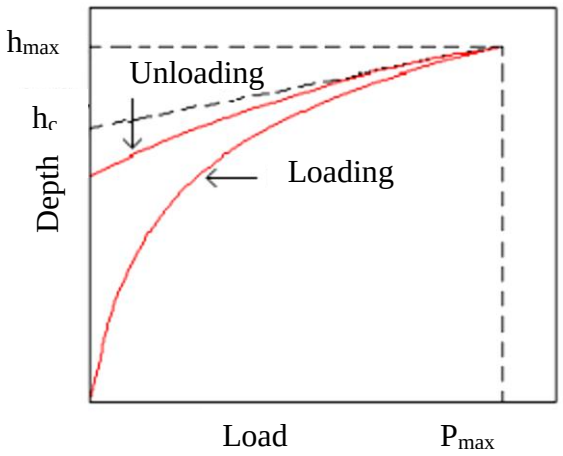


Figure 3.3-8 Depth vs. load curve for determination of plastic depth

For the unloading data, a power law fit is used, expressed in Equation 3.3-5.

$$P = a(h - h_c)^m \qquad \text{Equation 3.3-5}$$

where a and m are both constants, while P and h stand for the applied load and indentation depth respectively.

The plastic depth h_c is determined by Equation 3.3-6, 3.3-7 and 3.3-8.

$$h_c = h_{max} - \varepsilon(CP_{max}) \qquad \text{Equation 3.3-6}$$

$$C = \pi^{0.5}/(2E_r A^{0.5}) \qquad \text{Equation 3.3-7}$$

$$1/E_r = (1 - \nu_s^2)/E_s + (1 - \nu_i^2)/E_i \qquad \text{Equation 3.3-8}$$

The value of ε relates to the geometry of the indenter. For the test carried out, where a Berkvich indenter is used, ε=0.75, C is the contact compliance, E_r is the reduced module; ν_s and ν_i are the Poisson's ratio for the sample and indenter respectively, while E_s and E_i are the Young's modulus for the sample and indenter respectively.

The diamond area function $A(h_c)$ is an indenter geometry dependant function, which is related with the penetration depth of the indent. The hardness H is determined from the Equation 3.3-9.

$$H = P_{max}/A \qquad \text{Equation 3.3-9}$$

For a good reliability of the test, at least five indentations were carried out at the same conditions, and the average value was used. It should also be noted that the load used for the surface nanohardness test was 5 mN for an accurate measurement of the thin coatings hardness, while 30 mN was adopted for hardness depth profile so that the

indents are big enough for a measurement of distance between sample surface and indents.

3.3.3 Corrosion test

In order to evaluate the corrosion resistance of the CC and duplex treated samples in comparison with the untreated materials, potentiodynamic polarisation tests were conducted on both untreated and treated samples in 3.5 wt% NaCl solution using Interface 1000-06014 potentiostat from Gamry Instruments (US). The experimental electrochemical cell set up and electrode connections of the corrosion test are shown in details in Figure 3.3-9. The reference electrode (RE), counterpart electrode (CE) and working electrode (WE) used in the setting are Hg/Hg_2Cl_2 (saturated) electrode, platinum coated rod and the tested sample respectively.

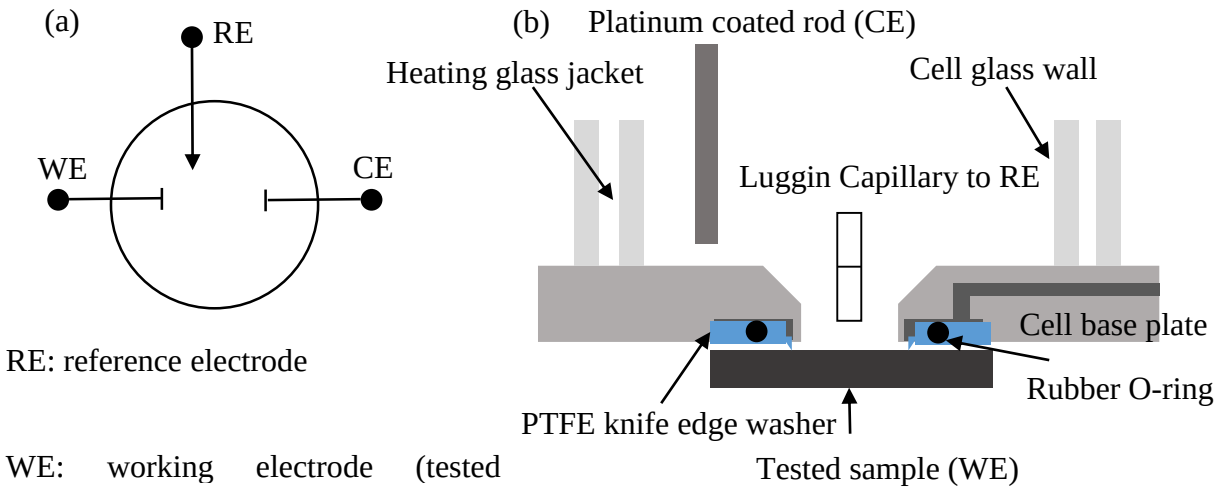


Figure 3.3-9 Schematic diagram showing electrochemical cell electrode connections (a) and cross section (b) of set-up for potentiodynamic polarisation test

For each test, 250 mL of 3.5 wt% NaCl solution was added into the cell with the temperature maintained at 25 °C. The Open Circuit Potential (OCP) would be running and recorded for 3600s before potentiodynamic polarisation scan. The sweep was

performed at a scanning rate of 1 mV/s with sample period of 1 s from -0.2 V vs. E_{OCP} to 1.5 V vs. E_{REF}. The sample was attached to the electrochemical cell through a rubber O-ring using a screw fastened at the bottom, as shown in Figure 3.3-9 (b). The tested area is 0.503 cm^2.

The results obtained were analysed using Gamry Echem Analyst software for the E_{corr}, i_{corr} values and etc. Each sample was tested at least three times for reliability and repeatability.

3.3.4 Surface roughness and tribological test

3.3.4.1 Surface roughness

A stylus profilometer, Ambios XP-200 (USA), was used for the surface roughness measurement of both as-received and treated samples. The whole equipment is placed on an air-cushioned table for anti-vibration purpose. During the test, the stylus scans the sample surface for a length of at least 0.5 mm is run through the surface with a maximum contact force of 10 mg. A test result of R_a roughness value was given in the end at the data analysis window. At least three repeated measurements were conducted for each surface, and then the average value was calculated and reported. The standard deviations of measured values for the samples was used as the errors.

3.3.4.2 Reciprocating wear test

In order to evaluate the wear resistance of the surface treated samples, a reciprocating ball-on-disc sliding wear tester was used. A schematic diagram of the tester is shown in Figure 3.3-10. The tests were carried out at room temperature at dry/unlubricated conditions. During the tests, the untreated and surface treated samples were mounted on a sample holder sliding against a 12.5 mm diameter WC/Co ball, with a stroke length of

5 mm at a frequency of 0.92 Hz for 30 minutes. The counterpart ball contains 94 % tungsten carbide and 8 % cobalt. According to the product specification, the ball has a Vickers' hardness of 1500 HV and the Elastic/Young's modulus is 629 GPa.

The contact radius and the maximum Hertzian pressure could be calculated out using Equation 3.3-10 and 3.3-11 respectively[184, 185].

$$a = \sqrt[3]{\frac{3F}{8}\frac{(1-\nu_1^2)/E_1+(1-\nu_2^2)/E_2}{1/D_1}} \qquad \text{Equation 3.3-10}$$

$$p_{max} = \frac{3F}{2\pi a^2} \qquad \text{Equation 3.3-11}$$

Where a – contact radius; D_1 – the diameter of the ball;ν_1, ν_2 – the passion ratio of the ball and plane material respectively; E_1, E_2 – the elastic/Young's modulus of the ball and plane material respectively; p_{max} – the maximum Hertzian pressure.

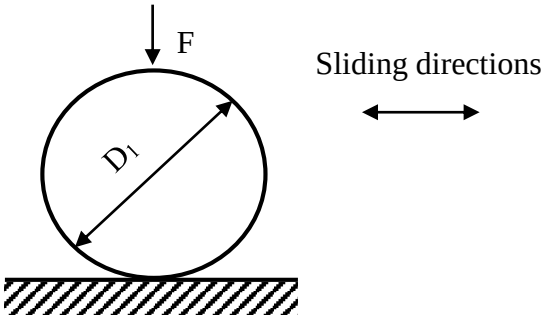


Figure 3.3-10 Schematic diagram of the reciprocating wear tester

Different loads, resulting in different Hertzian contact pressures, were used to evaluate the anti-wear performance of surface treated samples. Each test was repeated at least three times. The wear volume loss of tested samples was obtained by employing 3D profilometer (Ambios XP-200 stylus profilometer), as used in the surface roughness test, for a cross sectional scanning of the wear track. This measured cross section area is

noted as A_s, which is then multiplied by the wear track length (L) to calculate out the wear volume loss.

$$V_l = A_s \times L \qquad \text{Equation 3.3-12}$$

Wear rate was then calculated by dividing the wear volume loss by normal load.

$$R = V_l / F \qquad \text{Equation 3.3-13}$$

On each sample the wear test was carried out for at least three times for accuracy and repeatability. The standard deviation is used as the error. In addition, wear tracks were cleaned thoroughly using acetone for post wear examination by SEM and EDX. The combined results are used for wear mechanism analysis.

3.3.4.3 Coefficient of friction

A multi-axis tribological tester (Phenoix TE-79) was employed for the Coefficient of Friction (COF) characterisation of samples. The machine is controlled by the Compend 200 software.

The sample and the counterpart ball WC/Co inch ball were mounted onto their respective holders. The tribological pair were then put into contact gently. Tests were run at a programmed speed with an amplitude of 5mm under different normal load of 20 N for 100 cycles. The Hertzian pressure was calculated out with the same method mentioned in section 3.3.4.2. A friction coefficient vs. time graph was obtained at the end of the test and the steady friction coefficient value was taken in the end. The tests were repeated at each condition for at least three times to ensure repeatability.

3.3.4.4 Fretting wear test

Fretting wear test was carried out on sample Zry4-UN and Zry4-5310 due to Zircaloy-4's wide application in nuclear industry. Tests were carried out at Southwest Jiaotong University (China) using a fretting wear tester, schematic diagram shown in Figure 3.3-11. As it shows, for an accurate control of the small movement, precision-screw control unit was used. During test, the WC/Co ball was used as the counterpart ball because of its high hardness. Tested sample were placed at a normal load of 10 N. The fretting amplitude is 40 μm, with the frequency of 5 Hz.

The friction coefficient changes were recorded throughout the test, together with the load vs. displacement loop at cycle 1000 and 10000. In addition, wear volume loss of tested samples was obtained by Bruker profilometer. Post fretting scars were observed under optical microscopy for the wear mechanism analysis.

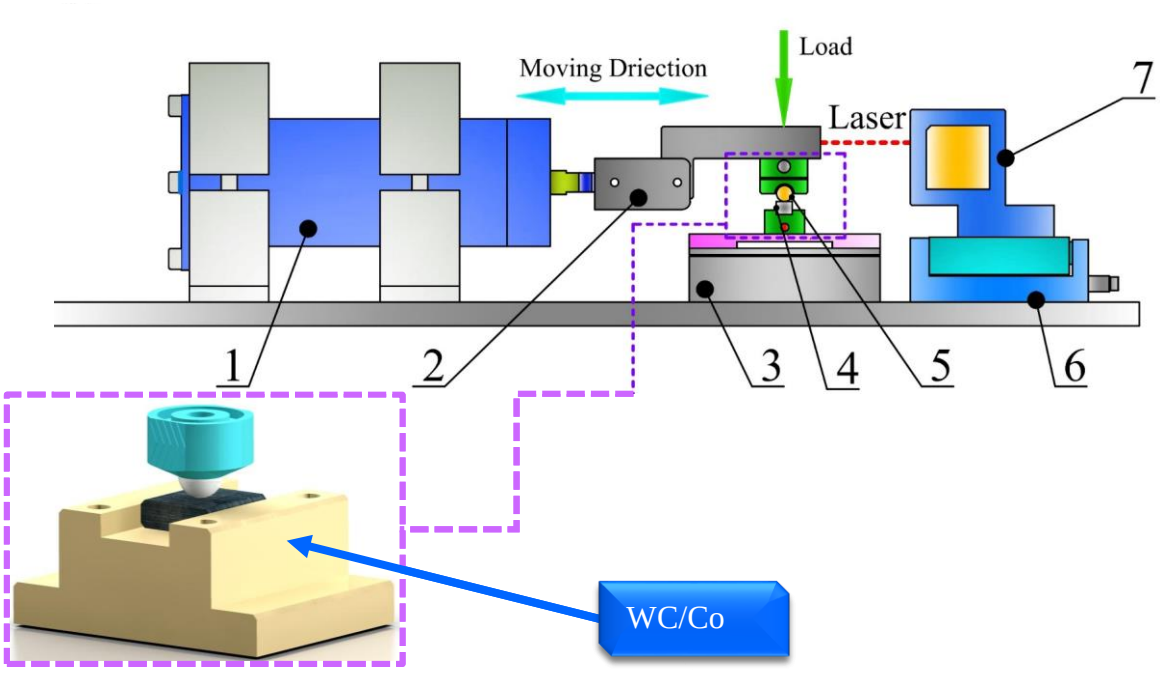


Figure 3.3-11 Schematic diagram of fretting test machine: (1) piezoelectric ceramic actuator; (2) test fixture; (3) force transducer; (4) test sample; (5) counterpart ball; (6) precision-screw controlled transmission unit; (7) displacement transducer.

4 EXPERIMENTAL RESULTS

As described in the experimental chapter, a series of CC treatment and duplex treatment were designed and conducted on zirconium alloys, i.e. Zr702 and Zircaloy-4, to identify the optimal heat treatment conditions (time and temperature) for anti-wear and anti-corrosion applications.

In this chapter, the experimental results will be presented in following sections. Microstructure of as-received zirconium alloys (Zr702 and Zircaloy-4) was firstly described in Section 4.1. Sections 4.2 and 4.3 report the layer characteristics of the modified surfaces (CC treated and duplex treated samples respectively): including surface morphology, surface roughness, composition depth profile, microstructure and phase constituents. Section 4.4 presents the mechanical properties such as surface hardness and the hardness depth profiles, together with load bearing capacity. The corrosion properties and tribological properties of surface treated samples are reported in Sections 4.5 and 4.6 respectively.

4.1 Microstructure of as-received materials

Microstructure observation of as-received materials, Zr702 and Zircaloy-4 was carried out using a polarised optical microscope, Scanning Electron Microscopy (SEM) and Electron BackScattered Diffraction (EBSD). The obtained images of Zr702 and Zircaloy-4 are shown in Figure 4.1-1 and Figure 4.1-2 respectively.

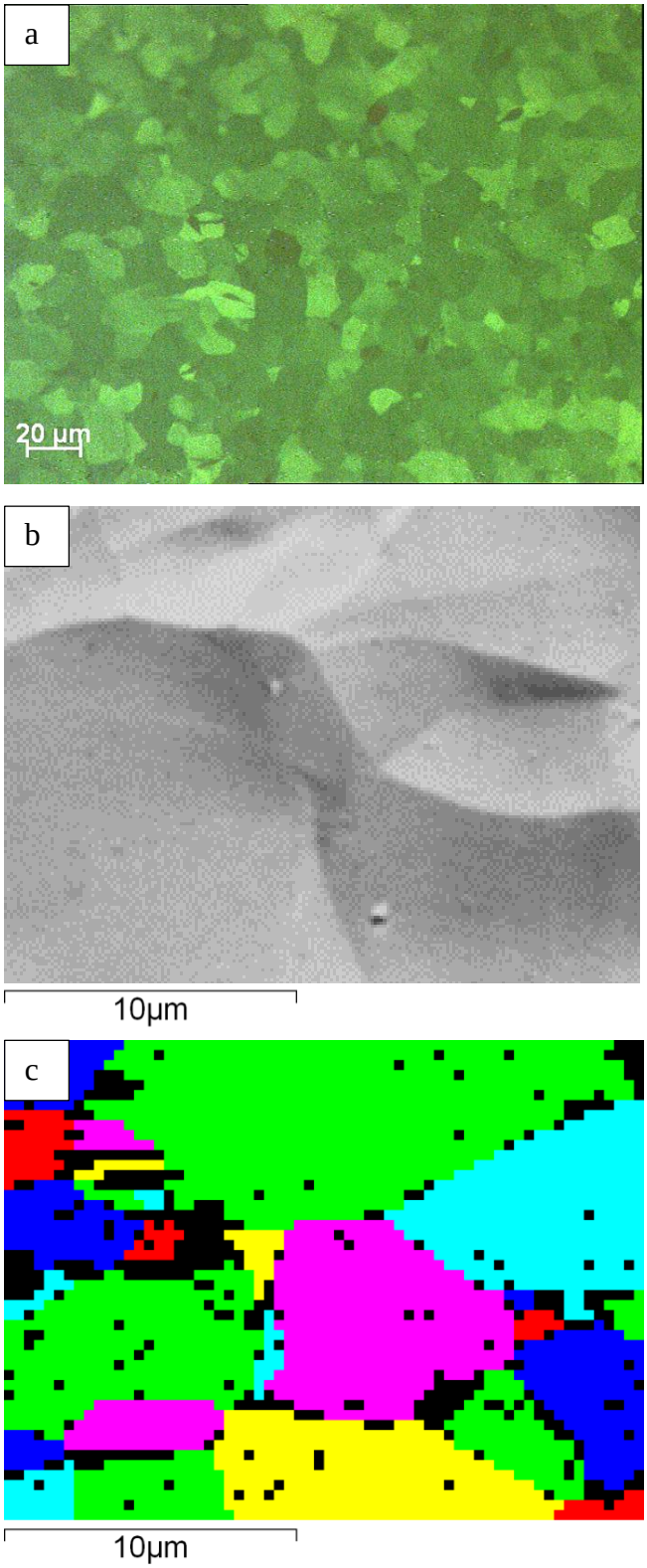


Figure 4.1-1 Microstructural images of as-received Zr702 using (a): polarised microscopy, showing equiaxed grain microstructure; (b): SEM; (c): EBSD phase mapping depicting the average grain size of about 8 µm, black spots standing for unidentified phases

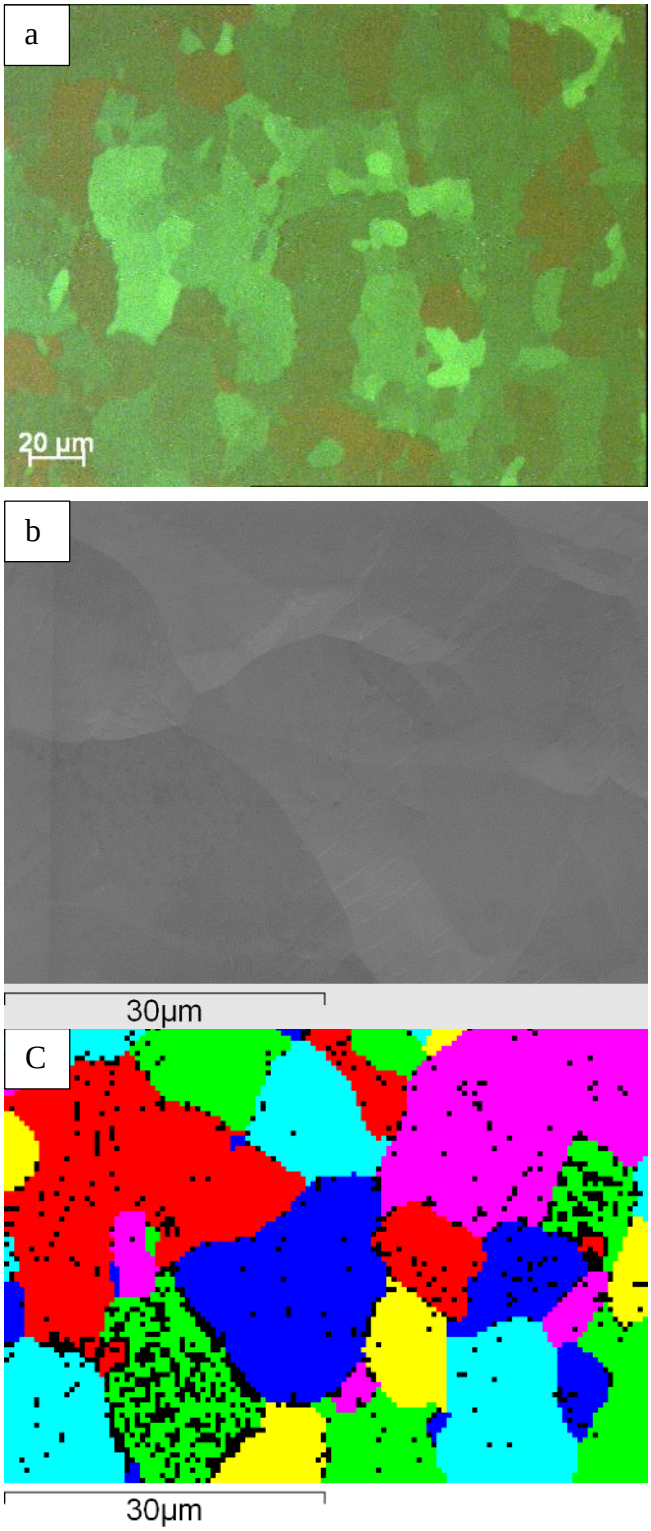


Figure 4.1-2 Microstructure of as-received Zircaloy-4, (a): polarised microscopy; (b): SEM; (c): EBSD phase mapping image showing an average grain size of about 15 µm, black spots standing for unidentified phases

As has been mentioned in Section 3.3.1.2, crystals with different orientations are demonstrated in different colour in the polarised microscopy images. From Figure 4.1-1 (a) small equiaxed grains microstructure can been noticed on as-received Zr702 alloy, though grain boundaries were not clearly depicted due to the close orientation of adjacent grains which, therefore, induces similar colour under polarised light. Image (b) obtained from SEM, however, only shows an ion etched metal surface with ion sputtering marks, hence, no microstructure features were revealed. Grains features are then better illustrated in Figure 4.1-1 (c) from the EBSD phase mapping image. Single phase Zr was identified and shown in the image. The black dots stand for the unidentified phases. The INCA grain analysis shows that the equiaxed grain structure has a grain size of about 8 μm. Not any noticeable second phase partible could be observed.

Similar to Zr702, Zircaloy-4 revealed an equiaxed grain structure as depicted in Figure 4.1-2 (a), (b) and (c) from polarised microscopy, SEM and EBSD respectively. Image (b) from SEM reveals the same ion etched topography of the prepared surface as that of as-received Zr702 alloy. It is evident by combining Figure 4.1-2 (a) and (c) that Zircaloy-4 has an equiaxed grain structure with a relatively large grain size of about 15 μm.

In order to study the phase constituents, XRD analysis was also conducted on the as-received samples. The XRD patterns shown in Figure 4.1-3 reveal that both Zr702 and Zircaloy-4 are made up of hexagonal close packed (HCP) zirconium i.e. α-Zr (PDF code 03-065-3366).

It can also be seen that the strongest diffraction peak from Zr702 is (002) plane, while it is (101) for Zircaloyo-4, indicating different preferred orientation parallel to the measured sample surface. Meanwhile, besides the strongest peaks identified coming from zirconium matrix, a small peak at 2θ position of 32° was detected from Zr702 samples, which is indexed to be (100) plane of hafnium (Hf) as supported by the fact that Zr702 contains about 4.5 wt% Hf (Table 3.1-1).

As it shows from Table 3.1-1, the main composition difference between Zr702 and Zircaloy-4 is that Zr702 contains no tin (Sn) while Zricaloy-4 has about 1.5 wt% Sn, which is an α-stabilizer for zirconium. It should be noted that the Hf and Zr have great similarities on both chemical and physical properties hence Zr702 (Zr-Hf) is often treated as commercial pure zirconium. It should also be noted that there have been previous reports on secondary phase particles, such as $Zr(Fe, Cr)_2$, in Zircaloy alloys which are mainly located at the grain boundaries[186]. However, no such particles could be identified in both alloys using either optical microscopy, EBSD or XRD. This is largely because the fraction of $Zr(Fe, Cr)_2$ could be too low(less than 5%) to be detected by the X-ray machine used while the resolution of both EBSD and optical microscopy is not high enough to resolve such very fine particles.

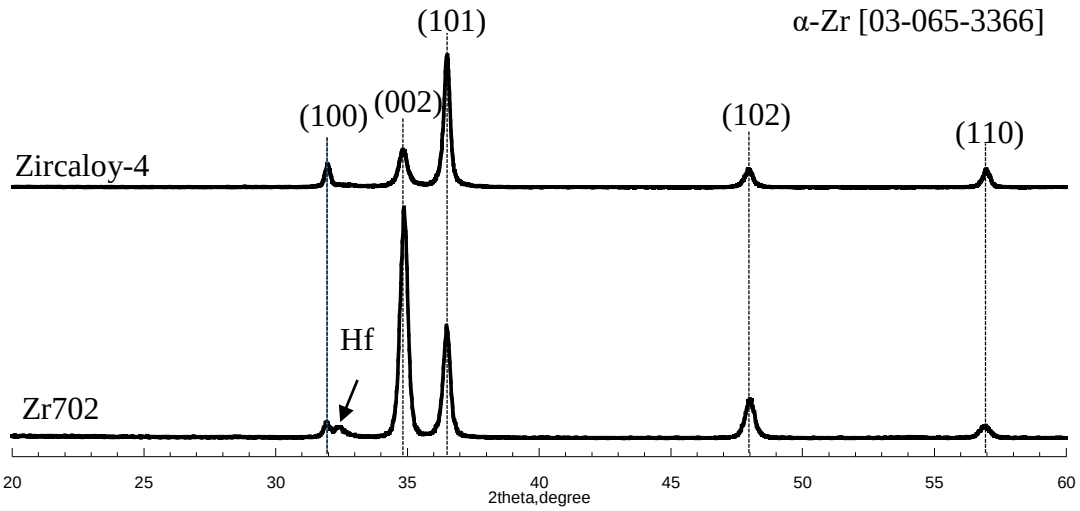


Figure 4.1-3 XRD patterns of Zr702 and Zircaloy-4 as-received materials

4.2 Microstructure of CC treated samples

Microstructure of surface CC treated samples were studied using optical and electrical microscopy, XRD, SEM, TEM and the corresponding results are reported in this section.

4.2.1 Surface morphology

Visual observation, shown in Figure 4.2-1, reveals a surface colour variation on CC treated Zr702 samples. After the treatment, a blueish colour can be observed for sample Zr702-4010, then the colour changed to black when increasing the treatment time and/or temperature. Some beige blisters were noticed to appear on the black surface when the CC treatment temperature is higher than 700 °C for 10 hours, i.e. Zr702-7010, Zr702-8010.

As for Zircaloy-4 in Figure 4.2-2, no blueish surface colour could be observed when samples were treated at 400 °C for 10 hours i.e. Zry4-4010. A more obvious surface colour change from black to beige could be clearly noticed when increasing the treatment temperature and/or time. Under current study conditions, the surfaces are in

black colour for the treatment conditions below 560 °C (500 °C/ 50 hours excluded), i.e. Zry4-4010, Zry4-5010, Zry4-5310 and Zry4-5610, which is similar to the colour on most treated Zr702 samples. However, when treated at 600 °C (sample Zry4-6010, Zry4-6020 and Zry4-6030), the samples are in dark greyish colour with beige dispersion. The same phenomenon was observed on the surfaces of samples Zry4-5050 and Zry4-5350, but the beige dispersion increased with the increasing of treatment temperature. It should be noted that these beige dispersions are in patches instead of in the blister form. In the end, the surface colour changed to fully beige colour when treated above 600 °C, i.e. for sample Zry4-7010 and Zry-8010. In addition, visually noticeable surface cracks could be seen especially for Zry4-8010. It is clear by comparing Figure 4.2-1 with Figure 4.2-2 that the beige colour appeared at a lower temperature and/or for a shorter time for Zircaloy-4 than for Zr702.

Further surface morphology observation was carried out using polarised optical microscopy. Selected typical images are presented in Figure 4.2-3 and Figure 4.2-4 for Zr702 and Zircaloy-4 samples, respectively.

As it can be noticed despite the similar black colour (with the exception of Zr702-4010 sample) of treated Zr702 samples by visual observation, under a polarised microscope a structure revelation could be observed for sample when treated at certain conditions, especially for the ones treated at 400 °C for 10 hours and 100 hours, as shown in Figure 4.2-3 (a) and (b). Both of them revealed a high contrast microstructure with equiaxed grains, but in different colour visions. This phenomenon is similar to heat tinting, which is a commonly used complementary technique for the metallographic preparation of zirconium alloys, where normally an unmounted chemically polished sample would

be put into a small oven for 3 minutes to 10 minutes at 300 ~ 370 °C depending on the alloy [187]. After heat tinting sample is able to improve their polarised light capacity and the visibility of grain structure can be greatly enhanced for a better microstructure revelation. Different colours were revealed for different grains due to the difference in oxide scale thickness on the surfaces caused by their chemical reactivity of the grains with different orientation.

With the increasing of the treatment temperature and time, the difference between grains gradually decreases with the typical images shown in Figure 4.2-3 (c) and (d) from sample Zr702-40200 and Zr702-5010. It can be seen that they exhibited similar colour on the whole surface with only traces of bright colour. This is due to the relatively thick oxide layer formed on the sample surface. However, with the keep increasing of treatment conditions, some blisters and surface cracks could be noticed on the formed ceramic surface, as marked in images shown in Figure 4.2-3 (e) and (f) from sample Zr702-7010 and Zr702-8010, respectively.

Similar phenomena are observed on CC treated Zircaloy-4 samples. The equiaxed grain microstructure was observed only on sample Zry4-4010 (Figure 4.2-4 (a)), while sample Zry4-40100 and Zry4-40200 (Figure 4.2-4 (b) and (c)) show typical surface morphology with similar surface colour under polarised microscope as similar as Figure 4.2-4 (d) and (e) from sample Zry4-5010 and Zry4-6010 respectively. Sample Zry4-7010 and Zry4-8010, typical image shown in Figure 4.2-4 (f) from Zry4-8010 as an example, depict a yellowish colour and large surface cracks. This yellow colour may be related with the beige surface as mentioned in visual observation. Different from Zr702 samples, when treated at high temperatures, Zircaloy-4 showed clear grain boundaries

as revealed by the dark spots as marked in Figure 4.2-4. In addition, as it can be noticed, for the same phenomena observed, lower CC treatment temperature and/or time was needed for Zircaloy-4 than for Zr702 (the same for the visual surface colour revelation as aforementioned), which indicates that Zircaloy-4 oxides faster than Zr702.

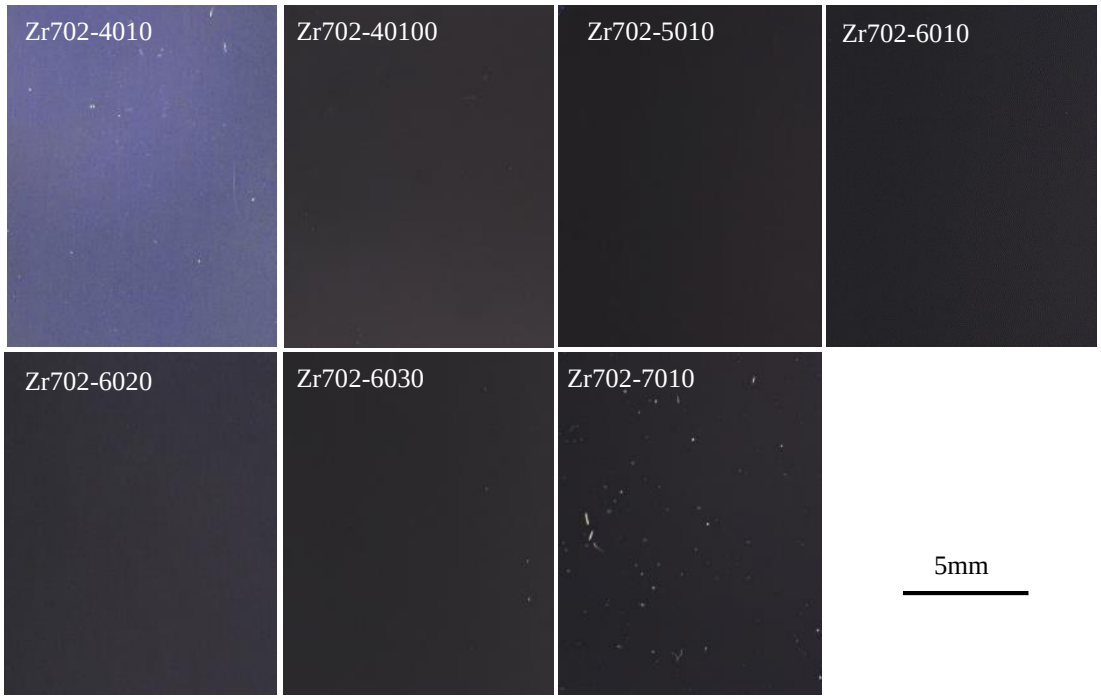


Figure 4.2-1 Visual observation of CC treated Zr702 samples, showing surface colour variation as a function of different conditions

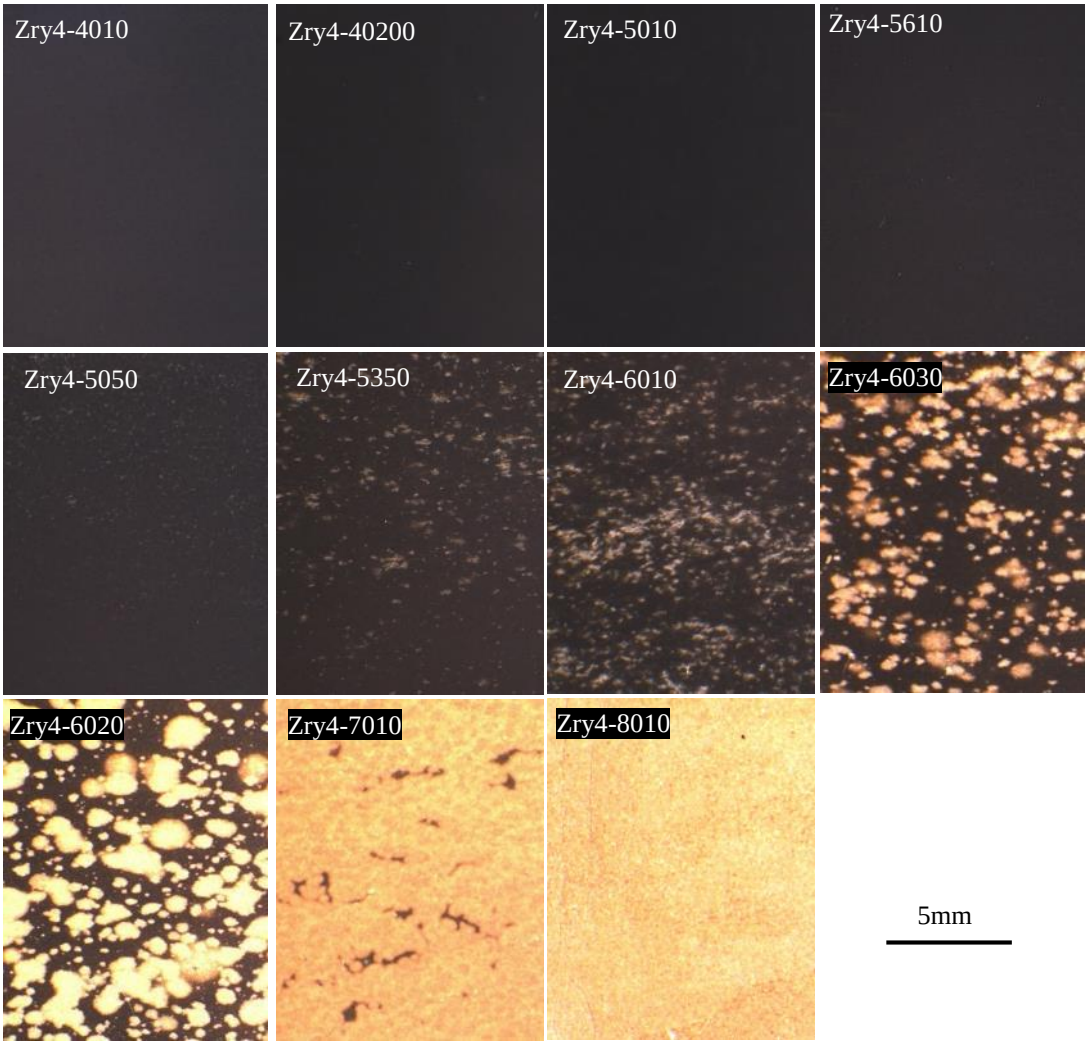


Figure 4.2-2 Visual observation of CC treated Zircaloy-4 samples, showing surface colour variation as a function of treatment conditions

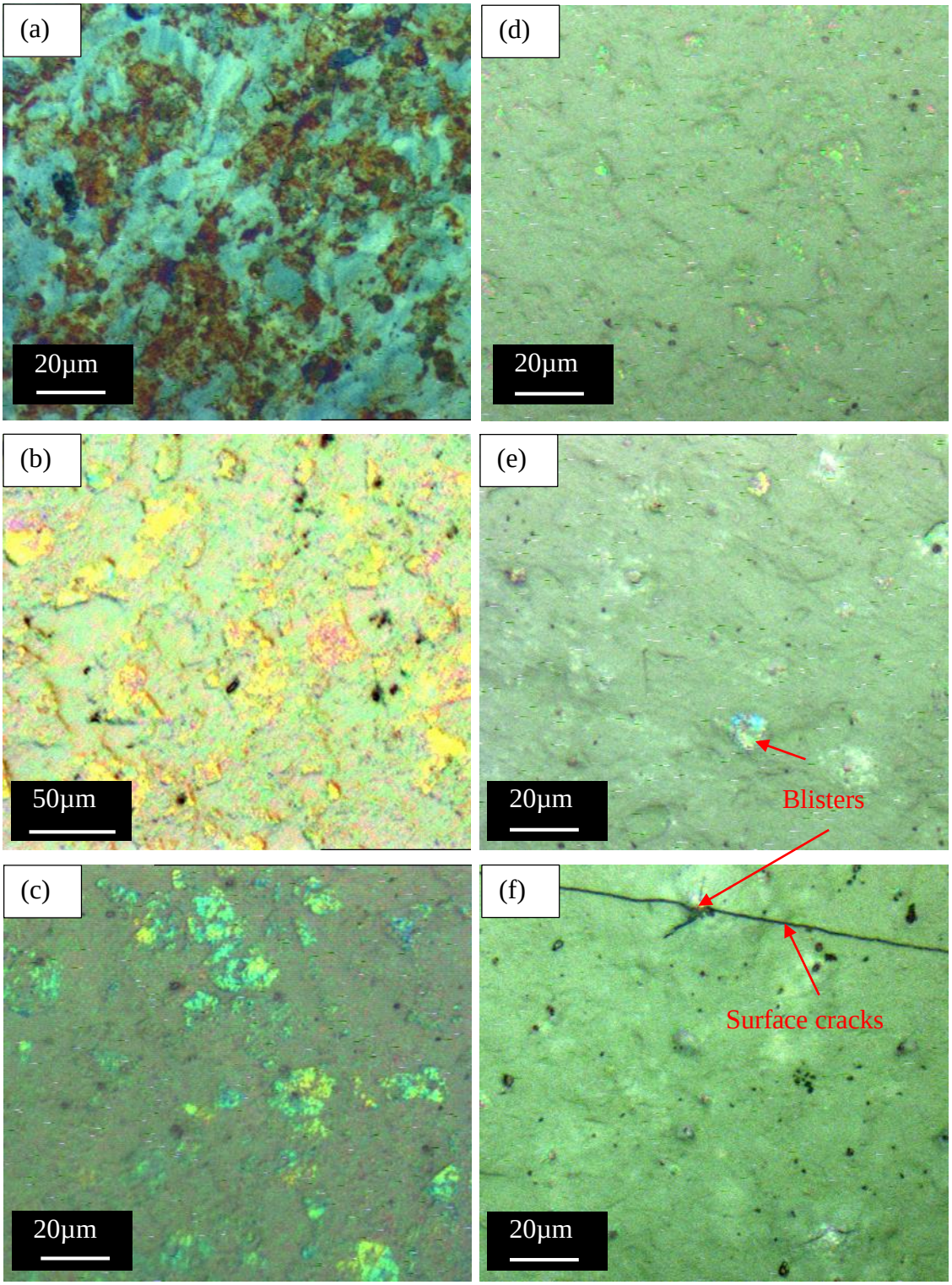


Figure 4.2-3 Optical microscopy images for selected Zr702 treated samples: (a) Zr702-4010; (b) Zr702-40100; (c) Zr702-40200; (d) Zr702-5010; (e) Zr702-7010; (f) Zr702-8010

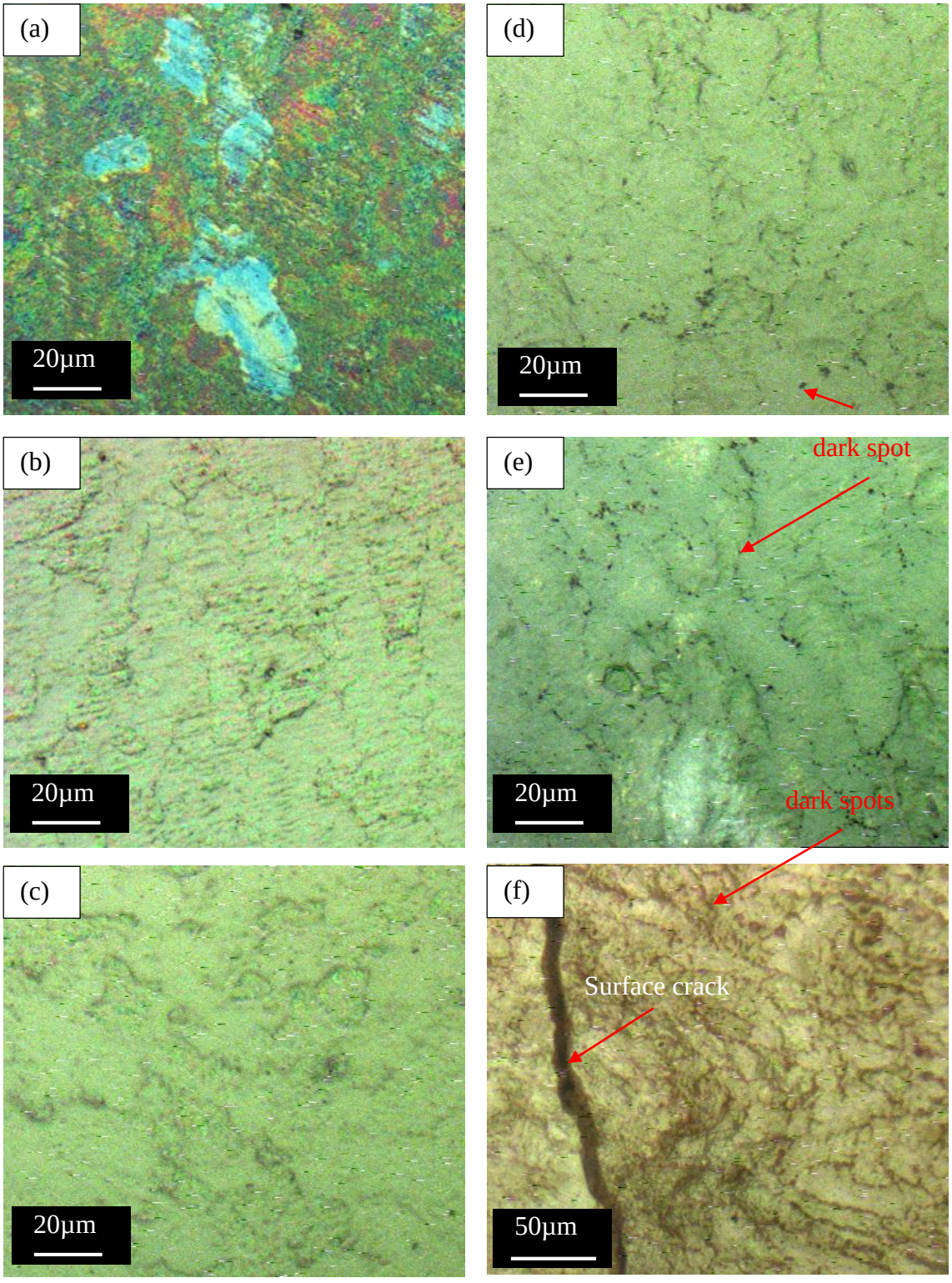


Figure 4.2-4 Optical microscopy images for selected Zr702 treated samples: (A) Zry4-4010; (B) Zry4-40100; (C) Zry4-40200; (D) Zry4-5010; (E) Zry4-6010; (F) Zry4-8010

4.2.2 Surface roughness

Figure 4.2-5 ~ Figure 4.2-7 demonstrate the surface roughness changes before and after CC treatment for both Zr702 and Zircaloy-4 samples. As reported in Chapter 3 that the surface roughness (Ra) of untreated Zr702 and Zircaloy-4 samples were both as low as 0.02 μm (final surface polishing finish), which generally increased after the treatment despite of the treatment conditions.

When comparing the surface roughness of samples treated at the same temperature of 400 °C for a time period varying from 10 hours through 100 hours to 200 hours, it can be seen from Figure 4.2-5 that with the increasing of treatment time period the surface roughness increasing gradually from an Ra value of 0.02 μm for untreated sample to 0.03, 0.04 and 0.05 μm for Zr702-4010, Zr702-40100 and Zr702-40200 respectively; and 0.04, 0.05 and 0.06 μm for Zry4-4010, Zry4-40100 and Zry4-40200 respectively. The same increasing tendency on roughness with the increasing treatment time period was observed for samples when treated at 500, 530 and 600 °C on as depicted on Figure 4.2-6 and Figure 4.2-7. It is clear that when treated under the same conditions, a slightly rougher surface was produced on Zircaloy-4 than on Zr702. As it can also be noticed, the surface roughness generally increased only slightly when increasing the treatment time period rises for the studied treatment temperatures: the only exception is Zircaloy-4 alloy treated at 600 °C (Figure 4.2-6) where a large increase of roughness was observed, which agrees with the development of the beige patch dispersion variations on the surface (Figure 4.2-2) as reported in section 4.2.1.

Figure 4.2-8 depicts the surface roughness changes for samples treated for 10 hours at a varying temperature from 400 °C to 800 °C. In general, the surface roughness of treated samples increased with the treatment temperature. At the same time, it can also be

found that there is a critical treatment condition beyond which the surface roughness of the treated sample will increase significantly. For Zr702 if the treatment temperature is below 700 °C, the surface roughness is lower than 0.1 μm, otherwise the Ra value can reach 0.15 μm for Zr702-7010 and up to 0.30 μm for Zr702-8010. Similar to Zr702, Zircaloy-4 has a critical treatment temperature of 600 °C. The surface roughness is about 0.23 μm for Zry4-6010 which is more 2 times than Zry4-5610 (0.09 μm). The roughness for Zry4-7010 and Zry4-8010 can be as high as 1.75 and 2.21 μm respectively due to the complete formation of beige ceramic layer during the CC treatment.

It should be noted that the critical treatment condition agrees with the surface colour changes especially for Zircaloy-4. The surface roughness corresponds to the formation of beige dispersion for Zircaloy-4 alloy (Figure 4.2-2): for Zry4-5610, Ra is 0.09 μm while it increased to 0.10 μm for Zry4-5050, and then surface roughness increased significantly and the treated surface became more and more dominated by the beige coloured area. Eventually the 800 °C/10 hours treated Zry4-8010 is fully beige coloured with an extremely high surface roughness of about 2.21 μm.

In terms of Zr702, the appearance of the beige blisters accompanies the large increasing of Ra value which is 0.15 μm for Zr702-7010 and then 0.30 μm for Zr702-8010.

In short, the surface roughness values of treatment samples of Zircaloy-4 are always higher than those of Zr702 when treated at the same CC treatment conditions.

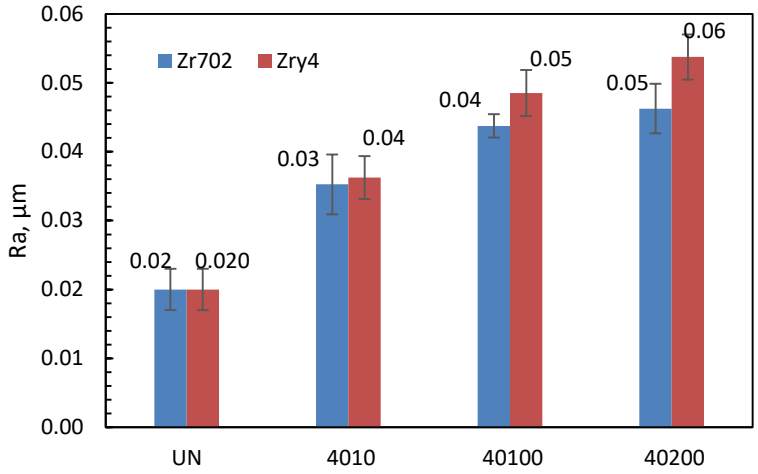


Figure 4.2-5 Surface roughness of Zr702 and Zircaloy-4 samples CC treated at 400 °C

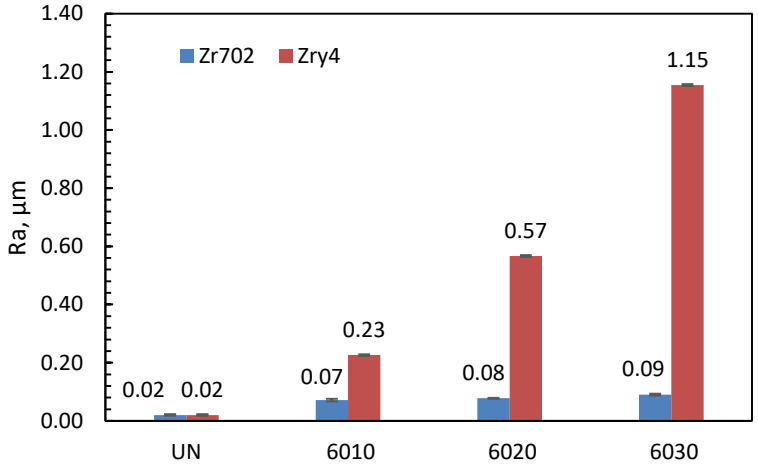


Figure 4.2-6 Surface roughness of Zr702 and Zircaloy-4 samples CC treated at 600 °C

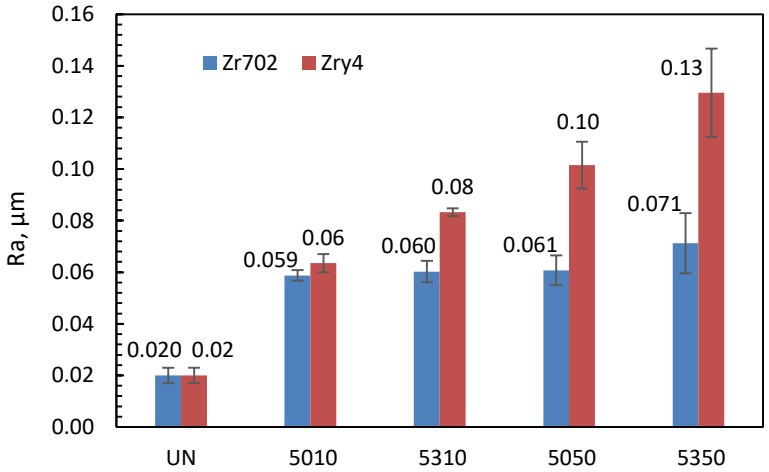


Figure 4.2-7 Surface roughness changes of samples CC treated at 500 and 530 °C

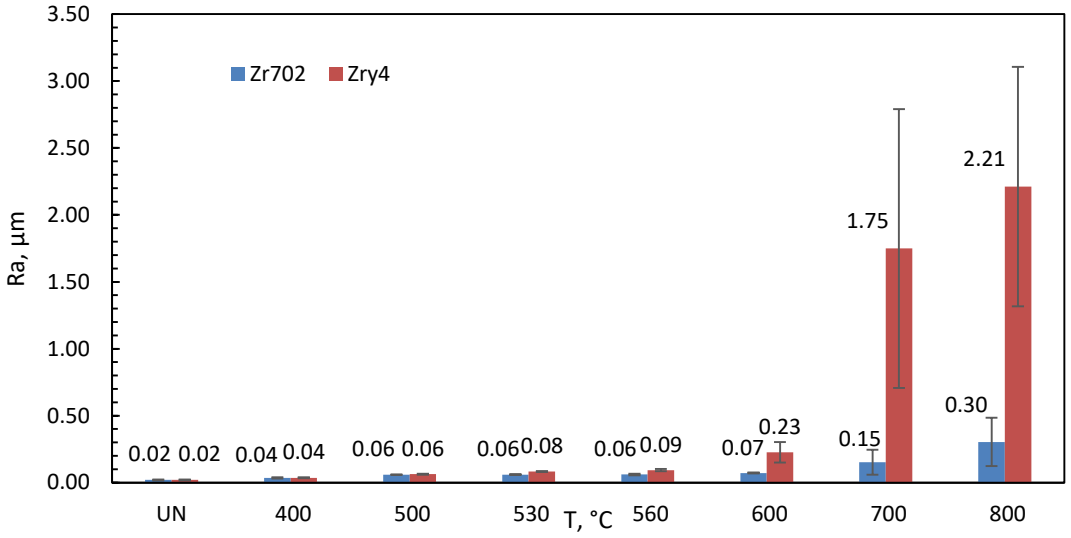


Figure 4.2-8 Surface roughness changes of samples CC treated for 10hours

4.2.3 GDOES chemical composition depth distribution in sample layers

As described in section 3.3.1.4, GDOES test was carried out to probe the composition depth distribution in CC treated samples. It should be noted that for certain treatment conditions, composition depth profiling cannot be obtained due to the poor conductivity of the sample surface and hence sputtering could not be triggered. These samples are Zr702-8010, Zry4-6020, Zry4-6030, Zry4-7010 and Zry4-8010. It is noted that the surfaces of these samples are strongly beige blistered (for Zr702 alloy) or patched (for Zircaloy-4).

For the other measured samples due to the great similarities, only selected composition depth profiles are presented in Figure 4.2-9. It can be seen that generally there is a composition plateau was generated during the CC treatment, which is followed by an increase and decrease in mass concentration for element Zr and O respectively. It should be also noted that the increased mass concentration measured on CC treated samples is caused by the atmospheric influence.

For both Zr702-5310 and Zry4-5310 (Figure 4.2-9 (a)), the composition plateau, where the oxygen maintained at a concentration of about 26 (± 2) %, is about 1.5 μm in thickness. This suggests the formation of an oxide layer of about 1.5 μm for both samples. Following the high oxygen concentration plateau the oxygen content reduced gradually with the depth until 3.0 μm where oxygen dropped to about zero for sample Zr702-5310, which implies an oxygen diffusion case beneath the oxide layer. Compared with Zr702-5310, Zry4-5310 has a narrower oxygen diffusion zone underneath the CC treated layer, which only reached a depth of about 2.7 μm.

Figure 4.2-9 (b) compares the composition depth profiles for Zr702-7010 and Zry4-6010. It can be seen that sample Zr702-7010 also exhibited a high oxygen plateau ($C_O \approx 26$ %) with a much larger thickness (about 9.0 μm) when compared with Zr702-5310 (<1.5 μm). The oxygen diffusion zone reached a depth of about 19 μm, which is over 6 times than that of Zr702-5310. For sample Zry4-6010, it can be noticed from Figure 4.2-9 (b) that an oxygen plateau until about 6 μm was also formed followed by an oxygen diffusion zone to about 11 μm.

Combined with the ceramic layer thickness measurement (Figure 4.2-20), it can be drawn that the high oxygen concentration plateau corresponding to the ceramic layer formed on the surface. This difference in the measured plateau width is therefore due to variation on layer thickness formed at different CC treatment conditions.

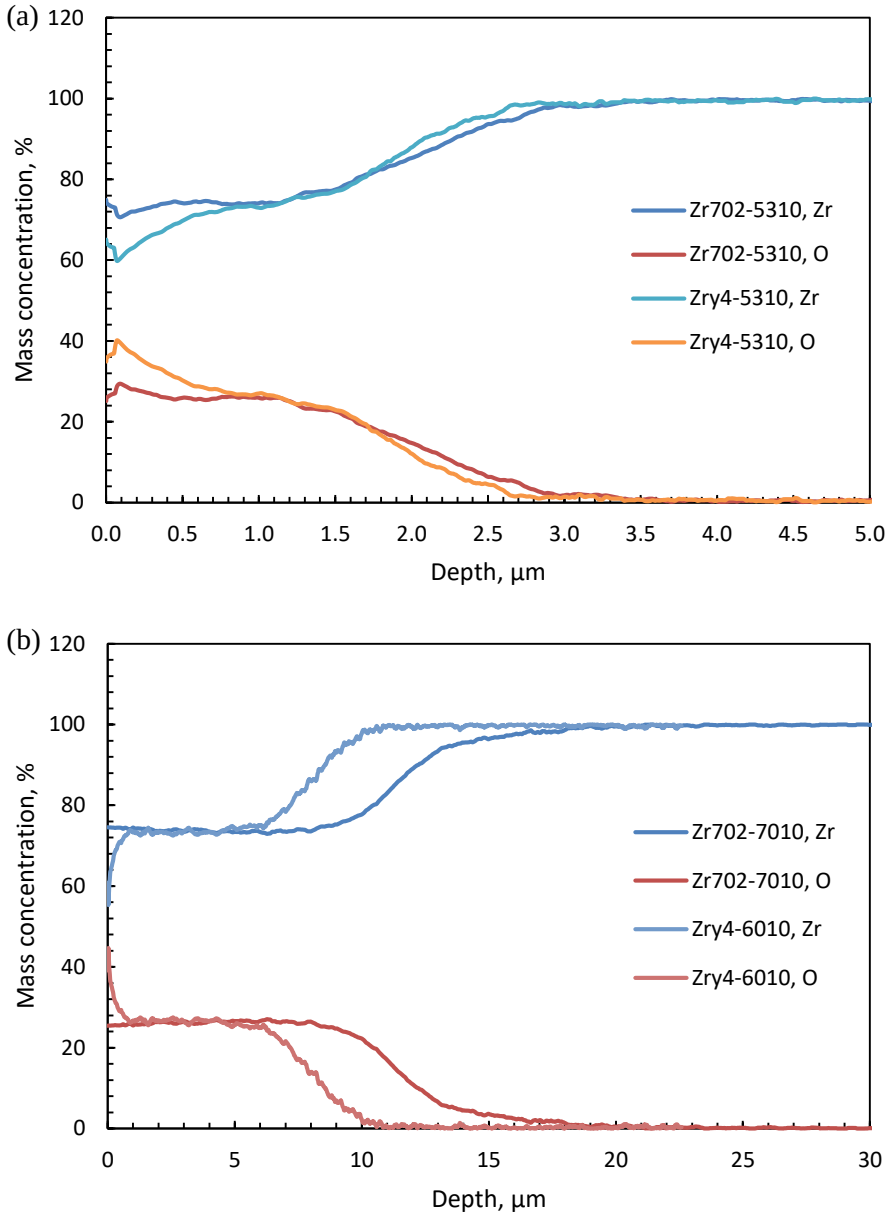


Figure 4.2-9 GDOES composition depth profiles of CC treated sample (a) Zr702-5310 and Zry4-5310, (b) Zr702-7010 and Zry4-6010

4.2.4 XRD analysis of the sample layer

X-ray diffraction (XRD) characterisation was carried out to identify the phases formed on sample surfaces after CC treatment and the results are reported in this section.

4.2.4.1 Zr702

Figure 4.2-10 shows the XRD patterns of Zr702 treated for 10 hours at different temperatures. It can be seen that during these ceramic conversion treatments, the sample surfaces were converted from α-Zr to zirconia layer which is made up of mainly monoclinic ZrO_2 (m-ZrO_2) phase and traces of tetragonal ZrO_2 (t-ZrO_2). The Powder Diffraction File (PDF) numbers for α-Zr and m-ZrO_2 and t-ZrO_2 are 03-065-3366, 03-065-1025 and 01-079-1769 respectively.

It can also be seen from Figure 4.2-10 that with the increasing of treatment temperature new peaks were gradually generated at the left side of plane (002) and (101) from α-Zr (2θ position 34.8 ° and 36.5 °); where newly generated peaks are indexed as plane (002) and $(\bar{1}02)$ from m-ZrO_2. Meanwhile, with the increasing of treatment temperature there is an increase on the number of new detected peaks from m-ZrO_2. At the same time, all the other peaks from α-Zr became weaker and weaker until they finally disappeared on Zr702-7010 and Zr702-8010.

It should be also noted that tetragonal zirconia phase exists even though the corresponding peaks are not very strong in Figure 4.2-10 as it can be more easily seen when the vertical axis is in lg(relative intensity) scale at 2θ position 30.2 ° which is the strongest peak for t-ZrO_2 (distinguished from m-ZrO_2) as shown in Figure 4.2-11.

The diffraction pattern of sample Zr702-4010, as demonstrated in Figure 4.2-11 (a), besides the formed zirconia phase (both m-ZrO_2 and t-ZrO_2), the diffraction peaks from the hexagonal Zr substrate were still detected. Further analysis showed that the peak at 2θ position 33.07 ° came from (020) plane of orthorhombic HfO_2 (o-HfO_2) with its PDF reference code 01-089-6225. This comes from the oxidation of hafnium (Hf) in the as-

received material (see Figure 4.1-3). It is also noticed that a zirconium suboxide $ZrO_{0.27}$ (h-$ZrO_{0.27}$) at 2θ position 43.3 ° is recognised, which has a hexagonal structure. The PDF code for this suboxide is 01-089-2340. It should be noted that the 3 strongest peak positions for h-$ZrO_{0.27}$ are 36.2 °, 34.6 ° and 31.7 ° (as indicated by arrows in Figure 4.2-11 (a)), all of which are the left shoulder positions for α-Zr while 43.3 ° is not included among them. Hence, further TEM analysis (in section 4.2.5.2) was carried out to confirm the existence of h-$ZrO_{0.27}$. Based on the identified diffraction peaks, samples that could possibly detected h-$ZrO_{0.27}$ are Zr702-4010, Zr702-5010 and Zr702-5310.

Figure 4.2-11 (b) depicts the diffraction pattern from sample Zr702-5610 which was treated at a higher temperature of 560 °C. It shows that the diffraction peaks from the hexagonal zirconium suboxide $ZrO_{0.27}$ and orthorhombic HfO_2 became unnoticeable. On the other hand, the peak intensities and the numbers of zirconium oxide (both m-ZrO_2 and t-ZrO_2) increased, while those from the substrate hexagonal zirconium decreased, which indicates a more oxidised Zr702 surface.

When the temperature went up to 700 °C and 800 °C, the XRD diffraction patterns of treated samples (i.e. Zr702-7010 and Zr702-8010), are made up of zirconium oxides (m-ZrO_2 and t-ZrO_2) without detected peaks from substrate zirconium as evidence by the typical diffraction pattern from Zr702-8010 which is exemplified in Figure 4.2-11 (c).

Figure 4.2-12 shows the XRD patterns of Zr702 treated at 600 °C as a function of treatment period ranging from 10, through 20 to 30 hours. No HfO_2 peaks could be detected from these three 600 °C treated samples. It can also be found by comparison that the intensity of the peaks from oxide increased whilst that from α-Zr decreased with increasing the treatment time, which suggests an increase of the surface oxide layer

thickness. However, peaks from the substrate can still be detected from the 600 °C treated samples even for 30 hours. This implies that the oxide layer formed on the sample is relatively thin and its thickness is smaller than the X-ray's penetration depth, which applies to all Zr702 samples treated below 700 °C.

It can also be noticed that for XRD patterns from all treated samples, there are unrecognised small peaks at different 2θ positions, e.g. 25.6 °, 29.0 ° and 33.3 ° as question marked in Figure 4.2-11. This is mainly due to the complexity of the oxide film.

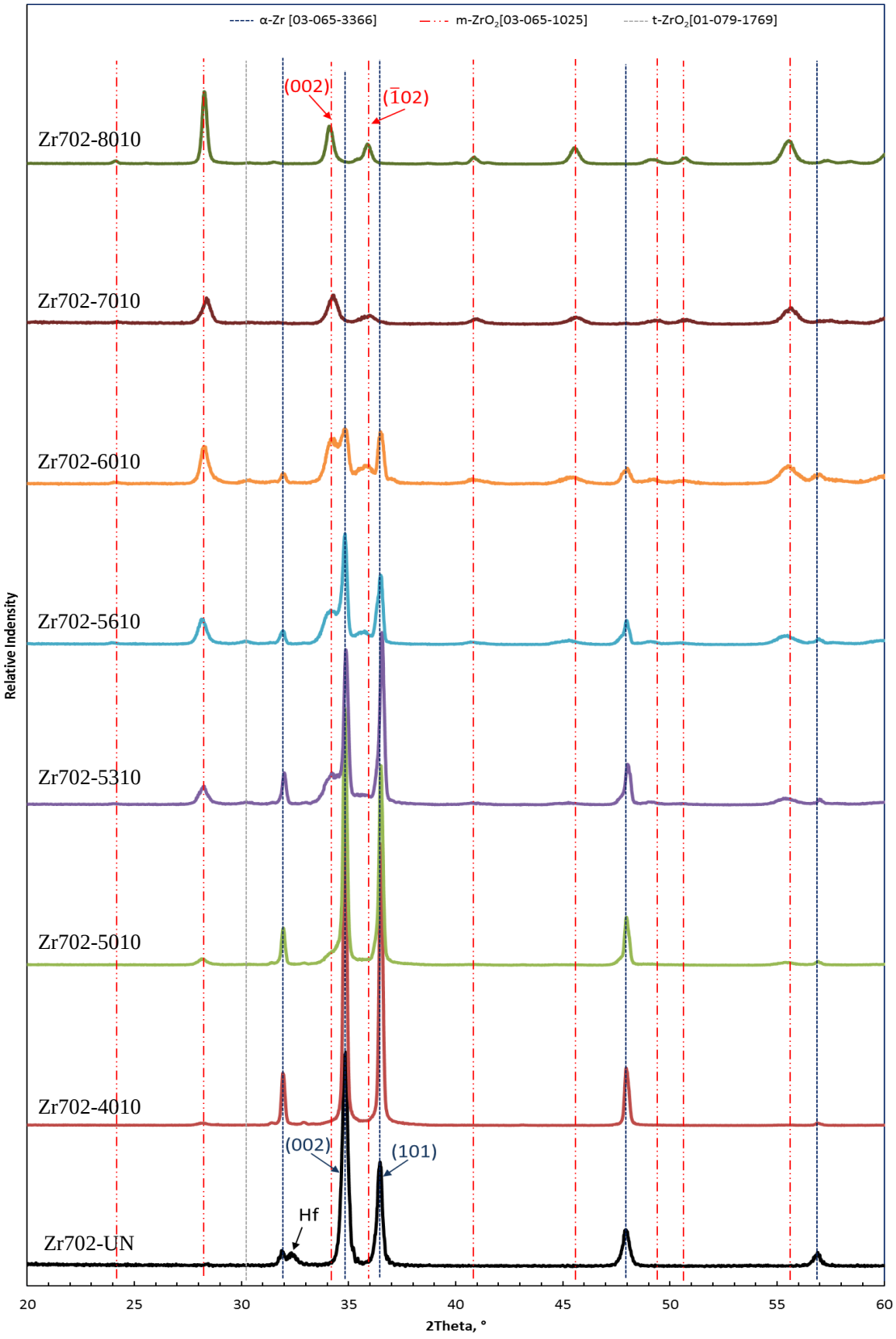


Figure 4.2-10 XRD patterns of Zr702 alloy CC treated for 10 hours at different temperature

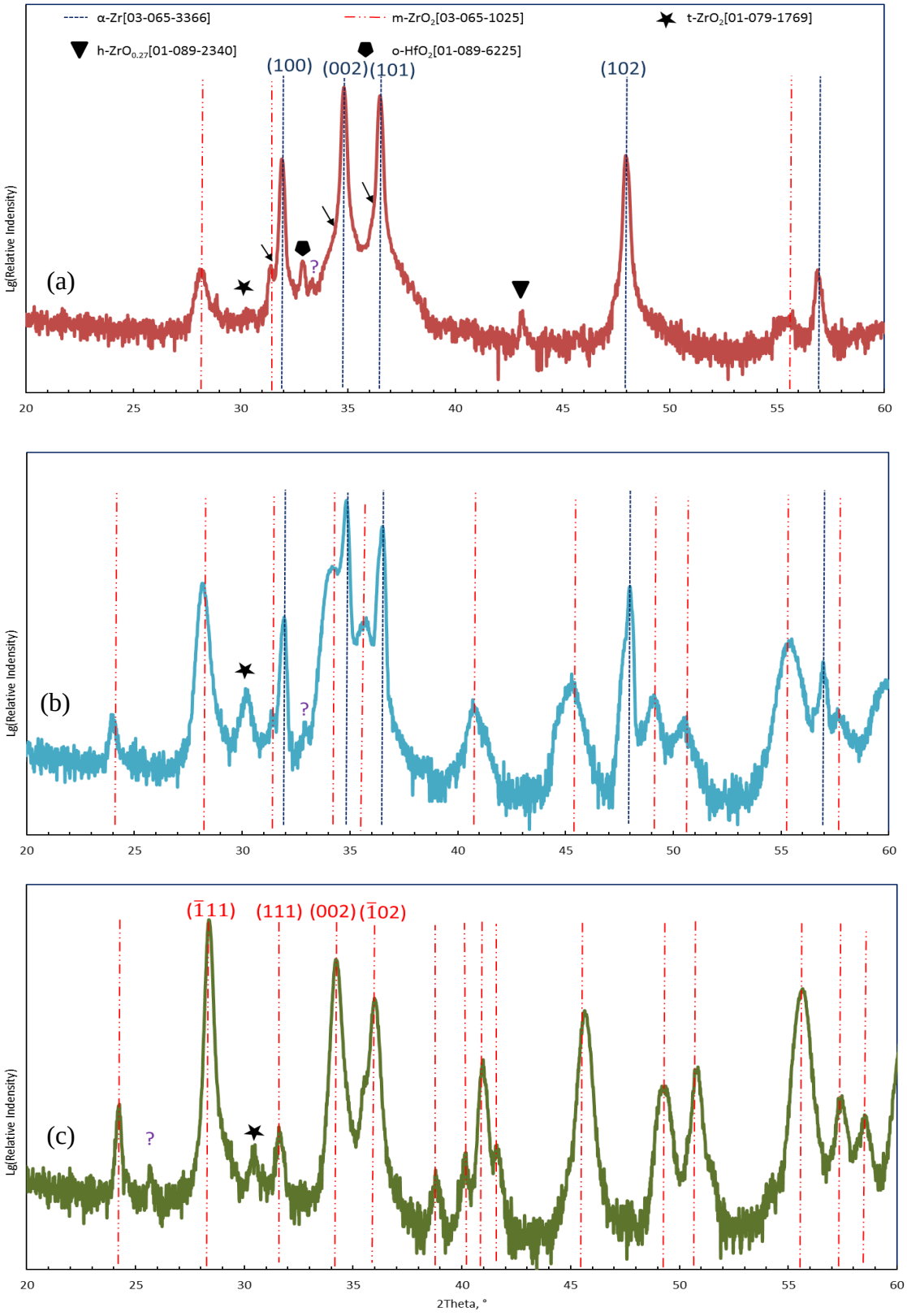


Figure 4.2-11 XRD patterns of (a)Zr702-4010, (b)Zr702-5610, (c)Zr702-8010

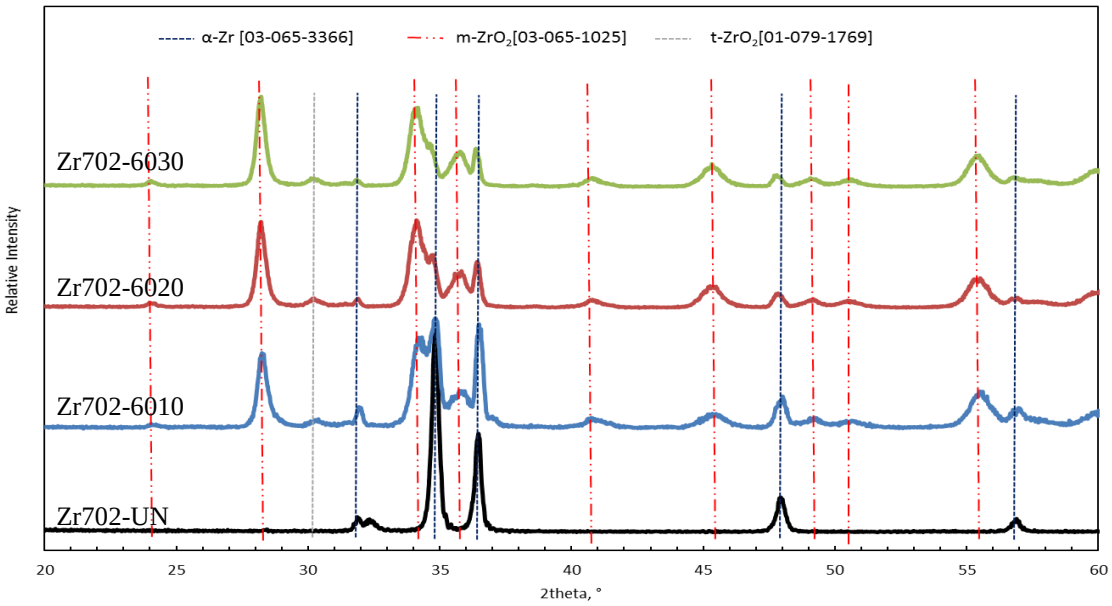


Figure 4.2-12 XRD patterns of Zr702 alloy CC treated at 600 °C for different time

4.2.4.2 Zircaloy-4

XRD patterns from Zircaloy-4 sample after CC treatment are shown in Figure 4.2-13 ~ Figure 4.2-15. As can be seen from Figure 4.2-13, similar to Zr702 samples, the surface of Zircaloy-4 gradually changed from α-Zr (PDF 03-065-3366) to a ceramic layer made up of mainly m-ZrO_2 (03-065-1025) and a minority of t-ZrO_2 (PDF 01-079-1769); in addition, peaks from plane (002) and ($\bar{1}$02) of m-ZrO_2 were gradually generated from (002) and (101) of α-Zr, together with more m-ZrO_2 and t-ZrO_2 peaks, when the CC treatment temperature increases.

Figure 4.2-14 depicts the diffraction patterns from Zry4-4010, Zry4-5010 and Zry4-7010 with a logarithmic intensity y-axis to adequately show the weak peaks. It can be seen from Figure 4.2-14 (a) that similar to Zr702-4010, a substoichiometric zirconium suboxide $ZrO_{0.27}$ could be detected on Zry4-4010 sample which could come from the metal/oxide interface due to the reasons aforementioned.

Figure 4.2-14 (b) shows the diffraction pattern of sample Zry4-5010. When the treatment temperature increased to 500 °C, more peaks were detected from the m-ZrO_2 phase, which means that more zirconium is oxidized during the CC treatment. When the treatment temperature is above 700 °C, i.e. sample Zry4-7010 and Zry4-8010, no peak from the substrate was detected as evidenced by Figure 4.2-14 (c), where the treated surface should mainly consist of m-ZrO_2 and t-ZrO_2. Similar to that of Zr702 samples, the unrecognised small peaks, though at different 2θ position, are attributed to the complexity of the oxide layer.

Figure 4.2-15 depicts the effect of treatment time at 600 °C, i.e. Zry4-6010, Zry4-6020 and Zry4-6030 with their corresponding diffraction patterns shown in (a), (b) and (c) respectively. As the treatment time increased, the diffraction peak intensity from the oxide phase increased while those from the α-Zr decreased. It can also be noticed that the unrecognised peak at 29.6 ° on Zry4-6010 remained on sample Zry4-6020 and Zry4-6030, which is also attributed to the complexity of the oxide layer.

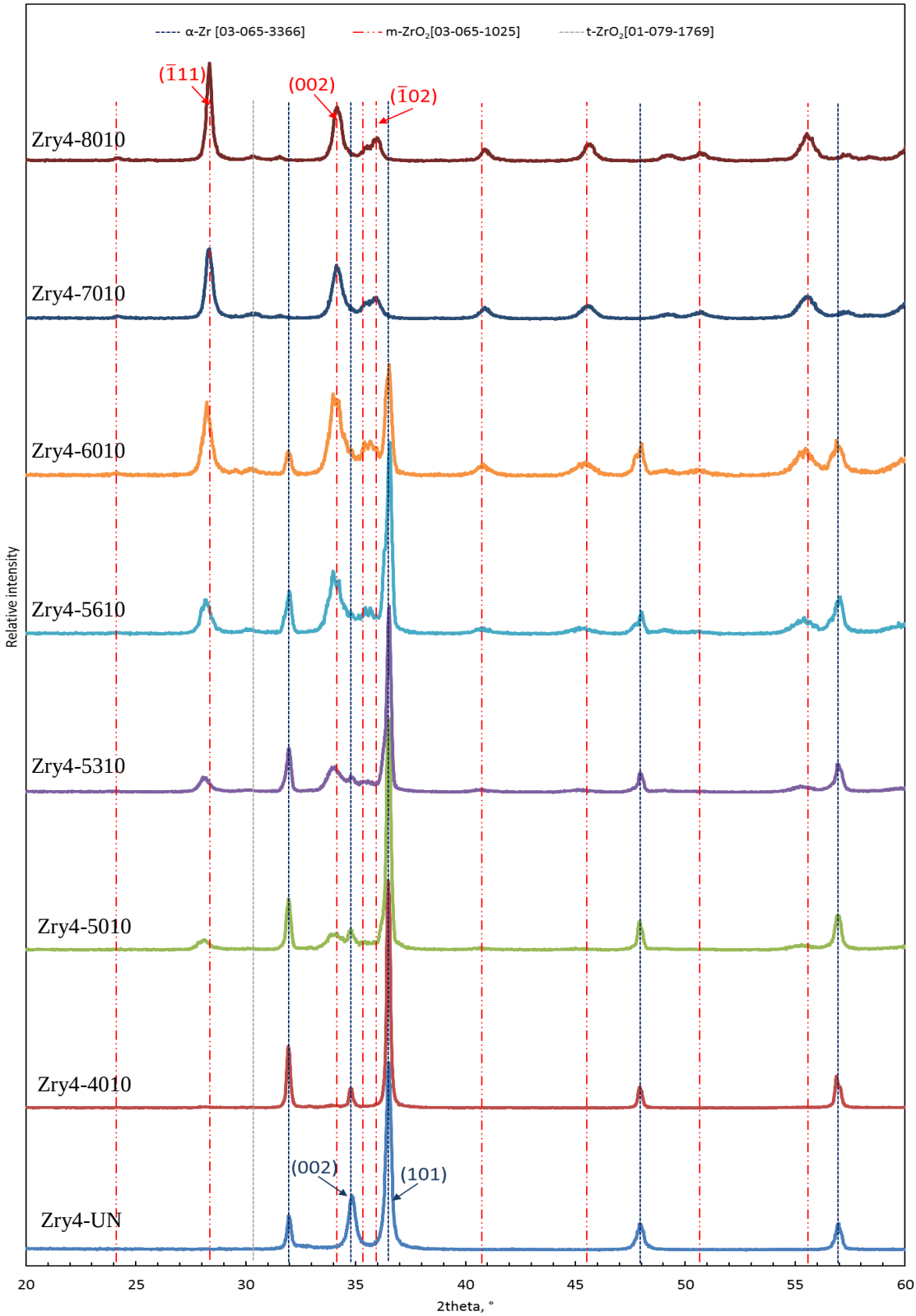


Figure 4.2-13 XRD patterns of Zircaloy-4 alloy CC treated for 10 hours at different temperature

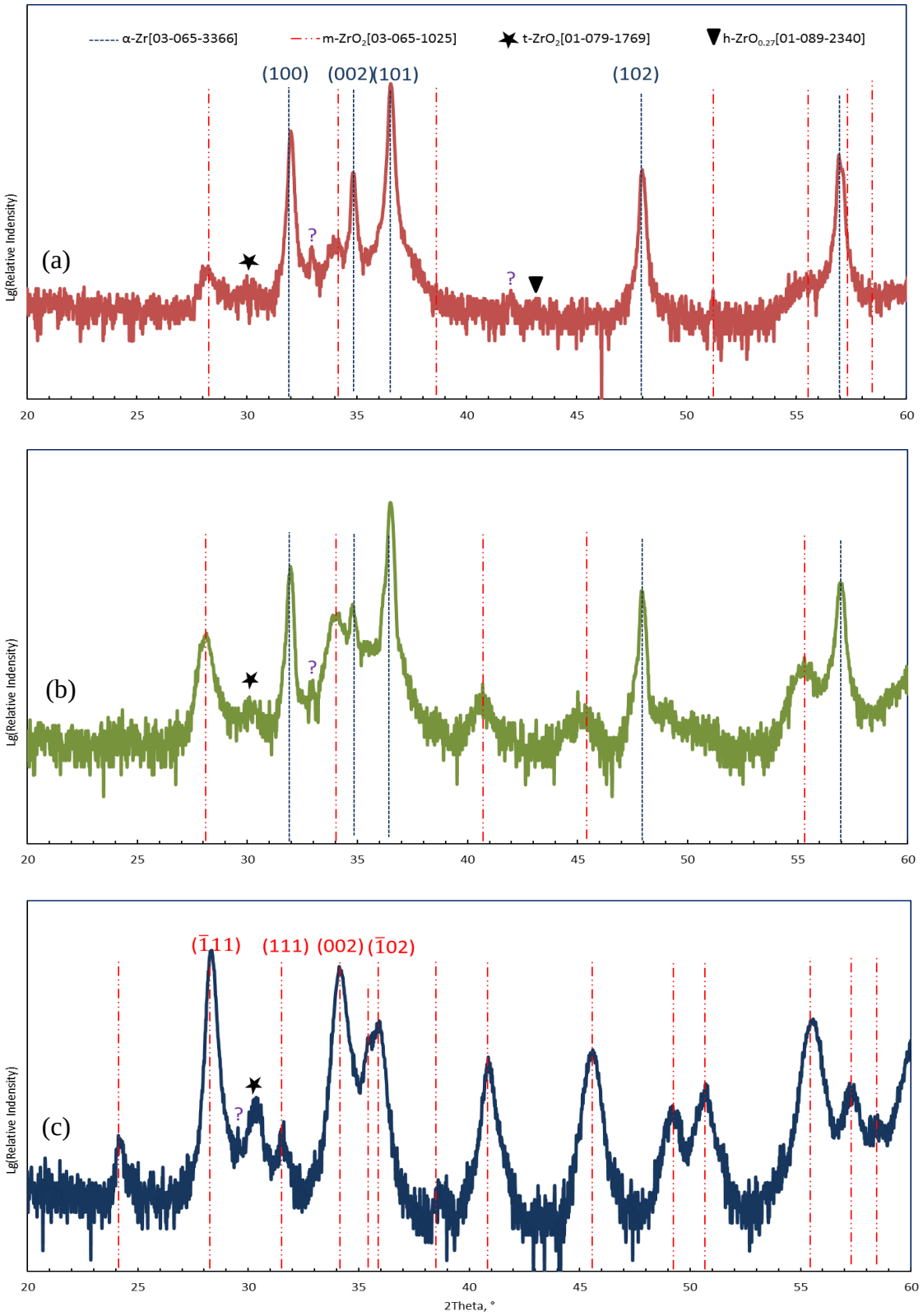


Figure 4.2-14 XRD pattern of (a)Zry4-4010, (b)Zry4-5010, (c)Zry4-7010

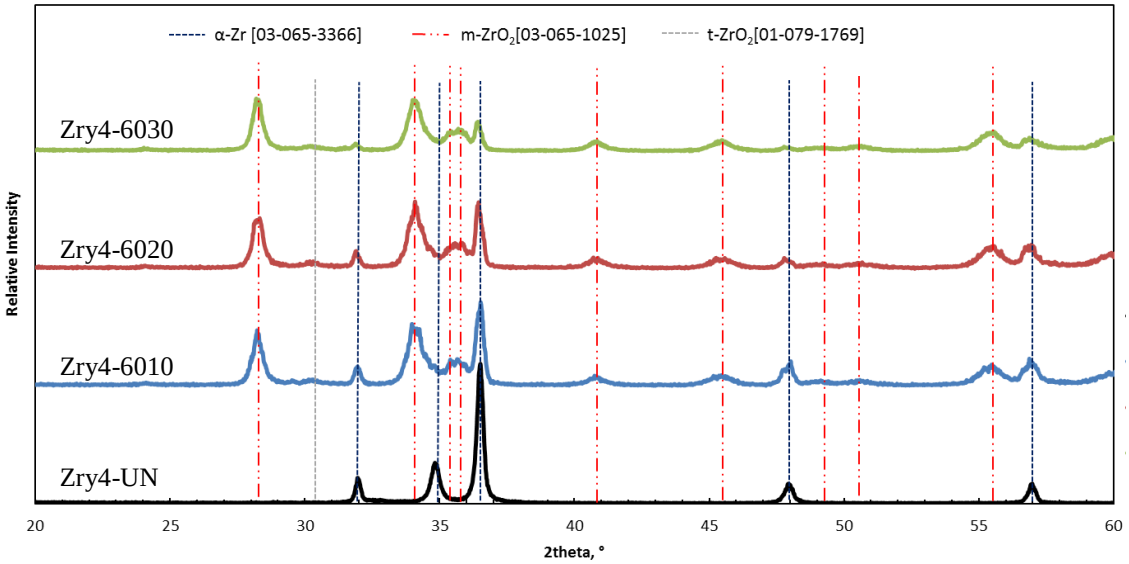


Figure 4.2-15 XRD patterns of Zircaloy-4 alloy CC treated at 600 °C for different time

4.2.4.3 Metal/oxide interface

In order to study the phase composition at the metal/oxide interface, the top oxide layer on a Zr702-7010 sample was firstly removed prior to XRD measurement. A typical XRD pattern from the interface (denote as Interface) was therefore obtained, which is then compared with that from the top ceramic layer (TOP) and from the substrate/untreated (UN) as shown in Figure 4.2-16.

From the interface pattern it can be seen that there are peaks from m-ZrO_2 in addition to the peaks from the substrate α-Zr. It is interesting to note here that some shoulder peaks to the left of the peaks from α-Zr were detected from the interface. Those peaks can be identified to $ZrO_{0.27}$; however, it could be the expanded peaks coming from the zirconium oxygen solid solution noted as Zr(O). It is known from the position of these diffraction peaks that there is generally a peak overlapping between α-Zr, m-ZrO_2 and $Zr_{0.27}O$; while Zr(O) has an overall leftward shifted peaks from the α-Zr peaks. The peak at position 43.3 ° is only indexed as $ZrO_{0.27}$ which is also the same situation as for

Zr702-4010 as shown in Figure 4.2-11 (a). However, as has been mentioned, this small peak at 43.3 ° is not one of the 3 strongest peaks from h-$ZrO_{0.27}$, hence further confirmation of it from TEM was carried out with relevant results included in section 4.2.5.2.

In addition, it can also be found that a peak from the interface patterns could be indexed as t-ZrO_2; however, similar to that identified from the samples with a thin ceramic layer (for example Zr702-4010 in Figure 4.2-11 (a)), the t-ZrO_2 peaks are not as strong as those from m-ZrO_2. It has been shown earlier in Figure 2.3-1, t-ZrO_2 phase is not stable at temperature below 1205 °C[21]. However, as concluded from previous researches[188-190], t-ZrO_2 can be stabilised by the presence of dopants (such as yttrium, cerium etc.) or internal stress. It should be noted that during the sample preparation process, relaxation would occur due to the removal of surface oxide layer and the temperature induced by the grinding, both of which would considerably change the intensity of the t-ZrO_2 peaks generated from the tested sample.

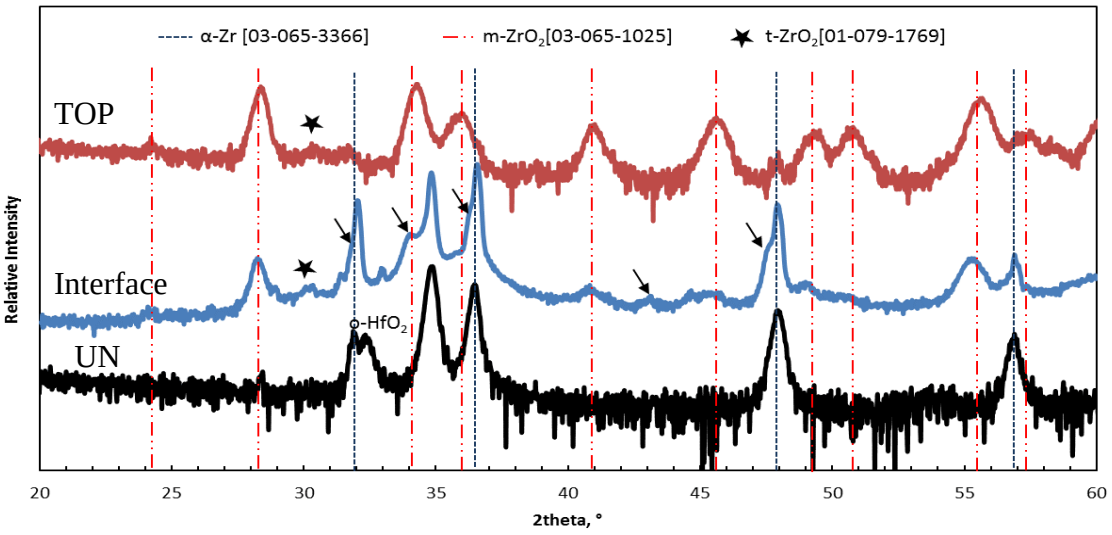


Figure 4.2-16 Depth XRD patterns of metal/oxide interface (Zr702-7010)

4.2.4.4 In situ XRD

To better understand the formation of oxides and the phase evolution, *in situ* XRD study has been conducted. Figure 4.2-17 demonstrates the *in situ* XRD patterns recorded during the treatment, with images (a) and (b) for Zr702 and Zircaloy-4 respectively.

It can be seen that initially with the increasing of chamber temperature, there is barely any change until the scan number 7, which corresponds to a treatment temperature of 600 °C. At this point new peaks at 2θ position 28.2 ° and 34.1 ° were generated which were identified to be plane $(\bar{1}11)$ and (002) of m-ZrO_2 (PDF 03-065-1025) respectively. Meanwhile, an overall leftward shifting of the original α-Zr (03-065-3366) peaks is also noticed. As aforementioned (Figure 2.3-1), the oxygen solubility in zirconium matrix is up to 29 at%. Therefore, this may be an indicator of an oxygen solid solution formed in zirconium (noted as Zr(O)). However, it may also imply the formation of a new zirconium suboxide phase $ZrO_{0.27}$. Hence due to the great overlapping between Zr(O) and $ZrO_{0.27}$, this will be further characterised under TEM (section 4.2.5.2).

With the increase of scanning number, a t-ZrO_2 (PDF 01-079-1769) peak was generated at 2θ positon 30.2 ° on both Zr702 and Zircaloy-4 alloys, which can be indexed to plane (101). However, the scanning number at which the peak was firstly observed is 9 and 8 for Zr702 and Zircaloy-4 respectively. Along with the developing of new t-ZrO_2 peaks, more peaks coming from m-ZrO_2, together with a decrease of the substrate α-Zr peaks, are also noticed as the process went on.

After a decrease of the intensity, the shifted α-Zr peaks on Zircaloy-4 became fully unnoticeable at scan number 11 (i.e. 700_4 °C, the 4th scan at 700 °C), the α-Zr peaks on Zr702 could last up to scan number 21 (i.e. 700_{14} °C, the 14th scan at 700°C). This

implies the difference on the oxidation rate between Zr702 and Zircaloy-4. Zircaloy-4 can generally be oxidized faster than Zr702; meanwhile, a high oxidation rate will reduce oxygen diffusion zone (i.e. oxygen solid solution). Another difference between both alloys is that t-ZrO_2 phase disappeared after scan number 22 (700_{15} °C) for Zr702, while t-ZrO_2 phase still can be detected under the test conditions up to scan number 46 for Zircaloy-4. This could be attributed to the stabilisation effect on t-ZrO_2 from the alloying element Sn in Zircaloy-4. It should be noted that the disappearing of the peak at 30.2 ° from t-ZrO_2 doesn't mean the nonexistence of tetragonal phase, only that the peaks intensity became weak but not impossible as evidenced Zr702-8010 (Figure 4.2-11 (c)).

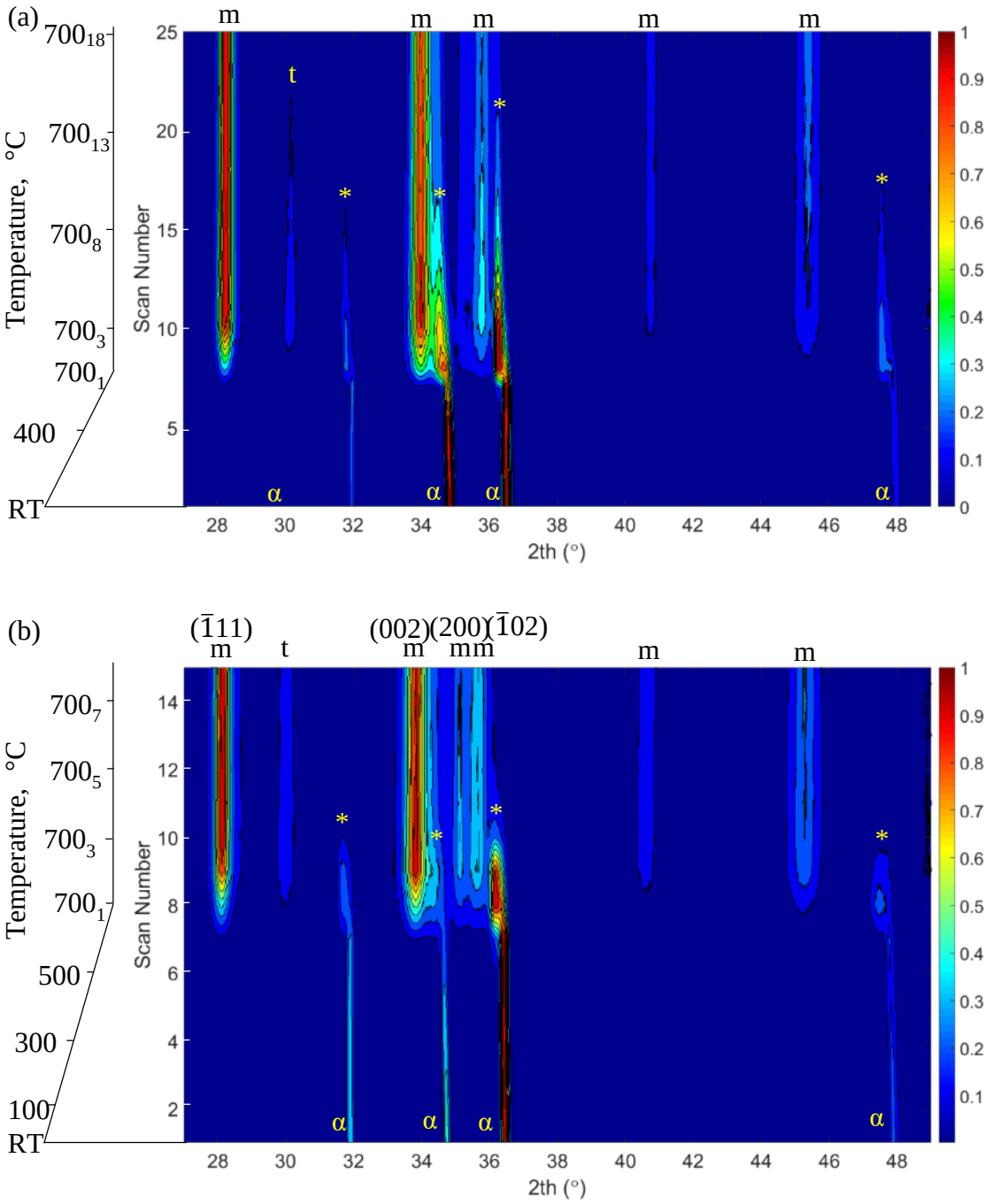


Figure 4.2-17 *In situ* phase transition of (a) Zr702 and (b) Zircaloy-4 alloy during the CC treatment at 700 °C: m and t refers to m-ZrO_2 (PDF 03-065-1025) and t-ZrO_2 (PDF 01-079-1769) respectively; * stands for shifted peak; α represents α-Zr (PDF 03-065-3366). The lowercase means the scanning number at 700 °C, e.g. 700_1 means the first XRD scan at 700 °C; each scan lasted approximately 20 minutes.

4.2.5 Layer structures

4.2.5.1 SEM observation

As reported in section 4.2.4, a ceramic oxide layer is formed on the CC treated surface. SEM was employed to observe the quality of the formed layer on the cross-section. The relevant results are shown and compared in this section.

Figure 4.2-18 demonstrates the cross section images from CC treated Zr702 for a fixed time of 10 hours at a varying treatment temperature from 400 °C to 700 °C. Image (a) in Figure 4.2-18 depicts the layer structure of sample Zr702-4010 which has a nickel plated layer on top of the CC treated surface. As can be seen from Figure 4.2-18 (a) and (b), for a fixed treatment time of 10 hours, when the sample was treated at 500 °C or below, the formed ceramic layers are dense, intact and adherent. However, as shown in Figure 4.2-20, the average layer thickness for Zr702-4010 and Zr702-5010 is only 0.16 μm and 0.67 μm respectively.

Figure 4.2-18 (c) and (d) are the cross sectional images from oxide layers formed at 530 °C and 560 °C for 10 hours. Both Zr702-5310 and Zr702-5610 depicted columnar structured oxide grains (as indicated by arrows) perpendicular to the metal/oxide interface with a few pores.

For samples treated at 600°C and 700°C, Figure 4.2-18 (e) and (f), the surface layer consisted of a well-developed columnar structure (Figure 4.2-18 (h)) with small and large lateral cracks distributed mostly within the oxide layer and at the metal/oxide interface, respectively. It can also be noticed that the large lateral cracks present along the interface with an arch shape, concave to the substrate (see marked arrows in Figure 4.2-18 (e) and (f)).

When the treatment temperature goes up to 800°C (Figure 4.2-18 (g)), severe cracks concentrated at the interface were observed, together with the devastating vertical cracks going through the whole layer. This observation is consistent with the morphology observation shown in Figure 4.2-3 (f), where cracks were observed at the surface.

Observation of layer structure of treated Zircaloy-4 samples through cross sectional SEM images revealed (Figure 4.2-19) similar oxidation dependence on treatment temperature as for Zr702. After treatment, a ceramic layer, composed of mainly m-ZrO_2 with traces of t-ZrO_2 (as indexed in the XRD patterns in Figure 4.2-13), is formed on the surface. This oxidation layer is intact and dense for treatment temperature at 400 °C and 500 °C as shown in Figure 4.2-19 (a) and (b) respectively. The thicknesses of modified layers formed on the surface are 0.25 μm and 0.97 μm for Zry4-4010 and Zry4-5010 respectively as demonstrated in Figure 4.2-20. The formed oxide layer is thicker on Zircaloy-4 than that on Zr702 at the same treatment conditions.

When the sample was treated at 530 °C and 560 °C, Figure 4.2-19 (c) and (d), the oxide layer became the thicker oxidation layer but also depicted cracks within the layer. When compared with Zr702 treated at the same conditions (Figure 4.2-18 (c) and (d)), although the layer thickness is similar (Figure 4.2-20), more cracks were observed in Zircaloy-4 than in Zr702.

With further increase of the treatment temperature, sample Zry4-6010, Zry4-7010 and Zry4-8010 as shown in Figure 4.2-19 (e), (f) and (g) respectively, exhibited dramatically increased cracks formed across the oxidation layer. It is also noticed that the lateral cracks formed on the surface seem to be periodic, especially on Zry4-7010

and Zry4-8010 (Figure 4.2-19 (f) and (h)), with a periodic length of about 2.5 μm. This is an indication of the periodic characteristics of the zirconium oxidation which is in agreement with the kinetics research about zirconium by A. Yilmazbayan and A.T. Motta et.al [132]. Vertical cracks were developed when Zircaloy-4 was CC treated at 800 °C or above (Figure 4.2-19 (g)), the formation of which is widely reported to be detrimental for the anti-corrosion performance of zirconium alloys.

Figure 4.2-20 shows the ceramic layer thickness variation as a function of the treatment temperature for both Zr702 and Zircaloy-4 alloys when treated for a fixed period of 10 hours. It can be seen that although the ceramic layer thickens increased with increasing the temperature for both alloys, rapid formation of oxide layer for Zircaloy-4 and Zr702 occurred at 600 and 700 °C respectively. It can also be noticed that the oxide layer thickness formed on Zircaloy-4 samples is generally larger than that formed on Zr702 samples: the higher the treatment temperature, the larger the difference in their thicknesses. This could be attributed to the difference in composition, microstructure and phase constituents between those two zirconium alloys.

Figure 4.2-21 depicts the cross sectional BSE images of both Zr702 and Zircaloy-4 treated at 400 °C for 10 hours, 100 hours and 200 hours. Samples were nickel plated for a protection of the thin layer. The formed ceramic layer is in dark grey colour in the BSE images, as marked in Figure 4.2-21. It can be seen that there are no noticeable cracks either lateral or vertical within the layer for both alloys and the layers maintained dense but with a waved interface. However, lateral crack along the interface started to form sample Zry4-40200 (Figure 4.2-21 (f)), which is similar to sample Zry4-5310 in Figure 4.2-19 (c) but with fewer cracks. The thickness of the formed ceramic layer

increased with the increase of the treatment period of time. As shown in Figure 4.2-24 (a), the thickness increased from 0.16 μm (Zr702-4010) to 0.39 μm (Zr702-40100) until 0.60 μm (Zr702-40200); while it is 0.25, 0.52 and 0.80 μm for Zry4-4010, Zry4-40100 and Zry4-40200 respectively.

SEM images for 600 °C treated samples (both Zr702 and Zircaloy-4) are shown in Figure 4.2-22, and it can be seen that a longer treatment time led to a thicker ceramic layer formed on the sample surface. For Zr 702, measurement of the thickness (3.0 μm, 4.9 μm and 5.8 μm for Zr702-6010, Zr702-6020 and Zr702-6030 respectively) showed a thickness growth of 3.0 μm, 1.9 μm and 0.9 μm over each 10 hours of CC treatment (see Figure 4.2-24 (c)). Hence, there is a decreasing of oxidation rate as the treatment goes on at the fixed temperature. On the other hand, it can also be noticed that more lateral cracks appeared within the oxide layers with the increase of the treatment period of time. This suggests that the formation of lateral cracks would hinder the diffusion of oxygen during the process, which could be beneficial for anti-oxidation properties. In terms of Zircaloy-4, as shown in Figure 4.2-22 (b), (d) and (f) for Zry4-6010, Zry4-6020 and Zry4-6030 respectively, it can be seen that not only there is an increasing of the thickness for the long-time treated sample, but also that both sample Zry4-6020 and Zry4-6030 revealed similar periodic cracks as observed on Zry4-8010. For Zry4-6020 and Zry4-6030 the observed arch shape at the metal/oxide interface, which accompanies the cracks formation, is towards the metal instead of the oxide when compared with the CC treated Zr702 samples (Figure 4.2-18 (e) and (f)).

Figure 4.2-23 demonstrated the cross sections for sample treated at 500 °C and 530 °C for 50 hours. In comparison with the samples treated for 10 hours at the corresponding

temperature, it can be seen that while the thickness increased (Figure 4.2-24 (b) and (d)), none of them showed the periodic cracking as observed on Zry4-6020 and Zry4-6030. However, while the lateral cracks at the metal/oxide interface obviously increased on Zr702 samples, those cracks became interconnected on Zry4-5350, as shown in Figure 4.2-23 (d).

It should be noted that the errors bars used in Figure 4.2-20 and Figure 4.2-24 are the standard deviations calculated from the four thickness measured from the BSE images. As it can be noticed, for the same treatment conditions, the formed ceramic layers on Zircaloy-4 samples are generally more uniform than those on Zr702, as evidenced by the bigger errors on Zr702 thickness.

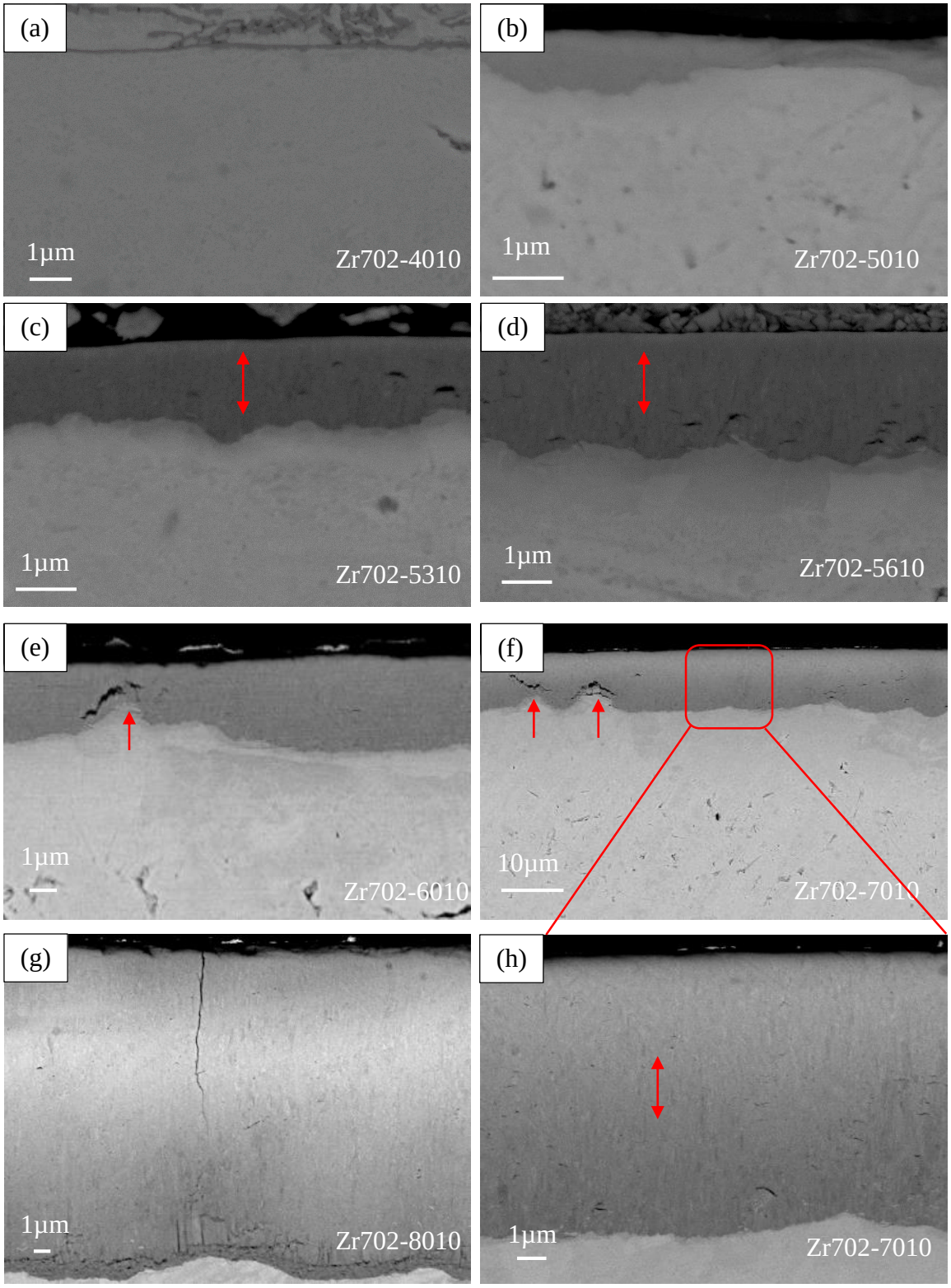


Figure 4.2-18 Cross sectional BSE images of CC treated Zr702: Zr702-4010 samples are protected with an electro-plated nickel layer on top of CC treated surface, while Zr702-5010 without nickel plating protection; Zr702-5310 and Zr702-5610 showing longitudinal columnar gains at the oxide layer

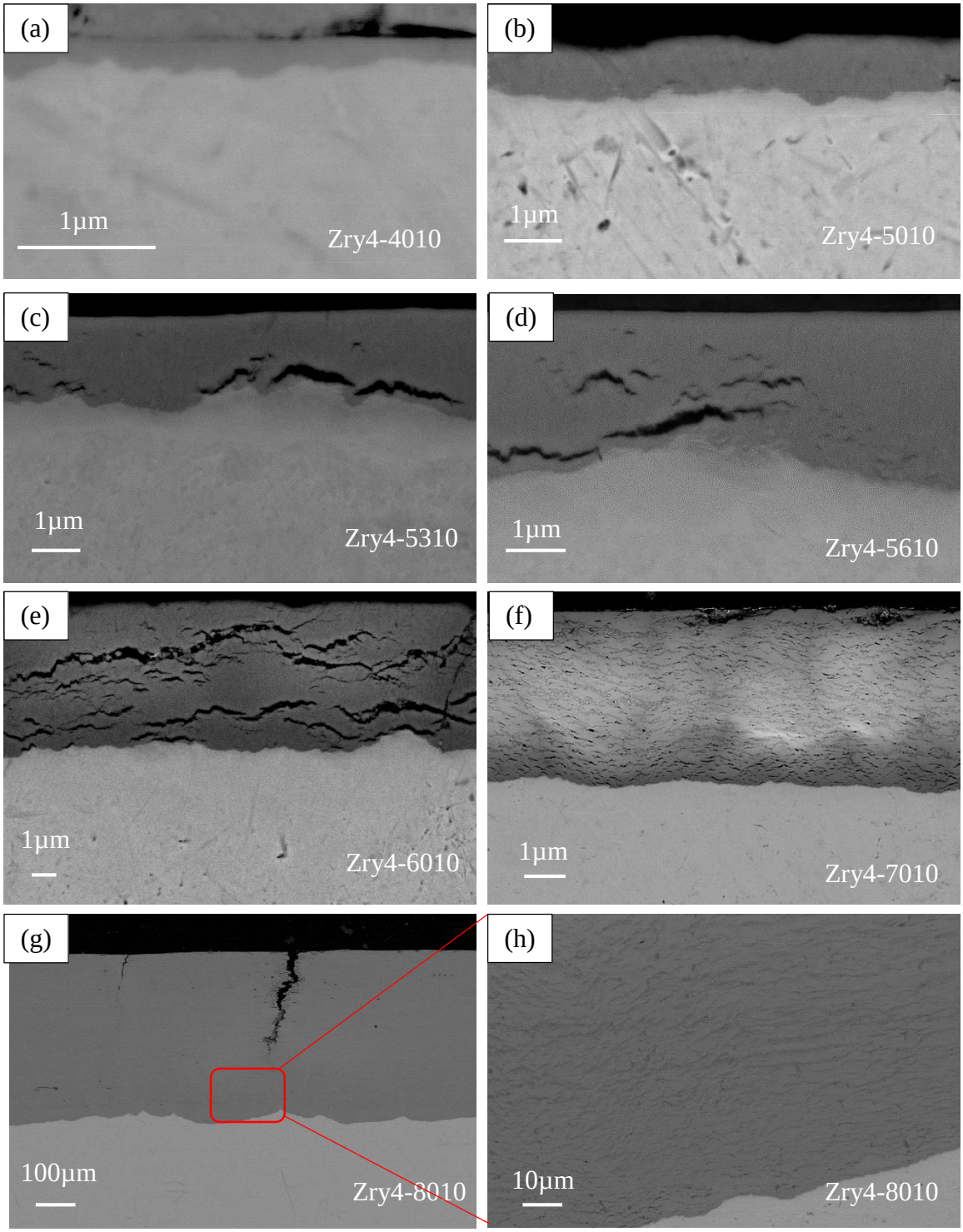


Figure 4.2-19 Cross sectional BSE images of CC treated Zircaloy-4: (a) Zry4-4010, (b) Zry4-5010; (c) Zry4-5310; (d) Zry4-5610; (e) Zry4-6010; (f) Zry4-7010; (g) Zry4-8010. Zry4-7010 and Zry4-8010 demonstrated the periodic layer on ceramic surface.

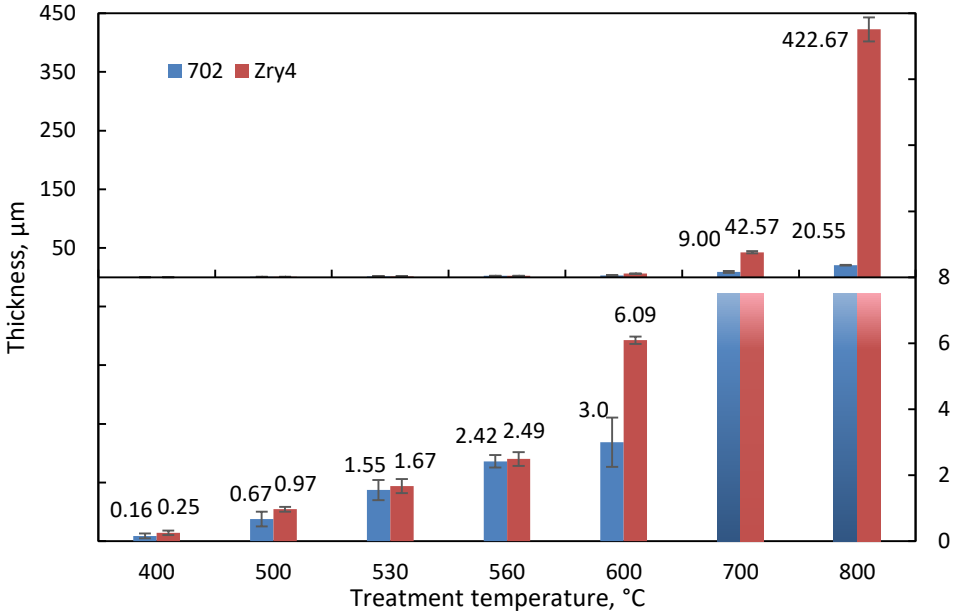


Figure 4.2-20 Ceramic layer thickness for Zr702 and Zircaloy-4 after 10 hours of CC treatment at different temperature varying from 400 to 800 °C

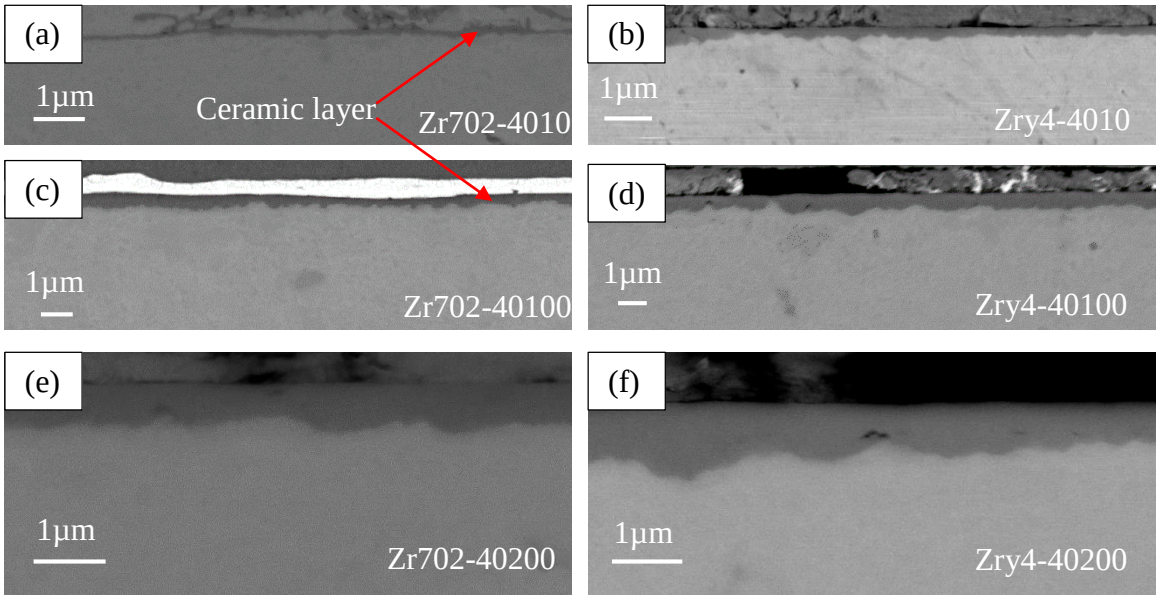


Figure 4.2-21 SEM observation of samples treated at 400 °C: (a) Zr702-4010; (b) Zry4-4010; (c) Zr702-40100; (d) Zry4-40100; (e) Zr702-40200; (f) Zry4-40200. Nickel were plated on the sample surface for a protection of the ceramic layer; ceramic layer is grey as indicated in the images

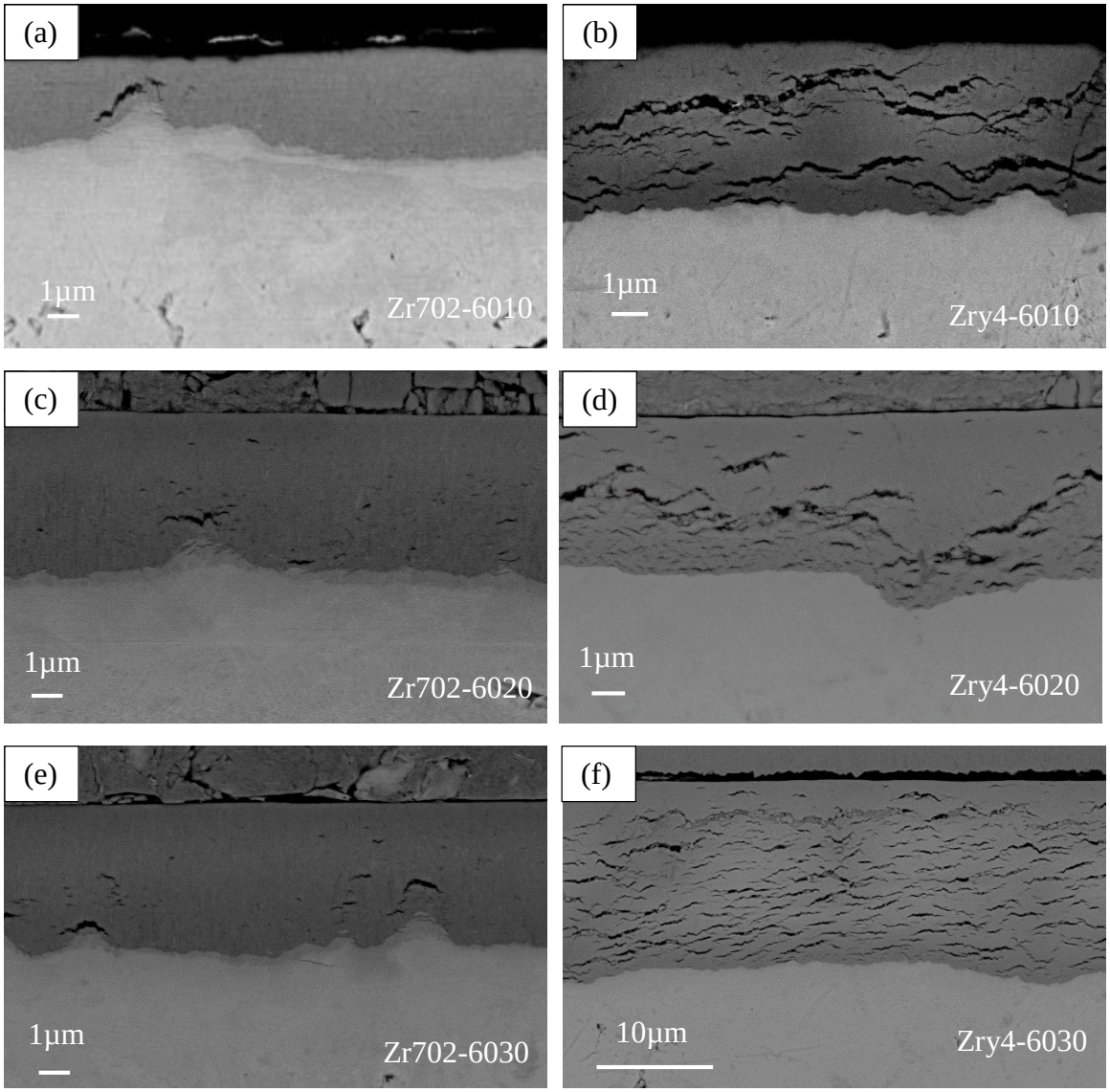


Figure 4.2-22 SEM observation of Zr702 and Zircaloy-4 treated at 600 °C: (a) Zr702-6010; (b) Zry4-6010; (c) Zr702-6020; (d) Zry4-6020; (e) Zr702-6030; (f) Zry4-6030: (c)~(f) having nickel plating layer on top of the image.

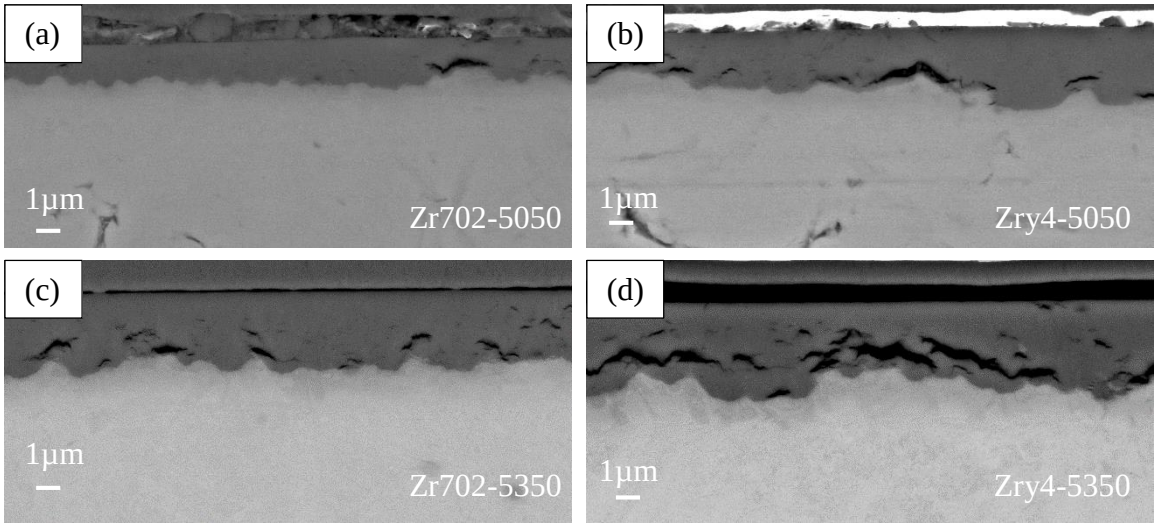


Figure 4.2-23 SEM observation of treated Zr702 and Zircaloy-4 samples: (A) Zr702-5050; (B) Zry4-5050; (C) Zr702-5350; (D) Zry4-5350; samples all having nickel plating on top of the image.

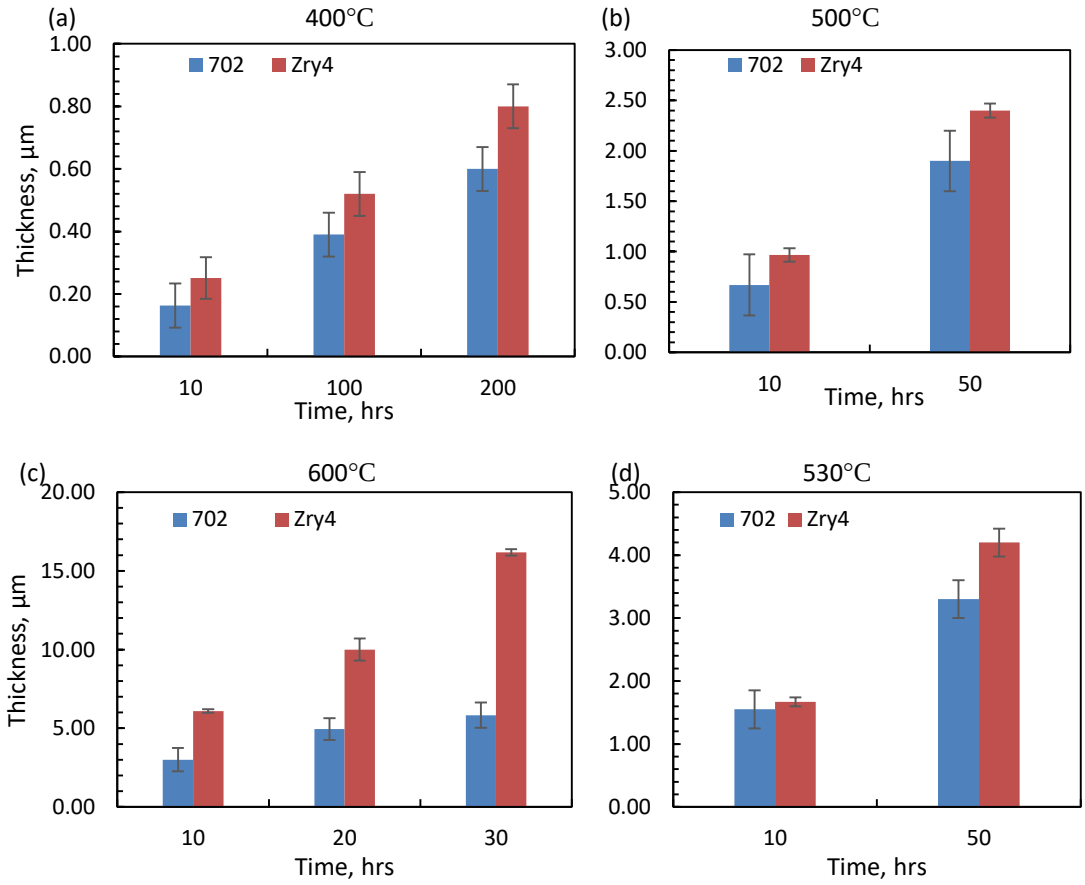


Figure 4.2-24 Ceramic layer thickness changes in corresponding to CC treatment time

4.2.5.2 TEM characterisation

Samples Zr702-5310 and Zry4-5310, representatives of CC treated Zr702 and Zircoly-4, were prepared using the method as aforementioned in section 3.3.1.6 and then characterised using a Transmission Electron Microscope (TEM). Each sample were observed in terms of layer structures, phase constitutes by Selected Area Diffraction (SAD) patterns indexing and chemical composition by Energy-dispersity X-ray Diffraction (EDX) detecting on spots.

Zr702 alloy

Figure 4.2-25 shows TEM microstructure observation images from sample Zr702-5310. It can be seen that the surface layer composes a top fine columnar grain layer, oriented in the direction perpendicular to the oxide/metal interface (Figure 4.2-25 (a)) and a prolate grain interface layer with along oxide/metal interface (Figure 4.2-25 (b)).

It is also noticed from Figure 4.2-25 and Figure 4.2-26 (a) that the columnar grain width is in the range of 80 ~ 100 nm and the grain boundaries between the columns are dense and hardly to see any defects. However, some lateral cracks, 50-150 nm in length, were observed within the oxide layer. The relatively large cracks are usually parallel to the oxide/metal interface, associated with the regions of the waved interface, where the oxide layer is thinner than the adjacent areas. This is because the lateral cracks were the obstacles for oxidation when they were created during the treatment, which hindered the growth of the oxide layer in front of the metal/oxide interface[141].

The corresponding SAD patterns taken from the oxide layer (Figure 4.2-26 (a)) revealed a ring pattern. A typical one is exemplified in Figure 4.2-26 (b) and the enlarged image and the indexing are shown in Figure 4.2-27. The indexing shows a preponderance of

the monoclinic ZrO_2 phase with traces of tetragonal phase in the oxide layer, evidenced by the bright dense rings for the formal and weak diffused rings for the later. It should also be noted that the diffraction rings contributed from tetragonal t-ZrO_2 are very weak and diffused, such that it is difficult, if not impossible, to identify the grains of this phase in the microstructure. The indexing for the oxide diffractions is in good agreement with the previous indexing of the X-ray diffraction patterns as reported in section 4.2.4.

Figure 4.2-26 (d) is a $[0001]_{Zr}$ taken from the substrate just beneath the metal/oxide interface layer, while Figure 4.2-26 (e) taken from the Zr substrate area far away from the interface shows a $[2\bar{1}\bar{1}0]_{Zr}$ SAD pattern. From the comparison of these two SAD patterns (Figure 4.2-26 (d) vs. (e)), it can be seen that the diffraction spots of the latter are elongated and diffused, indicating a high density of the defects in the area beneath the oxide layer. This is contributed from the residue stress between the oxide layer and the substrate and the diffused-in oxygen in the interstitial space of the HCP Zr crystal.

Indexing the SAD patterns from the grains at the interface layer (Figure 4.2-26 (c)) shows that a zirconium substoichiometric phase i.e. $ZrO_{0.27}$ was identified. This confirms the existence of suboxide layer ($ZrO_{0.27}$) which is mentioned earlier in the XRD results section 4.2.4. In addition, a preferred orientation of a metal/oxide front $ZrO_{0.27}$ grain to the substrate was observed: $[2\bar{1}\bar{1}0]_{ZrO_{0.27}} //[0001]_{Zr}$, $(0002)//(\bar{1}010)$.

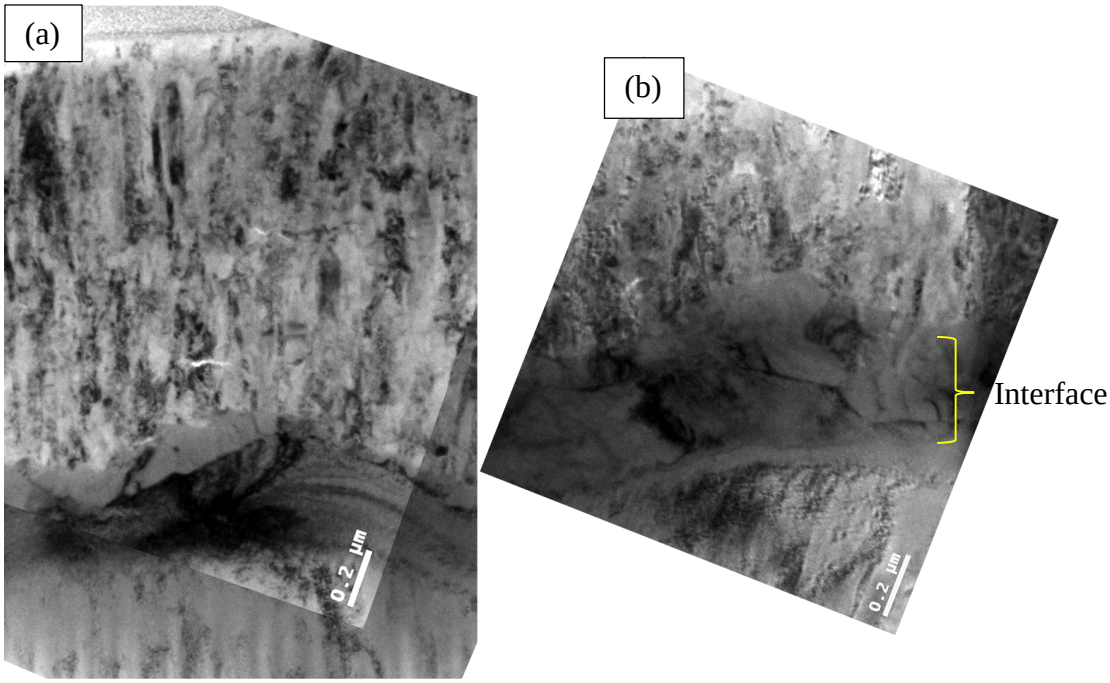


Figure 4.2-25 TEM microstructure of sample Zr702-5310 (a) whole surface layer (b) metal/oxide interface

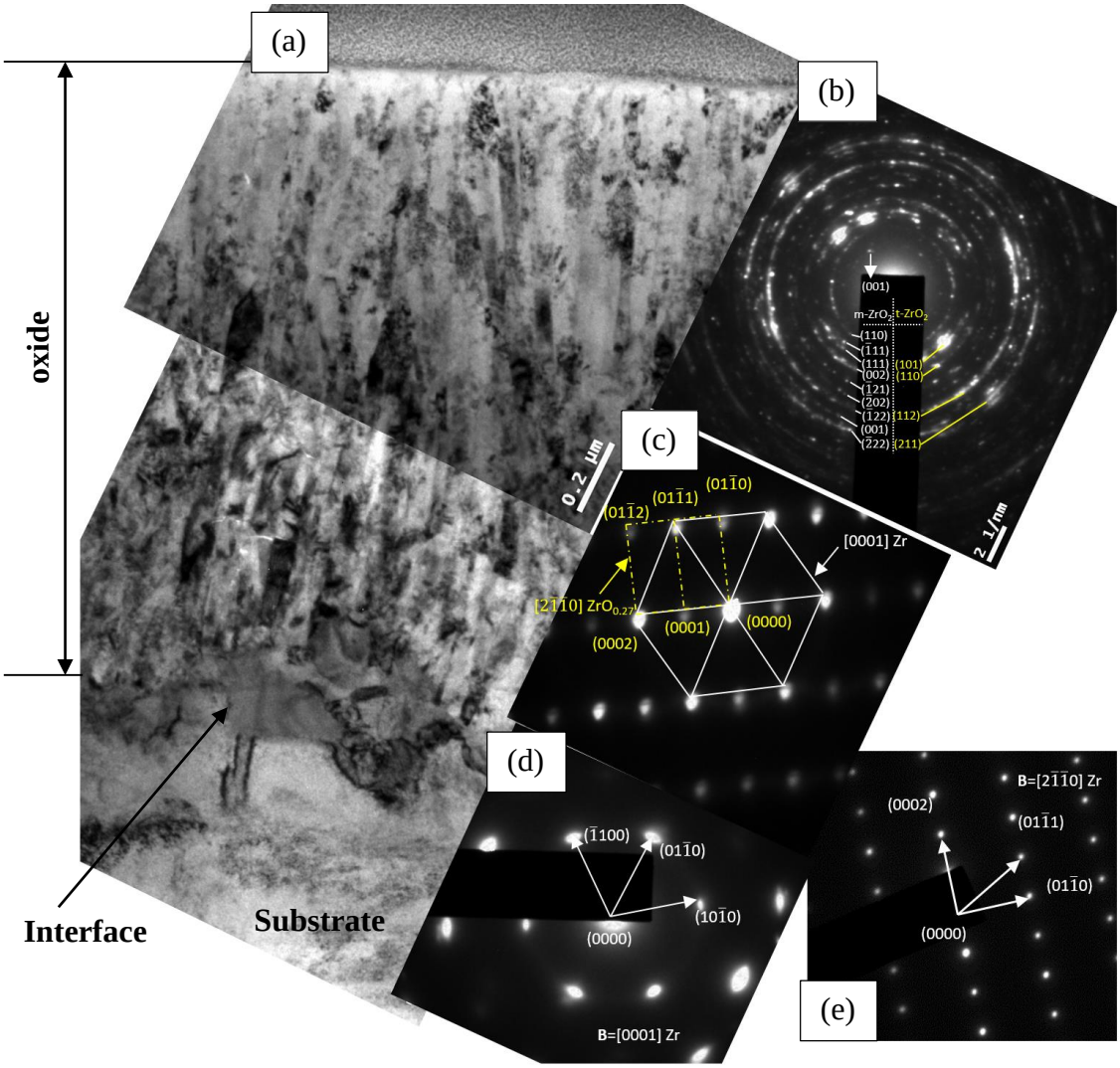


Figure 4.2-26 TEM images from Zr702-5310: (a) microstructure of surface layer; and the corresponding SAD patterns (b) surface oxide layer; (c) metal/oxide interface; (d) substrate just beneath interface; (e) substrate far away from the interface.

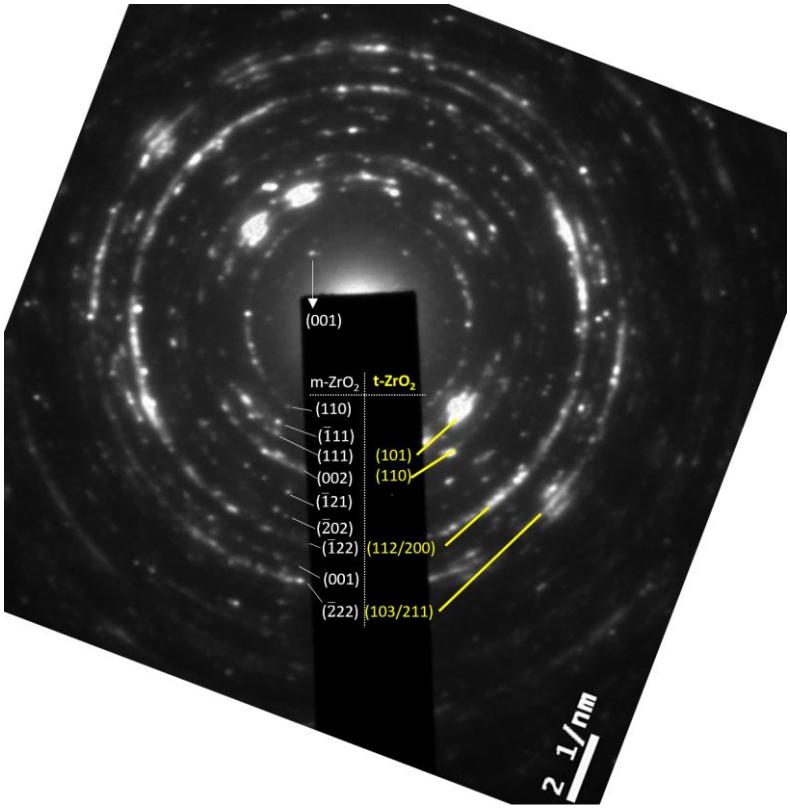


Figure 4.2-27 An enlarged image of Figure 4.2-26 (b) showing the SAD pattern and it's indexing for the oxides formed in the oxide layer of sample Zr702-5310

Zircaloy-4 alloy

Figure 4.2-28 (a) shows the microstructure of the oxide layer formed on CC treated sample Zry4-5310. It can be seen that the surface layer structure of the sample is similar to that of Zr702-5310: a top oxide layer consisting of columnar grains and a prolate grain at the metal/interface layer. However, the microstructure is different from that of the Zr702-5310 sample. The columnar grains are fine and the interface layer is only about 50 nm in thickness, which is much thinner than the interface layer of sample Zr702-5310. There are some small lateral cracks distributed across the top half of oxide layer and at the same time some large ones are observed along the oxide/interface-layer

interface. This feature is consistent with the microstructure observations from SEM (Figure 4.2-19 (c)).

Indexing the SAD patterns from the oxide layer reveals a similar preponderance of the monoclinic ZrO_2 phase, evidenced by those unindexed rings (as the index will be the same as in Figure 4.2-27, shown in Figure 4.2-28 (b). However, it can also be found that the intensity of the diffraction rings corresponding to the tetragonal t-ZrO_2 phase, as indexed in Figure 4.2-28 (b), are stronger than the Zr702-5310 sample. This implies that more t-ZrO_2 is formed during the CC treatment process on Zircaloy-4 alloy than on Zr702 alloy. This could be responsible for the cracks observed in the SEM and TEM images within the oxide layer since the cracks are related to the formation of t-ZrO_2 phase, which will be discussed in section 5.1.4.

From the SAD patterns at the metal/oxide interface shown in Figure 4.2-28 (c), it can be seen that the spots of $[0001]_{Zr}$ pattern are distorted with diffusion cloud around. It can also be noticed that the observed diffraction spots indexed to be $ZrO_{0.27}$ phase become much weaker when compared with the Zr702-5310 sample.

Further microstructure observation of the substrate from sample Zry4-5310 is shown in Figure 4.2-29 (a) and the corresponding SAD pattern is given in Figure 4.2-29 (b). As has been shown earlier in Figure 4.1-2, the average grain size of the as-received material is about 8 μm. TEM microstructure in Figure 4.2-29 (a) has revealed a lath structured domain within one grain. Analysis of the SAD pattern from this area revealed two sets of twining structures of the HCP Zr (Figure 4.2-29 (b)).

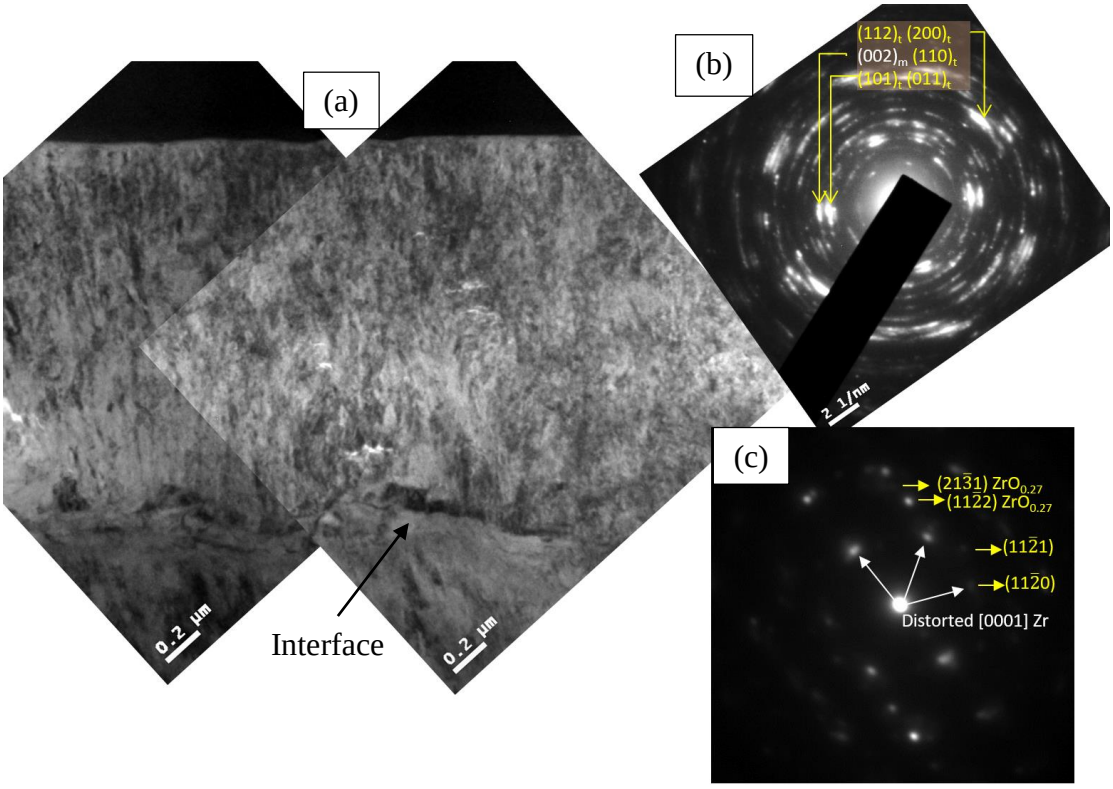


Figure 4.2-28 TEM images from Zry4-5310 (a) microstructure of oxide layer; and the corresponding SAD patterns at (b) oxide layer (c) metal/oxide interface

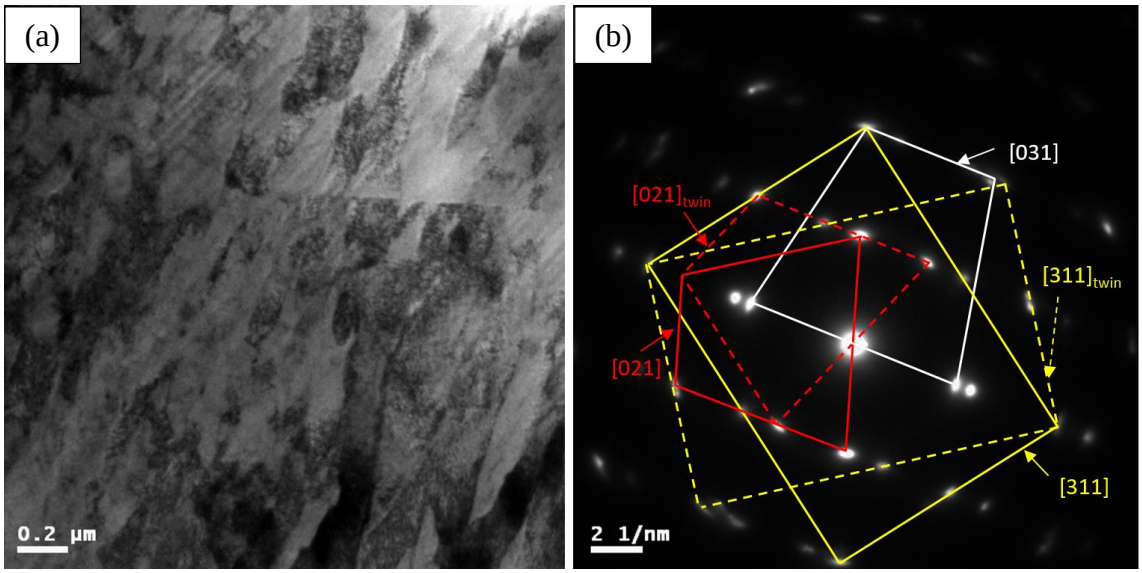


Figure 4.2-29 TEM images from Zry4-5310: (a) substrate structure (b) the corresponding SAD pattern; revealing the lath structure and the twining defects in the substrate

4.3 Microstructure of duplex treated (CC+OBD) samples

As mentioned in Section 3.2.2, Zr702 samples which were initially treated at 700 °C for 10 hours (noted hereunder as CC7) were oxygen boosted diffusion (OBD) treated in a vacuum furnace for developing a thick diffusion case underneath the oxide layer. Detailed microstructure characterisation work was conducted on the duplex treated sample and the results are reported in this section.

4.3.1 Surface morphology

Figure 4.3-1 reveals the visual observation results for duplex surface treated samples. It can be seen that after OBD treatment samples are generally in black colour, with the only exception of sample CC7-8030 which exhibited a dark greyish colour. In conjunction with the results reported in section 4.2.1, it is noticed that there is no obvious colour change during the OBD treatment when compared with the CC treated sample i.e. CC7/Zr702-7010.

It can also be noticed that the beige blisters on the CC7 sample surface gradually faded away with the increasing of OBD treatment temperature and time, especially for CC7-8030 sample, on which no clear blister was observed. However, further observation under SEM as shown in Figure 4.3-2 depicts a lumpy surface together with cracks over the sample surface.

4.3.2 Surface roughness

The surface roughness of duplex surface treated samples was measured and the obtained results are shown in Figure 4.3-3. As can be seen, the surface roughness is reduced from 0.15 μm for the CC only treated CC7/Zr702-7010 to 0.09 and 0.06 μm by OBD at 600°C for 10 hours (CC7-6010) and 30 hours (CC-6030) respectively. On the other

hand, when the OBD treatment temperature increased to 700 and 800°C for 30 hours, the surface roughness is increased respectively to 0.19 μm for CC7-7030 and 0.49 μm for CC7-8030, even though the number of surface beige surface blisters is reduced significantly or eventually disappeared. This is probably due to the formation of the cracked surface as shown in Figure 4.3-2.

It is also noticed from Figure 4.3-1 that samples with more beige blisters and/or cracked surface exhibit larger variation ranges as evidenced by the big errors of samples CC7, CC7-7030 and CC7-8030.

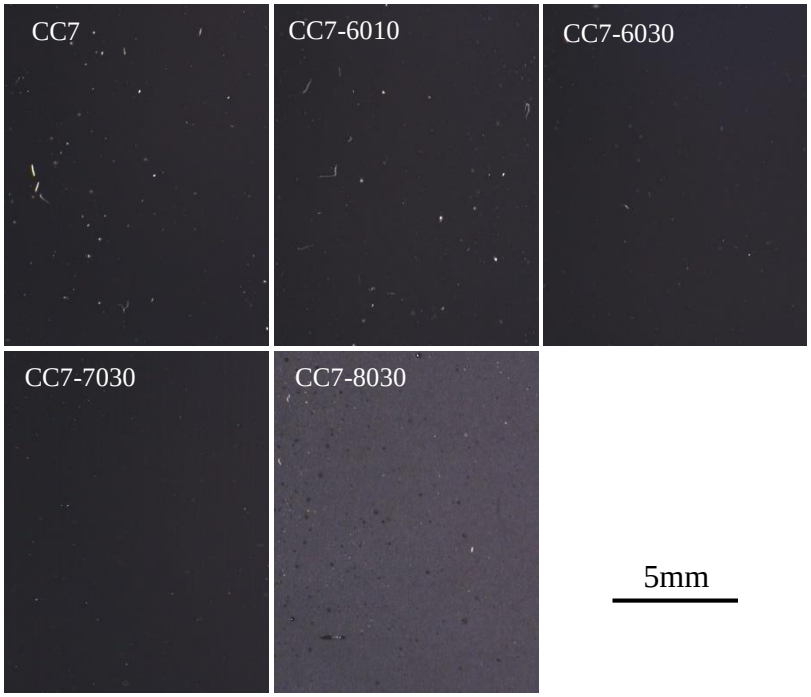


Figure 4.3-1 Visual observation images of duplex treated samples

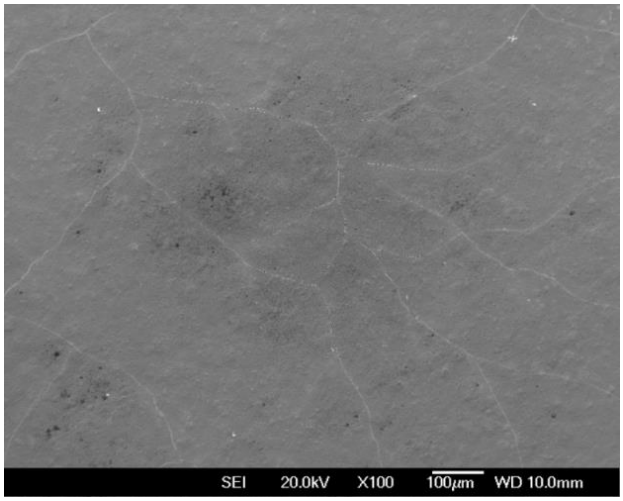


Figure 4.3-2 SEM surface morphology observation of CC7-8030 revealing cracks over surface

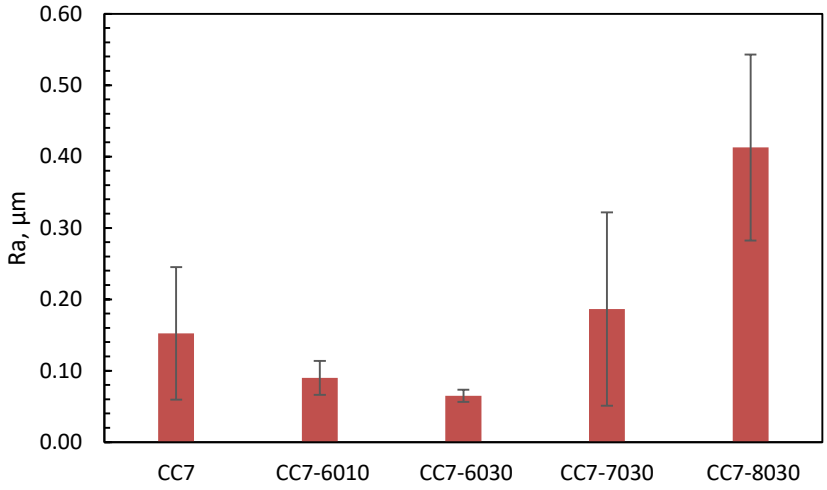


Figure 4.3-3 Surface roughness changes for duplex surface treated samples

4.3.3 GDOES depth chemical composition of the sample layer

Similar to the CC treated samples, GDOES tests were also carried out on duplex treated samples. The relevant results are shown in Figure 4.3-4.

As mentioned in section 4.2.3 (Figure 4.2-9 (b)), sample CC7 (i.e. Zr702-7010) exhibited an oxygen concentration decreasing zone (or oxygen diffusion zone) to a depth of about 20 μm after the high oxygen plateau about 9.0 μm in width. With this taken into consideration, it can be seen from Figure 4.3-4 that after duplex surface

treatment, an increase of the range of oxygen decreasing zone was noticed. For sample CC7-6030 (Figure 4.3-4 (a)), the oxygen diffusion zone ranged from 10.3 µm ($C_O \approx$ 26 %) to 21 µm (C_O =0) (i.e. 10.7 µm in width). Sample CC7-7030 (Figure 4.3-4 (b)) exhibited an oxygen diffusion zone ranging from about 7.7 µm to 30 µm (i.e. 22.3 µm in width). While for sample CC7-8030 (Figure 4.3-4 (c)), an oxygen diffusion zone started from the surface (0 µm) to up to 60 µm without appreciable oxygen plateau. This suggests the formation of wider oxygen diffusion zone during the OBD treatment.

It is also noted that within in the consideration of high oxygen concentrated detected at the close to surface area due to the influence from the atmospheric condition, the high oxygen plateau for CC7-6030 and CC7-7030 both showed in increasing tendency from the surface, which suggests a decomposition of CC formed oxide layer into the atmosphere at the same time. While CC7-8030 exhibited a full decomposition.

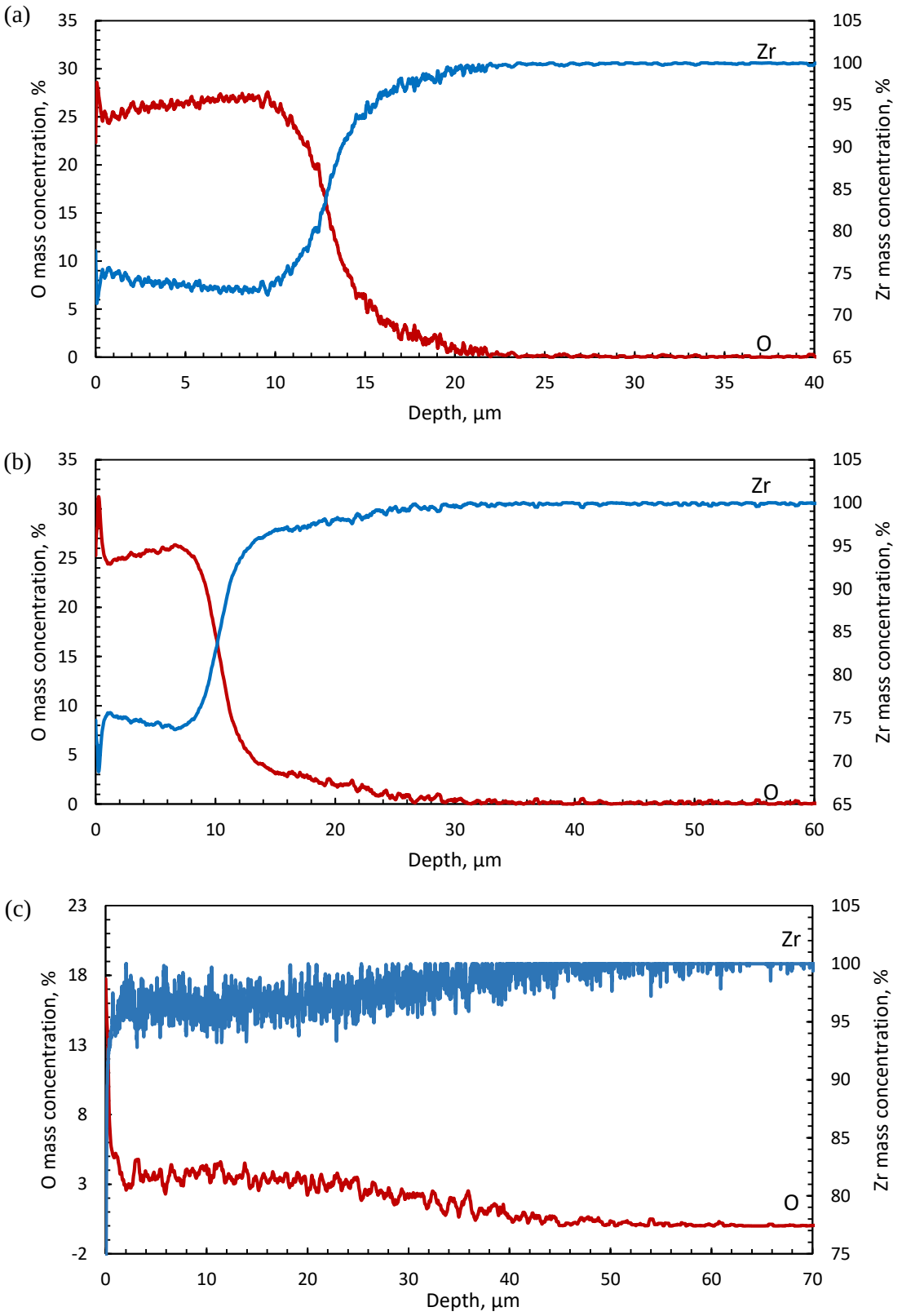


Figure 4.3-4 GDOES composition depth profiles of duplex treated sample (a) CC7-6030, (b) CC7-7030 and (c) CC7-8030

4.3.4 XRD analysis of the sample surface

XRD characterisation was also carried out on all the duplex surface treated sample for an analysis of the phase constituent of the surfaces. Due to the great similarity between samples CC7-6010 and CC7-6030, only typical XRD pattern from CC7-6030 is shown in Figure 4.3-5 (a). While the resultant XRD patterns from CC7-7030 and CC-8030 are presented in Figure 4.3-5 (b) and (c) respectively.

As it shows in Figure 4.3-5 (a), all of the zirconium oxide peaks from sample CC7-6030 shifted slightly rightwards, which means a decrease of d-spacing when compared with the standard ZrO_2, deducing from the Bragg Equation shown in Equation 3.3-1. During the OBD process, there is indeed a zirconium decomposition reaction, as listed in Equation 4.3-1 and 4.3-2.

$$ZrO_2 + Zr \rightarrow 2Zr(O) \qquad \text{Equation 4.3-1}$$

$$ZrO_2 \rightarrow ZrO_{2-x} + \frac{x}{2}O_2 \qquad \text{Equation 4.3-2}$$

The lacking of oxygen in the ZrO_2 matrix therefore caused the detection of shifted diffraction peaks on the sample surfaces. This also explained the GDOES increasing tendency across the ceramic layer as the decomposed oxygen diffused into either the zirconium matrix or the vacuum atmosphere.

When OBD process was carried out at higher temperature of 700°C for a longer time period of 30 hours (i.e. CC7-7030), substrate α-Zr (PDF 03-065-3366) would be detected as evidenced by Figure 4.3-5 (b). Interestingly, instead of standard peaks, a rightwards shifted zirconium peaks was detected, which means the d-spacing became smaller. Further confirmation needs to be carried out on TEM in section 4.3.5.2.

Figure 4.3-5 (c) depicts the phase identification of sample CC7-8030, where a main phase structure of the zirconium matrix (peaks rightward shifted) and some lower stoichiometric zirconium oxide peak can be identified. The detected zirconium oxide is a cubic structured ZrO (PDF ref. code 01-089-4768, noted c-ZrO). As can also be seen neither m-ZrO_2 nor t-ZrO_2 not detected, which indicates a complete decomposition of the ceramic surface formed during the prior CC treatment.

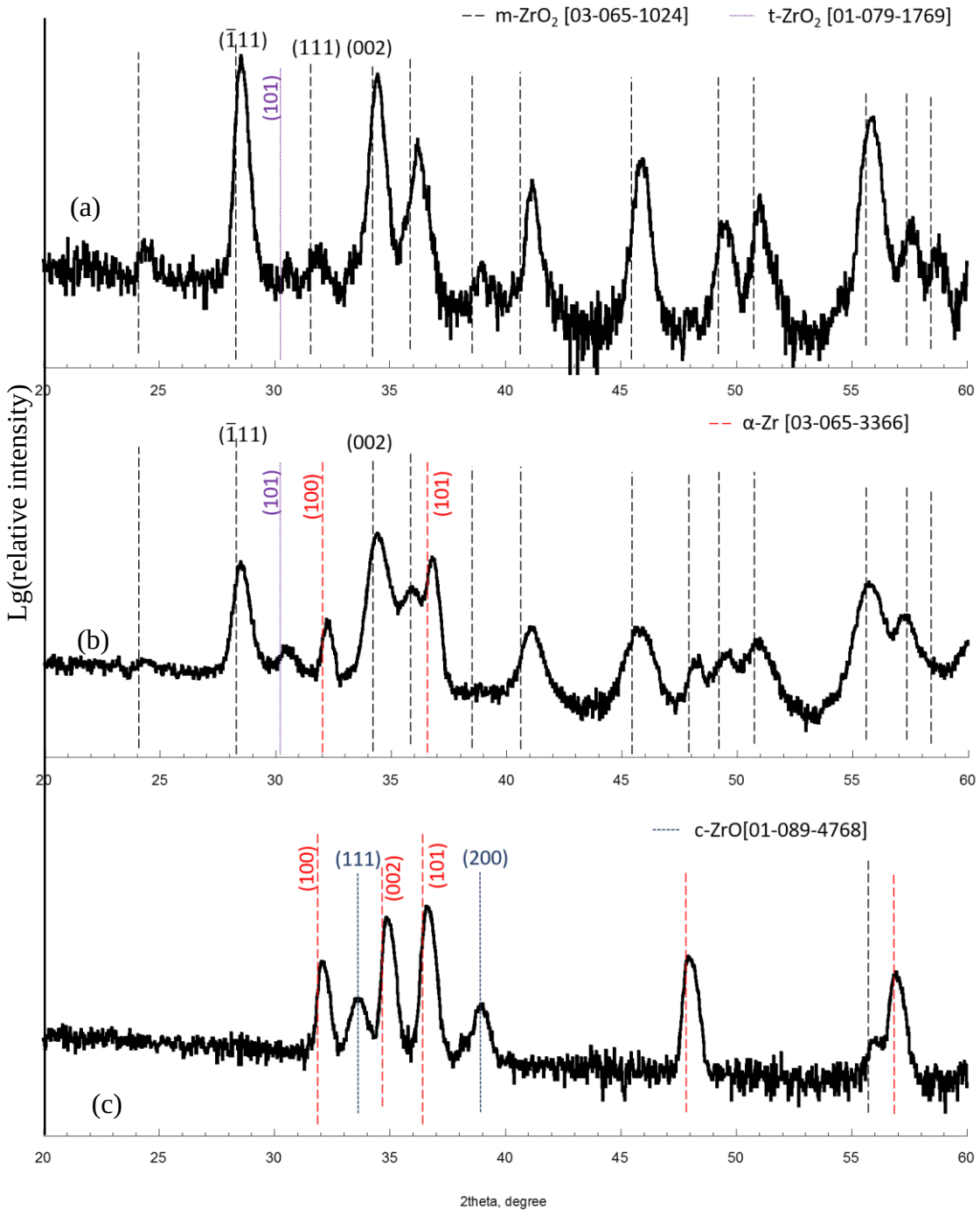


Figure 4.3-5 Typical XRD patterns of duplex treated samples (A) CC7-6010; (B) CC7-7030; (C) CC7-8030

4.3.5 Layer quality observation (SEM)

4.3.5.1 SEM observation

SEM observation was also carried out on duplex treated samples for an examination of the effect of OBD treatment on the ceramic layer formed from the CC treatment for the OBD. The relevant results are presented in this section.

Figure 4.3-6 shows the cross section images after OBD treatment together with the corresponding CC7 sample for comparison. It should be noted that on top of the images was a plated nickel layer.

For sample CC7, shown in Figure 4.3-6 (a) and (b) of the BSE and SE image respectively, a relatively thick ceramic layer was formed from the CC treatment. As it can be noticed, pore/cracks existed throughout the ceramic film. The oxide layer is bright in the SE image in Figure 4.3-6 (b). This bright colour is caused by the secondary electron charging due to the low conductivity of the formed zirconia layer.

After OBD treatment, both the size and the number of the pores/cracks existing in the ceramic layer formed on CC treatment were reduced when compared with sample CC7 (see Figure 4.3-6 (c), (e), (g) and (h) for BSE image of CC7-6010, CC7-6030, CC7-7030 and CC7-8030 respectively). The only exception is sample CC7-8030 which exhibited a cracked layer underneath a fairly thin oxide layer (unmeasurable due to the nickel plated layer on top). This observation on CC7-8030 is in consistent with the GDOES (Figure 4.2-4 (c)) and XRD (Figure 4.2-5 (c)) analysis, and the cracked surface matches the surface morphology image in Figure 4.3-2. It can also be seen that the SE images of samples CC7-6010 and CC7-6030 (Figure 4.3-6 (d) and (f)) exhibit a darkened top surface layer with of about 1 μm in thickness, beneath which is a bright

ceramic layer which is the same as the oxide layer observed on sample CC7. A thickened dark layer can also be seen at the Metal/Oxide interface. The darkened layer indicates an increase of the conductivity due to the generation of oxygen vacancies at the top surface layer as evidenced by the Figure 4.2-4 (a) and Figure 4.2-5 (a).

Table 4.3-1 summarises the relevant thickness measurement results. It can be seen that when the OBD treatment condition was 600 °C, there is an increasing of the ceramic layer thickness with the increase of the treatment time. The ceramic layer thickness is 9.01 µm, 9.65 µm and 10.52 µm for CC7, CC7-6010 and CC7-6030 respectively. When the treatment time was fixed at 30 hours, the thickness decreased from 10.52 µm for CC7-6030 to 7.71 µm for CC7-7030 and eventually to 3.79 µm (cracked zone included) for CC7-8030 with the increasing of treatment temperature.

Table 4.3-1 Duplex treatment conditions and ceramic layer thicknesses

Sample Code	OBD T, °C	OBD Time, hours	Layer thickness, µm	Error, µm
CC7	--	--	9.01	1.55
CC7-6010	600	10	9.65	0.28
CC7-6030	600	30	10.52	0.32
CC7-7030	700	30	7.71	0.17
CC7-8030	800	30	3.79 (fracture layer included)	0.68

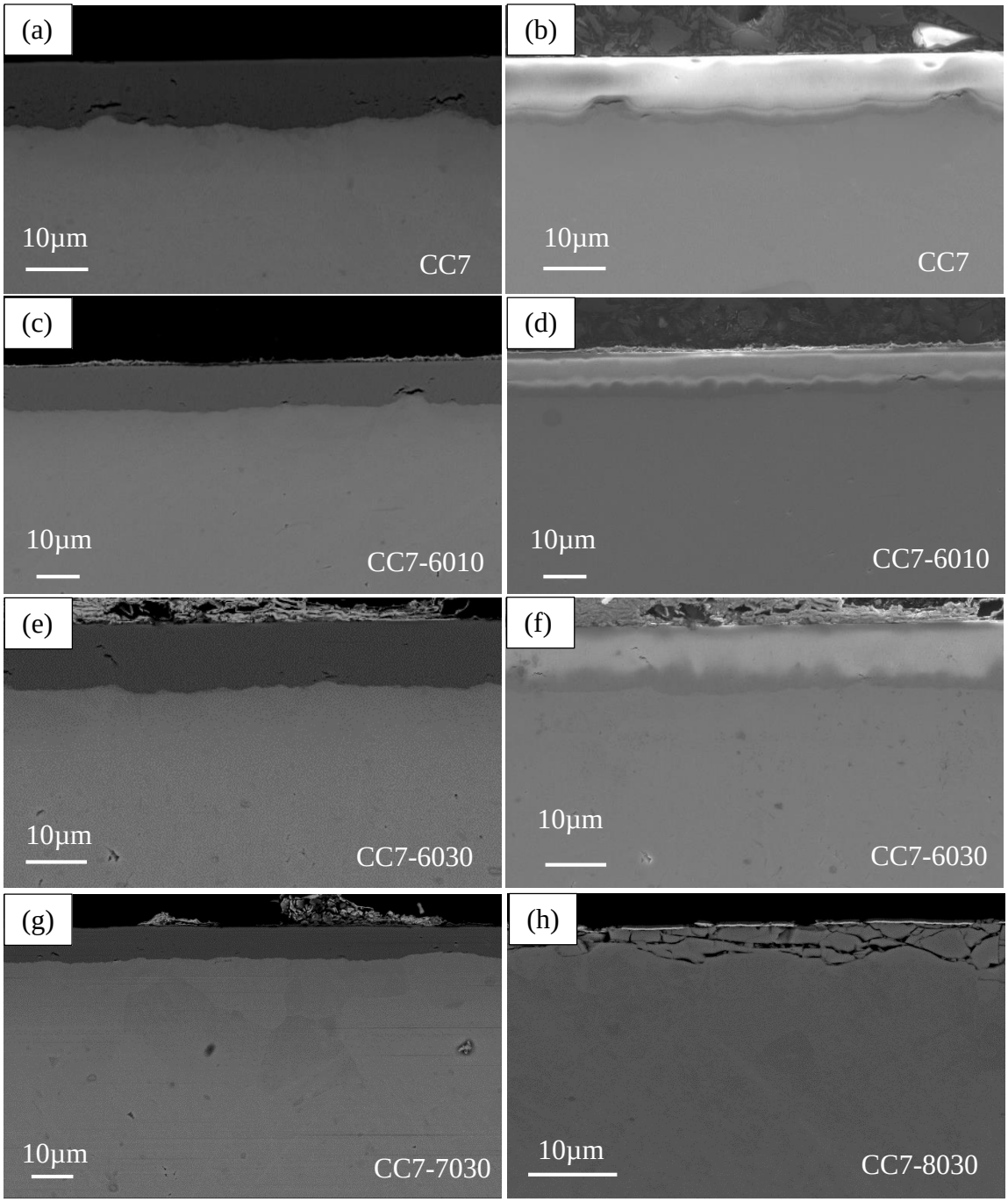


Figure 4.3-6 Cross sectional SEM images of duplex treated samples: (a) CC7 BSE; (b) CC7 SE; (c) CC7-6010 BSE; (d) CC7-6010 SE; (e) CC7-6030 BSE; (f) CC7-6030 SE; (g) CC7-7030 BSE; (h) CC7-8030 BSE; samples having nickel plated layer on top of the image.

4.3.5.2 TEM characterisation

Sample CC7-6030 was characterised using TEM in terms of the layer structure, phase constitutes through SAD patterns indexing and chemical composition using EDX detecting on spots. The relevant results are shown as below.

TEM observation on this sample revealed that the surface oxide layer remained the feature of columnar grained structure with dominant m-ZrO_2 and traces of t-ZrO_2 phases (Figure 4.3-7 (a) and (b). Interestingly, the interface layer presented after the CC treatment between the oxide/metal was still there but the grain shape changed from the prolate long grains along the interface to equiaxed gains and the $ZrO_{0.27}$ phase changed to a Zr HCP phase (reference code 00-26-1399, Figure 4.3-8 (b)) which only forms under pressure, noted as ω phase as aforementioned in section 2.1.3.1[26]. SAD pattern taken from the area beneath the interface layer revealed substrate HCP Zr structure but with ordered interstitial oxygen diffraction spots as denoted by the arrows in Figure 4.3-8 (c). This observation implies that the oxygen diffused into the octahedron interstitial of HCP Zr structure during the OBD process, which could contribute to the hardness improvement in this area (to be revealed in Figure 4.4-9).

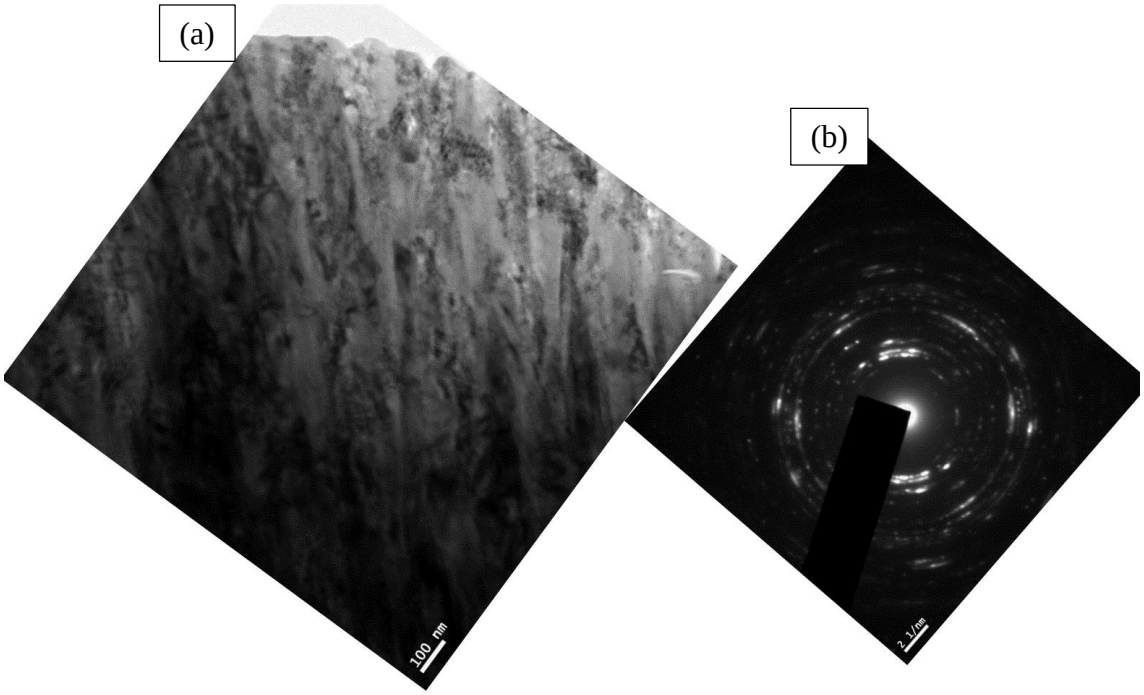


Figure 4.3-7 TEM (a) oxide microstructure of CC7-6030; (b) corresponding SAD pattern

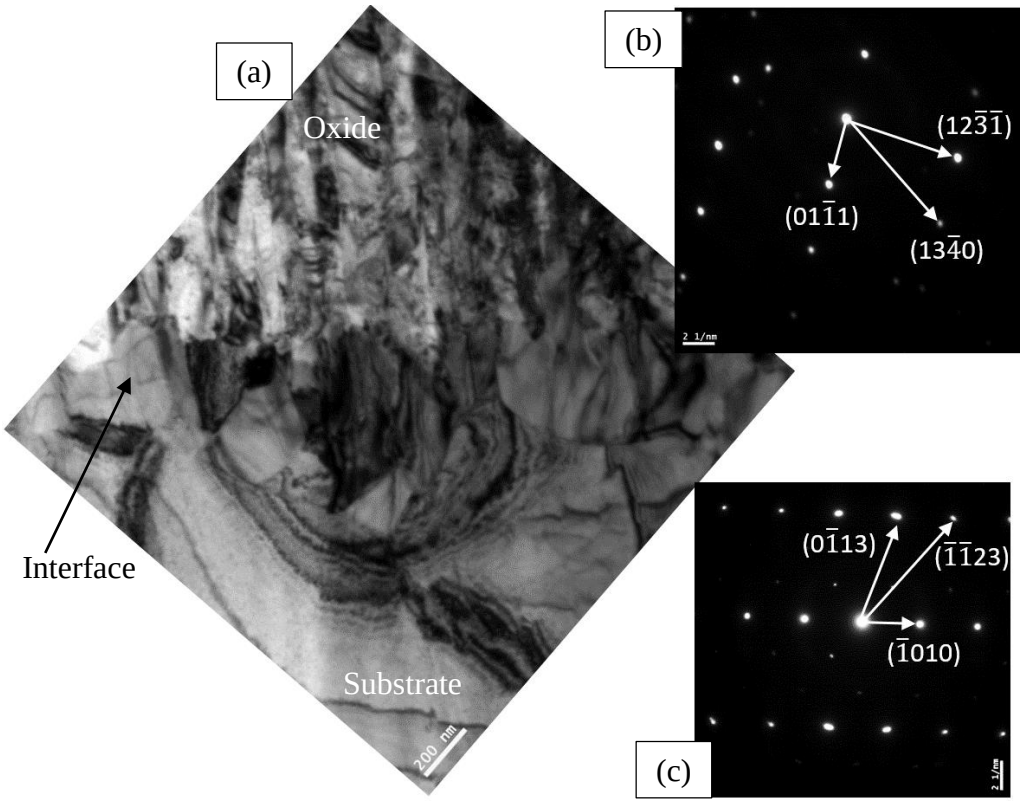


Figure 4.3-8 TEM image of CC7-6030: (a) interface; corresponding SAD patterns (b) interface and (c) substrate

4.4 Mechanical properties

4.4.1 Hardness of CC treated samples

As discussed in section 3.3.2.2, the surface hardness of both treated and untreated samples was measured using a nanoindentation machine. At least five indents were repeated on each sample for an accurate measurement and duplicity test. Figure 4.4-1 presents the typical load vs. depth curve for sample Zr702-5310 showing the repeatability and accuracy of the data collected. The average hardness was taken and the standard deviation was then used as the errors.

In addition, a small indentation load is preferred for better characterisation of the coating hardness without influence from the substrate, especially for the ones with thin ceramic layer formed on the surface, i.e. Zr702-4010, Zry4-4010 etc. The load as small as 5 mN was used due to the machine restriction caused by the vibration and thermal drifting of the load vs. depth curve.

Figure 4.4-2 depicts the surface hardness of CC treated and untreated (for comparison) Zr702 and Zircaloy-4 samples. It can be seen that the untreated Zr702(UN) has a hardness of 3.02 GPa which is slightly higher than that (2.79 GPa) of untreated Zry4(UN). As can also be seen, for both Zr702 and Zircaloy-4 alloys the surface hardness increased initially with the treatment conditions until it reached the highest value (Zr702-5010 and Zry4-5010); then it slightly decreased to a relative steady value of about 12.5 GPa and 12 GPa for Zr702 and Zircaloy-4 respectively. As aforementioned, this is consistent with the hardness of ZrO_2 ceramic, which has been reported to be 1100 ~ 1500 HV[191, 192].

The measured surface hardness of 400°C treated samples (Figure 4.4-2) is between the hardness of the zirconium substrate and zirconia ceramics for both alloys. This measured relatively low hardness especially for short-time treated samples could be the composite hardness of the substrate and the thin surface oxide layer. Because the oxide layer is very thin, the indentation depth could be more than $1/10^{th}$ of the oxide layer thickness, which is the minimum requirement for an accurate measurement of the intrinsic hardness of thin surface layer (modified layer or coating) without substrate effect. As an example, the load vs depth plot (Figure 4.4-3) of Zr702-40100 sample shows a maximum penetration depth of 140 nm. However, the formed ceramic layer on Zr702-40100 only has a thickness of ~ 0.39 μm, as mentioned in section 4.2.5 (Figure 4.2-24). Therefore, although they have dense and porous free layer structure as shown in the SEM cross sectional images (Figure 4.2-21), the nanohardness test under 5 mN produced a combination hardness of both the hard oxide layer and the soft zirconium matrix since the thickness of the surface oxide film is less than $1/10^{th}$ of the total penetration depth. Hence, with increasing the oxide thickness by increasing the treatment temperature and/or time, the contribution from the zirconium became less, thus the overall surface hardness could be measured.

The surface hardness reached the highest value at treatment condition of 500°C for 10 hours (i.e. 5010 condition) for both Zr702 and Zircaloy-4. As shown in Figure 4.4-2, the highest hardness value is 14.5 GPa and 15.5 GPa for Zr702-5010 and Zry4-5010 respectively. This is because the dense ceramic layer is thick enough to bear the load without substrate effect.

After this peak point at 500°C/10hours, the surface hardness for both Zr702 and Zircaloy-4 stabilised at a relatively steady hardness value, 12.5 and 12 GPa for Zr702 and Zircaloy-4 respectively. That means for CC treatment at a higher temperature and/or for a longer time, a thicker ceramic layer can be produced but this ends up with a slightly decreased hardness. Considering the SEM layer quality observation results reported in section 4.2.5.1, this reduced surface hardness could be related to the defects (cracks and blisters) formed in the ceramic layer and at the metal/oxide interface.

In addition, it is also noted from Figure 4.4-2 that for samples treated at 400°C, a higher hardness is probed from Zircaloy-4 than from Zr702 for the same treatment time. This is because the oxide formed is dense without appreciable defects and hence the measured hardness is related mainly to the thickness of the oxide layer due to the reasons discussed above. However, when treated at a temperature at 530°C or above, the surface hardness of Zr702 samples is slightly higher than that of Zircaloy-4 samples. This is because the thickness of the oxide layer formed on these samples is well beyond the minimum value required to avoid substrate effect and hence the hardness is decided by the quality of the oxide layers. For example, when comparing the ceramic layer formed at the same CC treatment conditions, Zr702-5310 (Figure 4-2.18 (c)) vs. Zry4-5310 (Figure 4-2-19 (c)), the number of cracks within the ceramic layer and at metal/oxide interface is considerably more on Zry4-5310 than on Zr702-5310.

The Young's modulus values of CC treated Zr702 and Zircaloy-4 samples are shown in Figure 4.4-4. As it shows, the Young's modulus variations of the CC treated both alloys follow similar or almost the same trend as for the surface hardness. The Young's modulus of the treated samples is generally increased by the CC treatment with the only

exception of treatment condition 4010 when compared with the untreated materials (121 GPa and 121 GPa for Zr702-UN and Zry4-UN respectively). Figure 4.4-5 shows the Young's modulus and hardness ratio variation of these samples. It can be seen that the ratio follows a decreasing tendency when compared with the corresponding untreated samples, which suggests an improved resistance towards plastic deformation.

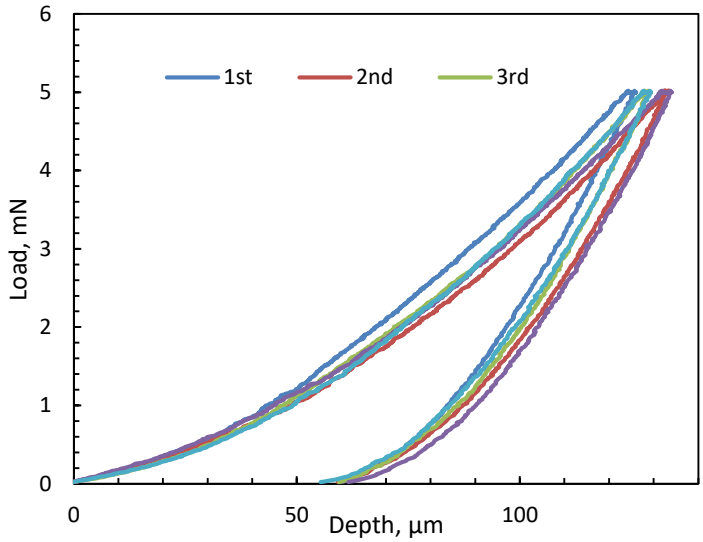


Figure 4.4-1 Typical load vs. depth curves for sample Zr702-5310 at the load condition of 5 mN

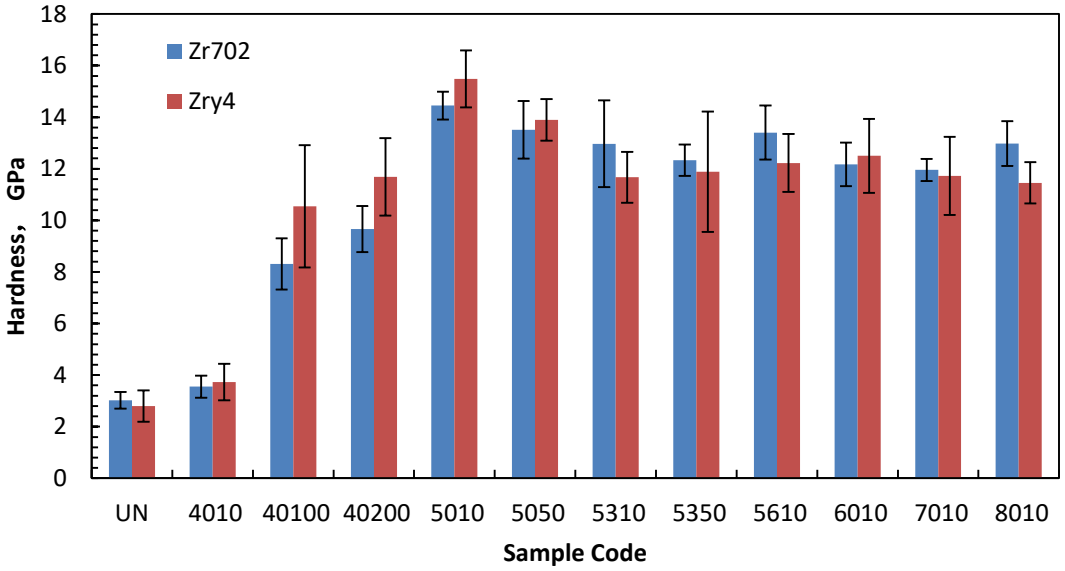


Figure 4.4-2 Surface nanohardness changes before and after CC treatment for both Zr702 and Zircaloy-4

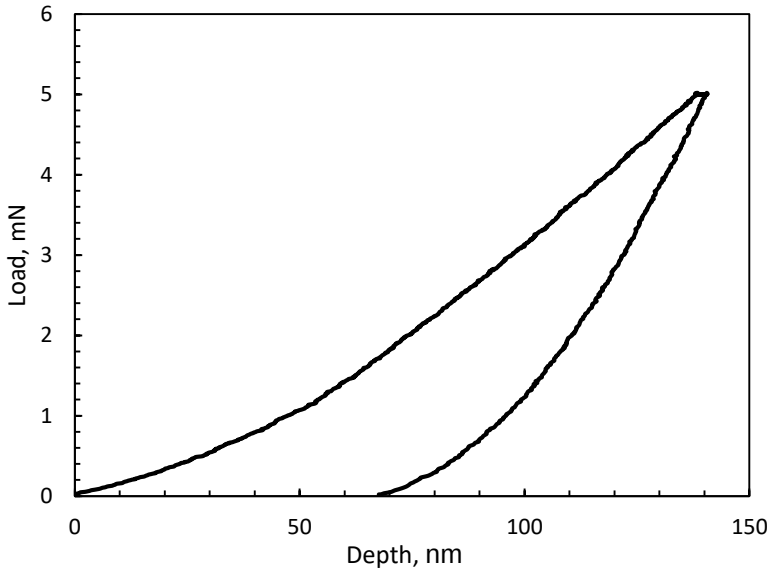


Figure 4.4-3 Load vs. depth curve for sample Zr702-40100 at the load condition of 5 mN

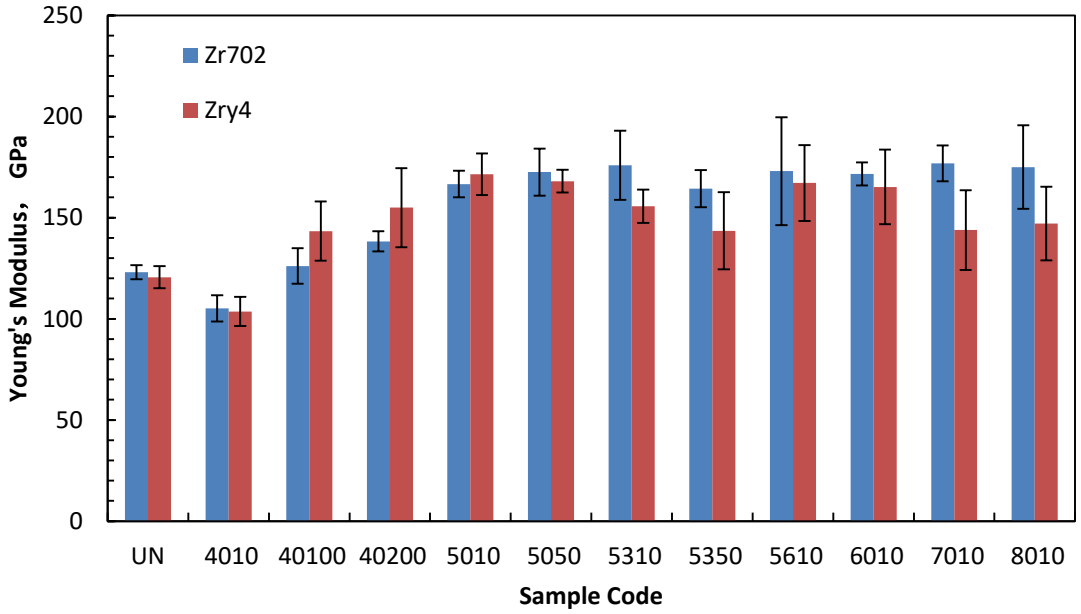


Figure 4.4-4 Young's modulus variation of CC treated Zr702 and Zircaloy-4 sample

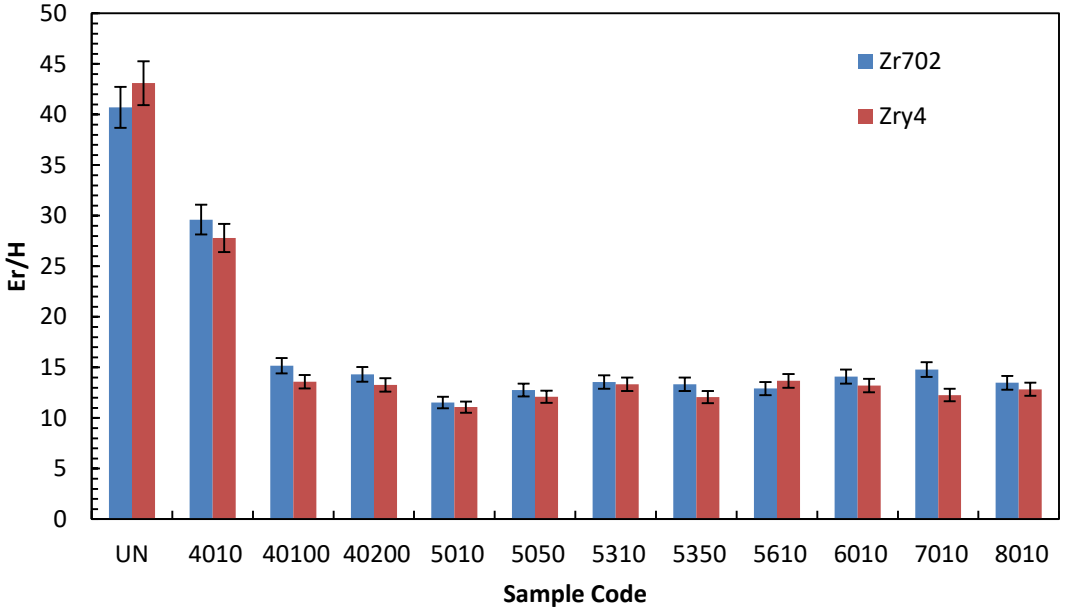


Figure 4.4-5 Young's Modulus vs. hardness ratio changes before and after CC treatment for both Zr702 and Zircaloy-4

Nanoindentation on the cross section of treated samples at a load of 30 mN was used to produce hardness depth profiles. The load of 30 mN was selected instead of 5 mN used for the surface hardness measurement in order to generate indents large enough to be easily located by SEM.

After the nanoindentation test, samples were then observed under SEM for a measurement of the depth of the produced indents. An example SEM image showing the indents along the cross section of the ceramic layer is shown in Figure 4.4-6. Based on the measured depth, the hardness vs. depth profiles were then plotted. It should be note here that the hardness at the surface (0 μm position) came from the surface hardness (Figure 4.4-2) measured under 5 mN to reduce or exclude the influence from the substrate.

Due to the great similarities of the hardness depth profiles on different CC treated samples for both Zr702 and Zircaloy-4 alloys, only typical hardness-depth profiles from Zr702-5310, Zr702-7010 and Zry4-6010 samples are exemplified in Figure 4.4-7. It can be seen that there is a fluctuated high hardness plateau near the surface which is followed by a hardness decreasing zone (HDZ) where the hardness dropped until it reaches a steady substrate hardness.

Combined with the SEM observation (Figure 4.2-18 and Figure 4-2-19) and the thickness results (Figure 4.2-20), together with the GDOES compostion profile (Figure 4.2-9), it can be found that the fluctuated hardness plateau corresponds to the ceramic layer formed during the CC treatment and the fluctuation comes from the crack defects across the layer. As an example for Zr702-7010, the high hardness plateau continues until a depth of about 8.5 μm which is comparable with the ceramic layer thickness and the high oxygen plateau (9.0 μm) if the experimental errors are taken into account. On the other hand, both the HDZ and the oxygen diffusion zone (ODZ) reaches a similar depth e.g. about 20 μm for Zr702-7010. Hence the hardness decreasing zone caused by the oxygen distribution in zirconium matrix in view of the strong solid solution hardening of oxygen in zirconium.

Meanwhile, it can also be seen that after the CC treatment the hardness of the substrate is about 2.5 GPa, which is lower than that of the untreated materials (~ 3.0 GPa for Zr702-UN). This is mainly due to the CC treatment induced microstructure changes in the zirconium matrix.

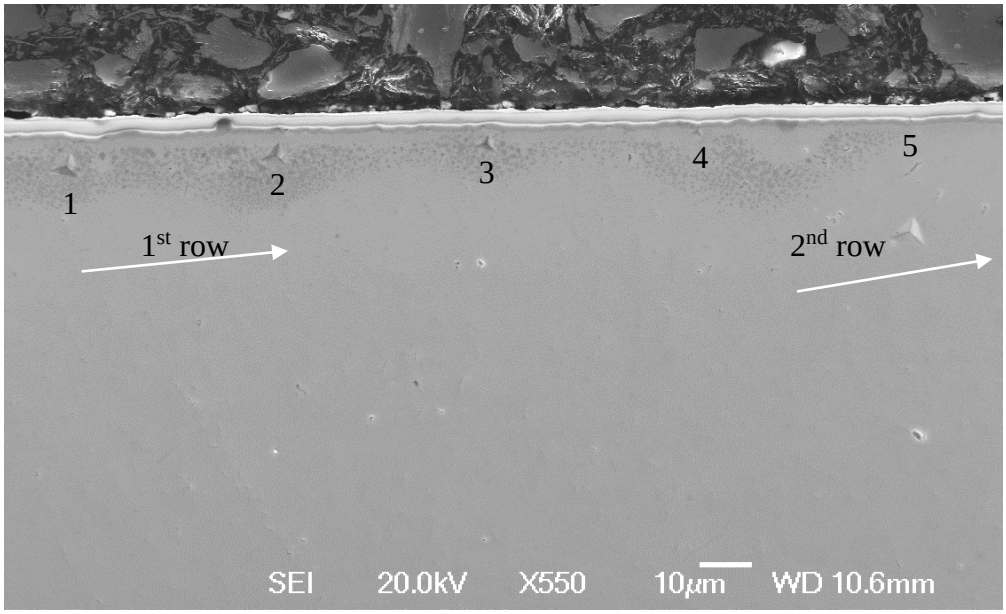


Figure 4.4-6 SEM image of cross sectional nanoindentation showing distribution of the indent marks

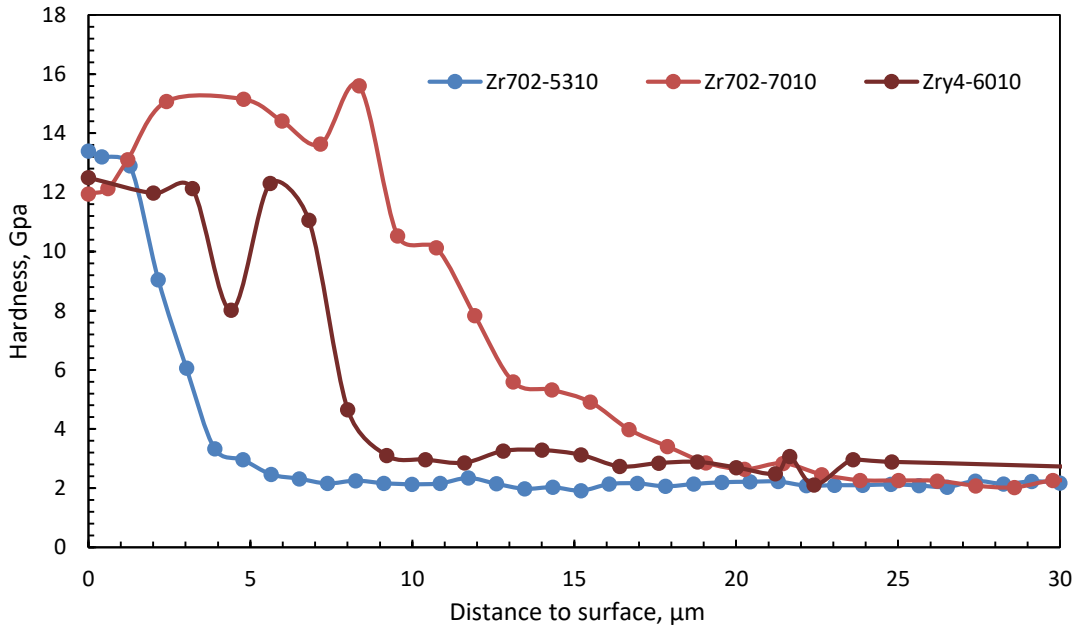


Figure 4.4-7 Hardness depth profiles of Zr702-5310, Zr702-7010 and Zry4-6010

4.4.2 Hardness of duplex treated samples

Figure 4.4-8 presents the surface hardness and elastic modulus of duplex treated samples and it can be seen that the hardness and Young's modulus have shown similar

trend. Both the surface hardness and the Young's modulus of the duplex treated samples are higher than those of the CC treated sample i.e. CC7 (Zr702-7010), with the only exception of CC7-8030.

It can also be noticed that with the increase of treatment time at OBD temperature 600 °C (i.e. CC7-6010 and CC7-6030), the hardness and Young's modulus both witnessed an increase of their values. When the treatment temperature increased from 600 °C to 700 °C for a fixed time of 30 hours, the surface hardness and Young's modulus increased from 15.8 GPa to 17.7 GPa and 216 GPa to 223 GPa respectively. The general increasing tendency for the hardness and Young's modulus is related to integrity of the ceramic layer, as less porous/crack defects were observed (Figure 4.3-6). With further increasing the treatment temperature to 800 °C, i.e. CC7-8030, both the hardness and the Young's modulus decreased to 11.7 GPa and 175 GPa respectively in comparison of sample CC7 because of the full decomposition of the ceramic layer as well as the cracked surface (Figure 4.3-6 (h)). However, the hardness still increased if compared with the Zr702-UN sample (3.0 GPa) which is due to contribution of the oxygen diffusion zone towards the surface hardness and Young's modulus properties.

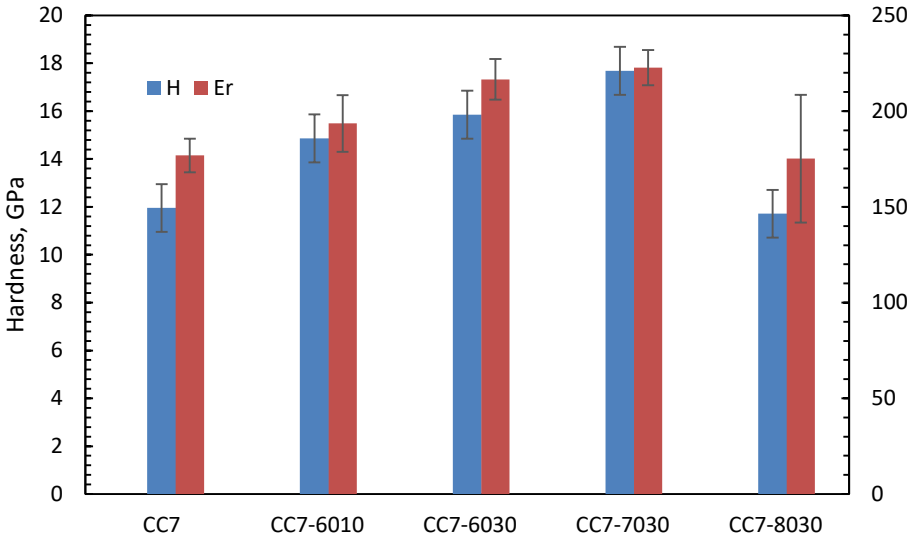


Figure 4.4-8 Surface hardness and Young's Modulus of duplex treated samples

Hardness vs. depth profiles of duplex treated samples are shown in Figure 4.4-9. It can be seen that after OBD treatment at 600 °C, CC7-6010 and CC7-6030 samples exhibited similar hardness depth distribution to that of the CC treated sample: a hardness plateau zone close to the surface, which corresponds to the oxide layer, followed by a gradual hardness deceasing zone until it reaches the substrate hardness

A thickening of the hardness decreasing zone was clearly observed underneath the ceramic layer as evidenced by an increase of the hardness decreasing zone from about 20 µm for sample CC7 to about 35 µm for both CC7-6010 and CC7-6030. This suggests that the increase of the OBD treatment time from 10 to 30 hours at 600 °C did not make appreciable changes in the hardness depth profile for these two samples. In terms of sample CC7-7030, it can be seen from Figure 4.4-9 (b) that the hardness decreasing zone continued until a distance of up to about 60 µm which may indicate a thicker oxygen diffusion zone when compared with CC7-6010 and CC7-6030. For CC7-8030 (Figure 4.4-9 (b)), however, even though the hardness deceasing zone can

reach as deep as ~ 150 µm, no obvious hardness plateau is noticed, which suggests a complete decomposition ceramic layer and diffusion of oxygen into the zirconium matrix. These are in agreement with the cross section observation reported in section 4.3.5.1 (Table 4.3-1) as well as the high oxygen plateau measurement in the GDOES test (Figure 4.3-4).

It should also be noted that in comparison with the GDOES results (Figure 4.3-4), there is a big variation between the oxygen diffusion zone (ODZ) and hardness decreasing zone (HDZ) in the hardness depth profile, as an example for CC7-6030 the ODZ reaches a depth of about 21 µm, while the hardness keeps decreasing until about 35 µm. This is partially attributed to the oxygen solid solution hardening in the zirconium matrix as the case of CC treated samples. On the other hand, it is also related with the formation of high pressure ω-Zr phase as evidenced by the SAD pattern from TEM observation (Figure 4.3-8 (b)). It can also be seen that the core hardness of zirconium matrix after duplex treatment maintained at about 2.5 GPa, which is the same as for the CC alone treated samples. It thus follows that the OBD treatment did not cause any change in the substrate hardness.

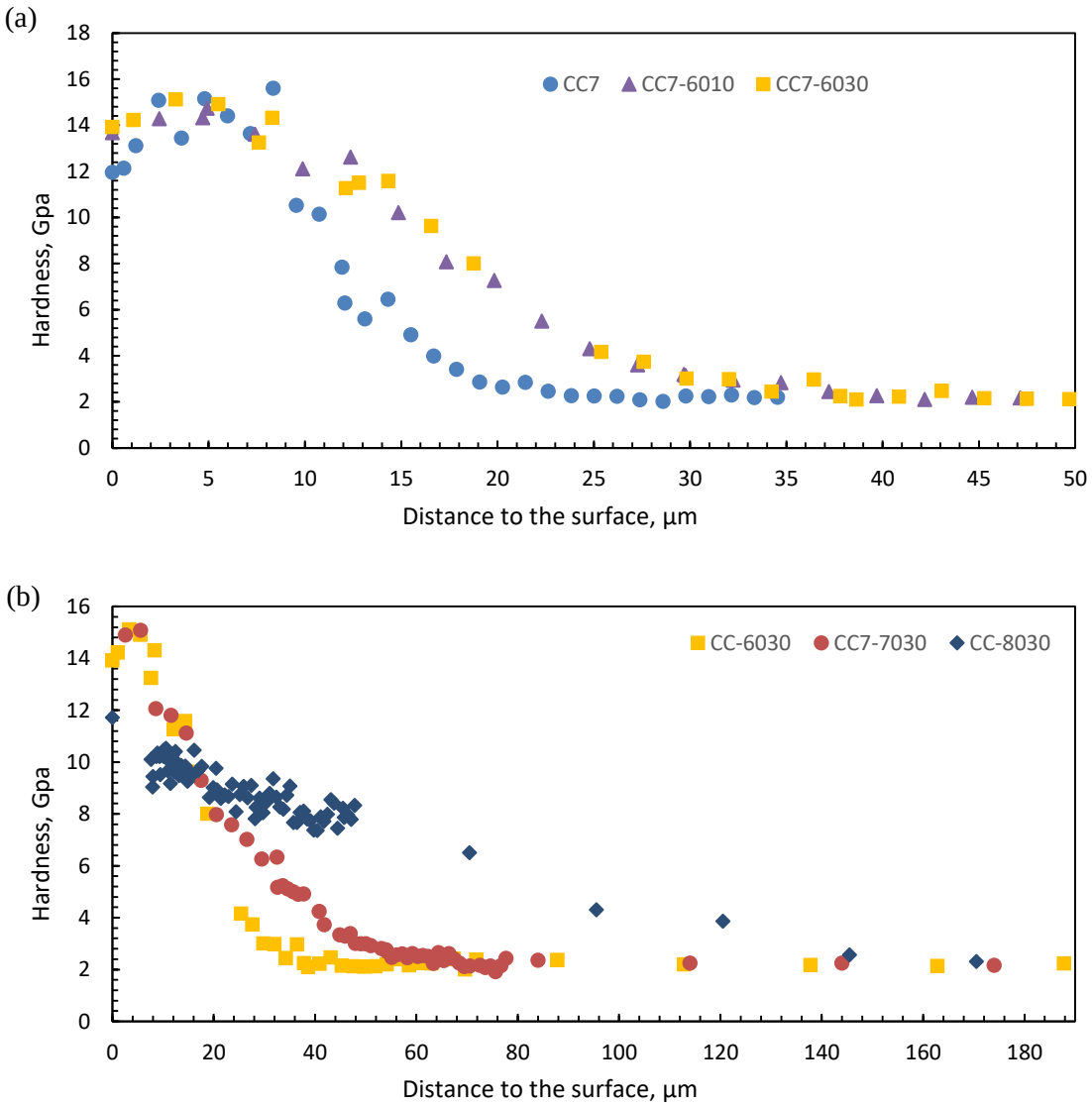


Figure 4.4-9 Hardness depth profiles of duplex treated samples (a) CC7, CC7-6010 and CC7-6030; (b) CC7-6030, CC7-7030 and CC7-8030

4.4.3 Load bearing capacity

4.4.3.1 CC Treated samples

Indentations were made on the samples surfaces under a series of indent loads varying from 10 g to 1 kg using a Vickers microhardness machine to evaluate the load bearing capacity (LBC). The hardness values measured under different indentation loads are

plotted in Figure 4.4-10 and Figure 4.4-11 of selected (for clarity) Zr702 and Zircaloy-4 samples respectively.

It can be clearly seen that generally the measured surface hardness decreased with increasing the applied load. At the same indentation load, the hardness of the 10 hours OBD treated Zr702 samples increased with the increase of the treatment temperature. This is because the overall hardness represents the resistance to the indentation from both the hard surface ceramic layer and the subsurface case. The critical load on which a nearly substrate hardness was measured was observed to be 10 g, 100 g and 200 g for samples Zr702-5010, Zr702-5310 and Zr702-6010; 25 g, 100 g, 200 g, 300 g for sample Zry4-4010, Zry4-5010, Zry45610 and Zry4-6010. Samples CC treated at over 700 °C for 10 hours (i.e. Zr702-7010, Zr702-8010 Zry4-7010) exhibit gradual hardness changes with the indentation load without reaching the substrate hardness even under the maximum load of 1 kg as shown in Figure 4.4-10 and 4.4-11.

Microscopy examination was conducted to observe cracks around generated indents. There are generally two kinds of cracks observed, with their typical images shown in Figure 4.4-12 (a) and (b). Formation of circumferential/cone cracks around the indent, typical image from sample Zry4-5610 under a load of 100 g shown in Figure 4.4-12 (a), indicates the influence of the soft zirconium matrix. This is formed mainly due to different plastic and elastic responses during the loading and unloading period in the test. This is intrinsically related to difference in hardness and Young's modulus properties between the formed ceramic layer and the substrate, especially when the surface hard layer or coating is thin hence needs strong support from the substrate[193].

When the sample is treated at high temperatures for a long period, a thicker ceramic layer followed by a wider oxygen diffusion case is formed on sample's surface. Generally, a high load bearing capacity is expected, but the formed ceramic layers become relatively brittle. A typical example shown in Figure 4.4-12 (b) depicts the second form of cracks around the indent from Zr702-8010 at a load of 200 g. The long cracks were initiated from the corner and propagated into the surrounding areas i.e. so-called radial cracks. The formation of these long cracks, which is catastrophic, indicates the brittleness of the modified surface and poor load bearing capacity of samples.

In order to efficiently improve the LBC of samples whilst maintaining a relatively thick ceramic layer on surface, an oxygen boost diffusion process to improve the thickness of the diffusion zone underneath the surface oxide was designed and the relevant LBC properties results are presented in the next section.

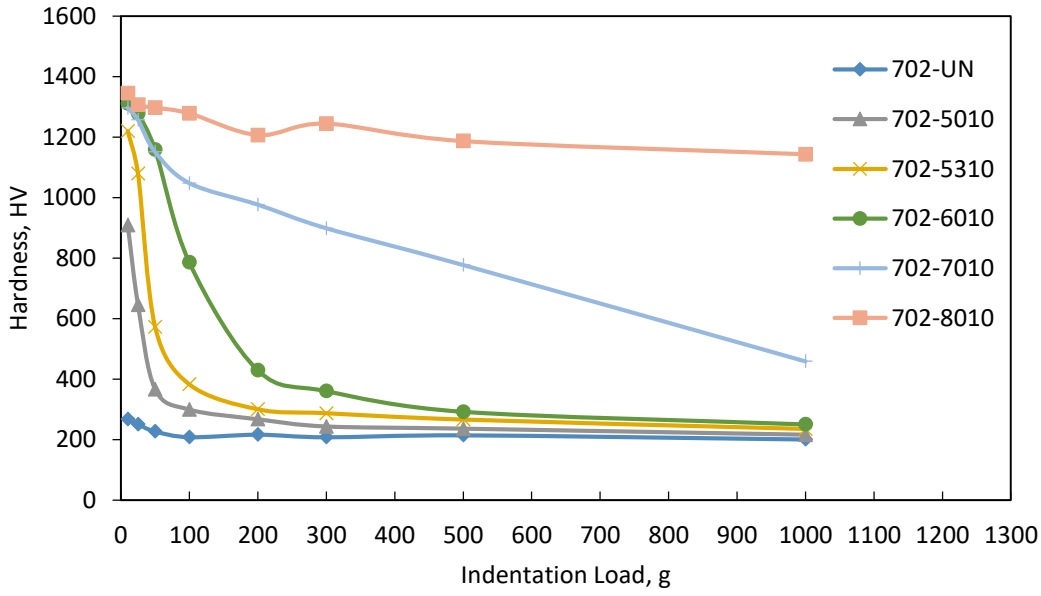


Figure 4.4-10 Load bearing capacity of CC treated samples for Zr702

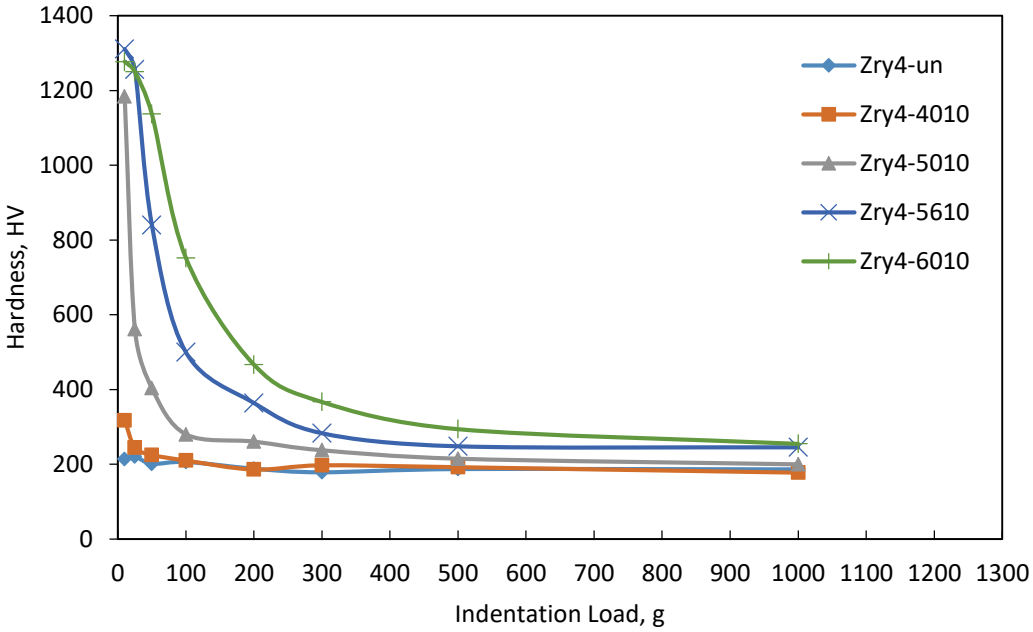


Figure 4.4-11 Load bearing capacity of CC treated samples for Zircaloy-4

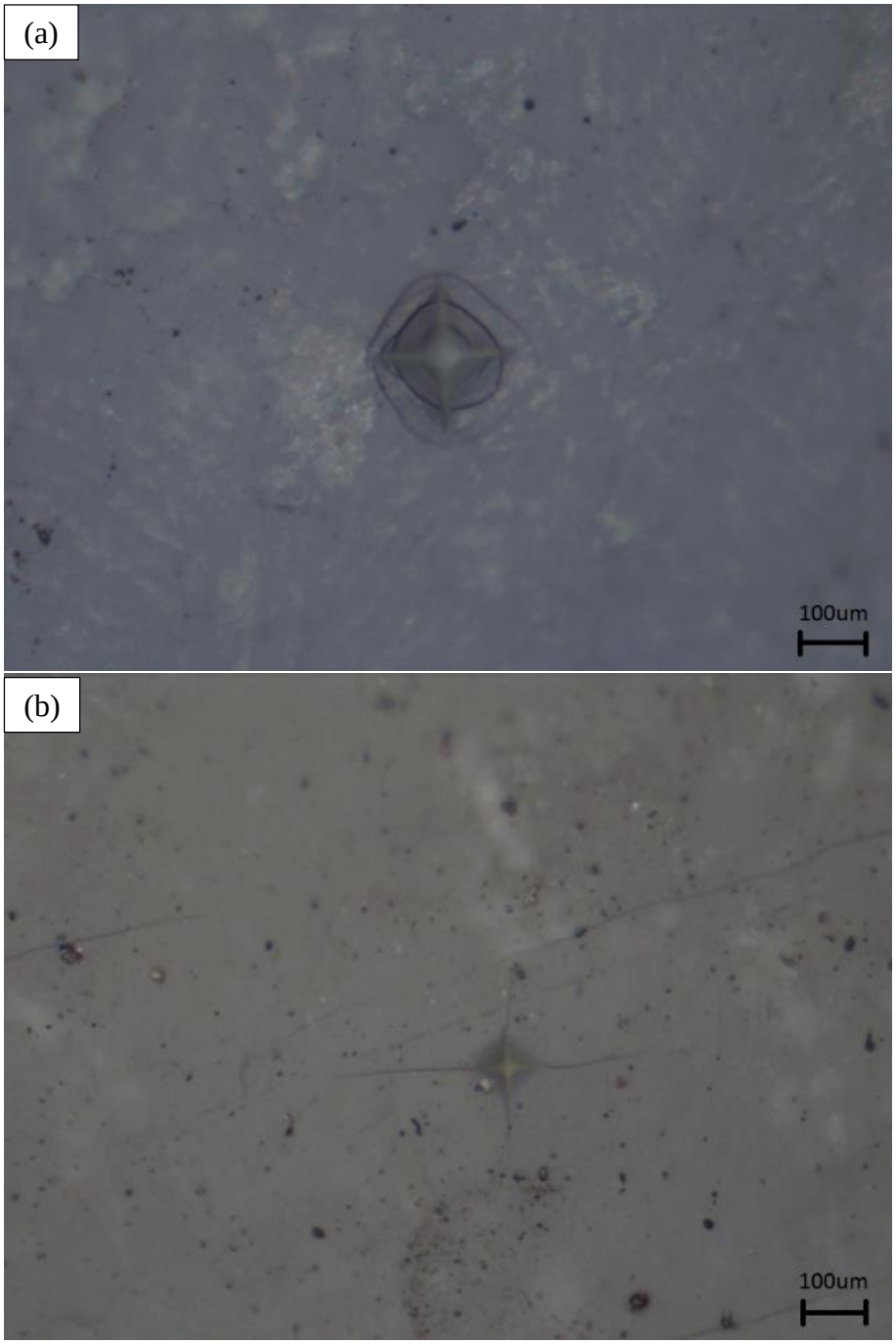


Figure 4.4-12 Two kinds of cracks around indents: (A) circumferential/cone crack around indent from Zry4-5610 under a load of 100 g; (B) radical cracks around indent from Zr702-8010 under a load of 200 g.

4.4.3.2 Duplex treated samples

Duplex surface treatment was carried out on Zr702 alloys to examine the effect of OBD process on the layer quality of ceramic layer, especially for the purpose of generating a

thick oxygen diffusion zone underneath the converted oxide for improved loading bearing capacity and other mechanical properties. The relevant LBC results are shown in Figure 4.4-13. It can be seen that the LBC property under the maximum load of 1000 g increased after the OBD treatment.

Comparing the LBC curves for CC7-6030 and CC7 (Figure 4.4-13) reveals that the measured hardness from CC7-6030 is the same as that of CC7(i.e. Zr702-7010) sample with the exception of indent loads 10 g and 1000 g. At 10 g, it is 1357 HV and 1297 HV for CC7-6030 and CC7 respectively. This is related with the ceramic layer integrity, as less cracks defects on duplexed treated sample are observed (Figure 4.3-6). In terms of load condition 1000 g, CC7-6030 exhibits a hardness of 536 HV while it is 459 HV for CC7, which is related to the thickened ceramic layer (Table 4.3-1).

The hardness of CC7-7030 is consistently higher than that of sample CC7. Bearing in mind the decreased thickness from 9.0 μm for CC7 to 7.7 μm for sample CC7-7030 (Table 4.3-1), it can be deduced that the increased diffusion zone by the OBD treatment should have played a significant role in improving the loading bearing capacity of the OBD treated CC7-7030 sample.

For CC7-8030, however, the hardness vs. load curve is below that for all other OBD treated samples when the applied load is below 850 g, which is due to the complete decomposition of the ceramic layer formed on the surface during the first treatment (i.e. CC7 or Zr702-7010).

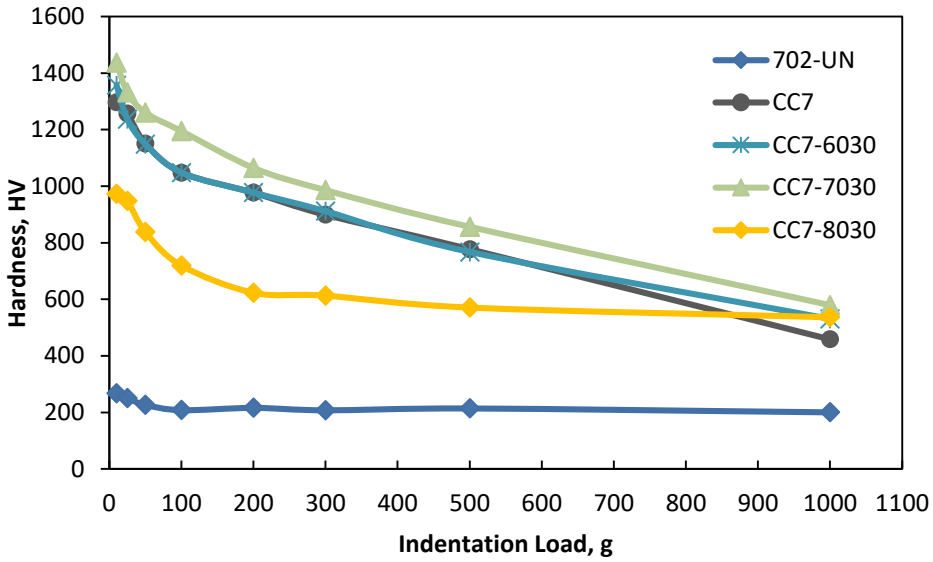


Figure 4.4-13 Load bearing capacity of CC7 duplex treated samples

4.5 Electrochemical corrosion

In order to investigate anti-corrosion behaviour of surface treated samples, as described earlier, electrochemical potentiodynamic polarisation tests were carried out on the treated surfaces. The polarisation curves were plotted and analysed. The tested samples were then further examined under SEM to study the corrosion mechanism involved. The relevant results are presented in this section.

4.5.1 CC treated samples

4.5.1.1 Zr702

The potentiodynamic polarisation curves of both as-received and selected (for clarity) CC treated Zr702 samples are shown in Figure 4.5-1. It can be clearly seen that after the CC treatment anti-corrosion property of Zr702 samples is increased due to the formation of ceramic layer on surface, with the only exception of Zr702-8010. It can also be noticed from Figure 4.5-1 that the polarisation curves of Zr702 sample can generally divided into three groups, marked as A, B and C. Samples in Group A are

characterised by pitting corrosion behaviour, where the exchange current has a sudden rise at a certain potential (pitting potential). While for Group B, they have a peak at high potentials after which is the transpassivity region. Group C samples exhibit a general uniform corrosion characteristic where the exchange current gradually increases with the increase of the applied potential.

It can be seen that the anodic zone of the polarisation cure for Zr702-UN depicts a sudden increase of corrosion current at a potential of about 0.35 V_{SCE} (Voltage against Supersaturated Calomel Electrode (SCE)), which is the pitting potential for the sample. After the pitting potential with further increasing the applied potential, the corrosion current remained as a high value above 1 mA. Therefore, it can be suggested that for the untreated Zr702 surface it is broken down mainly by localised pitting corrosion, which is often caused by anions, especially chloride ions[100, 101]. Another typical example belonging to Group A is treated sample Zr702-4010. It also exhibits a current plateau at potential ranging from -0.1 ~ 0.4 V_{SCE} with the current being about 720 pA followed by pitting corrosion which breaks down the passivation film formed on Zr702-4010 during CC treatment. Pitting corrosion of sample Zr702-4010, as shown in Figure 4.5-1, starts from 0.43 V_{SCE}, which is marginally more positive than that of Zr702-UN. This suggests a slightly improved pitting corrosion resistance. It should also be noted here that the very low steady current on the plateau (720 pA), so-called the passive current (noted as i_p), which represents the protectiveness of the film.

For the Group B samples, a current plateau is also noticed but not as flat as that for Zr702-4010. On the other hand, different from Group A samples, an transpassivity region was observed, where water dissolution reaction is believed to take place. The

readouts for the passivation current are 1.8 nA, 660 pA and 9.1 nA for Zr702-5310, Zr702-5350 and Zr702-5610 respectively.

The potentiodynamic curve for Group C samples with very thick ceramic layers formed, such as Zr702-8010, is presented in Figure 4.5-1. It can be seen that Zr702-8010 is characterised by the lowest E_{corr} among all the treated samples and an exchange current even larger than that of Zr702-UN, which is caused by localised corrosion through blisters formed on the sample surface during CC treatment. Therefore, this indicates a poor corrosion resistance of Zr702-8010 sample.

The measured E_{corr} and i_{corr} values together with the i_p for typical tested samples are listed in Table 4.5-1. E_{corr} is a strong indicator for good corrosion resistance in terms of the starting potential for the corrosion reaction to occur, while i_{corr} indicates how fast the corrosion reaction is. The more positive the E_{corr} is and the smaller i_{corr} is, the better corrosion resistance the sample will have. It can be clearly seen that Zr702-5350 exhibits the most positive E_{corr} and the smallest i_{corr}, with their values being -29.9 V_{SCE} and 0.07 nA respectively.

Sample Zr702-4010 and Zr702-5310 have relatively good corrosion resistance properties in term of their E_{corr} and i_{corr} values. Zr702-5310 shows a more positive E_{corr} (-48.1 mV) than Zr702-4010 (-66.5 mV); while Zr702-4010 has the smaller corrosion current density of 0.5 nA compared that (1.5 nA) of Zr702-5310. However, it should also be mentioned that Zr702-4010 is characterised by a low pitting potential of 0.43 V_{SCE}; no pitting corrosion has occurred to samples within B Group during the whole electrochemical corrosion test.

In overall, judging by all the electrochemical corrosion parameters including E_{corr}, i_{corr}, i_p and corrosion potential, Zr702-5350 has demonstrated the best anti-corrosion properties among all of the CC treated Zr702 alloys, followed by samples Zr702-5310, Zr702-5610, Zr702-4010 and Zr702-8010.

Post-test SEM observation of the electrochemical tested samples surfaces was conducted and the results are shown in Figure 4.5-2. Figure 4.5-2 (a) shows a part of the corroded area of Zr702-UN due to the large size of the corroded surface which couldn't be captured under microscopy (both electron and optical). Figure 4.5-2 (b) shows the corrosion pit observed on tested Zr702-4010 surface. Those observations confirm pitting as the main corrosion failure mechanism for both Zr702-UN and Zr702-4010. It should be noted that the corrosion pits are relatively large because the SEM image was taken after the electrochemical test and therefore, it is not an *in situ* record of the pit.

High magnification images taken inside the corrosion pits formed on Zr702-UN and Zr702-4010 are presented in Figure 4.5-2 (c) and (d) respectively. It can be clearly seen that even both Zr702-UN and Zr702-4010 exhibit a pitting macro-morphology, the micro-morphologies are different: beecave-like morphology with many micro pits on severely corroded Zr702-UN surface; scale-like morphology from Zr702-4010 sample. Meanwhile, Zr702-4010 also exhibited 2nd corrosion pits inside the primary corrosion pit. Considering the morphology changes on the edge of the corrosion pit in Figure 4.5-2 (a), those different morphologies observed indicate different stages during the electrochemical corrosion test.

Uniform corrosion morphology was observed on the corroded surface of Group B samples, and a typical image shown in Figure 4.5-2 (e) was taken from corroded Zr702-5610 sample. It can be seen that there are no clear corrosion features on the corroded surface indicating the good anti-corrosion properties under the tested conditions.

For high-temperature CC treated Zr702-8010, localised corrosion started from the defected surface blisters around which cracks were also observed (Figure 4.5-2 (f)). The cracked modified layer and enlarged gaps between columnar grains observed on cross sections are believed to provide a short-circuit passage for reaction anions.

Table 4.5-1 Measured E_{corr} and i_{corr} of as-received and treated CC samples of Zr702

Sample Code	E_{corr}, mV	i_{corr}, nA	i_p, nA
Zr702-UN	-560	13.1	N/A
Zr702-4010	-66.5	0.5	0.72
Zr702-5310	-48.1	1.5	1.8
Zr702-5350	-29.9	0.07	0.66
Zr702-5610	-283.3	4.4	9.1
Zr702-7010	-400	1060	N/A

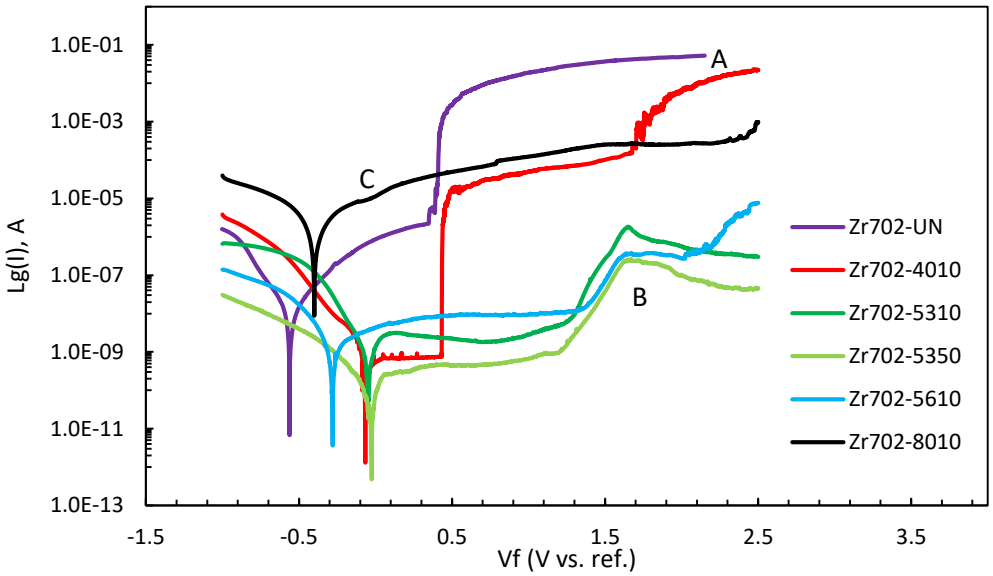


Figure 4.5-1 Polarisation curves of treated and untreated Zr702 samples in 3.5 wt% NaCl

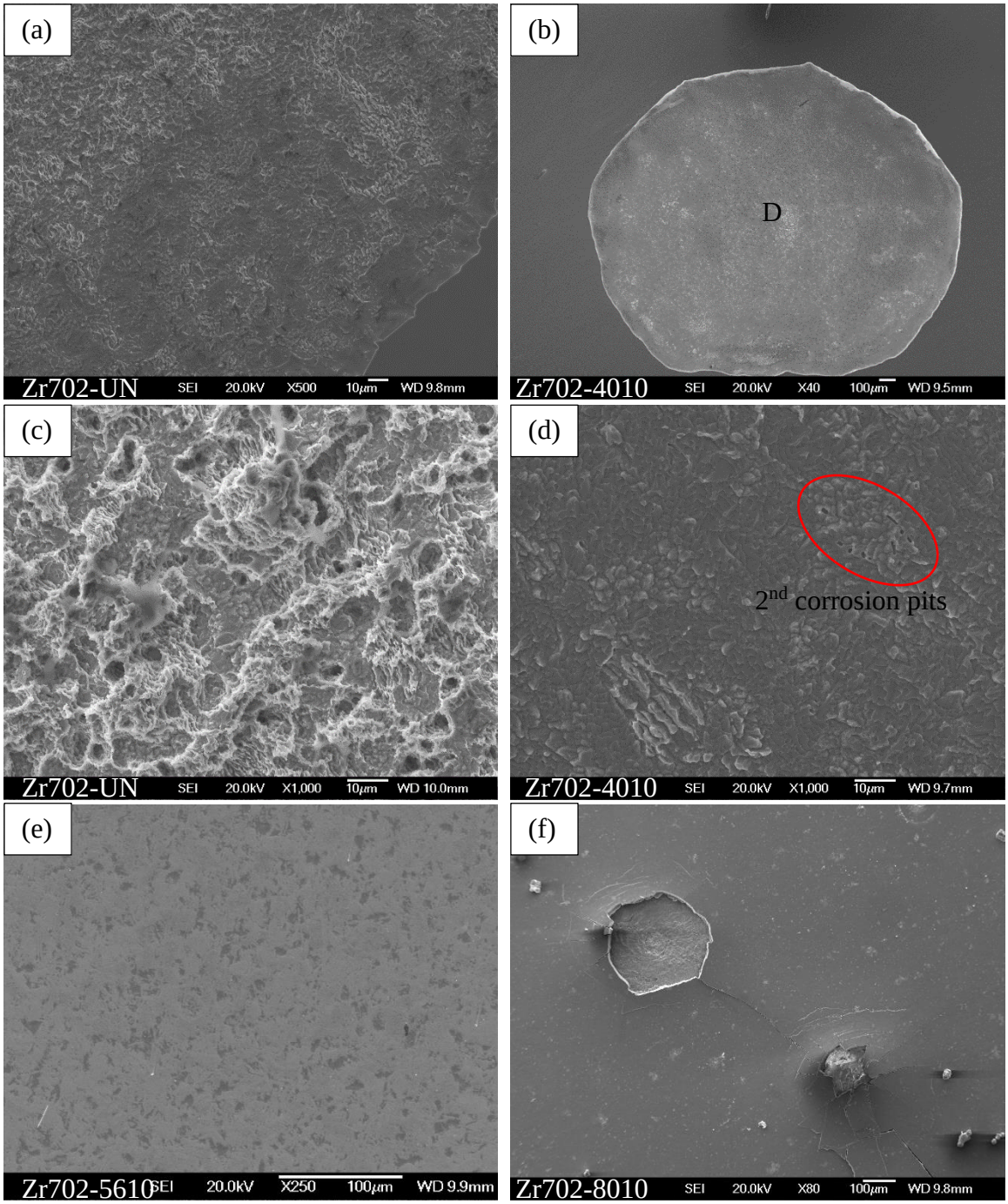


Figure 4.5-2 SEM images of Zr702 corrosion tested samples: (a) Zr702-UN, edge of the corroded area; (b) Zr702-4010, corrosion pit; (c) Zr702-UN, corrosion morphology inside corrosion pit of Zr702-UN; (d) Zr702-4010, showing micro-pit inside corrosion pit of Zr702-4010; (e) Zr702-5610, showing uniform corrosion; (f) Zr702-8010, showing localised corrosion through ceramic surface blisters.

4.5.1.2 Zircaloy-4

Results of electrochemical polarisation tests on Zircaloy-4 alloys are given in Figure 4.5-3, while Figure 4.5-4 depicts the post-test corrosion morphology observed under SEM. Similar to those of Zr702 samples, typical polarisation curves for Zircaloy-4 can generally be divided into 3 groups as marked A, B and C in Figure 4.5-3.

For Zry4-UN sample, the corrosion current density increases gradually with the increasing of potential until the pitting potential E_p 1.75 V_{SCE} which is much more positive than 0.43 V_{SCE} of Zr702 sample, suggesting better pitting corrosion resistance. Corrosion morphology is shown in Figure 4.5-4 (a), which reveals pits at the corroded surface of sample Zry4-UN.

Unlike Zry4-UN, sample Zry4-4010 demonstrates a quick increase of current with the applied voltage. The increasing gradient is up to 18 mA/V_{SCE}, which is nearly 2×10^5 times than that of Zry4-5310 (9.4×10^{-6} mA/V_{SCE}) at between 0.6 to 1.0 V_{SCE}. However, it is still marked as Group A due to the pitting corrosion morphology observed in Figure 4.5-4 (b). High magnification images inside the corrosion pits for Zry4-UN and Zry4-4010 are shown in Figure 4.5-4 (c) and (d). Both of them exhibit a highly corroded surface.

Examples of Group B polarisation curves are from Zry4-5310 and Zry4-5610, which exhibited a transpassivity region characterised by a peak at 1.67 V_{SCE} which is the same as those Zr702 CC treated sample as aforementioned in section 4.5.1.1. The current densities for Zry4-5310 and Zry4-5610 are comparable, both of which are the smallest among all the CC treated Zircaloy-4 samples. In addition, sample Zry4-5310 depicts a current plateau between 0.08 V_{SCE} and 0.55 V_{SCE} which is similar to that of Zr702-4010

and the passivity current i_p is 65 nA. Therefore, overall Zry4-5310 and Zry4-5610 exhibit the best anti-corrosion properties. From the post corrosion morphology observation (Figure 4.5-4 (e)), it can be seen clearly that different from that of Zr702 samples, grain boundaries have played a significant role in the electrochemical-corrosion process. Interestingly, those grain come from the substrate zirconium instead of the ceramic layer (about 50 nm in width as shown in TEM section 4.2.5.2 Figure 4.2-28 (a)). This is believed to be related with the un-oxidised secondary phase in Zircaloy-4 as reported by Pecheur et al.[194].

Group C sample demonstrates the lowest corrosion potential and a higher corrosion current in comparison with Group B sample. A typical post corrosion morphology under SEM observation is given in Figure 4.5-4 (f), showing cracks on the corroded surface. This increased current is therefore attributed to the cracks. Formation of the cracks during the corrosion is believed to be related to cracks on the surface, as mentioned in previous modified layer observation in section 4.2.5 (Figure 4.2-19 (f)).

The measured E_{corr} and i_{corr} values are shown in Table 4.5-2. It can be seen that sample Zry4-5610 depicts the most positive E_{corr} i.e. 23.6 mV_{SCE}, followed by Zry4-5310 with a slightly more negative value of -27.0 mV_{SCE}. Therefore, the corrosion for Zry4-5310 needs a lower voltage to initiate. Comparison of the i_{corr}, however, shows that Zry4-5310 and Zry4-5610 exhibit a corrosion current of 5.2 nA and 0.7 nA respectively, which suggests a slower reaction rate for Zry4-5610. Zry4-4010 also demonstrates a relatively positive E_{corr} of -89.5 mV, together with the smallest i_{corr} among all CC treated Zircaloy-4 samples. However, the rapid increase of corrosion current and the

abnormal pitting morphology as aforementioned, suggests a relatively poor corrosion resistance at high voltages.

Table 4.5-2 Measured E_{corr} and i_{corr} of as-received and treated CC samples of Zircaloy-4

Sample Code	E_{corr}, mV	i_{corr}, nA
Zry4-UN	-283	83.5
Zry4-4010	-89.5	0.2
Zry4-5310	-27	5.2
Zry4-5350	-408	40.4
Zry4-5610	23.6	0.7
Zry4-6010	-176	0.8
Zry4-7010	-481	15.1

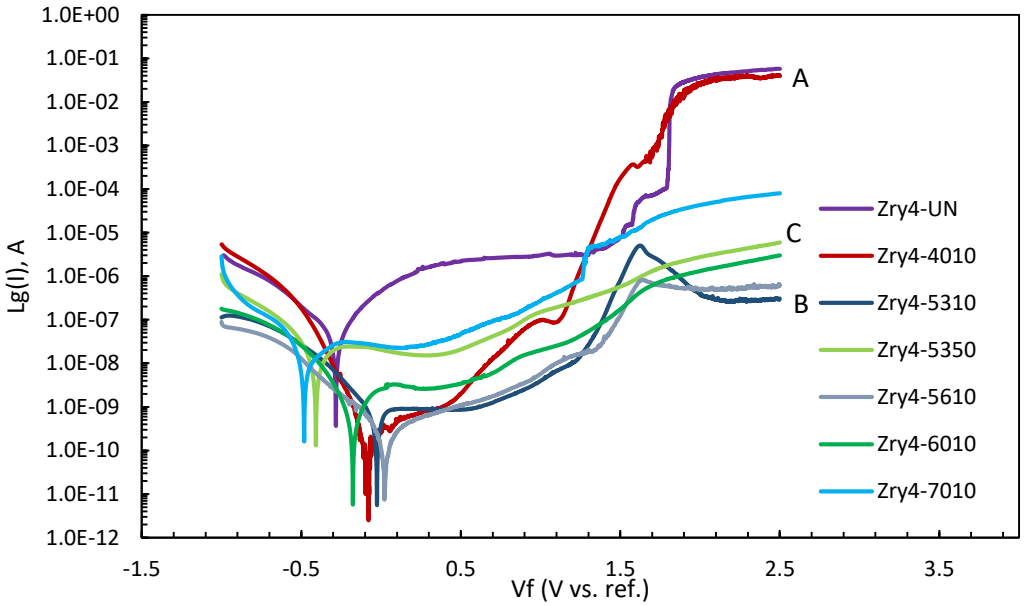


Figure 4.5-3 Polarisation curves of typical Zircaloy-4 samples in 3.5 wt% NaCl

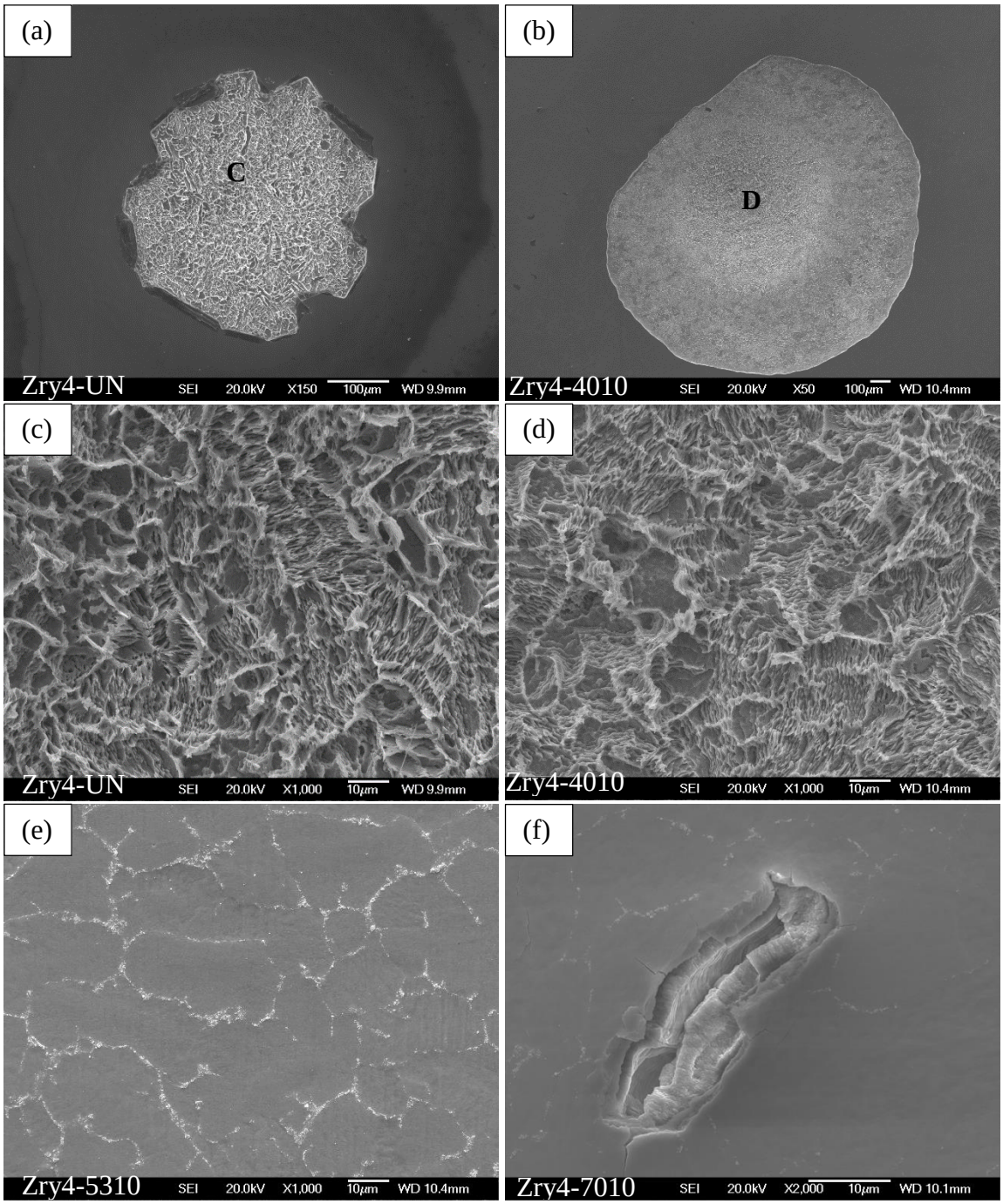


Figure 4.5-4 SEM images of Zircaloy-4 corrosion tested samples: (a) Zry4-UN, showing corrosion pit; (b) Zry4-4010; (c) Zry4-UN, corrosion morphology inside corrosion pit of Zry4-UN; (d) Zr702-4010, corrosion morphology inside corrosion pits; (e) Zry4-5310, showing uniform corrosion through grain boundaries; (f) Zr702-7010, showing corrosion crack on the surface.

4.5.2 Duplex treated samples

Similar potentiodynamic polarisation test was also carried on duplex surface treated samples. The resultant curves are shown in Figure 4.5-5, which depict the improved anti-corrosion performances of duplex treated samples in comparison with the untreated Zr702 and sample CC7 (i.e. Zr702-7010).

It can be clearly see that CC7-6010 and CC7-6030 depict almost the same polarisation curve regardless of the treatment time. Hence, the treatment time has no significant effect on the corrosion resistance of 600 °C OBD treated samples. On the other hand, when compared with the CC treated sample, i.e. CC7(Zr702-7010), they showed an increased E_{corr} but increased i_{corr}, which means that the corrosion reaction is more difficult to initiate but reacts quicker once it starts. Considering the relevant XRD results reported in section 4.3.4, the corrosion behaviour of the OBD treated samples is believed to be related to the oxygen in the zirconia matrix. Figure 4.5-6 (a) and (b) depict the typical post corrosion SEM morphology from tested CC7 and CC7-6030 respectively. Both of them exhibit blister accelerated localised corrosion.

As shown in Figure 4.5-5, CC7-6010 and CC7-6030 depict the similar E_{corr} and i_{corr} values, while the exchange current at the anodic curve for CC7-7030 is generally slightly larger when compared with CC7-6030, only that there is a small sudden rise of the exchange current for CC7-7030 at about 0.72 $V_{SCE,}$ which is related to the further localised corrosion on the tested surface. Besides the localised corrosion through surface, corrosion cracking is observed on sample CC7-7030 (Figure 4.5-6 (c)). After the sample is corroded and oxidized at a local pit, the increased volume expansion induced by corrosion will generate and form the crack around this area.

Sample CC7-8030 exhibits a typical pitting corrosion polarisation curve, which is similar to that of Zr702-UN. The pitting potential of CC7-8030 is 0.5 V_{SCE}, which is higher than 0.35 V_{SCE} for sample Zr702-UN. Meanwhile, the E_{corr} is clearly much more positive than that of Zr702-UN at the same time. Both of them suggest an increased anti-corrosion properties of CC7-8030 in 3.5 wt% NaCl solution than Zr702-UN. SEM observation reveals a different corrosion morphology (Figure 4.5-6 (d)) where hollows underneath the corroded surface are shown. This suggests a crevice corrosion failure on sample CC7-8030, which will be further discussed in section 5.3.3.

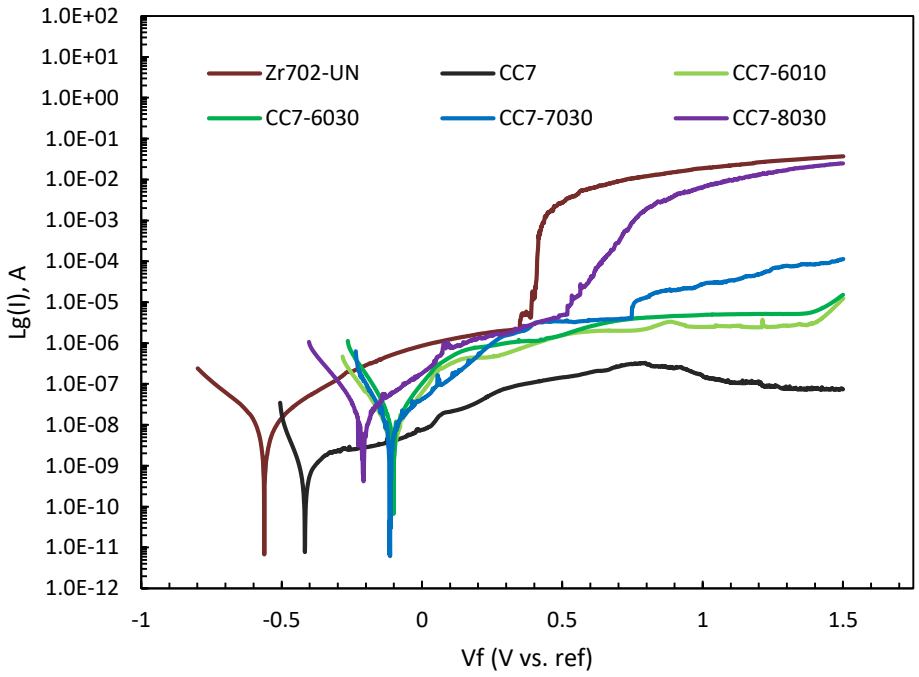


Figure 4.5-5 Potentiodynamic polarisation curves for duplex treated samples

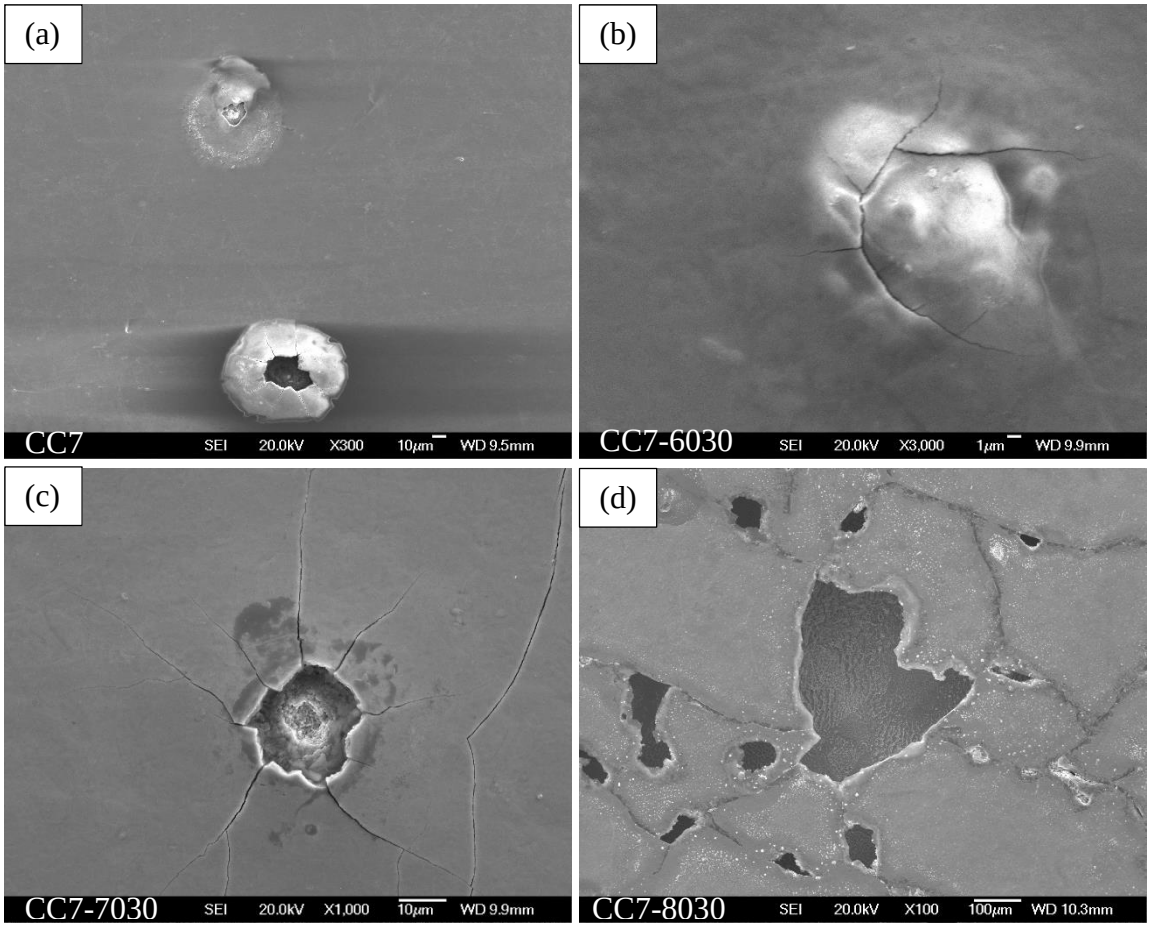


Figure 4.5-6 Typical post corrosion SEM images of duplex treated samples: (a) CC7, showing localised corrosion through blisters; (b)CC7-7030, showing localised corrosion cracking; (c) CC7-8030, showing crevice corrosion; (d) CC7-8030, zoom-in image of arrow mark region in (c) showing hollow underneath corroded surface.

4.6 Tribological properties

4.6.1 Reciprocating wear test

Reciprocating sliding wear tests were carried out against a WC/Co counterpart ball on selected samples from both CC treatment and duplex treatment. Samples are selected based on the quality, hardness and load bearing capacity, and corrosion performance of the ceramic layer. Coefficient of friction (CoF) values were recorded, wear volume loss was measured and post-wear observations were conducted, and the relevant results are reported in this section.

4.6.1.1 CC treated samples

Figure 4.6-1 presents the corresponding CoF results for Zr702 samples. The average CoF calculated from each 20 cycles was used to plot this bar graph. It can be seen that a decreased CoF within first 40 cycles was observed on CC treated samples in comparison with untreated Zr702-UN and that the medium temperature (500 and 600 ºC) treated samples showed much lower CoF values than the untreated material for the whole test period (i.e. 100 cycles).

As it shows, the untreated Zr702-UN exhibited a high coefficient of friction between 0.41 and 0.46 under the test conditions, which is in consistent with the CoF value (0.5 ~ 0.6) reported by previous studies[3, 74]. It is also noted that in general the CoF decreases with the test cycles. After CC treatment, the initial CoF within the first 20 cycles of all the samples decreased to 0.13 ~ 0.20. This is in agreement with the reported CoF of zirconia (< 0.3) at dry wear conditions against a cobalt-chromium counterpart[195, 196]. However, it can also be noted that unlike the 500 and 600 ºC treated samples which exhibited a relatively steady CoF value within 100 cycles, Zr702-4010 showed a CoF peak at 0.56 within 41-60 cycles, while Zr702-7010 depicted a steady increasing CoF value.

In order to observe the CoF variation of Zr702-4010 and Zr702-7010 with the wear cycles, Figure 4.6-2 shows the change of CoF within 100 cycles. As demonstrated in the graph, the CoF of Zr702-4010 was the range of 0.12 ~ 0.20 at the beginning of the test; however, with the test going on, it significantly increased from Cycle 23 and went up to a peak CoF value of 0.67 at Cycle 43 before it then gradually reduced to a relatively steady value of 0.40. In terms of Zr702-7010, even with a thick ceramic layer

of 9.0 μm as mentioned earlier, it depicted an almost monotonic increase of CoF from 0.15 to 0.58.

It is worthy to note that accumulative wear debris was observed during the sliding wear test process through visual observation, which is an indicator of the wear of the ceramic surface layer formed during the CC treatment. This is supported by the 2D wear track profile shown in Figure 4.6-3. It can be seen that the depth of the wear track can reach up to 10 μm, which is far beyond the ceramic layer thickness of 0.16 μm as reported in section 4.2.5 (depicted in Figure 4.2-24). Hence, initial wear occurred in the oxide layer and then resulted in a low CoF but when the oxide layer was gradually worn through the CoF increased step-by-step to the substrate value, which is typical for adhesive wear of Zr and Ti alloys.

In terms of Zr702-7010, during the whole wear test process, there was not as much wear debris as in the test for Zr702-7010. In addition, unlike the other CC treated samples, which exhibited a low surface roughness, the surface of sample Zr702-7010 is relatively rough (Ra = 0.152 μm) as mentioned in section 4.2.2 with beige blisters. Hence, when sliding against the counterpart WC/Co ball, the high asperities were worn off first and acting as the third body which induced an increasing CoF until a steady state was reached.

The CoF value variation of Zircaloy-4 samples is presented in Figure 4.6-4. As it shows, similar to CC treated Zr702 samples, the CoF values of Zircaloy-4 samples are decreased by CC treatment, which is favourable for tribological application.

It can be seen from Figure 4.6-4 that the untreated Zry4-UN has a CoF value of about 0.38 ~ 0.40, which is lower than that of sample Zr702-UN (0.41-46). This is believed to

be related to the microstructural and composition differences between these two alloys. Samples after the treatment demonstrated similar CoF values between 0.18 ~ 0.25 with the only exception of sample Zry4-7010 which exhibited a value of about 0.29 ~ 0.33. All of them are within the range of the previously reported CoF for zirconia (<0.3)[195, 196].

Unlike Zr702-4010, Zry4-4010 exhibited a quite stable CoF of about 0.2 within 100 cycles (Figure 4.6-4). This is believed to be related to the thicker oxide layer formed on Zry4-4010 than on Zr702-4010 and hence with the wear occurred within the thick oxide layer for Zr702-4010. In the case of Zry4-7010, even though it exhibited a higher surface roughness (Ra = 0.8 μm) than Zr702-7010, the former depicted a much lower and more stable CoF than the latter. Indeed, as shown in Figure 4.6-2 the CoF of Zry4-7010 was almost constant throughout the whole test period. This is probably due to the elimination of the blisters observed on the surface of Zr702-7010.

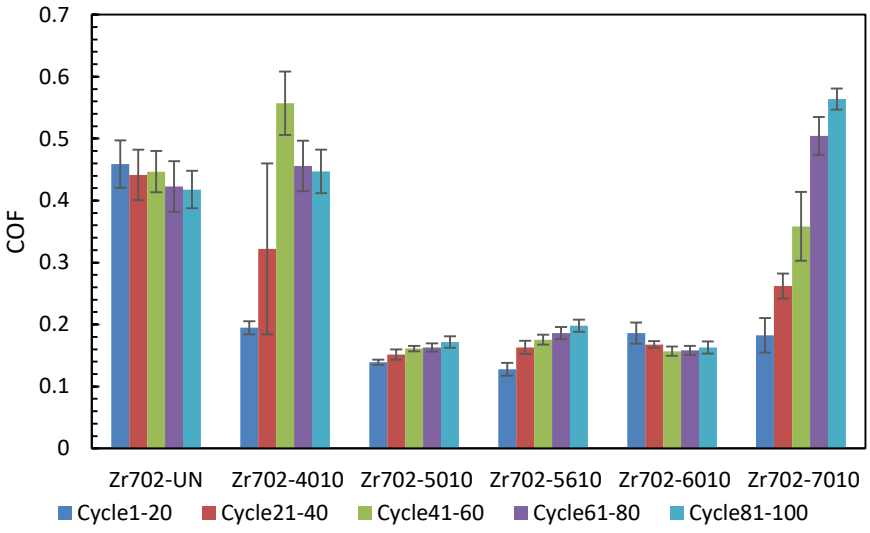


Figure 4.6-1 Measuered CoF of untreated and CC treated Zr702

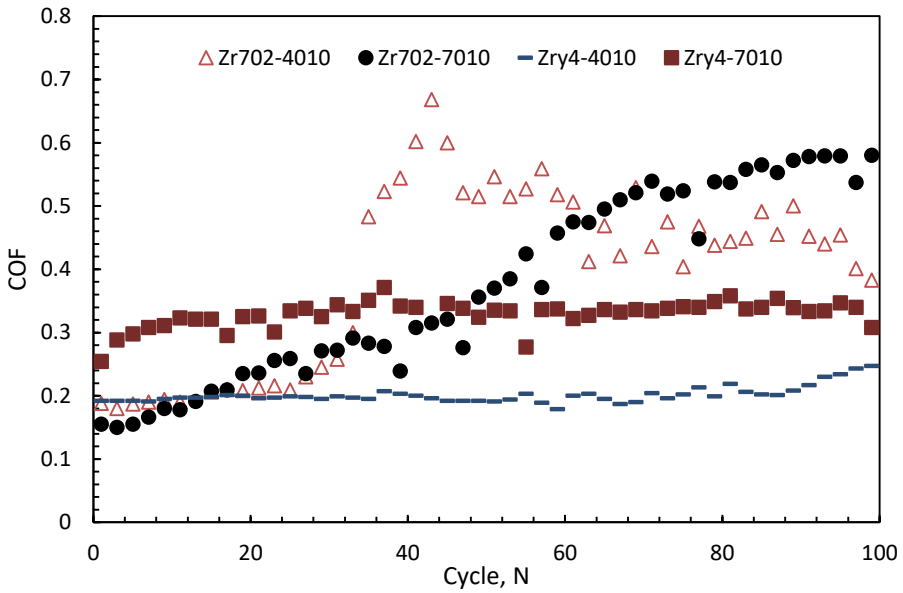


Figure 4.6-2 CoF variations of Zr702-4010, Zr702-7010, Zry4-4010, Zry4-7010 samples from cycle 1 to 100

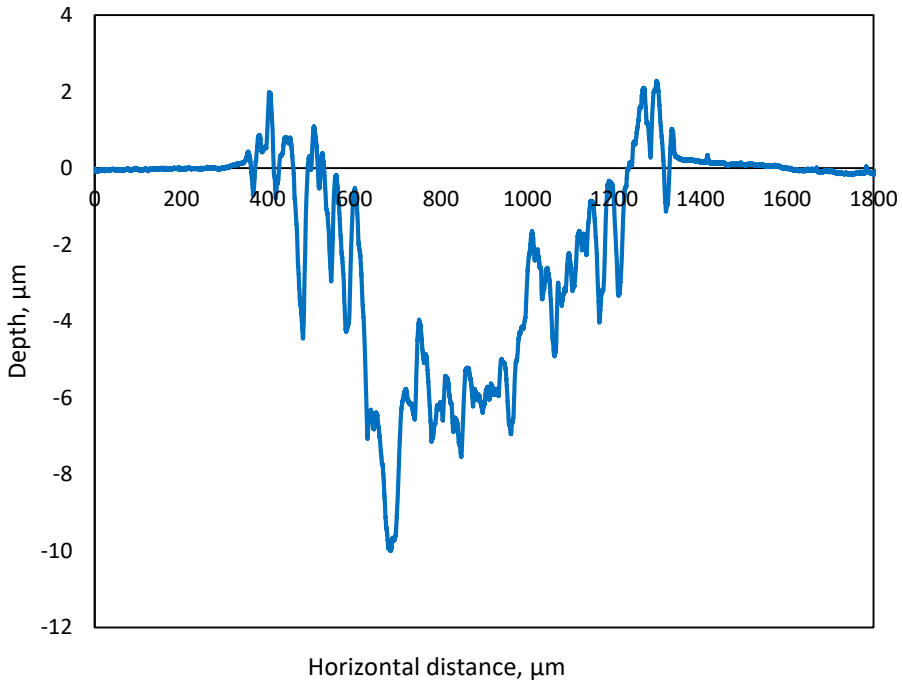


Figure 4.6-3 2D wear track profile for sample Zr702-4010

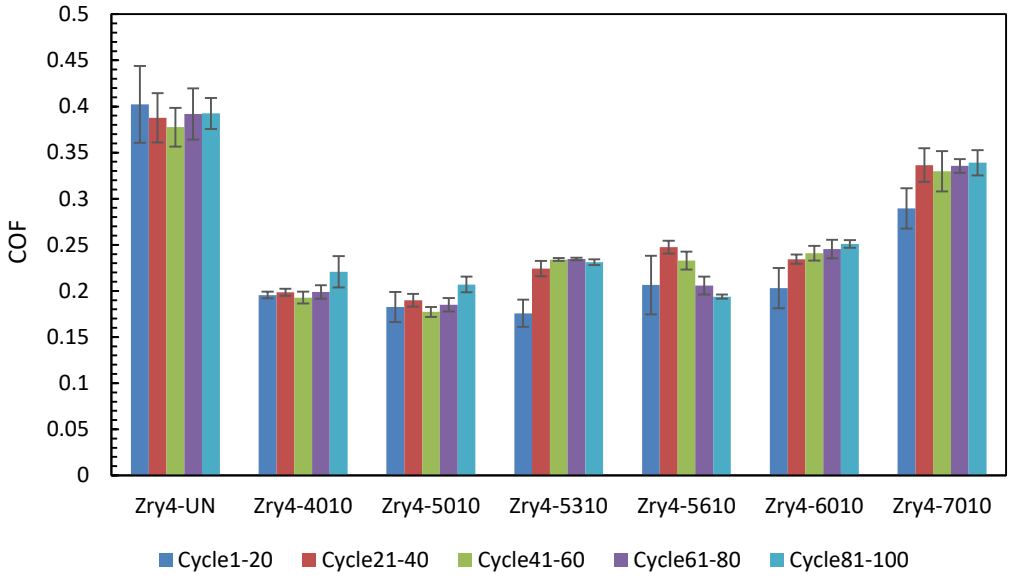


Figure 4.6-4 Measured CoF of untreated and CC treated Zircaloy-4

As it has been mentioned in the experimental section, the wear volume loss of the tested sample was calculated from the 2D profiles of the wear track. Then the wear rates were calculated by dividing the wear volume loss by the normal force. Wear test was carried out on each sample for at least three times. The average value was taken and the standard deviation was used as the error for each sample. The corresponding results are shown in Figure 4.6-5.

It can be seen that all the CC treatments can reduce the wear of Zr702 and Zircaloy-4 alloys reciprocating against a WC/Co ball. However, it is noted that whilst most CC treated samples can significantly reduce the wear rate by thousands of times compared with untreated Zr702 and Zircaloy-4 the low-temperature treated Zr702-4010, Zr702-5010 and Zry4-4010 showed only marginally reduced wear. This is mainly because the modified layers on these samples is too thin, less than 1 μm (Figure 4.2-20), to withstand the wear by the WC counterpart.

It can also be found from Figure 4.6-5 that the wear rates for both Zr702 and Zircaloy-4 samples decreased by increasing the treatment temperature to 530 and 560 ºC for 10 hours but followed by an increasing tendency when further increasing the treatment temperature. More specifically, the wear rate increased with the increasing of ceramic layer thickness provided that it was not worn through during the wear process. Considering the cross sectional layer quality observation mentioned in section 4.2.5.1, the defects as cracks and pores within the oxide layer and at the oxide/substrate interface can decrease the wear combat properties of the CC treated surface. The smallest wear rates of 1.5×10^3 $\mu m^3/N$ and 9.9×10^3 $\mu m^3/N$ have been achieved on Zr702-5310 and Zry4-5010. Therefore, the optimised CC treatment conditions for Zr702 and Zircaloy-4 are 530 °C/10 hours and 500 °C/10 hours respectively.

It can also be noted that Zr702-UN (untreated Zr702) exhibited better wear resistance than Zry4-UN (untreated Zry4-UN), with their wear rate being 5.5×10^6 $\mu m^3/N$ and 8.8×10^6 $\mu m^2/N$ respectively. This is most probably related to the oxidation property of the wear particles generated and accumulated in the wear process. When exposed to air, Zircaloy-4 readily reacts and forms zirconium oxide product quicker than Zr702. The formed zirconium oxide with a high hardness of about 1300 HV can then act as third-body abrasives and accelerate the wear of tested samples.

Comparing the CC treated two alloys, the wear rate of Zr702 is generally smaller than that of Zircaloy-4 with the exception of samples treated under the 5010 condition (i.e. 500 °C for 10 hours), where Zry4-5010 outperformed Zr702-5010 as the ceramic layer on Zr702-5010 was worn through. This is related to the quality of ceramic layer as reported in section 4.2.5.1. In general, the ceramic layer formed on Zr702 alloys is

denser with less porous smoother and harder than that formed on Zircaloy-4 samples when treated at the same CC conditions. However, it should be pointed out that the wear resistance of CC treated surface also depends on the thickness of the oxide layer and the oxygen diffusion zone beneath and hence the load bearing capacity. This is supported by the fact that the oxide layer formed on Zr702-5310 is 1.55 µm, which is much thinner than that (1.67 µm) formed on Zry4-5310 (Figure 4.2-20).

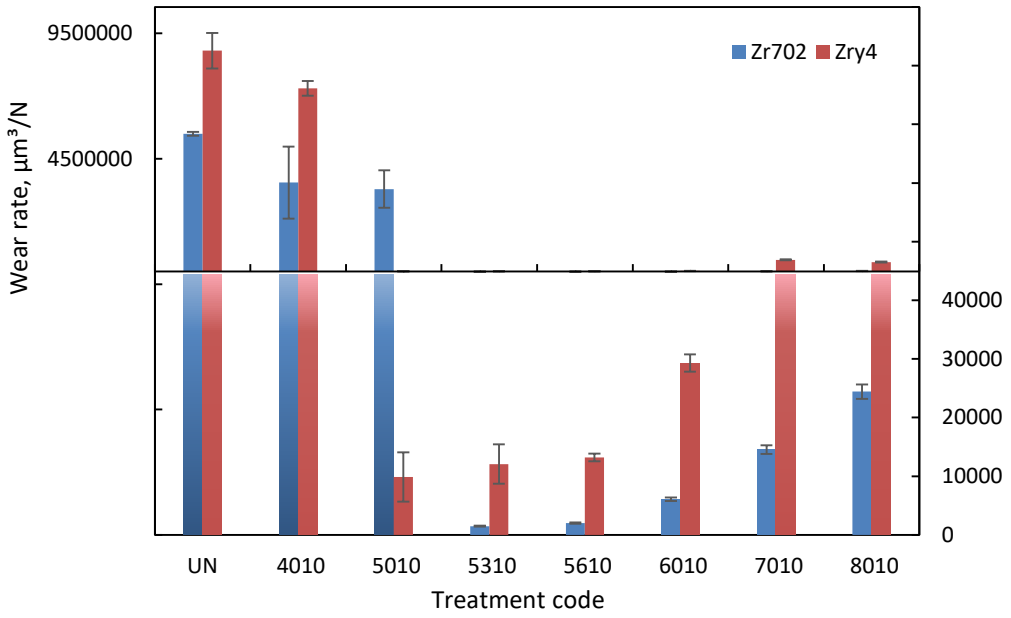


Figure 4.6-5 Wear rate comparision for CC treated samples of Zr702 and Zircaloy-4

Post-test wear morphology observation was carried out under SEM on wear tracks formed on both tested surface of selected samples for wear mechanism analysis. Typical wear track morphologies for Zr702 are shown in Figure 4.6-6.

It can be seen that for the untreated Zr702 the tested surface is rough, with ploughing grooves parallel to sliding directions and adhesive craters (as marked in Figure 4.6-6 (a)), which are typical features for adhesive wear. This can be understood based on the fact that zirconium and its alloys are ductile and chemically active, which lead to the

strong tendency to adhesion. The rupture of these adhesive joints within the weaker zirconium asperities then caused the craters formed on the worn surface. On the other hand, the transferred zirconium becomes work-hardened or even oxidized after a few wear slides, which in turn led to the severe abrasive wear grooves.

In the case of CC treated Zr702 samples, only a mild wear occurred on Zr702-5310, as evidenced by the greatly smoothened worn surface with only a few fine wear grooves (Figure 4.6-6 (b)). This is largely because the hardness of the modified surface is competent with that of WC/Co balls. The asperities in contact would be plastically deformed and even grinded off due to the sliding with the WC/Co counterpart ball, making the worn surface much smoother. However, it can also be seen in the BSE images that there are some vertical ripples (Figure 4.6-6 (d) which are perpendicular to the sliding direction on the wear track. The ripples are formed because of the plastic deformation of the substrate under the modified layer. This is part of the reason for samples to be duplex surface treated.

Severe wear was observed on Zr702-8010, as can be easily seen from the partial spallation of the surface (Figure 4.6-6 (c)). It is worth noting that the spalled area is not across the whole ceramic layer, but only located at the very top surface. As shown in the 2D wear track profile in Figure 4.6-7, the maximum wear track depth, where the surface was spalled as marked Figure 4.6-6 (c) is only 2.0 μm which is much smaller than the oxide thickness (20.5 μm). However, as discussed earlier, a thick oxide layer formed at high temperature contains many lateral cracks parallel to the oxide/substrate interface. Under the tangential fictional force, delamination or spallation of the cracked

oxide layer will occur. Delamination wear may also be caused by nucleation and propagation of microcracks at a subsurface area.

In the case of Zircaloy-4, shown in Figure 4.6-8, wear track on Zry4-UN depicts similar ploughing grooves and adhesive craters as Zr702-UN. For the CC treated samples, one typical image from Zry4-5310 after wear test shows similar smoothed surface as Zr702-5130 samples. However, spallation or delamination occurred to the wear surface on the 700 °C/10 hours treated Zry4-7010 samples. This is in agreement with the cross section observation of treated samples where Zircaloy-4 exhibited higher oxidation rates than Zr702 when treated at the same conditions.

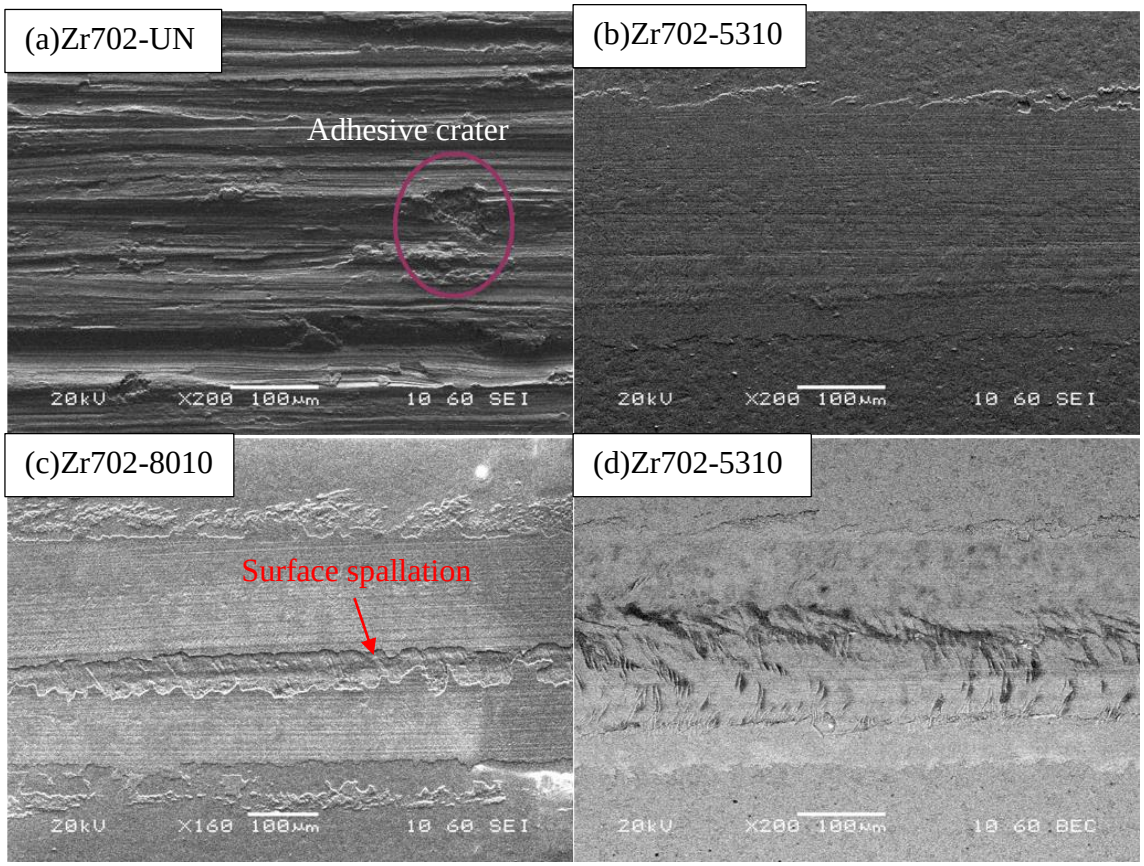


Figure 4.6-6 SEM images of typical wear tracks of CC treated Zr702 samples

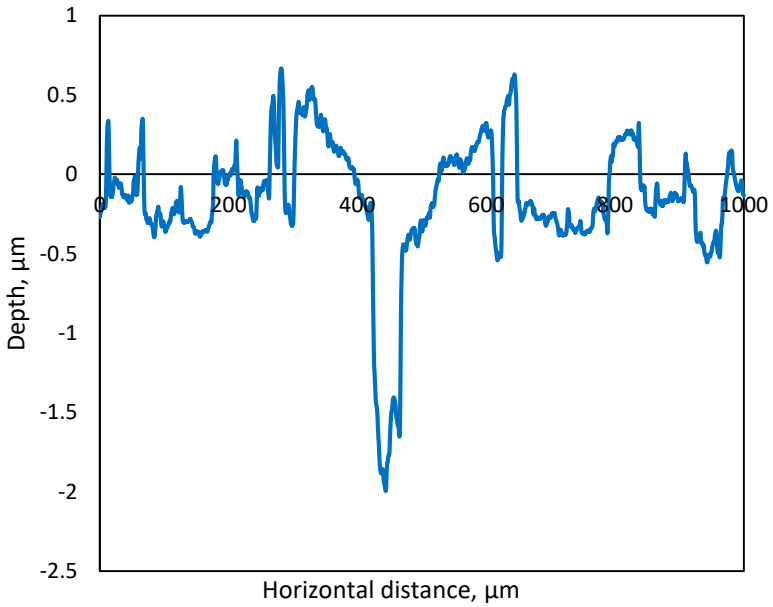


Figure 4.6-7 2D wear track profile of CC treated sample Zr702-8010

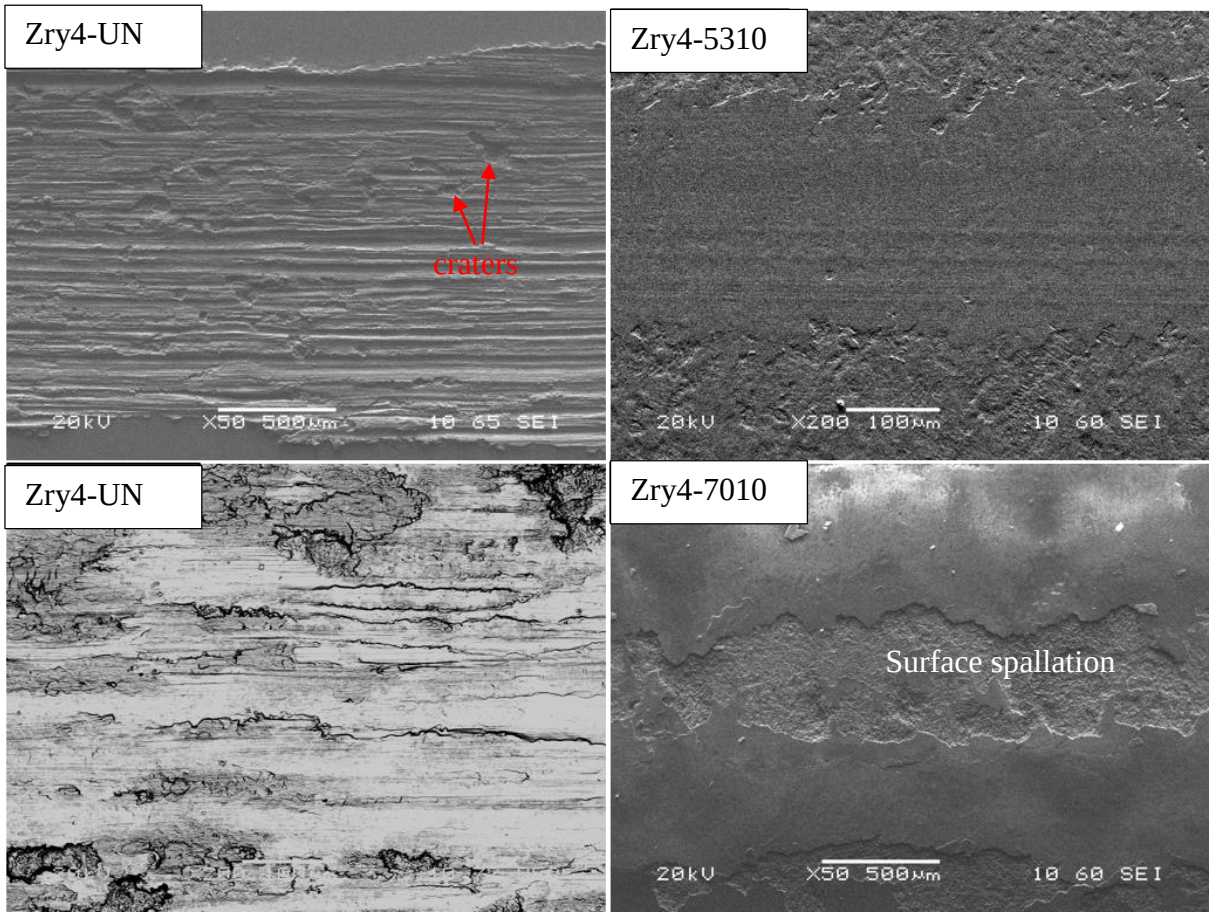


Figure 4.6-8 SEM images of typical wear tracks of CC treated Zircaloy-4 samples

4.6.1.2 Duplex treated samples

Similar to CC treated samples, CoF was also measured and recorded for duplex surface treated samples. The results are shown in Figure 4.6-9.

As aforementioned in section 4.6.1.1, the CoF of sample CC7 (i.e. Zr702-7010) increased gradually from 0.20 to 0.63 with the CoF test process going on. After OBD treatment, it can be clearly seen from Figure 4.6-9 that the OBD samples (excluding CC7-8030) showed a decreased and steady CoF value of about 0.17. This must be related to the change of ceramic layer property during the OBD treatment, which is to be discussed in section 5.5. CC7-8030 showed a comparable but much scattered CoF values, which is due to the lack of ceramic layer protection of the oxygen diffusion zone.

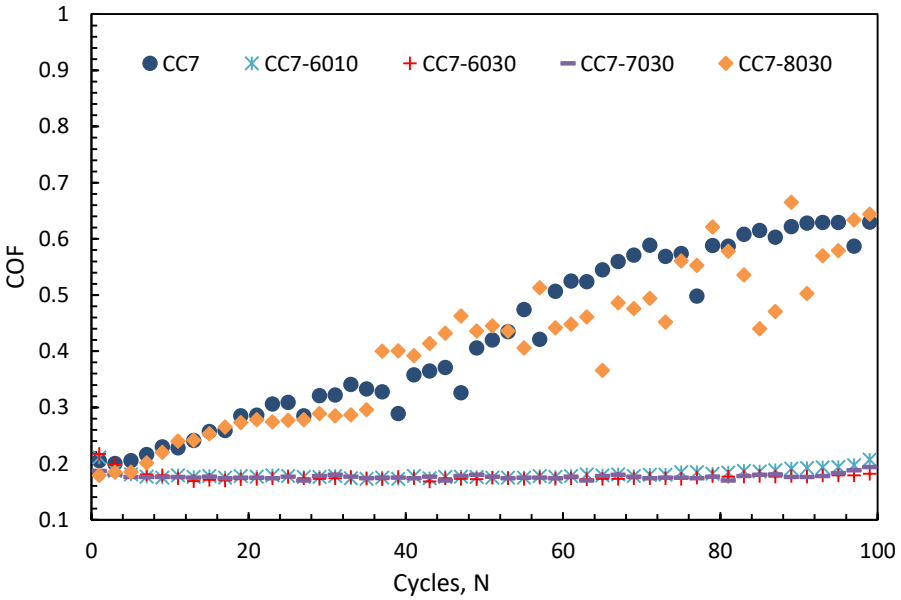


Figure 4.6-9 CoF comparison of duplex surface treated samples

Wear rate of duplex surface treated samples are depicted in Figure 4.6-10. As it shows, sample CC7 exhibited a wear rate of 14550 $\mu m^3/N$, which is dramatic decreased compared with the Zr702-UN (5.5×10^6 $\mu m^3/N$). After the OBD treatment, samples

exhibited a further decrease of wear rate, which means a further improvement of the wear resistant property.

The wear rate decreased with increasing the treatment time at 600 °C as evidenced by the comparison between CC7-6010 and CC7-6030, which showed a wear rate of 10500 $\mu m^3/N$ and 6500 $\mu m^3/N$ respectively. With temperature increasing from 600 °C to 700 °C for a fixed 30 hours of OBD treatment the wear resistance of the surface showed a slightly increased average wear volume loss from 6500 $\mu m^3/N$ for CC7-6030 to 7200 $\mu m^3/N$ for CC7-7030. Further increasing OBD treatment temperature to 800 °C vastly reduced the wear performance of the surface, which is due to the change of the composition and structure of the modified layer. As shown in Section 4.3.1 (Figure 4.3-6) the modified surface of sample CC7-8030 is hard, brittle and cracked with almost no oxide layer although a thick diffusion zone of about 300 μm is formed. When opposed to the counterpart ball at the wear test condition, wear debris can be easily formed and the accumulated wear debris would be further oxidized, thus accelerating the wear process.

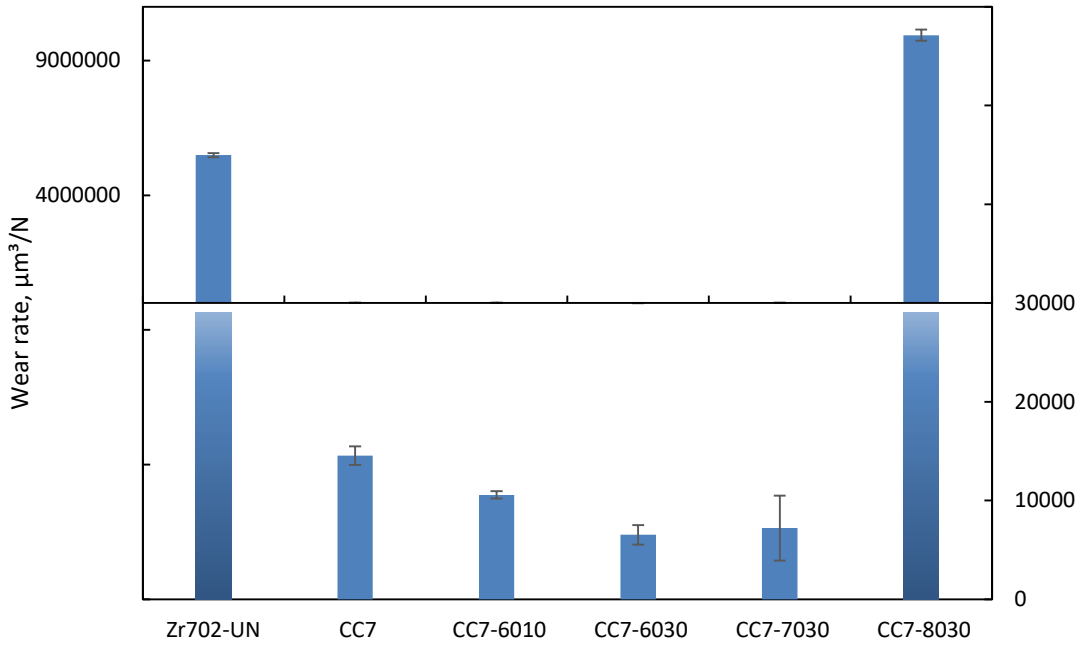


Figure 4.6-10 Wear volume loss comparison of duplex surface treated samples

Wear track observation showed three different wear tracks on the duplex treated samples and the typical SEM micrographs are shown in Figure 4.6-11 ~ Figure 4.6-13.

As illustrated in Figure 4.6-11 (a), a typical wear track formed on sample CC7-6010 indicates that plastic deformation, ploughing and cracking are major wear mechanisms throughout the test. The plastic deformation is attributed to the large shear stress acting on the tested surface. This comes from the smearing of wear debris, considering that the smearing grooves observed on the counterpart ball as well (Figure 4.6-11 (d)). EDX analysis of the wear debris shows a composition of mainly Zr and O, which is zirconium oxide worn out from the very surface of tested CC7-6010 sample.

Clear cracking patterns at both sides of the wear track which are perpendicular to the sliding direction are observed as shown in Figure 4.6-11 (b). This is because of the

brittleness of the very top surface of the modified layer. On the other hand, microcracks at the central area of the wear track is noticed.

Wear track morphology observed from sample CC7-7030 is shown in Figure 4.6-12 reveals only mild smear of the wear tested area. No clear microcracks on the wear tracks are observed. This is the reason why CC7-7030 demonstrated the best anti-wear performance among duplex treated samples with the consideration of the decreased ceramic layer thickness (7.7 μm as shown in Table 4.3-1).

In the case of CC7-8030, the main wear mechanisms are adhesive wear and wear debris induced abrasive wear, and the adhesive craters and deep ploughing grooves are observed in the wear track images shown in Figure 4.6-13. The zirconium patches observed on the counterpart ball, shown in Figure 4.6-13 (d), are also strong indications of adhesion. Along the wear track edges, beach-like craters (Figure 4.6-13 (c)) are observed because of the strong adhesion between the Zr(O) and the WC/Co ball within the dry sliding test. It is also interesting to note that the wear performance of CC7-8030 is even worse than Zr702-UN. This could be partially attributed to the brittle and cracked surface (Figure 4.3-6) and partially attributed the interstitial oxygen existed in the oxygen diffusion zone. The high level oxygen makes it easy for the wear debris to be oxidised to zirconia, which could act as hard abrasives, thus accelerating the wear process. Furthermore, the enlarged grain size of zirconium matrix is believed to be another factor that contributes to the increased wear volume loss through grain pull-out[197].

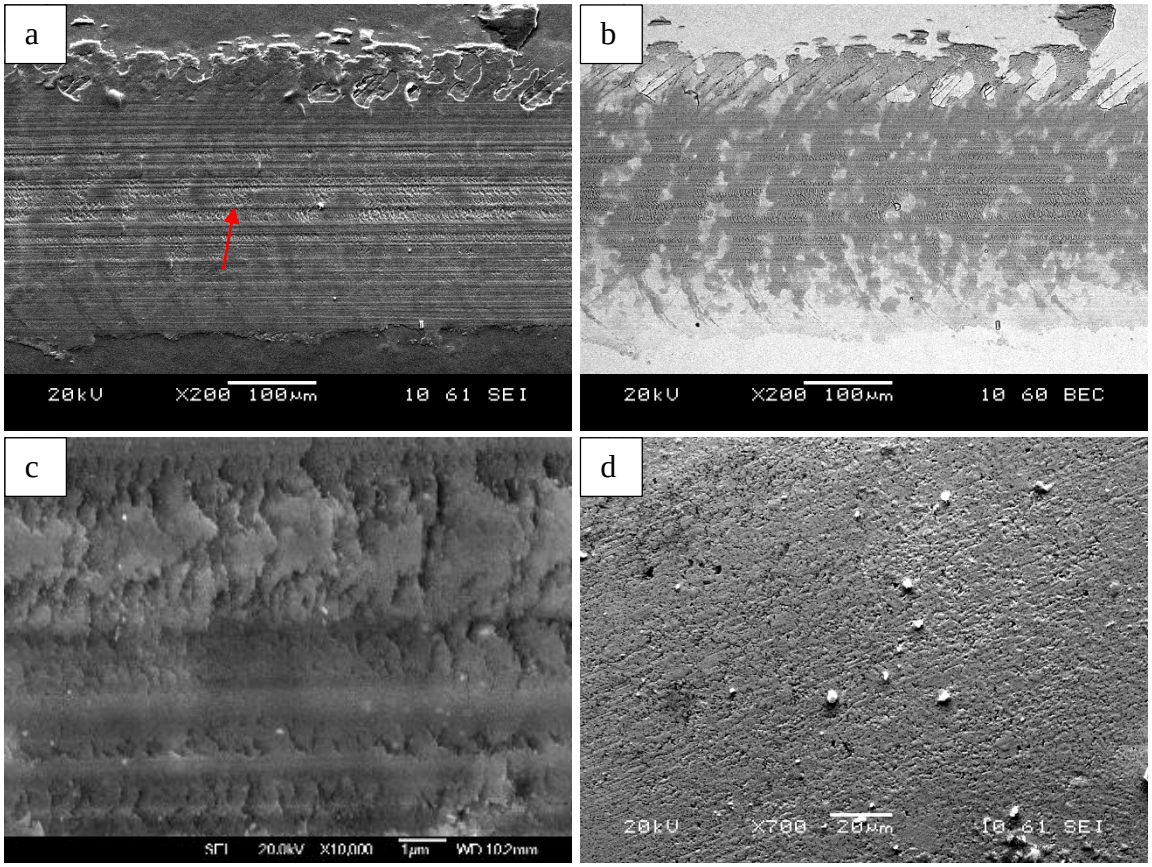


Figure 4.6-11 SEM images of tested sample CC7-6010 (a): wear track, SE, showing abrasive wear grooves; (b) wear track, BSE, showing vertical crack at wear track edges; (c) zoomed in image of arrow mark area in (a), showing the microcracks at inside the wear groove; (d) WC counterpart ball, showing the wear scratches.

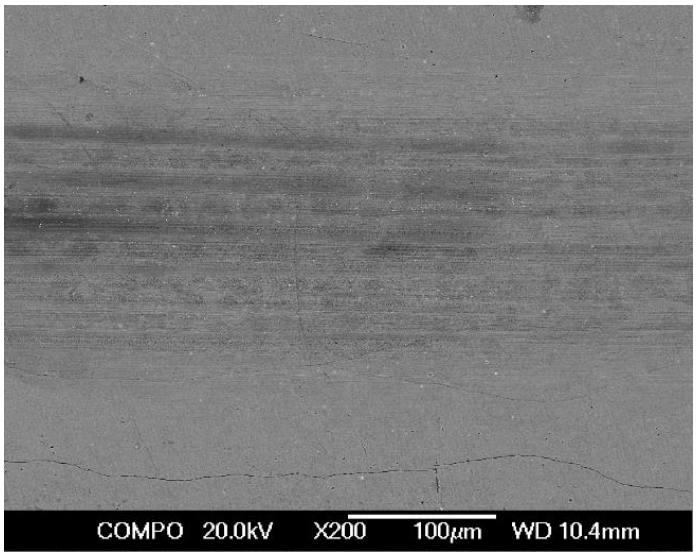


Figure 4.6-12 SEM images of wear track of sample CC7-7030

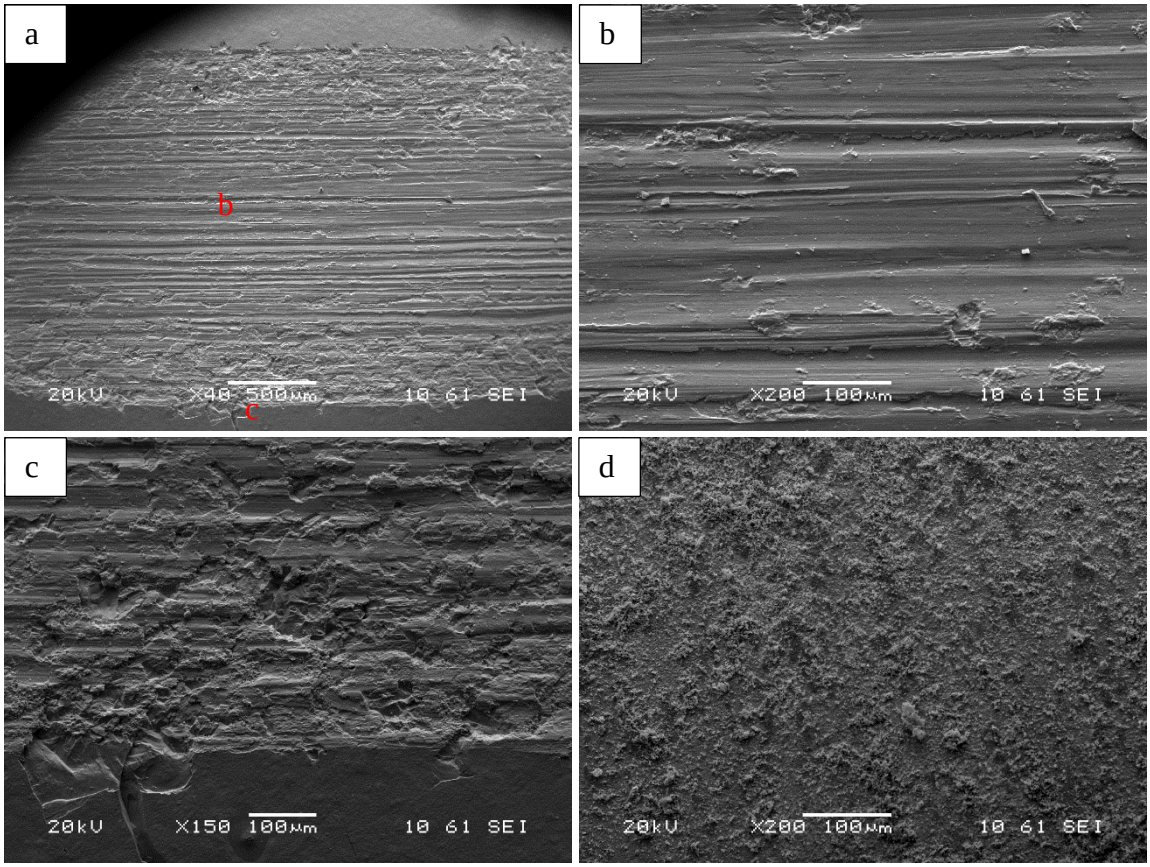


Figure 4.6-13 SEM images of tested CC7-8030: (a) wear track; (b) and (c) marked area in image (a), showing wear grooves and adhesive craters characteristics on the wear track (d) WC ball surfaces, (especially at the edge of the track track) with the of zirconium wear patches.

4.6.2 Fretting test

As mentioned earlier in the experimental section 3.3.4.4, fretting test was carried out on CC treated nuclear grade Zry4-5310 sample in comparison with the as-received Zircaloy-4 alloy in order to study its response to fretting damages due to the wide application of Zircaloy-4 alloy in the nuclear industry where fretting is encountered. The as-received Zirclaoy-4 and CC treated Zry4-5310 are noted as untreated and treated respectively from here afterwards. The relevant fretting test results are presented in this section.

4.6.2.1 Friction coefficients and fretting wear volume losses of tested samples

Figure 4.6-14 depicts the evolution of coefficient of friction (CoF) of both the treated and untreated samples in different lubrication conditions. It can be seen that the CoF of the samples tested in 3.5 wt% NaCl and DI water first increased gradually with the fretting test cycles until a relatively steady value. Therefore, the whole fretting test period could be divided into two stages: running-in stage and stable stage. It took about 1000 and 2000 cycles to reach the stable stage when both the treated and untreated nuclear grade Zirclaoy-4 alloy were tested in 3.5 wt% NaCl and DI water respectively . The steady CoF measured for the untreated sample is about 0.30 and 0.20 in DI water and 3.5 wt% NaCl solution respectively; while it is about 0.50 and 0.42 for the treated samples accordingly.

The following observations could be noticed by comparing the CoF shown in Figure 4.6-14. Firstly, the CoF values for both the treated and untreated materials are lower when samples are measured in 3.5 wt% NaCl solution than in DI water. Secondly, the CoF for the treated sample is higher than that of the untreated materials when tested in both solutions used. This is the opposite to the CoF results reported in section 4.6.1.1 where reduced CoF by the CC treatment is demonstrated during reciprocating sliding tests. This is because CoF is not an intrinsic property of a material but rather a function of test conditions including the load, counterpart, the mode of relative movement, speed, frequency, amplitude, lubrication and environment (temperature, humidity etc.).

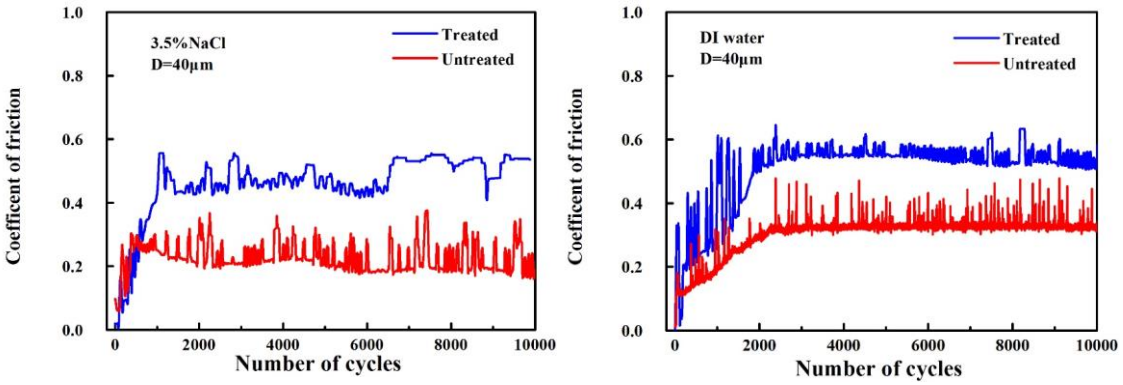


Figure 4.6-14 Friction coefficient of treated and untreated samples at fretting amplitude of 40 μm: in solution (a) 3.5 % NaCl; (b) DI water.

Figure 4.6-15 demonstrates the force vs. displacement (F-D) records when treated and untreated samples were tested in different solutions at 1000 and 10000 cycles. It can be seen that in general the F-D loops for different test conditions for both samples exhibited a parallelogram shape, which corresponds to the gloss slip regime (see Figure 2.2-15) of fretting wear. The shape of the parallelogram is known to be related with the full slip and partial slip (as marked in Figure 4.6-15) period[198]. Hence, while both treated and untreated sample behaved in a similar partial and full slip in DI water, the untreated sample endured more full slip than the treated sample in 3.5 wt% NaCl.

In order to quantitatively investigate the effect of the ceramic layer formation on Zircaloy-4 sample, the wear volume loss during the fretting test was quantified. They were calculated from the whole fretting scars on the tested sample instead of from the cross section as in the previous reciprocating wear test due to the shape and depth of the wear scars. The results are presented in Figure 4.6-16.

It can be seen that the wear volume loss of untreated and treated sample is 140 μm^3 and 7.5 μm^3 respectively in 3.5 wt% NaCl solution while it is 138 $\times 10^3$ μm^3 and 7.2 $\times 10^3$ μm^3 in DI water accordingly. Evidenced by the dramatically reduced wear volume loss

of Zircaloy-4 alloy by the CC treatment it can be concluded that the introduction of the ceramic layer formed during the CC treatment can significantly increase the anti-fretting property of Zircaloy-4 alloy. Meanwhile it can also be noted that the addition of NaCl solute to the water solution can marginally increase the fretting wear of both treated and untreated Zircaloy-4 alloy samples for 2×10^3 μm^3 and 0.5×10^3 μm^3 respectively.

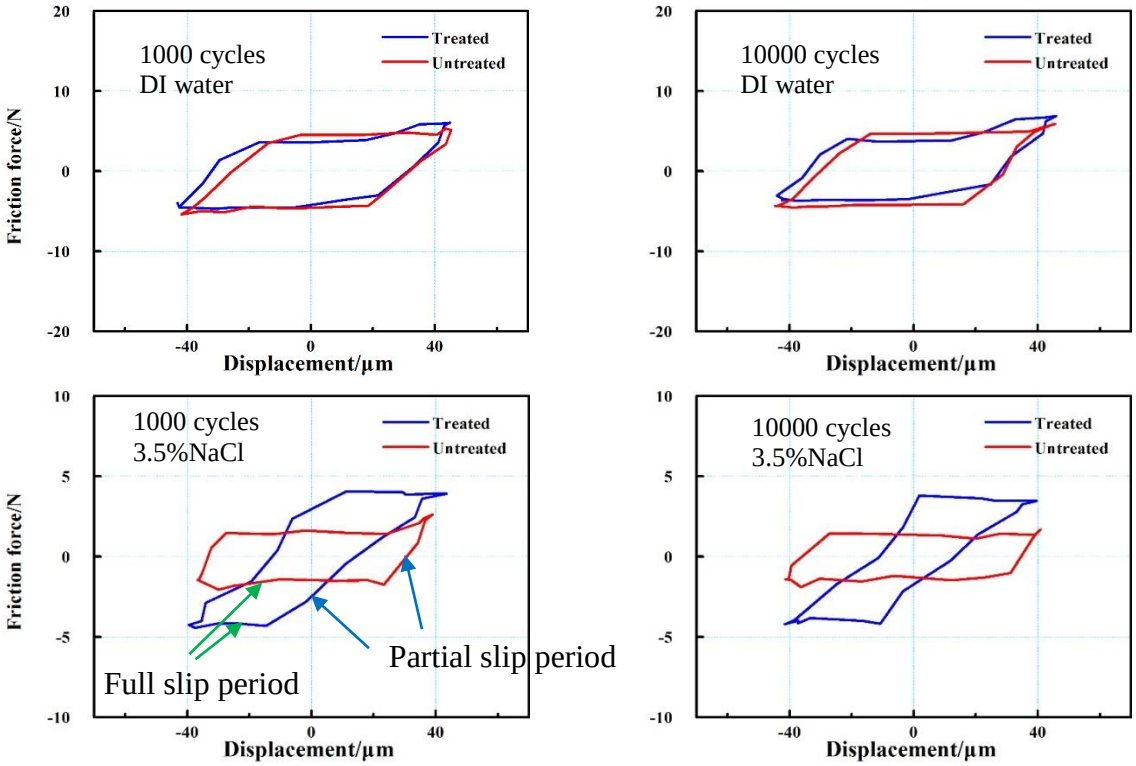


Figure 4.6-15 F-D loops at cycle 1000 and 10000 showing consistent gloss slip regime for different fretting test conditions of both untreated and treated samples

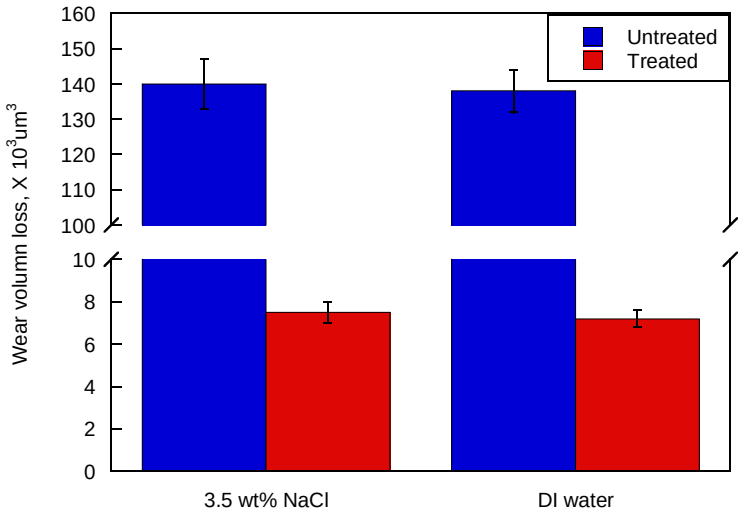


Figure 4.6-16 Wear volume loss of tested samples during the fretting test

4.6.2.2 Post fretting observation

Post fretting observation of the fretting scars was carried out under optical microscopy and some representative images are given in Figure 4.6-17, where (a) and (c) show the fretting scar of untreated samples in DI water and 3.5 wt% NaCl respectively, while (b) and (d) are for the treated samples accordingly. Figure 4.6-18 demonstrates the 2D fretting scar observation under confocal microscopy showing the scar contouring, while Figure 4.6-19 exhibits the 2D wear track profiles along the direction perpendicular to the fretting scars under different test conditions as labelled to present the scar depth more clearly.

As it can be clearly noticed from Figure 4.6-17, after CC treatment the fretting scar became significantly smaller on treated sample tested under both conditions when compared with that of the untreated sample. This is in good agreement with the wear volume measurement.

It is also found that on the fretting scar of untreated sample (Figure 4.6-17 (a) and (c)) black spots are clearly noticed, which correspond to the deeper craters shown in the confocal microscopy images (Figure 4.6-18 (b) and (d)). This is a clear sign for the galling craters where zirconium batches were pulled out from the sample surface during the fretting test. These craters observed on untreated sample in DI water are generally deeper (about -6 μm) than that in 3.5 wt% NaCl (about -3 μm) as more clearly shown in the wear depth profiles of the fretting scars (Figure 4.6-19). Hence, even though only little difference (2×10^3 μm^3 and 0.5×10^3 μm^3 in 3.5 wt% NaCl and DI water respectively) was shown in terms of the fretting wear volume loss as mentioned in section 4.6.2.1, the NaCl solution in the 3.5 wt% NaCl solution has more effect on the localised fretting scar depth coming from the corrosion acceleration oxidation effect, where the active tribosurface of tested samples was generally more easily to be oxidized and the newly oxidized surface prevented further galling of zirconium. Therefore, instead of a detrimental effect, the NaCl would reduce the localised fretting galling of untreated sample.

On the fretting scars from the treated sample in both DI water and 3.5 wt% NaCl solutions (Figure 4.6-17 (b) and (d)), fretting wear scratches parallel to the fretting direction were observed. Similar to those mentioned in the reciprocating wear track in section 4.6.1, these scratches came from the fretting abrasion between the hardness comparable tested sample and WC/Co counterpart balls. Meanwhile, it can also be seen from Figure 4.6-19 that the wear depths of the fretting scars about the same when tested in DI water and in 3.5 wt% NaCl. No clear wear/galling craters were noticed on the CC treated samples. Hence, no clear evidence was shown on the effect of the lubrications between 3.5 wt% NaCl and DI water on treated samples.

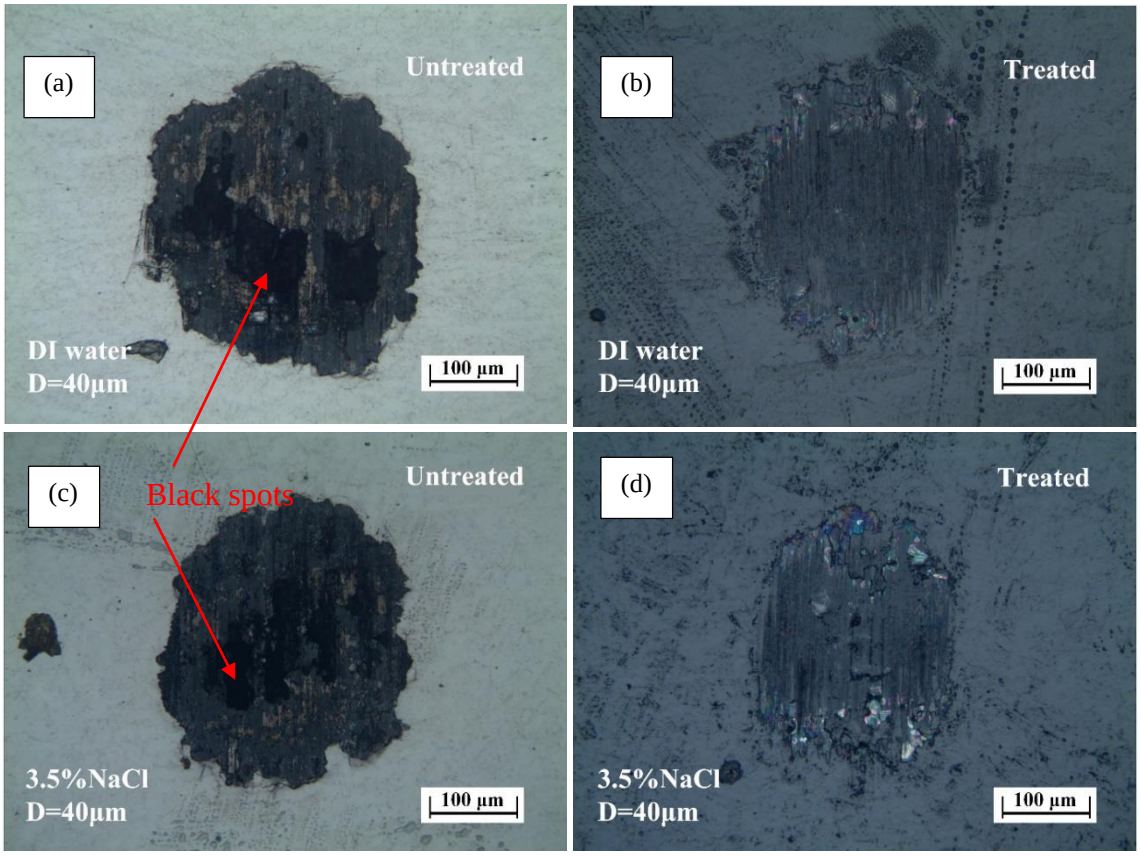


Figure 4.6-17 Microscopy observation of fretting scars at different test conditions as marked on each images

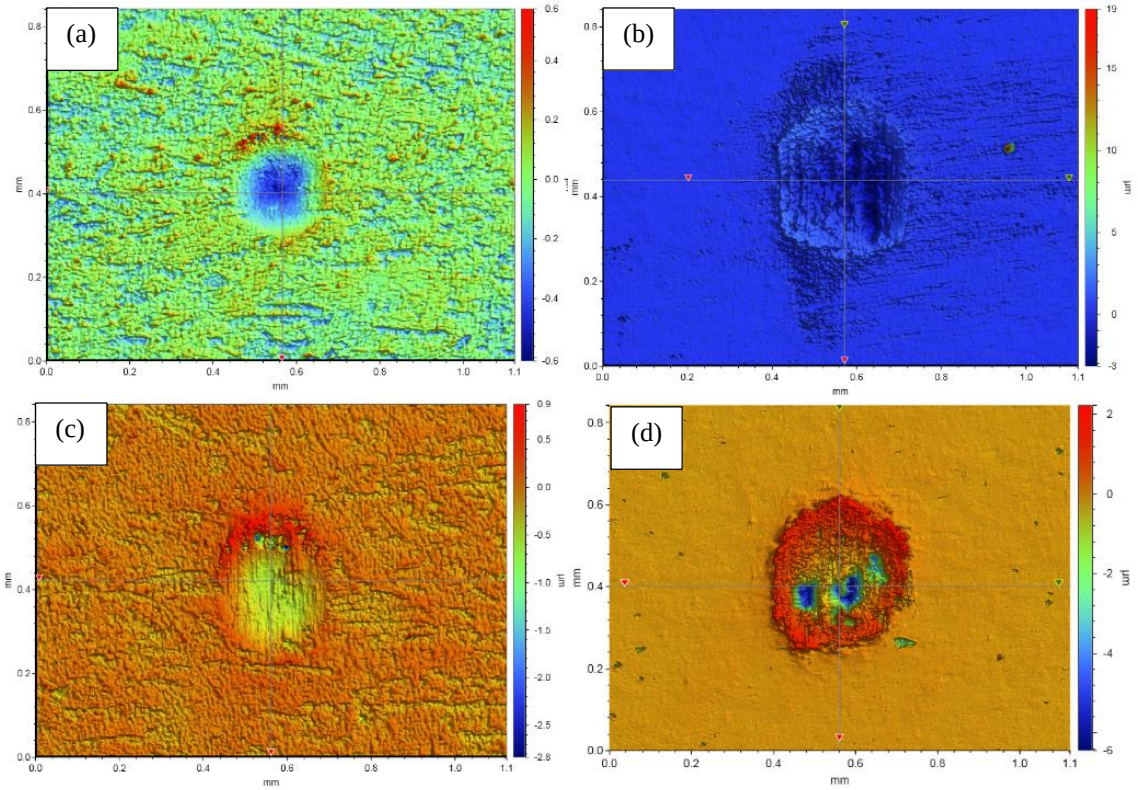


Figure 4.6-18 2D wear track observation at amplitude 40μm: (a) treated sample at 3.5 wt% NaCl; (b) untreated sample at 3.5 wt% NaCl; (c) treated sample at DI water; (d) untreated sample at DI water.

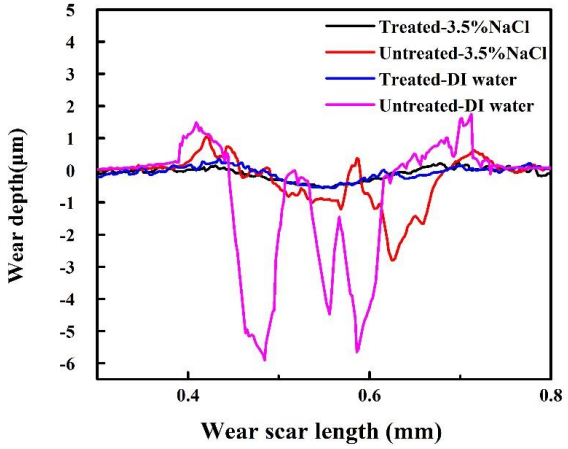


Figure 4.6-19 2D wear track depth profiles at the fretting scars at tested conditions

5 DISCUSSION

5.1 Microstructure of ceramic layer

5.1.1 Surface morphology

Although zirconia ceramic has long reported to have a tooth colour[199], as it has been reported Section 4.2.1, the oxide films formed on Zr702 and Zircaloy-4 alloys have revealed different visual colours under the treatment conditions used in this study. This ranges from the blueish colour of Zr702-4010, through the dark grey/black colour for most treated samples to the beige colour: beige blister (Zr702-7010 and Zr702-8010), beige batches (Zry4-6010, Zry4-6020, Zry4-6030 and Zry4-7010) and the full beige colour for Zry4-8010.

The varying surface colour has been observed during the oxidation of zirconium alloys in different atmospheres (e.g. air, oxygen, water and steam) and/or at different temperatures. The thickness of oxide film formed on zirconium alloys is thought to be contributed to the different surface colours formed on the treated samples, and indeed based on this relationship, the variation in colour could even be used as a method of oxide film thickness measurement[200, 201].

Combining Figure 4.2-20 with Figure 4.2-24 in Section 4.2.5.1 which depict the ceramic layer thickness as a function of different treatment conditions, it can be summarize that when the oxide thickness is less than 0.6 μm, the oxide layer is blueish coloured; when it is in the range between 0.6 μm and about 5 μm, the surface is dark black; and if it reaches to 5 μm or above, a beige blistered or patched surface is exhibited depending on the zirconium alloy composition. This is in line with the

findings by previous researchers [159] where anodized zirconium surface changed to gold, red, then green, blue and black when the thickness increases. Meanwhile, surface colour change from black to beige also implies an oxidation kinetics change, where the reaction order increased from parabolic to linear (see discussion in Section 5.2).

The reason for the observed colour variation after the oxidation of Zr and its alloys has also been attributed to the Zr/O ratio in the oxide layer. A lack of sufficient oxygen (i.e. non-stoichiometric) in zirconia can cause the dark colour (black, grey, brown) of zirconia thin films [202]. This blue to black colour change [203] depends on the zirconium and oxygen concentration in the oxidized alloy and process conditions: a low oxygen concentration (i.e. a high concentration of substrate zirconium) in the oxidized surface will generate a colour towards blue due to its non-stoichiometric nature and fully stoichiometric zirconia is beige coloured.

More recently, there has been further research by P. Tejland et al.[204] using spectrophotometry into the black coloured oxide formed on Zircaloy-2 alloys. This has revealed the excitation of localised surface plasmon (LSP) resonances in the metallic particles inside the oxide layer. A LSP is the result of the confinement of a surface plasmon in a nanoparticle size comparable or smaller than the wavelength of light used to excite plasmon[205]. Therefore, it follows that the beige colour is the overall effect coming from the un-oxidized nanoparticles and the lateral cracks throughout the ceramic layer formed at relatively high temperatures.

This is in consistent with the results from previous researches[206] and from the present work. This is evidenced by which the formation of cracks perpendicular to substrate especially (Figure 4.2-19 (f)).

5.1.2 Phases evolution

As reported in Section 4.2.4 and 4.2.5.2, static XRD and TEM phase identification have revealed that the ceramic layer formed during CC treatment is mainly made up of monoclinic zirconia together with traces of tetragonal zirconia. Dynamic XRD scan results also have shown some peaks from tetragonal zirconia phase for both Zr702 and Zircaloy-4 alloys. Those observations are in agreement with some precious researches [130, 188, 206-208] although there should not be tetragonal zirconia at room temperature according to the phase diagram (Figure 2.3-1). However, the formation mechanism of tetragonal phase has been a topic for debate. Godlewski et al.[209-211] attributed the stabilisation of tetragonal zirconia phase at room temperature to the compressive stress. However, earlier research also showed that the metastable tetragonal zirconia phase could exist at room temperature due to the crystallize size effect, and the critical size was found to be about 10 ~ 40 nm [212, 213].

Despite the fact that t-ZrO_2 has been detected in other researches and in this study, there is a discrepancy in its amount reported in the literature [207] and experimentally measured in this investigation. In the present research only a small proportion of t-ZrO_2 could be detected in the CC treated alloys at room temperature. However, Motta et al. [118] found out that the tetragonal phase fraction varied from 4-15% throughout the oxide film formed on Zircaloy-4 alloy using micro-beam synchrotron radiation. *In situ* XRD analysis by Petigny et al.[133] also revealed a tetragonal phase fraction up to 14% at the metal/oxide interface. But no strong peaks for t-ZrO_2 phase were detected from the dynamic X-ray test in this study.

However, decreasing tendency of the tetragonal phase fraction on the treated zirconium sample with increasing exposure time has been noticed for the *in situ* XRD

measurement especially on Zr702 alloy (Figure 4.2-17), which suggests that a phase transformation from t-ZrO_2 to m-ZrO_2 may have occurred inside the formed layer during the process. This diffusionless martensitic phase transformation is accompanied with a volume increase, which is hence believed to be the cause for the formation of cracks and porosity in the ceramic layer.

The potential reasons why a relatively low portion of tetragonal phase is identified by XRD (both static and dynamic) and TEM are as follows: (a) static XRD and TEM techniques are used at room temperature, and there is t-ZrO_2 → m-ZrO_2 transformation occurring during the cooling process; (b) X-ray analysis during the CC treatment, i.e. dynamic (*in situ*) test, only measured the phase constituent near the sample surface where the stress has already been relaxed; (c) the TEM technique which measures directly the phase constituent of the metal/oxide interface, is carried out on the sample that has been thinned to a thickness of less than 50 μm and hence the residual stress is almost fully relaxed during the sample preparation process.

In addition, the dynamic XRD test carried out in this project has also revealed shifted diffraction peaks as well as a new peak at position 2θ 43.3 °, which could be indexed to $ZrO_{0.27}$. This is mainly because when the surface starts to be oxidized, the formed ceramic layer is very thin so that the X-ray can penetrate through the thin oxide layer and detect the interface phase composition. This is a similar case for thin film formed at some treatment conditions e.g. Zr702-4010, Zry4-4010 and etc., as well as metal/oxide interface only that the XRD detection was carried out at room temperature. However, TEM characterisation clearly showed the SAD diffraction pattern from $[2\bar{1}\bar{1}0]_{ZrO0.27}$ (Figure 4.2-26 (c)).

The formation of CC treated surface can be deduced based on the discussions above. The diffusion of the oxygen atoms into the zirconium substrate firstly forms a zirconium-oxygen solid solution (denoted as Zr(O)), which gradually reaches a saturation state where the oxygen atomic concentration is 29 % as shown in zirconium-oxygen phase diagram in Figure 2.3-1. Then, the saturated solid solution transfers to $ZrO_{0.27}$ when oxygen further diffuses in as evidenced by SAD diffraction patterns from the interface (Figure 4.2-26 (c) and Figure 4.2-28 (b)). Therefore, the interface, where the zirconium and oxygen reaction takes place, consists of the un-oxidized metal zirconium and hexagonal $ZrO_{0.27}$. Finally, ZrO_2 (both tetragonal and monoclinic) is formed as more oxygen diffuses in. Allotropic transformation from the metastable t-ZrO_2 to more stable m-ZrO_2 occurs when cooling from the treatment temperature after the ceramic conversion treatment, which leads to a volume expansion of up to 5 %. Hence, the resistance to the phase transformation from t-ZrO_2 to m-ZrO_2 decreases with the distance away from the metal/oxide interface due to the gradually reduced constraint towards the surface. This also explains the decreasing trend of t-ZrO_2 phase fraction from the metal/oxide interface to the surface.

5.1.3 Structure

Layer microstructure on samples without generating periodic lateral cracks (therefore Zry4-7010 and Zry4-8010 exclusive) can be generally divided into three sublayers: surface oxide layer, metal/oxide interface, substrate.

The surface layer, where the sample in contact with the outside environment directly, is generally made up of zirconium oxides in terms of phase composition, which could be mainly m-ZrO_2 with traces of t-ZrO_2 as discussed earlier in Section 5.1.2. The typical cross section TEM image in Figure 4.2-26 has shown a columnar microstructure with

longitudinal grains perpendicular to the metal/oxide interface for samples treated under certain treatment conditions. The development of such longitudinal grains is oxide layer thickness dependent though. For example, the CC formed oxide layer is relatively thin when samples are treated at temperatures below 500 °C and the grain structure cannot be easily recognised. A growth from small grains to long columnar gains is therefore believed to happen during such surface treatments.

At the metal/oxide interface, as has been discussed in Section 5.1.2, the transition from zirconium substrate to suboxide $ZrO_{0.27}$ occurs. The revealed grain structure is a prolate long grain which is thinner in Zircaloy-4 samples than that in Zr702 (Figure 4.2-25 (b) and Figure 4.2-2 (a). As evidenced in Figure 4.2-26 (c), suboxide $ZrO_{0.27}$ has been successfully identified from the SAD pattern from the interface layer. This is further confirmed by the preferred orientation of a metal/oxide front $ZrO_{0.27}$ grain to the substrate Zr: $[2\bar{1}\bar{1}0]_{ZrO_{0.27}}//[0001]_{Zr}$, $(0002)//(\bar{1}010)$.

As reported in SEM observations in section 4.2.5, cracks and porosity have been observed in the oxide layer close to the metal/oxide interface in some treated samples. Further study of the cracks has revealed fine equiaxed grains of about 80 nm in size, as shown in Figure 5.1-1. Earlier researches showed the preference of equiaxed grains at the crack area to be t-ZrO_2 [214, 215].

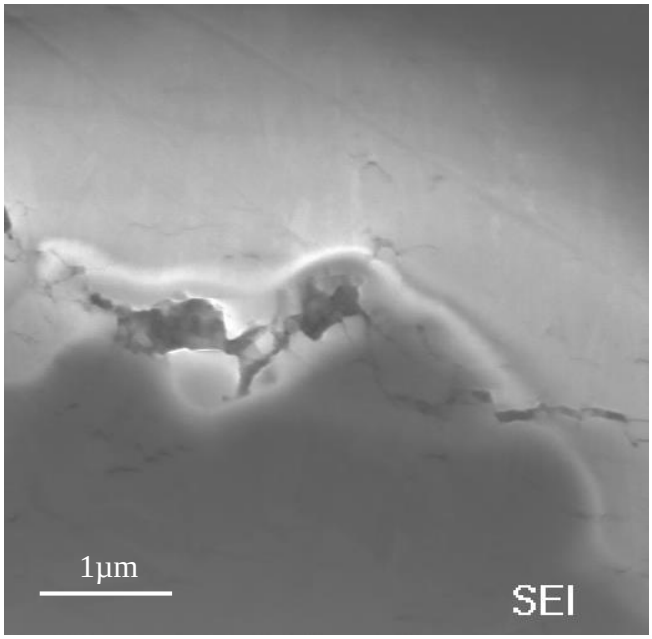


Figure 5.1-1 SEM observation on cracks showing equiaxed grains in the crack area with grain size of about 80nm

5.1.4 Cracks

In this research, it has been found that the occurrence of cracks is generally located at the area close to metal/oxide interface. This may seem contradictory to some previous work which reported a dense and porous-free inner layer and an outer layer with lots of cracks [206, 215, 216]. This seemingly contradiction could be caused by the difference in the observation scales. It can be seen from Figure 5.1-2 that they observed a fracture surface under a relatively low magnification whilst the SEM observation of the layer structures formed during CC treatment was carried out on metallographic surface under a relatively high magnification. Therefore, these micro-cracks in this study are too small to be observed under such a low magnification they used.

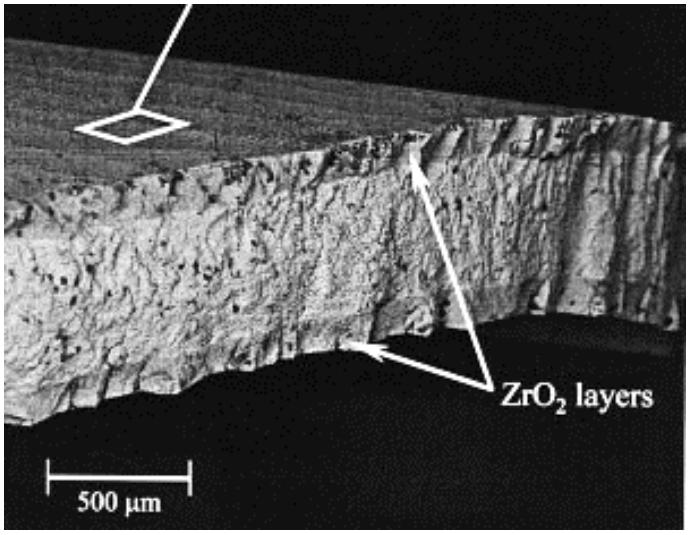


Figure 5.1-2 SEM graph of a fractured Zircaloy-4 sample with an oxide layer of about 120 μm[206]

It has been generally agreed that the observed cracks are related to the high compressive stress existing in the oxide layer. However, it is a topic for debate how the residual compressive stress is developed. Some researchers believe that this stress is attributed to the high Pilling-Bedworth ratio of about 1.56; others think it comes from the allotropic transformation from t-ZrO_2 to m-ZrO_2. This is a martensitic transformation accompanied by a volumetric expansion of up to 5% and therefore generates a compressive stress around the formed m-ZrO_2. In addition, previous experimental observations also have shown that the transition from columnar to fine equiaxed gains is generally accompanied by the appearing of cracks[214, 215].

Another phenomenon that has been noticed is that the cracks are observed to be accompanied by a localised thinning of the oxide film, for example Figure 4.2-18 and Figure 5.1-1 etc. This suggests a depletion of oxygen around the crack areas; otherwise the oxide film would be thickened from a kinetics point of view. Therefore, the reason

coming from the Pilling-Bedworth ratio cannot stand as it is an oxygen concentration increasing process.

The results of EDX composition line scan across the cracked area are shown in Figure 5.1-3. No alloying element peak is detected other than a silicon (Si) peak which could come from the liquid used for sample polishing. Hence, it seems that the formation of the cracks has nothing to do with the possible second phases inside the zirconium matrix. Hence, it is reasonable to deduce that these microcracks are caused by the zirconia allotropic transformation induced volume expansion.

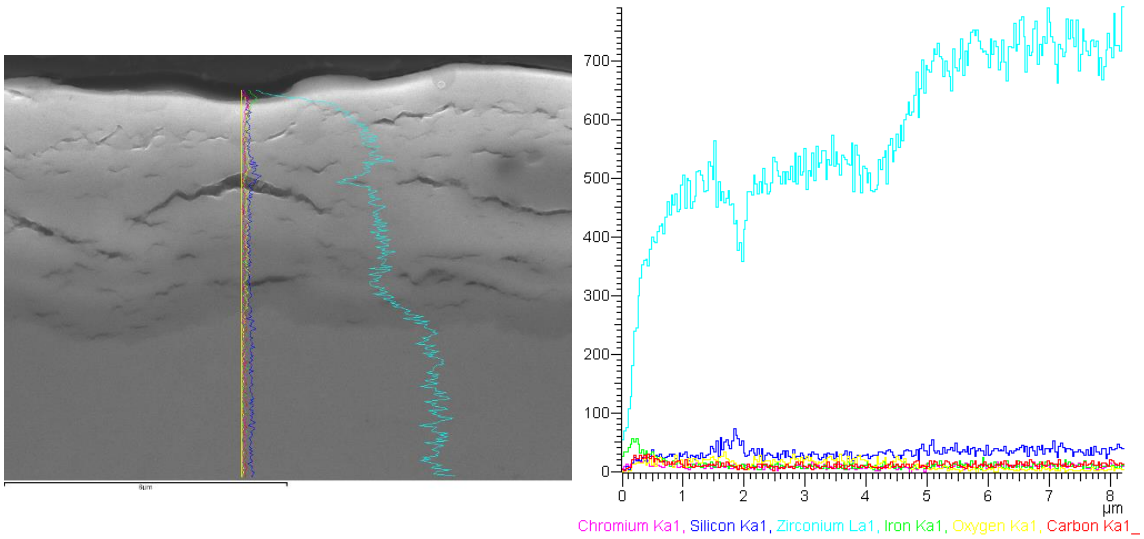


Figure 5.1-3 Typical EDX analysis across crack formed at modified ceramic layer, showing a silicon peak at the cracking area which comes from the polishing liquid

However, it still cannot explain why the cracks are generally parallel to the metal/oxide interface. One possible reason for the preferred orientation of the cracks – parallel to the oxide/substrate interface could be explained by considering the stress development associated with the zirconia allotropic transformation. As discussed above, this phase transformation will introduce up to 5% volume expansion. However, the expansion

parallel to the surface will be constrained by the surrounding oxide layer while the expand at the direction normal to the surface should be much easier due to the plane stress status. As a result, bulking or delamination occurs to partially release the stress caused by the zirconia allotropic transformation.

When it comes to the duplex treated samples, as has been noticed in Section 4.3.5.1, the observed cracks are decreased when comparing with the corresponding CC treated samples. This could be partially attributed to the thinning of the oxide layer formed by the pre-CC treatment during the OBD process; this could be also attributed to the inward diffusion of oxygen atoms and the resulting volume expansion of the substrate, which can reduce the residual compressive stress in the oxide layer formed during the CC treatment.

As the CC treatment process keeps going on, the size and the number of these small lateral cracks increase until they are internally connected especially for CC treated Zircaoy-4 samples. Periodic lateral cracks thus appeared as depicted in Figure 4.2-19 (f) and (g). Measurement of two adjacent lateral cracks on Zircaloy-4 treated samples showed an average distance of about 2.2 μm, which agrees with the 2.0 μm observed by Bossis et al[217]. Based on this assumption, if a treatment at a relatively high temperature is held for a long enough period, Zr702 alloys could also show similar periodic oxide layer on the surface as evidenced by sample Zr702-8010 where an interconnected cracked interface is observed (Figure 4.2-18 (g)).

In the end, the vertical cracks perpendicular to substrate formed as shown in Figure 4.2-18 (g) and Figure 4.2-19 (g). This is in consistent with the aforementioned previous research which also have shown the formation of cracks especially when the formed

oxide is thick enough, in Figure 5.1-2[206]. These vertical cracks are detrimental, which provide fast diffusion channels to oxygen and hydrogen and in the end contribute to the accelerated corrosion and hydrogen embrittlement. Both in return have been reported to promote the formation of cracks [218, 219].

5.2 Oxidation kinetics

5.2.1 Reaction order and breakaway oxidation

Reaction order has long been investigated for zirconium oxidation reaction. The widely reported are the cubic, parabolic and linear reaction, for which the reaction order is 3, 2 and 1 respectively. A transition from parabolic to linear reaction during the oxidation process is called break-away oxidation, after which change of the surface colour and large cracks formation can be easily noticed. Meanwhile, as previous research reported as well the oxide scale formed after breakaway oxidation is non-protective any more. Considering the results described in surface morphology and layer structure observation from both alloys, Zircaloy-4 has endured the breakaway oxidation in the current study.

The following equations are used to study the reaction order (n), where x is the oxide thickness:

$$x = kt^{1/n} \qquad \text{Equation 5.2-1}$$

$$lnx = lnk + \left(\frac{1}{n}\right) lnt \qquad \text{Equation 5.2-2}$$

Reaction temperatures of 400 and 600 °C are used for the examination of reaction order. The corresponding plots of $\ln x$ vs. $\ln t$ are shown in Figure 5.2-1 and Figure 5.2-2. According to the above equation, the slop of the linear line in Figure 5.2-1 is $1/n$.

Hence the calculated reaction orders for Zr702 and Zircaloy-4 at 400 °C are 2.7 and 2.3 respectively. This is between parabolic (n=2) and cubic (n=3), which is in agreement with the previous research results[220]. When the treatment temperature is raised to 600 °C, the corresponding reaction order is 1.6 and 1.1 respectively. Considering the previous slow reaction before the breakaway oxidation at relatively low temperatures, the reaction for Zircaloy-4 has changed to linear when the temperature is increased to 600 °C. This is in line with the visually observed surface colour change to beige.

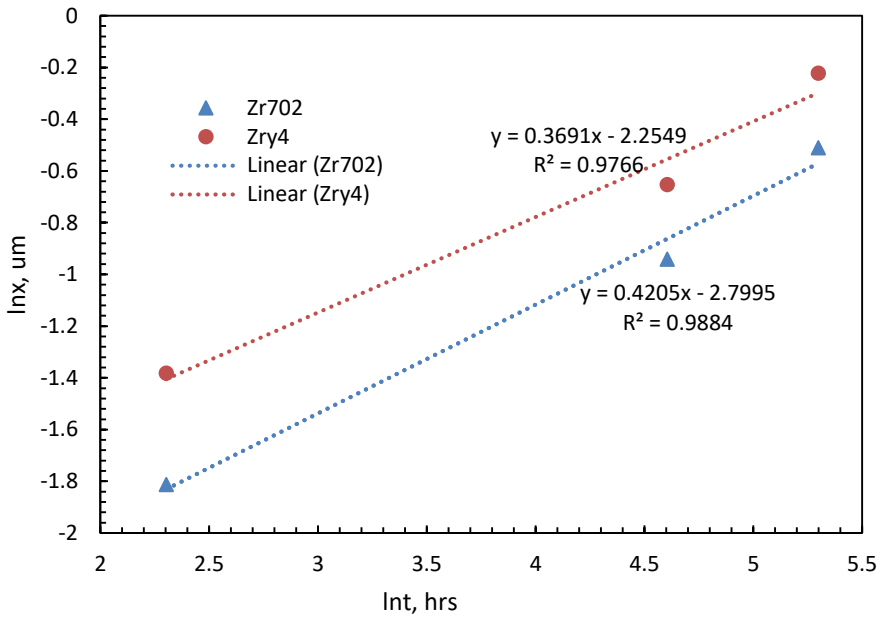


Figure 5.2-1 lnx vs. lnt for Zr702 and Zircaloy-4 alloy at treatment temperature 400 °C: x stands for the ceramic layer thickness; t represents the treatment period of time

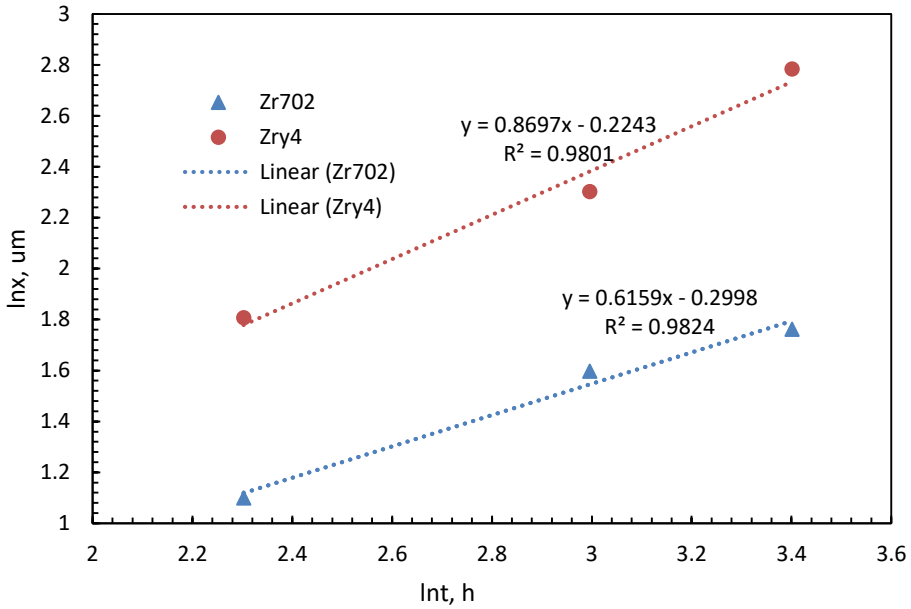


Figure 5.2-2 lnx vs. lnt for Zr702 and Zircaloy-4 alloy at treatment temperature 600 °C: x stands for the ceramic layer thickness; t represents the treatment period of time

5.2.2 Reaction process and activation energy

As it is widely accepted for the oxidation of zirconium alloys, the growth of the ceramic surface layer is controlled by the inward oxygen diffusion through the thin oxide film. Therefore, the denser and thicker the oxide film is, the more difficult the oxygen diffusion will be. Zirconium-oxygen reaction steps together with a simplified schematic diagram are shown in Figure 5.2-3.

1) Oxygen molecules in the surrounding atmosphere are absorbed onto the zirconium surface. As mentioned earlier air is used as the source of oxygen during the treatment. Therefore, oxygen concentration c_0 at the surface is 9.69×10^{-3} mol/L, which is deduced from 20.95 % (volume) of oxygen in the air.
2) Oxygen molecules decompose into oxygen atom. The reaction is shown in Equation 5.2-3.

$$O_2 = 2[O]$$ Equation 5.2-3

At the equilibrium state, μ_{O_2}=$\mu_{[o]}$, where μ_{O_2} and $\mu_{[o]}$ are the chemical potential of oxygen in gas and in solid Zr.

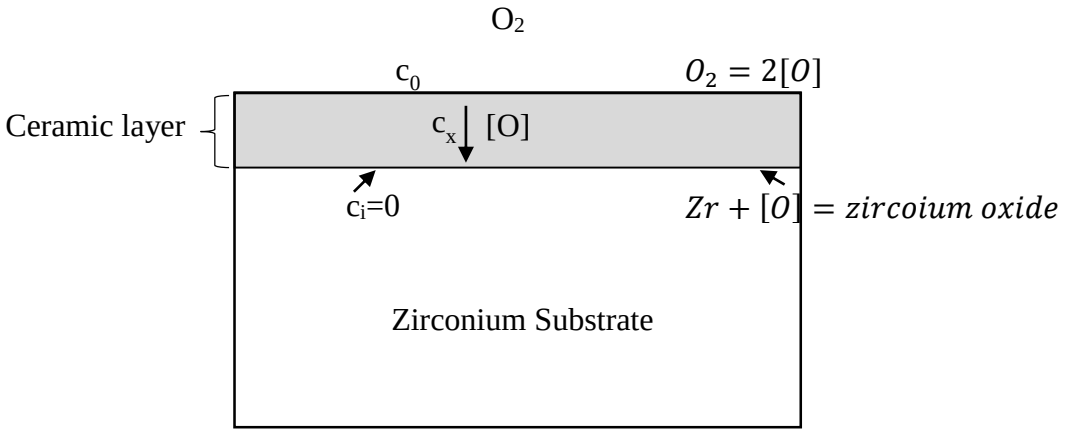


Figure 5.2-3 Simplified schematic diagram of zirconium and oxygen reaction during the CC treatment

3) Oxygen atom diffuses through the thin ceramic layer to the metal/oxide interface. The diffusion obeys the Fick's second Law, as shown in Equation 5.2-4.

$$\frac{\partial c}{\partial t} = -D\frac{\partial^2 c}{\partial x^2}$$ Equation 5.2-4

Where D is the diffusion coefficient, c is the oxygen concentration, x is the distance of the point to surface and t is the corresponding diffusion time.

4) The oxygen at the metal/oxide interface then reacts with zirconium to form Zr(O), $ZrO_{0.27}$, t-ZrO_2 and m-ZrO_2 respectively.

$$Zr + [0] \rightarrow Zr(O)$$ Equation 5.2-5

$$Zr(O) \rightarrow ZrO_{0.27}$$ Equation 5.2-6

$$Zr + O_2 \rightarrow t\text{-}ZrO_2$$ Equation 5.2-7

$$Zr + O_2 \rightarrow m\text{-}ZrO_2$$ Equation 5.2-8

$$t\text{-}ZrO_2 \rightarrow m\text{-}ZrO_2$$ Equation 5.2-9

The oxygen concentration at the metal/oxide interface is noted as c_i, as shown in Figure 5.2-3.

Semi-finite solid solution for Fick's second law is shown in Equation 5.2-10.

$$\frac{c_x - c_0}{c_i - c_0} = 1 - \text{erf}\left(\frac{x}{2\sqrt{Dt}}\right) \qquad \text{Equation 5.2-10}$$

The erf function is the error function and the mathematical definition of the error function is given in Equation 5.2-11.

$$\text{erf}(x) = \frac{2}{\sqrt{x}} \int_0^x \exp(-y^2)\, dy \qquad \text{Equation 5.2-11}$$

The oxygen will react with zirconium substrate and keeps at an equilibrium state where c_i will be kept as a constant value. Therefore, it can be deduced from Equation 5.2-10 that $\frac{x}{2\sqrt{Dt}}$ is a constant. This means that there is a linear relationship between x and $\sqrt{Dt}$, as shown in Equation 5.2-12, where k_1 is a constant.

$$x = k_1\sqrt{Dt} \qquad \text{Equation 5.2-12}$$

1) In the case of treatment temperature being constant, the diffusion coefficient is constant. Therefore,

$$x = k_2\sqrt{t} \qquad \text{Equation 5.2-12}$$

$$\text{Or} \qquad x^2 = k_3 t \qquad \text{Equation 5.2-13}$$

where k_2 and k_3 are constant.

Hence, a graph of x^2 vs. t is drawn in Figure 5.2-4, where a linear relationship can be noticed and the linear coefficient is 0.0031 and 0.0018 hours/μm^2 for Zircaloy-4 and

Zr702 respectively. This suggests a diffusion control of the reaction for both alloys at 400 °C.

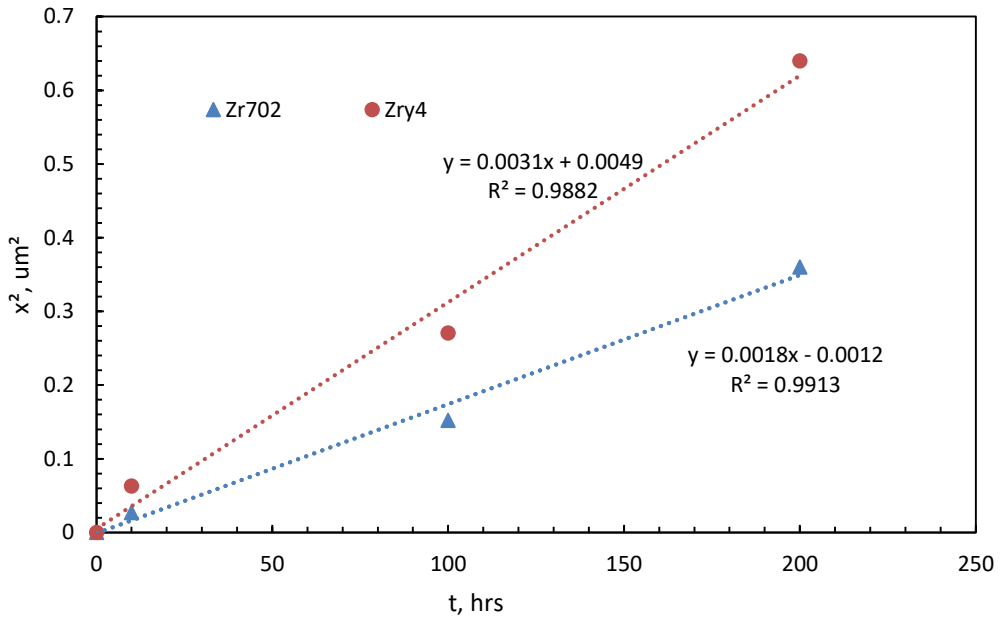


Figure 5.2-4 x^2 vs. t plots for Zr702 and Zircaloy-4 at treatment temperature 400 °C: x stands for the ceramic layer thickness; t represents the treatment period of time

2) If treatment time is constant, it would be

$$x = k_4\sqrt{D} \qquad \text{Equation 5.2-14}$$

Or $$x^2 = k_5 D \qquad \text{Equation 5.2-15}$$

where k_4 and k_5 are constant.

Equation 5.2-16 shows the Arrhenius Equation.

$$D = D_0 \exp(-\frac{Q}{RT}) \qquad \text{Equation 5.2-16}$$

where D and D_0 are the diffusion coefficient at the absolute temperature T (in K) and 0 K, while Q is the diffusion activation energy.

Deducing from Equation 5.2-14 or 5.2-15 and 5.2-16, it can be drawn that,

$$\ln(x^2) = lnk_6 - \frac{Q}{RT} \qquad \text{Equation 5.2-17}$$

Therefore, $\ln(x^2)$ is in linear relationship with reciprocal of absolute temperature. The linear coefficient can be used to calculate the diffusion activation energy.

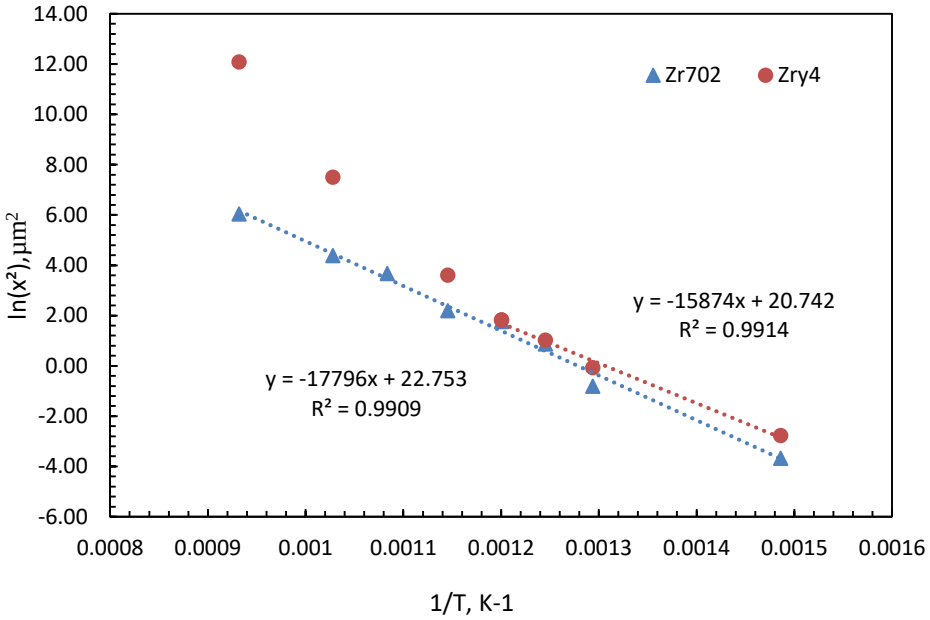


Figure 5.2-5 Plot of $\ln(x^2)$vs. 1/T at different treatment temperature for Zr702 and Zircaloy-4: x stands for the ceramic layer thickness; T represents the treatment temperature

A graph of $\ln(x^2)$ vs. 1/T is plotted in Figure 5.2-5. It can be seen that the linear relationship between $\ln(x^2)$ and 1/T is valid for the whole temperature range for Zr702 as evidenced by $R^2 > 0.99$. for Zr702.

It should also be noted that linear fit between $\ln(x^2)$ and the reciprocal of absolute temperature for Zircaloy-4 at the doesn't fit as well as that of Zr702. The changing

point is at 600 °C as evidenced by Figure 5.2-6 where the relationship between x^2 vs. t is not linear any more for Zircaloy-4. Therefore, the controlling process for the Zircaloy-4 reaction at 600 °C and above is changed. This also matches the reaction order change and beige colour revelation in the surface morphology observation.

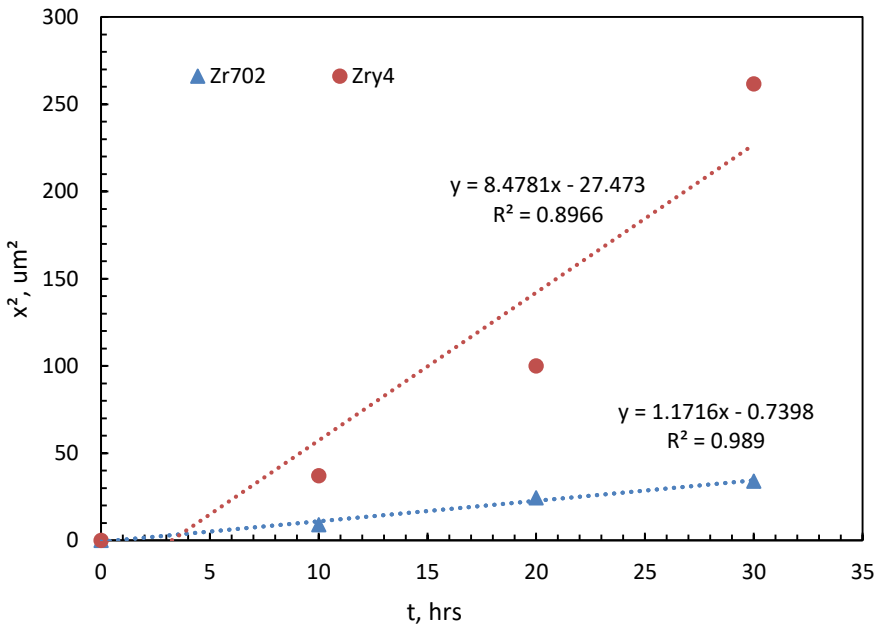


Figure 5.2-6 x^2 vs. t plots for Zr702 and Zircaloy-4 at treatment temperature 600 °C: x stands for the ceramic layer thickness; t represents the treatment period of time

Based on the points before 600 °C, the calculated diffusion activation energy for Zircaloy-4 is 147 kJ/mol where $R^2 > 0.99$. Therefore, the lower diffusion activation energy of Zircaloy-4 means higher diffusion rate through the formed ceramic layer on Zircaloy-4 alloy, which explains its higher oxidation rate than Zr702. Combining the TEM microstructure characterisation where the columnar grain was measured to be 80 ~100 nm in width oxide layer on Zr702-5310, while it is only about 50 nm for that on Zry4-5310. More grain boundaries therefore exist on Zircaloy-4 ceramic surface, which induces the lower oxidation activation energy.

5.2.3 Role of alloying element (Sn)

As mentioned in section 3.1, the main composition difference between Zr702 and Zircaloy-4 is the composition between Sn. As Zr 702 is often treated as a commercially pure Zr (due to the great similarity of physical and chemical properties between Zr and Hf), Zircaloy-4 is Zr-Sn alloys with a tin content of 1.2~1.7 wt%.

It has been reported by many researchers, an addition of Sn content into zirconium alloys will generally increase its oxidation resistance[136, 190, 221]. This is in good agreement with the experimental results in this study as evidenced by the lower diffusion activation energy in Zircaloy-4 (132 KJ/mol) than Zr702 (147 KJ/mon) which leads to a thicker ceramic layer formed on Zircaloy-4 than on Zr702 when their samples are treated under the same conditions.

Although the oxide thickness formed on both Zircaloy-4 and Zr702 increases with increasing the treatment temperature and/or time, the oxide layer on Zircaloy-4 is thicker than that on Zr702 when samples are treated under the same conditions. Regarding the layer quality, however, the oxide layer formed on Zircaloy-4 generally contains more cracks and porosity than that formed on Zr702 as described in Section 4.2.3 (e.g. Figure 2-18 (e) and Figure 2-19 (e)), which is due to the presence of Sn explaining as follows:

Presence of Sn in zirconium alloys is found to be able to stabilise the tetragonal zirconia phase in the oxide layer, as evidenced by the *in situ* XRD results (Figure 4.2-17). This is in agreement with recent research by Garner[136]. However, from this point of view, it would reduce the allotropic transformation and hence lead to less cracking formation on the modified surface, which is contradictory to the aforementioned results. It should

be pointed out that Sn may stabilise tetragonal zirconia during oxidation at a relatively high temperature and hence more t-ZrO_2 would form. However, when cooled from the treatment temperature, t-ZrO_2 will transfer to m-ZrO_2, thus resulting volume expansion. Therefore, the more t-ZrO_2 produced during CC treatment, the larger the total volume expansion when t-ZrO_2 transfer to m-ZrO_2 during cooling. This will lead to a larger residual stress and severe cracking, which therefore caused the more cracks treated on Zircaloy-4 samples than Zr702.

5.3 Corrosion property

Zirconium and its alloys are well known for their good corrosion resistance even at very severe conditions such as acids and alkalis, high temperature steam etc. The Pourbaix diagram of zirconium in water at 25 °C is shown in Figure 5.3-1 [222]. It can be seen that zirconium is passive at a wide PH range from 3.5 to 13. The anodic passivation reaction occurring on zirconium is shown in shown in Equation 5.3-1.

$$Zr + 2H_2O - 4e^- \rightarrow ZrO_2 + 4H^+ \qquad \text{Equation 5.3-1}$$

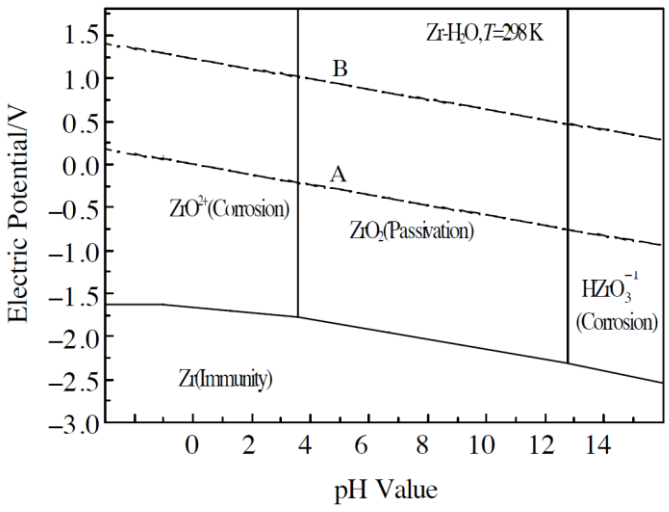


Figure 5.3-1 Potential-PH (Pourbaix) diagram of zirconium in 25 °C water[222], A and B are the water redox reaction $O_2 + 4H^+ + 4e^- = 2H_2O$ and $2H^+ + 2e^- = H_2$ respectively.

5.3.1 Pitting corrosion

When tested into a 3.5 wt% NaCl solution, as it has been observed in Section 4.5, both Zr702 (Figure 4.5-1) and Zircaloy-4 (Figure 4.5-3) have shown typical pitting characteristics in the polarisation curves. As it can be seen from Pourbaix diagram as shown in Figure 5.3-1, during pitting process, the oxidation reaction on the tested samples is the dissolution of Zr matrix into the solution (shown in Equation 5.3-2).

$$Zr + H_2O - 4e^- \rightarrow ZrO^{2+} + 4H^+ \qquad \text{Equation 5.3-2}$$

The pitting corrosion, which happens at the localised defected area, is caused by localized acidification during the corrosion process. The existence of Cl^- can also promote pitting on zirconium alloys, which is in consistence with the previous studies [6, 223-226]. The pitting potential is 0.35 V_{SCE} and 1.75 V_{SCE} for untreated Zr702 (Zr702-UN) and Zircaloy-4 (Zry4-UN) samples respectively. The better pitting corrosion resistance of Zry4-UN than that of Zr702-UN is due to the addition of Sn element, which is part of the reason for the development of Zircaloy series alloys because of the serious localised corrosion on pure zirconium Zr702.

It is noted from Tables 4.5-1 and 4.5-2 that the low temperature treated Zr702-4010 and Zry4-4010 have demonstrated significantly increased corrosion potential (E_{corr}) and effectively reduced corrosion current density (i_{corr}) when compared with the corresponding untreated materials. However, as evidenced in Figures 4.5-1 and 4.5-3, pitting corrosion still occur to Zr702-4010 and Zry4-4010. This is mainly because as shown in Figure 4.2-24 the oxide film formed on the low temperature (400 °C) and short time (10 hours) treated samples is very thin (about 0.2 μm). Therefore, the corrosive solution could relative easily penetrate through the thin oxide film to the

oxide/substrate interface through such defects as pinholes or pores, which are inevitable for thin ceramic layer. Therefore, although the very thin surface oxide layer can delay the corrosion to occur, rapid pitting will occur once the corrosive solution reached the substrate. It is also found by comparing the corrosion properties shown in Tables 4.5-1 and Table 4.5-2 that the corrosion behaviour of Zry4-4010 is better than that of Zr702-4010 in terms of corrosion potential and corrosion current density. This could be partially attributed to the slightly thicker oxide layer formed on Zry4-4010 than that on Zr702-4010 (see Figure 4.2-20) and partially to the better corrosion properties of the former than the latter.

5.3.2 Uniform corrosion

As mentioned electrochemical corrosion test, zirconium alloys generally exhibit a dramatic increase of the resistance towards pitting after CC treatment because of the ceramic layer formed during the surface treatment, which prevents the direct contact of zirconium matrix with the Cl^- cations from the corrosion solution.

A general uniform corrosion occurring on the treated sample surface, where there is a characteristic passivation current, which measures the protectiveness of the ceramic layer. After the passivation plateau, water dissolution region which starts after a peak at potential about 1.7 V_{SCE} on the polarisation curves of sample Zr702-5310, Zr702-5610, Zr702-6010, Zry4-5310, Zry4-5610. The thickness range for those samples are between 1 μm and 4 μm. This is the dissolution of water molecules that has been absorbed onto the tested sample surface. The corresponding reaction is shown in Equation 5.3-3.

$$2H_2O - 4e^- = O_2 + 4H^+ \qquad \text{Equation 5.3-3}$$

For the same CC treatment conditions, the current density on Zircaloy-4 sample is generally lower than that on Zr702 sample, which indicates a smaller reaction rate on Zircaloys-4 alloy. This is attributed to the thickness of the protective oxide layer formed at medium temperatures (500-600°C) as it is clearly shown by comparing the cross-sectional layer thickness of CC treated Zr702 (Figure 4.2-20).

5.3.3 Defects accelerated localised corrosion

When the ceramic layer becomes even thicker, the corrosion mechanism changes to localised corrosion for high-temperature treated samples Zr702-8010, Zry4-7010 and Zry4-8010, as evidenced by the cracks surrounding the burst area shown in Figure 4.5-1 (f) and Figure 4.5-2 (f). The surface begins to break at localised defected areas such as blisters and cracks. Corrosion solution flows and is trapped inside, and these locations then act as crevices[223]. In the occluded cell, the oxidation reaction which forms ZrO_2 keeps taking place until the cracks generated due to the corrosion induced compressive stress.

Therefore, the protectiveness of the ceramic layer formed during the CC treatment depends on the layer thickness as well as defects, i.e. blisters and cracks. The CC optimised treatment conditions are 530°C/10hours, 530°C/10hours and 560°C/10hours for Zr702; 5310°C/10hours and 560°/10hours for Zircaloy-4 alloy.

In terms of the duplex treated samples (Figure 4.5-5), when compared with Zr702-UN sample, the corrosion resistance is increased as evidenced by the more positive self-corrosion potential E_{corr}. However, the exchange current which stands for the corrosion reaction rate has significantly increased in comparison with the CC treated samples. This can be explained by the oxygen vacancies generated when zirconia formed by the

CC treated is decomposed in vacuum during the OBD process, as discussed in Section 4.3.4. Those oxygen vacancies will significantly increase the oxygen diffusion rate and therefore accelerate the corrosion reaction rate.

The corrosion mechanism for duplex treated sample is similar to that of CC treated samples, where the corrosion starts from the structure weak locations, normally porous and cracking areas, then crevice corrosion and compressive stress induced corrosion cracking followed. This is evidenced by the observed cracking and even exposed surface area on the corroded surface shown in Figure 4.5-6.

On the other hand, the OBD treatment temperature has a significant effect on the corrosion property of duplex treated sample. As described in Section 4.5.2, among CC7-6030, CC7-7030 and CC7-8030, the corrosion resistance decreases with the increasing of the OBD treatment temperature. This is mainly because the treatment temperature can dramatically increase the decomposition rate, which in turn lead to the significant and even complete decomposition of the ceramic layer on CC7-7030 and CC7-8030 respectively. With the loss of the ceramic layer on CC7-8030 which prevents the corrosion solution, especially Cl^- ion, from permeating into the zirconium matrix, corrosion liquid (NaCl) can therefore easily penetrate and be trapped inside the confined space inside the crack within limited access to the outside, severe corrosion is thus observed on the high temperature duplex treated sample surface, as shown in Figure 4.5-6 (d).

5.4 Tribological property

5.4.1 As-received Zr alloys

As reported in Section 4.6.1, untreated Zr702 and Zircaloy-4 samples exhibit high coefficient of friction (CoF) values up to about 0.5, which is consistent with the reported friction coefficient for zirconium alloys[4]. To better understand the frictional behaviour of the untreated materials, the CoF curves of these two materials as a function of reciprocating cycles up to 200 are compared in Figure 5.4-1. It can be seen that the CoF values for both alloys are reduced gradually with the test cycles and that the CoF of Zry4-UN is generally higher than that of Zr702-UN.

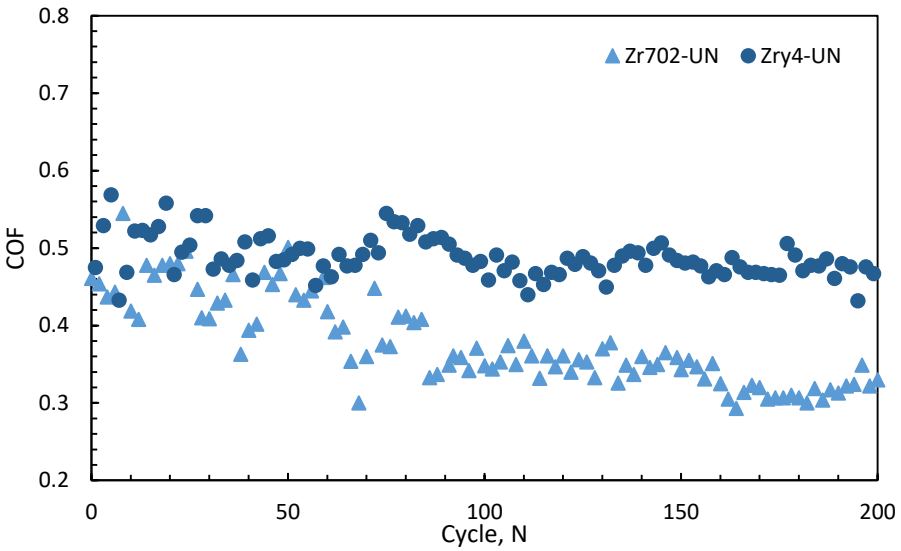


Figure 5.4-1 Measured CoF values of as-received Zr702 and Zircaloy-4 alloy within to 200 cycles

The above observations could be understood by the post-test observation of the wear tracks formed and the wear mechanisms involved. As shown in Figures 4.6-6 and 4.6-8, the wear tracks formed on untreated materials are characterised by parallel grooves and adhesive craters. It is well-known that zirconium and its alloys are chemically active

and have a high ductility. Both of them will lead to a strong adhesion tendency. The adhesive strength of the junctions formed is generally higher than the strength of the as-received Zr702 and Zircaloy-4 materials. The rupture of these joints at the weaker zirconium asperities, thus forming the craters observed on the worn surface. Meanwhile, the transferred zirconium becomes work-hardened or even oxidized after repeated reciprocating sliding, which therefore causes the severe abrasive wear damage as evidenced by the grooves observed on the wear track.

According to tribology theory as discussed in Chapter 2 (Figure 2.2-6), in essence adhesive wear the formation of adhesion junctions due to cold-weld, rupture of the junction friction force and transfer of material. It is known that the formation and strength of adhesion junctions is closely related to the plastic index of wearing surfaces, which is a measure of the tendency for plastic deformation and is proportion to the ratio of Young's modulus (E) to hardness (H). As reported in Figure 4.4-5, the E/H of the untreated materials is > 40 and hence strong adhesion and large CoF are expected. It is also noted that the E/H is slightly for Zry4-UN (43.1) than for Zr702-UN (40.5), which explains the higher CoF observed for the former than the latter.

As discussed above, zirconium and its alloys are chemically active. Therefore, oxidation of wear surface and wear debris could be promoted by the frictional heating and the high flash temperature[227, 228]. Therefore, the CoF of both untreated materials would reduce gradually with the reciprocating cycles.

It follows from the above discussion that the wear of the untreated Zr702-UN and Zry4-UN materials is dominated by severe adhesive wear and abrasive wear. This is strongly supported by the extremely large wear rates shown in Figure 4.6-5. As can be seen, the

wear rate of Zry4-UN is much larger than that of Zr702-UN. This could be mainly attributed to the higher adhesion tendency of Zry4-UN than Zr702-UN. Another important factor is the difference in hardness between these two materials, which is 3.0 and 2.8 GPa for Zr702-UN and Zry4-UN respectively. Based on the aforementioned adhesive wear mechanism, abrasive wear also occurs due to the hardened transferred material on the counterpart. According to Equation 2.2-2 and 2.2-3, wear is inversely proportion to surface hardness and a higher hardness would lead to lower wear loss. This may also have contributed to the larger wear rate of Zry4-UN as compared with Zr702-UN.

5.4.2 CC treated zirconium alloys

As has been reported in Section 4.6.1, the ceramic conversion (CC) treatment developed from this research can effectively reduce the coefficient of friction (CoF) and reciprocating wear of most tested samples when compared with the untreated zirconium alloys.

As evidenced in Figures 4.6-1, the CoF of Zr702 can be reduced from between 0.4-0.5 to less than 0.2 for samples Zr702-5010, Zr702-5610 and Zr702-6010; similarly, for Ziroaloy-4 (Figure 4.6-4), the CoF of Zircaloy-4 is reduced from between 0.35-0.40 for the untreated material to between 0.20 and 0.25 for samples Zry4-4010, Zry4-5010, Zry4-5310, Zry4-5610 and Zry4-6010. In addition, the CC treatment can dramatically improve the wear resistance of most treated samples as shown in Figure 4.6-5.

As discussed in Section 5.4.1, the severe wear and high CoF for untreated Zr alloys studied are related to their strong adhesion tendency and low hardness. The reduced

CoF and wear of the CC treated materials could be contributed to the ceramic layer formed on the surface.

Firstly, as has been shown in Figure 4.4-5, all the CC treatments conducted in the research can significantly reduce the E/H of untreated materials. Except for the low-temperature and short-time treated Zr702-4010 and Zry4-4010 samples, the E/H value of both alloys can be effectively reduced from above 40 to between 10 and 15 by CC treatment. This can effectively reduce the adhesion tendency of these two alloys and hence their friction and wear can be significantly reduced. This is supported by the post-test examination of the wear tracks formed on the CC treated surfaces. As evidenced in Figures 4.6-6 and 4.6-8, the wear track is much smoother than that formed on the untreated surfaces without any adhesion craters. Secondly, after CC treatment the hardness of the surfaces has been effectively increased mainly due to the formation of the hard zirconia layer. Therefore, the hardness difference between the sliding surfaces is significantly reduced. Accordingly, the abrasive wear of the CC treated surfaces is reduced as well and only narrow and shallow abrasion grooves could be observed (see Figures 4.6-6 and 4.6-8). In short, the wear mechanism of the Zr alloys investigated changes from severe adhesive wear and abrasive wear for the untreated materials to mild abrasive wear for the majority of the CC treated samples provided the surface oxide layer could survive under the test conditions.

Although the SE image (Figure 4.6-6 (b)) have shown a relatively smooth surface, ripples-like features perpendicular to the reciprocating direction are observed on the BSE image (Figure 4.6-6 (c)) for Zr702-5310. This means that micro-cracking has occurred but the bonding between the oxide and the substrate is strong as no spallation

is observed. These ripples-like micro-cracks are formed mainly due to the difference in hardness and Young's modulus between the ceramic layer and zirconium matrix, which agrees with the load bearing capacity where cracked indent was observed (see Section 4.4.3).

However, as shown in Figures 4.6-1 to 4.6-3, although the initial CoF of the 400°C /10h treated Zr702-4010 and Zry4-4010 is much lower than that of the untreated material, the CoF value has increased significantly after 43 cycles for Zr702-4010 and starts to increase after 87 cycles for Zry4-4010.

This increasing friction coefficient observed at a later stage implies the breaking down of the thin ceramic layer by wear. Hence, wear debris was produced at the beginning of the test from the hard ceramic layer on the surface. Once involved in the wear contacting surface, they act as the hard third body for abrasive wear and severely damage the wear surface. As a consequence, the wear process is accelerated, thus resulting the high wear rate and CoF for both materials. The same explanation can be applied to the high wear of Zr702-5010.

As shown in Figure 4.6-2, the observed friction behaviour for Zr702-7010 and Zry4-7010 samples is quite different from each other. Whilst the CoF for Zry4-7010 maintains low and stable for the whole test period, the CoF of Zr702-7010 has increased from a very value of 0.15 with the test cycles up to about 0.58. As described in the surface morphology and roughness section, the condition of 700°C/10hours is the critical point where the surface roughness increases significantly and beige blisters begins to be observed.

When tested against a WC/Co ball, Zr702-7010 surface is grinded to a smooth surface initially. The worn-out debris then act as hard third body. The modified ceramic layer, as shown in Figure 4.2-18 is dense without clear cracks or pores. The hard third body debris has been kept trapped at the contacting surface, thus generating more worn particle which in return continuously increase the friction coefficient. However, different from Zr702-7010, Zry4-7010 has a ceramic layer that is cracked as shown in Figure 4.2-19. Therefore, the worn out zirconia particles can easily be smashed and embedded into the whole test surface which leads to the even CoF value during the whole process.

However, the wear rate is much higher for Zry4-7010 than for Zr702-7010, which can be explained by close examination of the wear tracks formed. As shown 4.6-8, severe spallation of the surface oxide layer has been observed for tested Zry4-7010 mainly due to the lateral cracks in the very thick layer (~43 μm, Figure 4.2-20). When the WC/Co ball reciprocates against the ceramic layer, the cracked zone underneath the very top surface is spalled due to the large tangent force and the weak cohesive strength of the cracked oxide layer. This is evidenced by the white particles on the wear track surface generated during the process. Therefore, the high wear of Zry4-7010 is related to the spallation of the surface oxide layer. No such spallation is observed for the tested Zr702-7010 with a dense and relatively thin oxide layer of 9 μm (Figure 4.2-20). However, similar spallation occurs on Zr702-8010 when the oxide thickness increased to about 21 μm.

5.4.3 Duplex treated samples

In comparison with the single CC treated CC7 sample, the CoF (Figure 4.6-9) and wear rate (Figure 4.6-10) of duplex treated samples are significantly reduced as well, with the only exception of sample CC7-8030.

As shown in Figure 4.6-9, whilst the friction coefficient of CC7 increases almost linearly with the test cycles, the CoF of the duplex treated CC7-6010, CC7-6030 and CC7-7030 maintains around 0.2 throughout the whole test. Similarly, the wear rate is also reduced after these duplex treatments.

These improved tribological properties could be mainly attributed to the microstructure improvement by the oxygen boost diffusion treatment. For example, the very surface of the single CC treated sample, i.e. CC7, becomes more even, the surface roughness has decreased and the surface hardness is increased after the OBD treatment. Similar to CC treated surfaces, mild abrasive wear is the dominant wear mechanism of duplex treated sample as evidenced by the parallel grooves on the wear tracks (Figures 4.6-11 and 4.6-12). Therefore, the increased wear resistance can be attributed to the improved surface layer quality and the enhanced surface hardness (Figure 4.4-8).

Another major difference from the CC treated sample is that the wear tracks observed on the duplex treated samples have shown no large ripples as observed on the tested single treated surface; instead, only micro-cracks are observed within the ploughing grooves. This is attributed to the increased oxygen diffusion zone underneath the ceramic layer, which can effectively increase the LBC of the treated surfaces (Figure 4.4-13). Similar microcracks have been observed by some previous research on wear the performance evaluation of Partially Stabilised Zirconia (PSZ) samples which are

related to the phase transformation between tetragonal to monoclinic zirconia[79]. This phase transformation accompanies a volumetric change that can leads to formation of microcracks.

However, it is of interest to note that the CoF of duplex treated CC7-8030 is almost the same as the single CC treated CC7 (Figure 4.6-9) and the wear of the former is even worse than the latter (Figure 4.6-10). The diffusion zone can be dramatically increased on sample CC7-8030 to more than 250 μm, but no ceramic layer was left as shown in Figure 4.3-7 (h).

As discussed above, the improved tribological performance for most CC treated samples is contributed by the ceramic layer formed on the surface. Accordingly, without surface ceramic layer, the hardened oxygen diffusion zone with the cracked surface (see Figure 4.3-6) is easy to break down by the counterpart WC/CO balls and generated huge amount of wear debris. This wear debris is much harder than that from the untreated sample surface. Hence, the wear process is accelerated. Meanwhile, the coarser grains size, observed across the diffusion zone under SEM Electron Channel Contrast Image (ECCI) on CC7-8030 as shown in Figure 5.4-2, can also promote the wear process[197] and make it easier to pull out large particles, which therefore increases the wear volume loss. In order to confirm this assumption, the sample was put back into the oxidation furnace (530°C/10hours) to form ceramic layer on top, and hence three-step duplex treatment. Wear test on this sample, noted as CC+OBD+CC, has shown significant improvement in the wear performance, as evidenced by the 2D wear track graph shown in Figure 5.4-3.

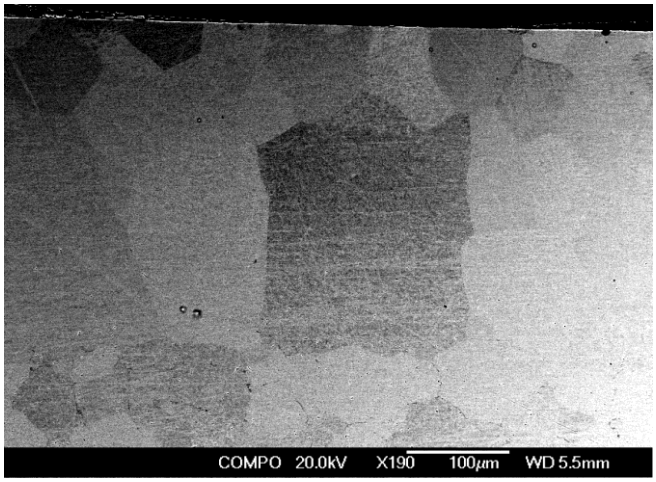


Figure 5.4-2 Electron Channel Contrast Images (ECCI image) of CC7-8030, showing large grains of the diffusion zone

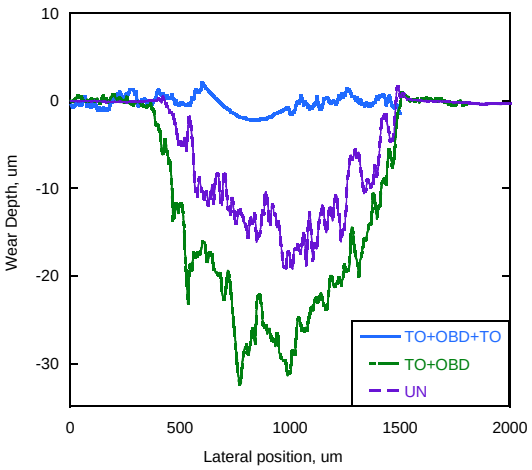


Figure 5.4-3 2D wear track profile comparison of samples Zr702-UN, TO+OBD (CC7-8030) and CC+OBD+CC

6 CONCLUSIONS

A series of ceramic conversion treatments (CCT) were carried out on both Zr702 (commercial grade) and Zircaloy-4 (nuclear grade) Zr alloys. In addition, some initial trials of duplex surface treatments for Zr702 alloy were also conducted. The following conclusions could be drawn based on the results and discussion in the previous two chapters.

Microstructure:

1. Ceramic conversion treatment based on thermal oxidation in air can successfully convert the surface of Zr702 and Zircaloy-4 into a ceramic layer consisting of zirconium oxides followed by an oxygen diffusion zone.
2. With the increase of CC treatment temperature and/or time, the colour of treated surface changes from bluish colour to black for Zr702 samples, but some with beige blisters formed at the studied conditions. Surface colour variation is more obvious for Zircaloy-4 alloy: from black through beige patche dispersion to fully beige colour.
3. Surface roughness increases with the increase of CCT temperature and/or time. The critical CCT condition for rapid increase in surface roughness is 700°C/10hours and 500°C/50hours for Zr702 and Zircaloy-4 respectively, which corresponds to the formation of beige blisters/patches on the treated surface.
4. Phase characterisation shows that the ceramic layer consists of mainly m-ZrO_2 with traces of t-ZrO_2. A substoichiometric phase $ZrO_{0.27}$ is formed at the metal/oxide interface, which has a preferred orientation to the substrate $[2\bar{1}\bar{1}0]_{ZrO_{0.27}}$ //$[0001]_{Zr}$, (0002)//($\bar{1}$010).

5. Microstructural characterisation reveals that the surface ceramic layer formed by CC treatment is made up of columnar grains perpendicular to the metal/oxide interface with a prolate long grain microstructure at the interface. The interface layer formed under the same CCT conditions is smaller on treated Zircaloy-4 than on Zr702.
6. The defects (such as cracks and pores) formed in surface oxide layer increase with increasing the CCT temperature and/or time. Long lateral cracks parallel to the metal/oxide interface are formed in surface layers treated at high temperature . There are more pores/cracks formed on Zircaloy-4 than Zr702 when samples are treated under the same CC treatment condition.
7. More t-ZrO_2 phase is formed on CC treated Zircaloy-4 samples than on Zr702 as evidenced by the stronger XRD and SAD diffraction patterns from the tetragonal phase. The allotropic transformation from t-ZrO_2 to m-ZrO_2 causes the formation of the cracks existing throughout the ceramic layer.

Oxidation kinetics:

8. The thickness of the ceramic layer formed on both Zr702 and Zircaloy-4 alloys during CC treatment increases with the CCT temperature and/or time. This is caused by the higher oxygen inward diffusion rate on Zircaloy-4 alloy than that on Zr702, as the diffusion activation energy for Zr702 and Zircaloy-4 is 147 kJ/mol and 132 kJ/mol respectively.
9. The alloying element Sn in Zircaloy-4 promotes the CC treatment as evidenced by the thicker oxide layer formed on Zircaloy-4 than on Zr702 when treated under the same CC treatment conditions.

Mechanical properties:

10. All CC treatments conducted in this research can significantly increase the surface hardness of both Zircaloy-4 and Zr702 alloys mainly due to the formation of zirconia layers. The highest hardness is achieved by the CC treatments carried out at 500 °C for 10 hours for both alloys, which is 14.5 GPa and 15.5 GPa for Zr702 and Zircaloy-4 respectively.
11. The hardness depth profiles of CC treated both alloys consist of a high hardness plateau (corresponding to the formed ceramic layer), followed by a hardness decreasing zone (HDZ) which is solid solution hardened by oxygen inward diffusion.

Corrosion properties:

12. Pitting is the main corrosion failure mechanism for the as-received Zr702 and Zircaloy-4 materials. The pitting potential of the as-received Zircaloy-4 and Zr702 is 0.43 and 1.75 V_{SCE} respectively. The better pitting corrosion resistance of Zircaloy-4 in comparison with Zr702 is related to the Sn containing in the nuclear grade Zircaloy-4 alloy.
13. After the CC treatment, improved corrosion properties are generally observed with the exception of high temperature treated Zr702-8010 and Zry4-7010, Zry40-8010 due to their poor ceramic layer quality.
14. The low-temperature and short-time treated Zr702-4010 and Zry4-4010 have shown marginally increased corrosion properties when compared with the untreated materials due to the very thin oxide layer formed on the surface. Medium-temperature treated samples exhibit the best corrosion resistance among all the CC

treated samples: Zr702-5350, Zr702-5310 and Zr702-5610 for Zr702; Zry4-5310 and Zry4-5610 for Zircaloy-4.

Tribological properties:

15. As-received Zr702 and Zircaloy-4 alloys exhibit high coefficient of friction (CoF) values between 0.4 and 0.5 mainly due to their low hardness, high E/H ratio and high adhesion tendency. In general, the CoF for both the as-received materials decreases with reciprocating cycles due to *in situ* oxidation promoted by frictional heat.
16. The CoF of Zr702 can be reduced from between 0.4~0.5 to less than 0.2 by the CC treatment for 10 hours at 500, 560 and 600°C; for Ziroaloy-4, the CoF is reduced from between 0.35~0.40 for the untreated material to between 0.20 and 0.25 by the CC treatment for 10 hours at 400, 500, 530, 560 and 600°C. The reduced CoF of the CC treated materials should be contributed to the ceramic layer formed on the surface with high hardness and low E/H ratio.
17. Zr702-UN (untreated Zr702) exhibits better wear resistance than Zry4-UN (untreated Zry4-UN) at as-received conditions, with their wear rate being 5.5×10^6 $\mu m^3/N$ and 8.8×10^6 $\mu m^2/N$ respectively, due to the better oxidation properties of Zircaloy-4 alloy than that of Zr702 which leads to the better oxidation hardened wear debris.
18. The high wear rate of the as-received Zr702 and Zircaloy-4 alloys can be reduced significantly by the most CC treatments. The wear rate for the optimally CC treated Zr702 (530 °C/10 hours) and Zircaloy-4 (500 °C/10 hours) is 1.5×10^3 $\mu m^3/N$ and

9.9×10^3 $\mu m^3/N$ respectively. This represents an improvement in wear resistance of 3.7×10^3 and 8.9×10^2 times over the untreated Zr702 and Zircaloy-4 respectively.

19. Wear mechanism studies have shown a change from severe adhesive wear together with abrasive wear for the as-received materials to mild abrasive wear for the CC treated samples due to the introduction of a ceramic surface layer with high hardness and low E/H ratio (hence low adhesion tendency).
20. When samples are treated for 10 hours, limited improvement in the tribological properties of these two Zr alloys can be achieved by low-temperature (400°C for both alloys and 400°C for Zr702) and high-temperature (700 and 800 °C Zircaloy-4 and 800 °C for Zr702) treatments. This is because a thin oxide layer with low load bearing capacity formed at low-temperatures can be easily worn through whilst partial spallation is the failure mechanism for the thick oxide layer formed at high temperatures due to the lateral cracks inside the thick oxide layer.
21. The optimised CC treated Zircaloy-4 (530°C/10hours) can effectively reduce the fretting wear of Zircaloy-4 in both DI water and 3.5 wt% NaCl solution from 138 $\times 10^3$ and 140 μm^3 to 7.2 $\times 10^3$ and 7.5 μm^3 respectively due to the elimination of wear/galling craters. This represents a reduction of fretting wear for 19.2 and 18.7 times in DI water and 3.5 wt% NaCl solution respectively.

Duplex surface treated samples:

22. Oxygen diffusion boost (OBD) can reduce the porosity and cracks in the oxide layer already formed during the first CC step and thicken the oxygen diffusion zone beneath the surface oxide layer.

23. While the ceramic layer (m-ZrO_2 and t-ZrO_2) maintains the columnar microstructure, the grain shape along the metal/oxide interface is changed from the prolate, long grains to equiaxed gains and the $ZrO_{0.27}$ phase is changed to a high pressure Zr HCP phase (ω-Zr) after the OBD treatment.
24. The corrosion resistance of the duplex treated surfaces is superior to the untreated sample but slightly inferior to the as-CC treated samples due to the oxygen vacancies generated by the OBD treatment.
25. Except for high-temperature OBD treated CC7-8030, the wear properties of the duplex treated samples (both two-step and three-step treatment) outperform the corresponding CC treated samples due to the improved load bearing capacity contributed from the thickened oxygen diffusion zone. The decreased wear resistance of the CC7-8030 sample is mainly caused by the elimination of the protective ceramic layer.

7 FUTURE WORK

This work has successfully shown that the optimal ceramic conversion treatment can effectively increase the dry sliding wear resistance, fretting wear behaviour and corrosion performance of zirconium alloys. Future lines of investigation into this topic could include:

1. Due to the shortage of nuclear grade Zircaloy-4 alloy, trial work on duplex surface treatment was carried out only on chemical grade Zr702 alloys. Hence a systematic study of both two-step and three-step duplex surface treatments is suggested to be carried out for both nuclear grade and chemical grade alloys.
2. Laboratory fretting testing has shown the good anti-fretting wear performance of CC treated Zircaloy-4 sample (Zry4-5310) based on the wear volume loss in both DI water and 3.5 wt% NaCl solution. Systematic work could be conducted to study the full slip, partial slip, stress distribution, dissipated energy etc.
3. Dry reciprocating wear and corrosion properties were evaluated separately in this work. However, in many real application cases, some of zirconium components are encountered in both wear and corrosion simultaneously. Therefore, tribo-corrosion tests are suggested.

8 APPENDIX

8.1 List of figures

Figure 2.1-1 Zr-Sn binary phase diagram[21] 7

Figure 2.1-2 Zr-Nb binary phase diagram[21] 7

Figure 2.1-3 Temperature-pressure phase diagram of zirconium[25] 8

Figure 2.1-4 Typical microstructures of zirconium alloys[29] 11

Figure 2.1-5 HCP crystallographic of Zirconium[32] 15

Figure 2.1-6 Fuel assembly and control rod cluster used in (a) PWR and (b) BWR[37]15

Figure 2.2-1 Zr-H binary phase diagram[21] 17

Figure 2.2-2 A schematic diagram showing a frictional force in (a) rolling and (b) sliding conditions[61] 19

Figure 2.2-3 True contact of two solid surface 20

Figure 2.2-4 (a) d-bond character and (b) Metallurgical compatibility chart for metals, derived from their two phase binary diagrams, the number given means the solubility of the two different phase[61, 72] 22

Figure 2.2-5 Schematic diagram of a tribocontact system implicating changes to the tribocontact layer[57] 23

Figure 2.2-6 Material transfer during the adhesive wear process: horizontal arrowing showing the moving directions of the contacting bodies; vertical arrows depicting the applied forced[50] 24

Figure 2.2-7 Morphological characteristics of adhesive wear: (a) adhesive craters on titanium (softer material) indicating material transfer; (b) transferred plate-like titanium

on a steel ball (harder material), arrow showing the moving direction of tested sample[75] 25
Figure 2.2-8 Wear tracks of Zircaloy-4 plate showing (a) wear grooves (b) patches of oxide on wear track[73] 25
Figure 2.2-9 Results of pin on disk test of zirconium against itself at different atmospheres: (a) Friction coefficient (b) Wear rate (positive)/transfer rate (negative)[74] 26
Figure 2.2-10 Three different forms of ploughing grooves[57] 28
Figure 2.2-11 Microfatigue and microfracture of worn surface from ductile and brittle materials respectively[77, 78] 28
Figure 2.2-12 Zirconium oxide wear rate vs. facture toughness [79] 29
Figure 2.2-13 Typical SEM images of wear track on zirconia plates with the arrows indicating the sliding direction: (a) K_{IC} = 2.5MPa·$m^{1/2}$, cracking; (b) K_{IC} = 11.6MPa·$m^{1/2}$, grooves with plastic deformation. Arrows showing the sliding direction and magnification scale[79] 30
Figure 2.2-14 Contact of sphere and flat: P and F stand for the normal load and tangential force respectively; p is the pressure distribution, μp and q are the stress distribution for the friction and tangential force respectively; a is the radius of Hertzian contact, while b is the radius of the central slip area[82, 83] 31
Figure 2.2-15 Different fretting regimes: (a) elastic; (b) partial slip; (c) gross slip where 1 and 2 refer to partial slip and full slip respectively[87] 31
Figure 2.2-16 Darken and Gurry plot of the thermodynamics of Zr/O and other relevant systems[96, 97] 35
Figure 2.2-17 Schematic anodic polarisation curve for a metal[100] 36

Figure 2.2-18 Typical polarisation curve and corrosion morphology on zirconium alloys[105] 37
Figure 2.2-19 Schematic diagram of tribocorrosion contact of two metals[106] 38
Figure 2.3-1 Phase diagram of the Zr-O system[21] 40
Figure 2.3-2 Schematic diagram of oxide film on Zircaloy-2 and the process occurring in it during oxidation[97, 98] 43
Figure 2.3-3 EELS scan of Oxide layer formed on ZIRLO^{TM} alloy[137] 45
Figure 2.3-4 Cross sectional SEM images of oxide formed on zirconium alloys showing cracking parallel to the metal/oxide interface[140] 46
Figure 2.3-5 Band contrast maps of oxide film formed on (a) ZIRLO^{TM} (b) Zr-1.0Nb-0.1Fe, showing multi-layered oxide[136] 47
Figure 2.4-1 (a) Surface coating: a layer of different material is added to the surface; (b) Surface modification: surface composition and/or microstructure is modified. 48
Figure 2.4-2 Cross-sectional SEM images of Zr702 after treated at 600°C for 30hours [130] 54
Figure 2.4-3 HRA indents for adhesion class measurements after treatments[181] 55
Figure 3.3-1 Schematic diagram of the nickel plating set-up 62
Figure 3.3-2 Schematic diagram showing working principal of GDOES machine{, #357} 64
Figure 3.3-3 Schematic diagram of Bragg's law 65
Figure 3.3-4 Schematic diagram showing slab cutting from treated surfaces 66
Figure 3.3-5 Schematic diagram showing (a) glued and (b) detached slabs 67
Figure 3.3-6 SEM images of FIB ion milled sampled prepared for TEM 67
Figure 3.3-7 A microhardness indent with its diagonals d_{v1} and d_{v2} 68

Figure 3.3-8 Depth vs. load curve for determination of plastic depth..... 69
Figure 3.3-9 Schematic diagram showing electrochemical cell electrode connections (a) and cross section (b) of set-up for potentiodynamic polarisation test 71
Figure 3.3-10 Schematic diagram of the reciprocating wear tester..... 73
Figure 3.3-11 Schematic diagram of fretting test machine: (1) piezoelectric ceramic actuator; (2) test fixture; (3) force transducer; (4) test sample; (5) counterpart ball; (6) precision-screw controlled transmission unit; (7) displacement transducer..... 75
Figure 4.1-1 Microstructural images of as-received Zr702 using (a): polarised microscopy, showing equiaxed grain microstructure; (b): SEM; (c): EBSD phase mapping depicting the average grain size of about 8 μm, black spots standing for unidentified phases 77
Figure 4.1-2 Microstructure of as-received Zircaloy-4, (a): polarised microscopy; (b): SEM; (c): EBSD phase mapping image showing an average grain size of about 15 μm, black spots standing for unidentified phases 78
Figure 4.1-3 XRD patterns of Zr702 and Zircaloy-4 as-received materials..... 81
Figure 4.2-1 Visual observation of CC treated Zr702 samples, showing surface colour variation as a function of different conditions..... 84
Figure 4.2-2 Visual observation of CC treated Zircaloy-4 samples, showing surface colour variation as a function of treatment conditions 85
Figure 4.2-3 Optical microscopy images for selected Zr702 treated samples: (a) Zr702-4010; (b) Zr702-40100; (c) Zr702-40200; (d) Zr702-5010; (e) Zr702-7010; (f) Zr702-8010 86

Figure 4.2-4 Optical microscopy images for selected Zr702 treated samples: (A) Zry4-4010; (B) Zry4-40100; (C) Zry4-40200; (D) Zry4-5010; (E) Zry4-6010; (F) Zry4-8010 87

Figure 4.2-5 Surface roughness of Zr702 and Zircaloy-4 samples CC treated at 400 °C 90

Figure 4.2-6 Surface roughness of Zr702 and Zircaloy-4 samples CC treated at 600 °C 90

Figure 4.2-7 Surface roughness changes of samples CC treated at 500 and 530 °C..... 90

Figure 4.2-8 Surface roughness changes of samples CC treated for 10hours 91

Figure 4.2-9 GDOES composition depth profiles of CC treated sample (a) Zr702-5310 and Zry4-5310, (b) Zr702-7010 and Zry4-6010..... 93

Figure 4.2-10 XRD patterns of Zr702 alloy CC treated for 10 hours at different temperature 97

Figure 4.2-11 XRD patterns of (a)Zr702-4010, (b)Zr702-5610, (c)Zr702-8010 98

Figure 4.2-12 XRD patterns of Zr702 alloy CC treated at 600 °C for different time 99

Figure 4.2-13 XRD patterns of Zircaloy-4 alloy CC treated for 10 hours at different temperature 101

Figure 4.2-14 XRD pattern of (a)Zry4-4010, (b)Zry4-5010, (c)Zry4-7010..... 102

Figure 4.2-15 XRD patterns of Zircaloy-4 alloy CC treated at 600 °C for different time 103

Figure 4.2-16 Depth XRD patterns of metal/oxide interface (Zr702-7010)..... 104

Figure 4.2-17 *In situ* phase transition of (a) Zr702 and (b) Zircaloy-4 alloy during the CC treatment at 700 °C: m and t refers to m-ZrO_2 (PDF 03-065-1025) and t-ZrO_2 (PDF 01-079-1769) respectively; * stands for shifted peak; α represents α-Zr (PDF 03-065-

3366). The lowercase means the scanning number at 700 °C, e.g. 700_1 means the first XRD scan at 700 °C; each scan lasted approximately 20 minutes. 107
Figure 4.2-18 Cross sectional BSE images of CC treated Zr702: Zr702-4010 samples are protected with an electro-plated nickel layer on top of CC treated surface, while Zr702-5010 without nickel plating protection; Zr702-5310 and Zr702-5610 showing longitudinal columnar gains at the oxide layer 113
Figure 4.2-19 Cross sectional BSE images of CC treated Zircaloy-4: (a) Zry4-4010, (b) Zry4-5010; (c) Zry4-5310; (d) Zry4-5610; (e) Zry4-6010; (f) Zry4-7010; (g) Zry4-8010. Zry4-7010 and Zry4-8010 demonstrated the periodic layer on ceramic surface. 114
Figure 4.2-20 Ceramic layer thickness for Zr702 and Zircaloy-4 after 10 hours of CC treatment at different temperature varying from 400 to 800 °C 115
Figure 4.2-21 SEM observation of samples treated at 400 °C: (a) Zr702-4010; (b) Zry4-4010; (c) Zr702-40100; (d) Zry4-40100; (e) Zr702-40200; (f) Zry4-40200. Nickel were plated on the sample surface for a protection of the ceramic layer; ceramic layer is grey as indicated in the images 115
Figure 4.2-22 SEM observation of Zr702 and Zircaloy-4 treated at 600 °C: (a) Zr702-6010; (b) Zry4-6010; (c) Zr702-6020; (d) Zry4-6020; (e) Zr702-6030; (f) Zry4-6030: (c)~(f) having nickel plating layer on top of the image. 116
Figure 4.2-23 SEM observation of treated Zr702 and Zircaloy-4 samples: (A) Zr702-5050; (B) Zry4-5050; (C) Zr702-5350; (D) Zry4-5350; samples all having nickel plating on top of the image. 117
Figure 4.2-24 Ceramic layer thickness changes in corresponding to CC treatment time 117

Figure 4.2-25 TEM microstructure of sample Zr702-5310 (a) whole surface layer (b) metal/oxide interface 120
Figure 4.2-26 TEM images from Zr702-5310: (a) microstructure of surface layer; and the corresponding SAD patterns (b) surface oxide layer; (c) metal/oxide interface; (d) substrate just beneath interface; (e) substrate far away from the interface. 121
Figure 4.2-27 An enlarged image of Figure 4.2-26 (b) showing the SAD pattern and it's indexing for the oxides formed in the oxide layer of sample Zr702-5310 122
Figure 4.2-28 TEM images from Zry4-5310 (a) microstructure of oxide layer; and the corresponding SAD patterns at (b) oxide layer (c) metal/oxide interface 124
Figure 4.2-29 TEM images from Zry4-5310: (a) substrate structure (b) the corresponding SAD pattern; revealing the lath structure and the twining defects in the substrate 124
Figure 4.3-1 Visual observation images of duplex treated samples 126
Figure 4.3-2 SEM surface morphology observation of CC7-8030 revealing cracks over surface 127
Figure 4.3-3 Surface roughness changes for duplex surface treated samples 127
Figure 4.3-4 GDOES composition depth profiles of duplex treated sample (a) CC7-6030, (b) CC7-7030 and (c) CC7-8030 129
Figure 4.3-5 Typical XRD patterns of duplex treated samples (A) CC7-6010; (B) CC7-7030; (C) CC7-8030 132
Figure 4.3-6 Cross sectional SEM images of duplex treated samples: (a) CC7 BSE; (b) CC7 SE; (c) CC7-6010 BSE; (d) CC7-6010 SE; (e) CC7-6030 BSE; (f) CC7-6030 SE; (g) CC7-7030 BSE; (h) CC7-8030 BSE; samples having nickel plated layer on top of the image. 135

Figure 4.3-7 TEM (a) oxide microstructure of CC7-6030; (b) corresponding SAD pattern 137
Figure 4.3-8 TEM image of CC7-6030: (a) interface; corresponding SAD patterns (b) interface and (c) substrate 137
Figure 4.4-1 Typical load vs. depth curves for sample Zr702-5310 at the load condition of 5 mN 141
Figure 4.4-2 Surface nanohardness changes before and after CC treatment for both Zr702 and Zircaloy-4 141
Figure 4.4-3 Load vs. depth curve for sample Zr702-40100 at the load condition of 5 mN 142
Figure 4.4-4 Young's modulus variation of CC treated Zr702 and Zircaloy-4 sample 142
Figure 4.4-5 Young's Modulus vs. hardness ratio changes before and after CC treatment for both Zr702 and Zircaloy-4 143
Figure 4.4-6 SEM image of cross sectional nanoindentation showing distribution of the indent marks 145
Figure 4.4-7 Hardness depth profiles of Zr702-5310, Zr702-7010 and Zry4-6010 145
Figure 4.4-8 Surface hardness and Young's Modulus of duplex treated samples 147
Figure 4.4-9 Hardness depth profiles of duplex treated samples (a) CC7, CC7-6010 and CC7-6030; (b) CC7-6030, CC7-7030 and CC7-8030 149
Figure 4.4-10 Load bearing capacity of CC treated samples for Zr702 151
Figure 4.4-11 Load bearing capacity of CC treated samples for Zircaloy-4 152
Figure 4.4-12 Two kinds of cracks around indents: (A) circumferential/cone crack around indent from Zry4-5610 under a load of 100 g; (B) radical cracks around indent from Zr702-8010 under a load of 200 g. 153

Figure 4.4-13 Load bearing capacity of CC7 duplex treated samples..... 155
Figure 4.5-1 Polarisation curves of treated and untreated Zr702 samples in 3.5 wt% NaCl..... 160
Figure 4.5-2 SEM images of Zr702 corrosion tested samples: (a) Zr702-UN, edge of the corroded area; (b) Zr702-4010, corrosion pit; (c) Zr702-UN, corrosion morphology inside corrosion pit of Zr702-UN; (d) Zr702-4010, showing micro-pit inside corrosion pit of Zr702-4010; (e) Zr702-5610, showing uniform corrosion; (f) Zr702-8010, showing localised corrosion through ceramic surface blisters. 161
Figure 4.5-3 Polarisation curves of typical Zircaloy-4 samples in 3.5 wt% NaCl..... 164
Figure 4.5-4 SEM images of Zircaloy-4 corrosion tested samples: (a) Zry4-UN, showing corrosion pit; (b) Zry4-4010; (c) Zry4-UN, corrosion morphology inside corrosion pit of Zry4-UN; (d) Zr702-4010, corrosion morphology inside corrosion pits; (e) Zry4-5310, showing uniform corrosion through grain boundaries; (f) Zr702-7010, showing corrosion crack on the surface. 165
Figure 4.5-5 Potentiodynamic polarisation curves for duplex treated samples..... 167
Figure 4.5-6 Typical post corrosion SEM images of duplex treated samples: (a) CC7, showing localised corrosion through blisters; (b)CC7-7030, showing localised corrosion cracking; (c) CC7-8030, showing crevice corrosion; (d) CC7-8030, zoom-in image of arrow mark region in (c) showing hollow underneath corroded surface..... 168
Figure 4.6-1 Measuered CoF of untreated and CC treated Zr702 171
Figure 4.6-2 CoF variations of Zr702-4010, Zr702-7010, Zry4-4010, Zry4-7010 samples from cycle 1 to 100 172
Figure 4.6-3 2D wear track profile for sample Zr702-4010 172
Figure 4.6-4 Measured CoF of untreated and CC treated Zircaloy-4..... 173

Figure 4.6-5 Wear rate comparision for CC treated samples of Zr702 and Zircaloy-4 175
Figure 4.6-6 SEM images of typical wear tracks of CC treated Zr702 samples 177
Figure 4.6-7 2D wear track profile of CC treated sample Zr702-8010 178
Figure 4.6-8 SEM images of typical wear tracks of CC treated Zircaloy-4 samples ... 178
Figure 4.6-9 CoF comparison of duplex surface treated samples 179
Figure 4.6-10 Wear volume loss comparison of duplex surface treated samples 181
Figure 4.6-11 SEM images of tested sample CC7-6010 (a): wear track, SE, showing abrasive wear grooves; (b) wear track, BSE, showing vertical crack at wear track edges; (c) zoomed in image of arrow mark area in (a), showing the microcracks at inside the wear groove; (d) WC counterpart ball, showing the wear scratches. 183
Figure 4.6-12 SEM images of wear track of sample CC7-7030 183
Figure 4.6-13 SEM images of tested CC7-8030: (a) wear track; (b) and (c) marked area in image (a), showing wear grooves and adhesive craters characteristics on the wear track (d) WC ball surfaces, (especially at the edge of the track track) with the of zirconium wear patches. 184
Figure 4.6-14 Friction coefficient of treated and untreated samples at fretting amplitude of 40 μm: in solution (a) 3.5 % NaCl; (b) DI water. 186
Figure 4.6-15 F-D loops at cycle 1000 and 10000 showing consistent gloss slip regime for different fretting test conditions of both untreated and treated samples 187
Figure 4.6-16 Wear volume loss of tested samples during the fretting test 188
Figure 4.6-17 Microscopy observation of fretting scars at different test conditions as marked on each images..... 190

Figure 4.6-18 2D wear track observation at amplitude 40μm: (a) treated sample at 3.5 wt% NaCl; (b) untreated sample at 3.5 wt% NaCl; (c) treated sample at DI water; (d) untreated sample at DI water. 191
Figure 4.6-19 2D wear track depth profiles at the fretting scars at tested conditions .. 191
Figure 5.1-1 SEM observation on cracks showing equiaxed grains in the crack area with grain size of about 80nm 198
Figure 5.1-2 SEM graph of a fractured Zircaloy-4 sample with an oxide layer of about 120 μm[205] 199
Figure 5.1-3 Typical EDX analysis across crack formed at modified ceramic layer, showing a silicon peak at the cracking area which comes from the polishing liquid... 200
Figure 5.2-1 lnx vs. lnt for Zr702 and Zircaloy-4 alloy at treatment temperature 400 °C: x stands for the ceramic layer thickness; t represents the treatment period of time..... 203
Figure 5.2-2 lnx vs. lnt for Zr702 and Zircaloy-4 alloy at treatment temperature 600 °C: x stands for the ceramic layer thickness; t represents the treatment period of time..... 204
Figure 5.2-3 Simplified schematic diagram of zirconium and oxygen reaction during the CC treatment..... 205
Figure 5.2-4 x2 vs. t plots for Zr702 and Zircaloy-4 at treatment temperature 400 °C: x stands for the ceramic layer thickness; t represents the treatment period of time..... 207
Figure 5.2-5 Plot of lnx2 vs. 1/T at different treatment temperature for Zr702 and Zircaloy-4: x stands for the ceramic layer thickness; T represents the treatment temperature 208
Figure 5.2-6 x2 vs. t plots for Zr702 and Zircaloy-4 at treatment temperature 600 °C: x stands for the ceramic layer thickness; t represents the treatment period of time..... 209

Figure 5.3-1 Potential-PH (Pourbaix) diagram of zirconium in 25 °C water[221], A and B are the water redox reaction $O2 + 4H + +4e- = 2H2O$ and $2H + +2e- = H2$ respectively. 211

Figure 5.4-1 Measured CoF values of as-received Zr702 and Zircaloy-4 alloy within to 200 cycles 216

Figure 5.4-2 Electron Channel Contrast Images (ECCI image) of CC7-8030, showing large grains of the diffusion zone 224

Figure 5.4-3 2D wear track profile comparison of samples Zr702-UN, TO+OBD (CC7-8030) and CC+OBD+CC 224

8.2 List of tables

Table 2.1-1 Compositions of most commonly used zirconium alloys[12, 23, 24] 6

Table 2.1-2 Typical physical properties of zirconium [3, 32] 13

Table 2.2-1 The axel ratio of metals at room temperature[67] 20

Table 2.3-1 Main phase transformations in Zr-O phase diagram 40

Table 3.1-1 Chemical composition of as-received Zr702 and Zircaloy-4 57

Table 3.1-2 Sample preparation method 58

Table 3.2-1 CC Treatment codes and conditions of Zr702 and Zircaloy-4 59

Table 3.2-2 Two-step duplex surface treatment codes and conditions 60

Table 3.2-3 Three-step duplex surface treatment codes and conditions 60

Table 3.3-1 Ion polishing method for the as-received zirconium alloys using PECS II 61

Table 4.3-1 Duplex treatment conditions and ceramic layer thicknesses 134

Table 4.5-1 Measured E_{corr} and i_{corr} of as-received and treated CC samples of Zr702 159

Table 4.5-2 Measured E_{corr} and i_{corr} of as-received and treated CC samples of Zircaloy-4 164

8.3 List of abbreviations

ASTM	American Society of Testing
BCC	Body Centred Cubic
BSE	BackScattered Electron
CC	Ceramic Conversion
CCT	Ceramic Conversion Treatment
CE	Counterpart Electrode
CoF	Coefficient of Friction
DC	Direct Current
ECCI	Electron Channel Contrast Image
EDX	Energy Dispersive X-ray spectroscopy
FCC	Face Centred Cubic
FIB	Focused Ion Beam
GDOES	Glowing Discharge Emission Spectroscopy
HCP	Hexagonal Close Pack
HDZ	Hardness Decreasing Zone
LBC	Load Bearing Capacity

LSA	Laser Surface Alloying
LSM	Laser Surface Melting
OBD	Oxygen Boost Diffusion
OCP	Open Circuit Potential
ODZ	Oxygen Diffusion Zone
PDF	Powder Diffraction File
PECS II	Precision Etching Coating System II
PSZ	Partially Stabilised Zirconia
RE	Reference Electrode
SAD	Selected Area Diffraction
SEM	Scanning Electron Microscopy
TEM	Transmission Electron Microscopy
UNS	Unified Number System
WE	Working Electrode
XRD	X-ray Diffraction
Zr	Zirconium

9 REFERENCES

[1] Davis J. Metals Handbook: Desk Edition 2nd edn (Materials Park, OH: ASM International)1998.
[2] Hobbs LW, Rosen VB, Mangin SP, Treska M, Hunter G. Oxidation Microstructures and Interfaces in the Oxidized Zirconium Knee. International Journal of Applied Ceramic Technology 2005;2:221-46.
[3] Kutty TRG, Ravi K, Ganguly C. Studies on hot hardness of Zr and its alloys for nuclear reactors. Journal of Nuclear Materials 1999;265:91-9.
[4] Helmi Attia M. On the fretting wear mechanism of Zr-alloys. Tribology International 2006;39:1320-6.
[5] Fisher NJ, Weckwerth MK, Grandison DA, Cotnam BM. Fretting-wear of zirconium alloys. Nuclear engineering and design 2002;213:79-90.
[6] Palit G, Gadiyar H. Pitting corrosion of zirconium in chloride solution. Corrosion 1987;43:140-8.
[7] Malik F. The pitting corrosion of zirconium and zirconium-niobium alloys in sulphate solutions containing chlorides at 300–373 K. Surface and Coatings Technology 1990;43–44, Part 1:511-20.
[8] Philip A. Schweitzer PE. Metallic Materials: Physical, Mechanical, and Corrosion Properties. New York: Marcel Dekker Inc.; 2003.
[9] Cahn RW, Haasen P, Kramer EJ. Materials Science and Technology: a Comprehensive Treatment. Vol. 8. Structure and Properties of Nonferrous Alloys. VCH Verlagsgesellschaft mbH, P O Box 10 11 61, Weinheim, D-69451, Germany, 1996 837 1996.
[10] Schemel J. Astm Manual on Zirconium and Hafniium: Astm International; 1977.
[11] Stephens WW. Extractive Metallurgy of Zirconium 1945 to the Present. Zirconium in the Nuclear Industry: Proceedings of the Third International Conference, Quebec City, Canada, 10-12 Aug 1976: Philadelphia: ASTM; 1977. p. 1.
[12] Yau T-L. Corrosion of zirconium. CORROSION TECHNOLOGY-NEW YORK AND BASEL- 1996;11:195-252.
[13] Lemaignan C, Motta AT. Zirconium alloys in nuclear applications. Materials science and technology 1994.
[14] Rickover H, Geiger L, Lustman B. History of the development of zirconium alloys for use in nuclear reactors. Energy Research and Development Administration, Washington, DC (USA). Div. of Naval Reactors; 1975.
[15] Sabol GP. ZIRLO–an alloy development success. Journal of ASTM International 2005;2:2942-55.
[16] Adamson RB, Van Swam LF. Zirconium in the nuclear industry: seventh international symposium: ASTM International; 1987.
[17] Harada M, Kimpara M, Abe K. Effect of alloying elements on uniform corrosion resistance of zirconium-based alloys in 360 C water and 400 C steam. ASTM STP 1991;1132:368-91.
[18] Takeda K, Anada H. Mechanism of corrosion rate degradation due to tin. Zirconium in the Nuclear Industry: Twelfth International Symposium: ASTM International; 2000.
[19] Reynolds K. Materials for the Engineering Technician. International Metallurgical Reviews 1973;18:37-8.

[20] International JpoAI, Sae. Metals and Alloys in the Unified Numbering System (11th Edition). ASTM International.
[21] Handbook A. Vol. 3: Alloy Phase Diagrams. ASM International, Materials Park, OH, USA 1992:2.48.
[22] Northwood DO. The development and applications of zirconium alloys. Materials & Design 1985;6:58-70.
[23] ASTM B495-10 Standard Specification for Zirconium and Zirconium Alloy Ingots. ASTM International 2010.
[24] ASTM B350/B350M-11 Standard Specification for Zirconium and Zirconium Alloy Ingots for Nuclear Application. ASTM International 2011.
[25] Banerjee S, Mukhopadhyay P. Phase transformations: examples from titanium and zirconium alloys: Elsevier; 2010.
[26] Jamieson J. Zirconium: phases and compressibility to 120 kilobars. High Temperatures-High Pressures 1973;5:123-31.
[27] Ruch M, Arias D. βα transformation in dilute titanium and zirconium base alloys. Scripta Metallurgica et Materialia 1990;24:1577-82.
[28] Metals ASf, Davis JR. ASM handbook. 2. Properties and selection: nonferrous alloys and special-purpose materials: ASM international; 2009.
[29] Douglass DL. The physical metallurgy of zirconium. Atomic Energy Review (Austria) 1963;1.
[30] Douglass DL. The Metallurgy of zirconium: International Atomic Energy Agency; 1971.
[31] Callister WD, Rethwisch DG. Fundamentals of materials science and engineering: an integrated approach: John Wiley & Sons; 2012.
[32] Adamson RB, Rudling P. 4 - Properties of zirconium alloys and their applications in light water reactors (LWRs). In: Murty KL, editor. Materials Ageing and Degradation in Light Water Reactors: Woodhead Publishing; 2013. p. 151-245.
[33] Craig BD, Anderson DS. Handbook of corrosion data: ASM international; 1994.
[34] Cardarelli F. Materials handbook: a concise desktop reference: Springer Science & Business Media; 2008.
[35] Zieliński A, Sobieszczyk S. Hydrogen-enhanced degradation and oxide effects in zirconium alloys for nuclear applications. International journal of hydrogen energy 2011;36:8619-29.
[36] Sharma G, Limaye P, Jadhav D. Sliding wear and friction behaviour of zircaloy-4 in water. Journal of Nuclear Materials 2009;394:151-4.
[37] Zinkle SJ, Was G. Materials challenges in nuclear energy. Acta Materialia 2013;61:735-58.
[38] Good V, Ries M, Barrack RL, Widding K, Hunter G, Heuer D. Reduced wear with oxidized zirconium femoral heads. The Journal of Bone & Joint Surgery 2003;85:105-10.
[39] Cox B. Pellet-clad interaction (PCI) failures of zirconium alloy fuel cladding—a review. Journal of Nuclear Materials 1990;172:249-92.
[40] Kim K-T. A study on the grid-to-rod fretting wear-induced fuel failure observed in the 16× 16KOFA fuel. Nuclear Engineering and Design 2010;240:756-62.
[41] Cohen J, Lindenbaum B. Fretting corrosion in orthopedic implants. Clinical orthopaedics and related research 1968;61:167-75.
[42] Fontana MG, Stactile W. Corrosion Science and Technology. Plenum Press, London 1970;1:149.

[43] Kolotyrkin YM. Electrochemical behavior of metals during anodic and chemical passivation in electrolytic solutioins. First Int Cong on Metallic Corrosion. London1961. p. p. 10.
[44] Likhanskii V, Evdokimov I. Effect of additives on the susceptibility of zirconium alloys to nodular corrosion. Journal of Nuclear Materials 2009;392:447-52.
[45] Farina S, Duffo G, Galvele J. Stress corrosion cracking of zirconium and Zircaloy-4 in halide aqueous solutions. Corrosion science 2003;45:2497-512.
[46] Nagano H, Kajimura H. The stress corrosion cracking performance of pure zirconium and zirconium alloys in highly oxidizing nitric acid. Corrosion science 1996;38:781-91.
[47] Pierron ON, Koss DA, Motta AT, Chan KS. The influence of hydride blisters on the fracture of Zircaloy-4. Journal of Nuclear Materials 2003;322:21-35.
[48] Northwood D, Kosasih U. Hydrides and delayed hydrogen cracking in zirconium and its alloys. International metals reviews 1983;28:92-121.
[49] Fidleris V. The irradiation creep and growth phenomena. Journal of Nuclear Materials 1988;159:22-42.
[50] X.Y. Li UoB. Wear and wear mechanism. http://emrtk.uni-miskolc.hu/projektek/adveng/home/kurzus/korsz_anyagtech/1_konzultacio_elemei/wear_and_wear_mechanism.htm.
[51] Gagg CR, Lewis PR. Wear as a product failure mechanism – Overview and case studies. Engineering Failure Analysis 2007;14:1618-40.
[52] Priya R, Mallika C, Mudali UK. Wear and tribocorrosion behaviour of 304L SS, Zr-702, Zircaloy-4 and Ti-grade2. Wear 2014;310:90-100.
[53] Basu B, Vitchev RG, Vleugels J, Celis JP, Van Der Biest O. Influence of humidity on the fretting wear of self-mated tetragonal zirconia ceramics. Acta Materialia 2000;48:2461-71.
[54] Parlar Z, Bakkal M, Shih AJ. Sliding tribological characteristics of Zr-based bulk metallic glass. Intermetallics 2008;16:34-41.
[55] Han JG, Lee JS, Choi BH, Kim W, Tang G. Wear and fretting wear behaviour of ion-implanted Zircaloy-4. Surface and Coatings Technology 1996;83:307-12.
[56] Cho KH, Kim TH, Kim SS. Fretting wear characteristics of Zircaloy-4 tube. Wear 1998;219:3-7.
[57] Blau PJ. ASM Handbook, Volume 18 - Friction, Lubrication, and Wear Technology. ASM International; 1992.
[58] Lewis PR, Reynolds K, Gagg C. Forensic materials engineering: Case studies: CRC Press; 2003.
[59] Blau PJ. A multi-stage wear model for grid-to-rod fretting of nuclear fuel rods. Wear 2014;313:89-96.
[60] Hoeppner DW, Chandrasekaran V. Fretting in orthopaedic implants: A review. Wear 1994;173:189-97.
[61] Hutchings IM. Tribology: friction and wear of engineering materials. 1992.
[62] Dong H. Development of novel surface engineering technologies for Ti6A14V alloy. University of Birmingham: University of Birmingham; 1997.
[63] Sarkar AD. Friction and wear. Academic Press, xvi+ 423, 23 x 15 cm, illustrated 1980.
[64] Bowden FP, Tabor D. The Friction and Lubrication of Solids-{Part I}. 1950.
[65] Buckley DH, Johnson RL. The influence of crystal structure and some properties of hexagonal metals on friction and adhesion. Wear 1968;11:405-19.

[66] Karapetian SS, Korostelin YI. The dependence of the friction coefficient on the crystal structure of solids: Physical principles. Wear 1983;85:133-41.
[67] Bhansali KJ, Miller AE. The role of stacking fault energy on galling and wear behavior. Wear 1982;75:241-52.
[68] Chaudhuri DK, Xie D, Lakshmanan AN. The influence of stacking fault energy on the wear resistance of nickel base alloys. Wear 1997;209:140-52.
[69] Feller HG, Gao B. Correlation of tribological and metal physics data: The role of stacking fault energy. Wear 1989;132:1-7.
[70] Dieter GE, Bacon D. Mechanical metallurgy: McGraw-Hill New York; 1986.
[71] Buckley DH, Johnson RL. Friction and wear of hexagonal metals and alloys as related to crystal structure and lattice parameters in vacuum. ASLE TRANSACTIONS 1966;9:121-35.
[72] Rabinowicz E, Peterson M, Winer W. Wear control handbook. American Society of Mechanical Engineers, New York 1980:486.
[73] Sharma G, Limaye PK, Jadhav DT. Sliding wear and friction behaviour of zircaloy-4 in water. Journal of Nuclear Materials 2009;394:151-4.
[74] Murakami T, Mano H, Kaneda K, Hata M, Sasaki S, Sugimura J. Friction and wear properties of zirconium and niobium in a hydrogen environment. Wear 2010;268:721-9.
[75] Dong H, Bell T. Enhanced wear resistance of titanium surfaces by a new thermal oxidation treatment. Wear 2000;238:131-7.
[76] Archard J. Contact and rubbing of flat surfaces. Journal of applied physics 1953;24:981-8.
[77] Pooley CM, Tabor D. Friction and molecular structure: the behaviour of some thermoplastics. Proceedings of the Royal Society of London A: Mathematical, Physical and Engineering Sciences: The Royal Society; 1972. p. 251-74.
[78] Kovaříková I, Szewczyková B, Blaškoviš P. Study and characteristic of abrasive wear mechanisms. Materials Science and Technology [online]-ISSN:1335-9053.
[79] Fischer TE, Anderson MP, Jahanmir S. Influence of fracture toughness on the wear resistance of yttria‐doped zirconium oxide. Journal of the American Ceramic Society 1989;72:252-7.
[80] Fischer T, Tomizawa H. Interaction of tribochemistry and microfracture in the friction and wear of silicon nitride. Wear 1985;105:29-45.
[81] International A. ASM handbook: Friction, lubrication, and wear technology: ASM International; 1992.
[82] Johnson K. Surface interaction between elastically loaded bodies under tangential forces. Proceedings of the Royal Society of London A: Mathematical, Physical and Engineering Sciences: The Royal Society; 1955. p. 531-48.
[83] Mindlin R. Compliance of elastic bodies in contact. J of Appl Mech 1949;16.
[84] Waterhouse R. Occurrence of fretting in practice and its simulation in the laboratory. Materials evaluation under fretting conditions:3-16.
[85] Berthier Y, Vincent L, Godet M. Fretting fatigue and fretting wear. Tribology international 1989;22:235-42.
[86] Lee Y-H, Kim H-K. Effect of spring shapes on the variation of loading conditions and the wear behaviour of the nuclear fuel rod during fretting wear tests. Wear 2007;263:451-7.
[87] Duisabeau L, Combrade P, Forest B. Environmental effect on fretting of metallic materials for orthopaedic implants. Wear 2004;256:805-16.
[88] Hurricks P. The mechanism of fretting—a review. Wear 1970;15:389-409.

[89] Uhlig HH. Mechanism of fretting corrosion. JOURNAL OF APPLIED MECHANICS-TRANSACTIONS OF THE ASME 1954;21:401-7.
[90] Waterhouse R. The role of adhesion and delamination in the fretting wear of metallic materials. Wear 1977;45:355-64.
[91] King SJ, Young MY, Guérout FM, Fisher NJ. Fretting-Wear Behavior of Zircaloy-4, OPTIN™, and ZIRLO™ Fuel Rods and Grid Supports Under Various Autoclave and Hydraulic Loop Endurance Test Conditions. J of ASTM International 2005;2.
[92] Kim J, Park J, Park J, Jeon K. Sliding wear and friction behavior of zirconium alloy with heat-treated Inconel718. Nuclear Engineering and Design 2014;269:66-71.
[93] Calhoun SF. Effect of Metal Hardness and Surface Finish Upon Fretting Corrosion. DTIC Document; 1963.
[94] Baysinger G. CRC Handbook of Chemistry and Physics: National Institute of Standards and Technology; 2015.
[95] Wikipedia. Corrosion. http://en.wikipedia.org/wiki/Corrosion.
[96] Komarek K, Silver M. Thermodynamic Properties of Zirconium-Oxygen, Titanium-Oxygen and Hafnium-Oxygen Alloys. Thermodynamics of Nuclear Materials:749-74.
[97] IAEA. Corrosion of Zirconium Alloys in Nuclear Power Plants. In: Agency IAE, editor. Vienna, Austria1993.
[98] Cox B. Oxidation of Zirconium and its Alloys. Advances in Corrosion Science and Technology: Springer; 1976. p. 173-391.
[99] Schweitzer PA. Corrosion Engineering Handbook, -3 Volume Set: CRC Press; 1996.
[100] Gareth Hinds JT. THE ELECTROCHEMISTRY OF CORROSION http://www.npl.co.uk/upload/pdf/the_electrochemistry_of_corrosion_with_figures.pdf.
[101] Brown R, Mears R. The electrochemistry of corrosion. Transactions of the Electrochemical Society 1938;74:495-517.
[102] Perez N. Electrochemistry and corrosion science: Springer Science & Business Media; 2004.
[103] Kolotyrkin YM. Metal pitting corrosion. Khim Promyshl 1963:678-85.
[104] Hoar TP. The production and breakdown of the passivity of metals. Corrosion Science 1967;7:341-55.
[105] Wang L, Hu X, Nie X. Deposition and properties of zirconia coatings on a zirconium alloy produced by pulsed DC plasma electrolytic oxidation. Surface and Coatings Technology 2013;221:150-7.
[106] Fischer A, Mischler S. Tribocorrosion: fundamentals, materials and applications. Journal of Physics D: Applied Physics 2006;39:null.
[107] Landolt D. Electrochemical and materials aspects of tribocorrosion systems. Journal of Physics D: applied physics 2006;39:3121.
[108] Wood RJ. Tribo-corrosion of coatings: a review. Journal of Physics D: Applied Physics 2007;40:5502.
[109] Adamson R, Garzarolli F, Cox B, Strasser A, Rudling P. Corrosion mechanisms in zirconium alloys. ANT International 2007.
[110] Sumerling R, Garlick A, Stuttard A, Hartog J, Trowse F, Sims P. Further evidence of Zircaloy corrosion in fuel elements irradiated in a steam generating heavy water reactor. Zirconium in the Nuclear Industry: Fourth International Conference, ASTM STP1979. p. 107.

[111] Garlick A, Sumerling R, Shires G. Crud-induced overheating defects in water reactor fuel pins. 1977.
[112] Marlowe M, Armijo J, Cheng B, Adamson R. Nuclear Fuel Cladding Localized Corrosion. Light Water Reactor Fuel Performance 1985;1:73-90.
[113] Geringer J, Forest B, Combrade P. Fretting-corrosion of materials used as orthopaedic implants. Wear 2005;259:943-51.
[114] Doerffler WW. A Contribution to the Mechanism of Dissolution and Diffusion of Oxygen in Zirconium. Thermodynamics Vol II Proceedings of the Symposium on Thermodynamics with Emphasis on Nuclear Materials and Atomic Transport in Solids1966.
[115] Porte H, Schnizlein J, Vogel R, Fischer D. Oxidation of zirconium and zirconium alloys. Journal of the Electrochemical Society 1960;107:506-15.
[116] Yan Y, Burtseva T, Billone M. High-temperature steam-oxidation behavior of Zr-1Nb cladding alloy E110. Journal of Nuclear Materials 2009;393:433-48.
[117] Couet A, Motta AT, Comstock RJ. Hydrogen pickup measurements in zirconium alloys: Relation to oxidation kinetics. Journal of Nuclear Materials 2014;451:1-13.
[118] Motta A, Gomes da Silva M, Yilmazbayhan A, Comstock R, Cai Z, Lai B. Microstructural characterization of oxides formed on model Zr alloys using synchrotron radiation. J ASTM Intern 2008;5:20.
[119] Lin Y-P, DeLuca J. On the effects of heat treatment and surface orientation on corrosion and hydrogen ingress of Zr–2.5 Nb pressure tube material. Journal of nuclear materials 1999;265:1-11.
[120] Baek JH, Jeong YH. Breakaway phenomenon of Zr-based alloys during a high-temperature oxidation. Journal of Nuclear Materials 2008;372:152-9.
[121] Ahmed T, Keys L. The breakaway oxidation of zirconium and its alloys a review. Journal of the Less Common Metals 1975;39:99-107.
[122] Cox B. Processes occurring during the breakdown of oxide films on zirconium alloys. Journal of Nuclear Materials 1969;29:50-66.
[123] Ploc R. Transmission electron microscopy of thin (< 2000 å) thermally formed ZrO 2 films. Journal of Nuclear Materials 1968;28:48-60.
[124] Cox B, Donner A. The morphology of thick oxide films on Zircaloy-2. Journal of Nuclear Materials 1973;47:72-8.
[125] Xu C, Gao W. Pilling-Bedworth ratio for oxidation of alloys. Material Research Innovations 2000;3:231-5.
[126] Roy C, Burgess B. A study of the stresses generated in zirconia films during the oxidation of zirconium alloys. Oxidation of metals 1970;2:235-61.
[127] Maroto A, Bordoni R, Villegas M, Olmedo A, Blesa M, Iglesias A, et al. Growth and characterization of oxide layers on zirconium alloys. Journal of nuclear materials 1996;229:79-92.
[128] Bryner J. The cyclic nature of corrosion of Zircaloy-4 in 633 K water. Journal of nuclear materials 1979;82:84-101.
[129] Tejland P. Microstructure Investigation of the Oxidation Process in Zircaloy-2-The Effect of Intermetallic Particle Size: Chalmers University of Technology; 2012.
[130] Ji R, Li X, Dong H. Ceramic conversion treatment of zirconium alloys to combat corrosion wear. Surface Engineering 2010;26:30-6.
[131] Weidinger H. Raman spectroscopy study of the tetragonal-to-monoclinic transition in zirconium oxide scales and determination of overall oxygen diffusion by

nuclear microanalysis of O18. Zirconium in the Nuclear Industry: Proceedings of the International Conference: ASTM; 1991. p. 416.
[132] Yilmazbayhan A, Motta AT, Comstock RJ, Sabol GP, Lai B, Cai Z. Structure of zirconium alloy oxides formed in pure water studied with synchrotron radiation and optical microscopy: relation to corrosion rate. Journal of Nuclear Materials 2004;324:6-22.
[133] Pétigny N, Barberis P, Lemaignan C, Valot C, Lallemant M. In situ XRD analysis of the oxide layers formed by oxidation at 743 K on Zircaloy 4 and Zr–1NbO. Journal of Nuclear Materials 2000;280:318-30.
[134] Barberis P, Merle-Méjean T, Quintard P. On Raman spectroscopy of zirconium oxide films. Journal of Nuclear Materials 1997;246:232-43.
[135] Yilmazbayhan A, Breval E, Motta AT, Comstock RJ. Transmission electron microscopy examination of oxide layers formed on Zr alloys. Journal of Nuclear Materials 2006;349:265-81.
[136] Garner A, Hu J, Harte A, Frankel P, Grovenor C, Lozano-Perez S, et al. The effect of Sn concentration on oxide texture and microstructure formation in zirconium alloys. Acta Materialia 2015;99:259-72.
[137] Ni N, Hudson D, Wei J, Wang P, Lozano-Perez S, Smith G, et al. How the crystallography and nanoscale chemistry of the metal/oxide interface develops during the aqueous oxidation of zirconium cladding alloys. Acta Materialia 2012;60:7132-49.
[138] Nicholls RJ, Ni N, Lozano‐Perez S, London A, McComb DW, Nellist PD, et al. Crystal structure of the ZrO phase at zirconium/zirconium oxide interfaces. Advanced engineering materials 2015;17:211-5.
[139] Garzarolli F, Seidel H, Tricot R, Gros J. Oxide growth mechanism on zirconium alloys. ASTM STP 1991;1132:395-415.
[140] Preuss M, Frankel P, Lozano-Perez S, Hudson D, Polatidis E, Ni N, et al. Studies regarding corrosion mechanisms in zirconium alloys. J ASTM Int 2011;8:649-81.
[141] Ni N, Lozano-Perez S, Jenkins M, English C, Smith G, Sykes J, et al. Porosity in oxides on zirconium fuel cladding alloys, and its importance in controlling oxidation rates. Scripta Materialia 2010;62:564-7.
[142] Yardley SS, Moore KL, Ni N, Wei JF, Lyon S, Preuss M, et al. An investigation of the oxidation behaviour of zirconium alloys using isotopic tracers and high resolution SIMS. Journal of Nuclear Materials 2013;443:436-43.
[143] Tejland P, Andrén H-O. Origin and effect of lateral cracks in oxide scales formed on zirconium alloys. Journal of Nuclear Materials 2012;430:64-71.
[144] Fu Y, Wei J, Batchelor AW. Some considerations on the mitigation of fretting damage by the application of surface-modification technologies. Journal of Materials Processing Technology 2000;99:231-45.
[145] Goto T, Ishigaki H, Ito Y. Electrochemical surface nitriding of zirconium in LiCl–KCl–Li< sub> 3</sub> N systems. Materials Science and Engineering: A 2004;371:353-8.
[146] Healy MD, Smith DC, Rubiano RR, Springer RW, Parmeter JE. The organometallic chemical vapor deposition of transition metal carbides: The use of homoleptic alkyls. MRS Proceedings: Cambridge Univ Press; 1993. p. 127.
[147] Matykina E, Arrabal R, Skeldon P, Thompson G, Wang P, Wood P. Plasma electrolytic oxidation of a zirconium alloy under AC conditions. Surface and Coatings Technology 2010;204:2142-51.

[148] Cengiz S, Gencer Y. The characterization of the oxide based coating synthesized on pure zirconium by plasma electrolytic oxidation. Surface and Coatings Technology 2014;242:132-40.
[149] Varacalle Jr D, Lundberg L, Herman H, Bancke G, Riggs II W. Vacuum plasma sprayed zirconium carbide coatings. Surface and Coatings Technology 1994;68:86-91.
[150] Brückner J, Mäntylä T. Reactive magnetron sputtering of zirconium carbide films using Ar-CH< sub> 4</sub> gas mixtures. Surface and Coatings Technology 1993;59:166-70.
[151] Martin PJ, MacLeod HA, Netterfield RP, Pacey C, Sainty WG. Ion-beam-assisted deposition of thin films. Applied Optics 1983;22:178-84.
[152] He X-M, Shu L, Li H-B, Weng D. High corrosion resistant ZrC films synthesized by ion-beamassisted deposition. Journal of materials research 1999;14:615-8.
[153] Schulz U, Schmücker M. Microstructure of ZrO< sub> 2</sub> thermal barrier coatings applied by EB-PVD. Materials Science and Engineering: A 2000;276:1-8.
[154] Almeida D, Silva C, Nono M, Cairo C. EB–PVD TBCs of zirconia co-doped with yttria and niobia, a microstructural investigation. Surface and Coatings Technology 2006;200:2827-33.
[155] Kimura T, Goto T. Rapid synthesis of yttria-stabilized zirconia films by laser chemical vapor deposition. Materials Transactions 2003;44:421-4.
[156] Wang L, Hu X, Nie X. Deposition and properties of zirconia coatings on a zirconium alloy produced by pulsed DC plasma electrolytic oxidation. Surface and Coatings Technology 2013;221:150-7.
[157] Batchelor A, Stachowiak G, Stachowiak G, Leech P, Reinhold O. Control of fretting friction and wear of roping wire by laser surface alloying and physical vapour deposition coatings. Wear 1992;152:127-50.
[158] Schickner W, Beach J, Faust CL. Electroplating on Zirconium. Journal of The Electrochemical Society 1953;100:289-91.
[159] Cotell CM, Sprague JA, Smidt FA. ASM Handbook: Surface Engineering: ASM International; 1994.
[160] Goto T. Thermal barrier coatings deposited by laser CVD. Surface and Coatings Technology 2005;198:367-71.
[161] Peng D, Bai X, Chen X, Zhou Q. The air oxidation behavior of lanthanum ion implanted zirconium at 500 C. Nuclear Instruments and Methods in Physics Research Section B: Beam Interactions with Materials and Atoms 2003;201:589-94.
[162] Bai X, Xu J, He F, Fan Y. The air oxidation of yttrium ion implanted zircaloy-4 at 500° C. Nuclear Instruments and Methods in Physics Research Section B: Beam Interactions with Materials and Atoms 2000;160:49-53.
[163] Peng D, Bai X, Chen X, Zhou Q, Liu X, Deng P. Comparison of aqueous corrosion behavior of zirconium and zircaloy-4 implanted with molybdenum. Nuclear Instruments and Methods in Physics Research Section B: Beam Interactions with Materials and Atoms 2003;211:55-68.
[164] Anttila A, Keinonen J, Uhrmacher M, Vahvaselkä S. Nitrogen implantation of metals. Journal of Applied Physics 1985;57:1423-5.
[165] García J, Guétte A, Medrano A, Labrugére C, Rico M, Lahaye M, et al. Nitrogen ion implantation on group IVb metals:: chemical, mechanical and tribological study. Vacuum 2002;64:343-51.
[166] Lee S, Park C, Kwon H, Choi B. Corrosion resistance of nitrogen-implanted Zircaloy-4 in high-temperature water. Journal of nuclear materials 2000;282:223-31.

[167] Rawers J, Reitz W, Bullard S, Roub E. Surface and corrosion study of laser-processed zirconium alloys. Corrosion 1991;47:769-77.
[168] Reitz W, Rawers J. Effect of laser surface melted zirconium alloys on microstructure and corrosion resistance. Journal of materials science 1992;27:2437-43.
[169] Steen WM. Arc augmented laser processing of materials. Journal of Applied Physics 1980;51:5636-41.
[170] Mazumder J. Laser assisted surface coatings. Metallurgical and Ceramic Protective Coatings: Springer; 1996. p. 74-111.
[171] Arata Y. Plasma, electron and laser beam technology: development and use in materials processing. 1986.
[172] Lee S, Park C, Lim Y, Kwon H. Influences of laser surface alloying with niobium (Nb) on the corrosion resistance of Zircaloy-4. Journal of nuclear materials 2003;321:177-83.
[173] Vander Voort GF. ASM handbook: metallography and microstructures: ASM International (OH); 2004.
[174] Fraker AC. Corrosion Behavior of Zircaloy Spent Fuel Cladding in a Repository. Nat Inst Stds Tech July, 1989;(NISTIR)-89-4114.
[175] Shevtsov V, Valov A, Vlasov M, Gusachenko E, Stesik L. High-temperature oxidation of an alloy of zirconium and niobium. Combustion, Explosion and Shock Waves 1997;33:647-51.
[176] Yau T-L, Consultancy T-LY. Corrosion of Zirconium. ASM Handbook 2005;13:300.
[177] Rosa C. Oxidation of zirconium—A critical review of literature. Journal of the Less Common Metals 1968;16:173-201.
[178] Dong H. Surface engineering of light alloys: Aluminium, magnesium and titanium alloys: Elsevier; 2010.
[179] Dong H, Bell T. Tribological behaviour of alumina sliding against Ti6Al4V in unlubricated contact. Wear 1999;225:874-84.
[180] Dong H, Li X. Oxygen boost diffusion for the deep-case hardening of titanium alloys. Materials Science and Engineering: A 2000;280:303-10.
[181] Reif M, Scherm F, Galetz M, Glatzel U. An Enhanced Three-Step Oxidation Process to Improve Oxide Adhesion on Zirconium Alloys. Oxidation of Metals 2014;82:99-112.
[182] Pawar V, Jani SC, Weaver C. Diffusion-hardened medical implant. Google Patents; 2011.
[183] GDOES.
[184] Nisbett J, Budynas R. Shigley's mechanical engineering design. McGraw-Hill, New York; 2008.
[185] Beer FP, Johnston ER. Statics and mechanics of materials: McGraw-Hill; 1992.
[186] Meng XY, Northwood DO. A TEM study of the C15 type Zr (CrFe) 2 Laves phase in Zircaloy-4. Journal of Nuclear Materials 1985;136:83-90.
[187] Handbook A. Metallography and microstructures. Edited by GF Vander Voort, ASM Intenational 2004;9.
[188] Cox B. Are Zirconia Corrosion Films a Form of Partially Stabilised Zirconia (PSZ)?: Chalk River Nuclear Laboratories; 1987.
[189] Cox B. Some thoughts on the mechanisms of in-reactor corrosion of zirconium alloys. Journal of Nuclear Materials 2005;336:331-68.

[190] Wei J, Frankel P, Polatidis E, Blat M, Ambard A, Comstock R, et al. The effect of Sn on autoclave corrosion performance and corrosion mechanisms in Zr–Sn–Nb alloys. Acta Materialia 2013;61:4200-14.
[191] A comparison of Alumina and Zirconia Engineering Ceramics. AZO Materials2014.
[192] Zirconium Oxide, ZrO_2 ceramic properties. Accuratus2013.
[193] Alcalá J, Barone AC, Anglada M. The influence of plastic hardening on surface deformation modes around Vickers and spherical indents. Acta Materialia 2000;48:3451-64.
[194] Pêcheur D, Lefebvre F, Motta AT, Lemaignan C, Wadier JF. Precipitate evolution in the Zircaloy-4 oxide layer. Journal of Nuclear Materials 1992;189:318-32.
[195] Keith O, Kusy RP, Whitley JQ. Zirconia brackets: An evaluation of morphology and coefficients of friction. American Journal of Orthodontics and Dentofacial Orthopedics 1994;106:605-14.
[196] Moulzolf SC, Lad RJ, Blau PJ. Microstructural effects on the friction and wear of zirconia films in unlubricated sliding contact. Thin Solid Films 1999;347:220-5.
[197] He Y, Winnubst L, Burggraaf AJ, Verweij H, Varst PGT, With B. Grain‐Size Dependence of Sliding Wear in Tetragonal Zirconia Polycrystals. Journal of the American Ceramic Society 1996;79:3090-6.
[198] Fouvry S, Kapsa P, Vincent L. An elastic–plastic shakedown analysis of fretting wear. Wear 2001;247:41-54.
[199] Manicone PF, Rossi Iommetti P, Raffaelli L. An overview of zirconia ceramics: Basic properties and clinical applications. Journal of Dentistry 2007;35:819-26.
[200] Wilkins NJM. Infra-red interference measurements on oxide films on zirconium. Corrosion Science 1964;4:17-24.
[201] Wilkins NJM. Optical measurement of oxide films on zirconium in the range of wavelengths from 2000 to 2·5 μ. Corrosion Science 1965;5:3-18.
[202] Koski K, Hölsä J, Juliet P. Properties of zirconium oxide thin films deposited by pulsed reactive magnetron sputtering. Surface and Coatings Technology 1999;120–121:303-12.
[203] Davidson JA. Zirconium oxide and zirconium nitride coated stents. Google Patents; 1997.
[204] Tejland P, Langhammer C, Andrén H-O. On the black oxide colour of zirconium alloys. Journal of Nuclear Materials 2010;400:79-83.
[205] Localized surface plasmon.
[206] Moya JS, Diaz M, Bartolomé JF, Roman E, Sacedon JL, Izquierdo J. Zirconium oxide film formation on zircaloy by water corrosion. Acta Materialia 2000;48:4749-54.
[207] Roy C, David G. X-ray diffraction analyses of zirconia films on zirconium and zircaloy-2. Journal of Nuclear Materials 1970;37:71-81.
[208] Lin J, Li H, Nam C, Szpunar JA. Analysis on volume fraction and crystal orientation relationship of monoclinic and tetragonal oxide grown on Zr–2.5Nb alloy. Journal of Nuclear Materials 2004;334:200-6.
[209] Godlewski J, Gros J, Lambertin M, Wadier J, Weidinger H. Raman Spectroscopy Study of the Tetragonal-to-monoclinic Transition in Zirconium Oxide Scales and Determination of Overall Oxygen Diffusion by Nuclear Microanalysis of O18. Zirconium in the Nuclear Industry: 9th International Symposium: ASTM International; 1991.

[210] Godlewski J, Bouvier P, Lucazeau G, Fayette L. Stress distribution measured by Raman spectroscopy in zirconia films formed by oxidation of Zr-based alloys. Zirconium in the Nuclear Industry: Twelfth International Symposium: ASTM International; 2000.
[211] Bouvier P, Godlewski J, Lucazeau G. A Raman study of the nanocrystallite size effect on the pressure–temperature phase diagram of zirconia grown by zirconium-based alloys oxidation. Journal of Nuclear Materials 2002;300:118-26.
[212] Garvie RC. The occurrence of metastable tetragonal zirconia as a crystallite size effect. The journal of physical chemistry 1965;69:1238-43.
[213] Djurado E, Bouvier P, Lucazeau G. Crystallite Size Effect on the Tetragonal-Monoclinic Transition of Undoped Nanocrystalline Zirconia Studied by XRD and Raman Spectrometry. Journal of Solid State Chemistry 2000;149:399-407.
[214] Glavicic MG. Development and application of techniques for the microstructural characterization of hydrogen permeability in zirconium oxides1998.
[215] Ding Y, Northwood DO. TEM study of the oxide-metal interface formed during corrosion of Zr-2.5 wt.% Nb pressure tubing. Materials characterization 1993;30:13-22.
[216] Anada H, Takeda K. Microstructure of oxides on Zircaloy-4, 1.0 Nb Zircaloy-4, and Zircaloy-2 formed in 10.3-MPa steam at 673 K. Zirconium in the Nuclear Industry: Eleventh International Symposium: ASTM International; 1996.
[217] Bossis P, Thomazet J, Lefebvre F. study of the mechanisms controlling the oxide growth under irradiation: characterization of irradiated zircaloy-4 and Zr-1Nb-O oxide scales. Zirconium in the Nuclear Industry: Thirteenth International Symposium: ASTM International; 2002.
[218] Varias AG, Massih AR. Simulation of hydrogen embrittlement in zirconium alloys under stress and temperature gradients. Journal of Nuclear Materials 2000;279:273-85.
[219] Wäppling D, Massih AR, Ståhle P. A model for hydride-induced embrittlement in zirconium-based alloys. Journal of Nuclear Materials 1997;249:231-8.
[220] Cox B. The Oxidation and Corrosion of Zirconium and its Alloys V. Mechanism of Oxide Film Growth and Breakdown on Zirconium and Zircaloy‐2. Journal of The Electrochemical Society 1961;108:24-30.
[221] Garde AM, Pati SR, Krammen MA, Smith GP, Endter RK. Corrosion behavior of Zircaloy-4 cladding with varying tin content in high-temperature pressurized water reactors. Zirconium in the Nuclear Industry: Tenth International Symposium: ASTM International; 1994.
[222] Chen X, Bai X, Deng P, Peng D, Liu X. Potential-pH Diagrams of Zr-H 2 O System at the Increased Temperatures. Xiyou Jinshu Cailiao yu Gongcheng(Rare Metal Materials and Engineering) 2004;33:710-3.
[223] Lee SJ, Kwon HS, Kim W, Choi BH. Effects of compositional and structural change on the corrosion behaviour of nitrogen implanted Zircaloy-4. Materials Science and Engineering: A 1999;263:23-31.
[224] Hornkjøl S. Pitting corrosion of zirconium and hafnium. Electrochimica Acta 1988;33:289-92.
[225] Maraghini M, Adams GB, Van Rysselberghe P. Studies on the anodic polarization of zirconium and zirconium alloys. Journal of the Electrochemical Society 1954;101:400-9.

[226] Schully J, Sridhar N, Dunn D, Brossia C, Cragnolino G, Kearns J. Crevice Corrosion. Corrosion Tests and Standards: Application and Interpretation–second edition (2005). West Conshohocken, PA: ASTM International; 2005. p. 221-32.
[227] Blok H. The flash temperature concept. Wear 1963;6:483-94.
[228] Quinn T, Winer W. An experimental study of the “hot-spots” occurring during the oxidational wear of tool steel on sapphire. Journal of Tribology 1987;109:315-9.